University of Nottingham

UK | CHINA | MALAYSIA

The Design and Construction of a Scanning Probe Nitrogen Vacancy Centre Magnetometer

Ashley James Tyler

A thesis submitted to the University of Nottingham for the degree of Doctor of Philosophy

Contents

Abstract

The isolated spin of the nitrogen-vacancy (NV) centre in diamond, which is formed from a vacancy and an adjacent nitrogen atom replacing carbon atoms in the diamond lattice, provides a highly promising system to realise non-invasive high-sensitivity magnetometry, even at room temperatures. The combination of the atomically sized detection volume, which for a single NV centre is defined by the spatial extent of the wavefunction, and high magnetic field sensitivity makes the NV centre a highly promising sensor to investigate magnetism on the nanoscale. In recent years NV centres have been used to produce 2D maps of magnetic fields with nanoscale resolution by affixing single or small numbers of NV centres to the very tip of a scanning probe. To date, scanning probe NV magnetometers have produced images with some of the smallest probe-sample distances seen in magnetic field sensing, with probe-sample distances of the order 50 nm routinely achieved.

Scanning probe NV magnetometry utilises two established scientific techniques; atomic force microscopy, which provides the scanning probe element required for the formation of 2D images, and confocal microscopy for magnetic field readout out via measurement of the NV centre's magnetically sensitive photoluminescence. Therefore, an instrument designed for scanning probe NV magnetometry will feature both optical instrumentation optimised to collect luminescence from atomically sized sources, in particular NV centres fixed to functionalised AFM probes, and an atomic force microscope that can be operated while simultaneously making optical measurements. In addition to the established imaging techniques of confocal microscopy and AFM, an instrument focusing on NV centre magnetometry requires a method of applying a high-frequency magnetic field for spin state

manipulation and a variable strength, variable orientation bias magnetic field. While a prerequisite for NV magnetometry, these final components extend an NV magnetometer's functionality, enabling the study of other species that exhibit magnetically sensitive photoluminescence. As such, an instrument based on a scanning probe NV magnetometer will not only be able to perform high-resolution magnetometry, but also operate in a wide range of imaging modalities, providing a versatile tool for sub-micron sample characterisation. This thesis presents the design, assembly and performance of a custom-built sub-micron characterisation tool based on a scanning probe NV magnetometer.

This research project's main output is the instrument itself, with the key results the figures of merit for each imaging modality. A sample of nanodiamonds deposited onto a silicon/silicon dioxide wafer serves as the test target for most of the imaging modes. The optical imaging modes' performance is presented through diffraction-limited spatial maps, both where photoluminescence and backscattered laser light provide the dominant signal. To demonstrate this instrument's capability to measure the temporal and spectral characteristics from diffraction-limited luminescent sources, time-correlated single photon counting measurements and emission spectra from sources on the nanodiamond sample are presented. The performance of custom-built AFM is demonstrated through the measurement of a calibration sample and then the suitability for NV magnetometry demonstrated by presenting simultaneously recorded AFM confocal microscope measurements. This instrument's capability for NV centre magnetometry is presented by showing optically detected magnetic resonances from photoluminescent sources in nanodiamonds. Finally, the progress towards NV centre magnetometry in this instrument is reviewed.

The recent discovery of photoluminescence originating from single-photon sources in 2D materials, in particular from emitters in hexagonal boron nitride (hBN) which have shown such behaviour at room temperatures, has led to an active area of research investigating the structure and potential applications of point defects in 2D materials. To demonstrate this instrument's versatility and its potential to perform cutting-edge research in this emerging field, preliminary results characterising the nature of photoluminescence in a thin hBN film on a silicon carbide substrate are presented.

Acknowledgements

Thanks must, of course, go to my supervisor Dr Christopher Mellor whose experience and knowledge made this possible. Instrumentation projects such as this require a wealth of theoretical knowledge as well as a great deal of practical know-how; I'd like to thank Chris for always having a plan or suggestion no matter what unforeseen difficultly arose.

I'd also like to thank Dr Russell Vanhouse, who not only bought the project on leaps and bounds but provided excellent company during the hours spent in the lab. In particular, I'd like to thank Russell for continuing to provide helpful advice long after he completed his studies at Nottingham.

Thanks must to go my Family as well for all their support over the years. I am also grateful the support of my friends and housemates at Broadgate, Marlborough and Burrows, both the more permanent fixtures and the wide range of supporting characters. All of your company has been most welcome, but you can't make me do another Zoom quiz.

Chapter 1

Introduction

Advances in scientific instrumentation drive cutting edge science with the invention of novel instruments enabling the study of fundamental physics previously impossible with existing technologies. For example, the invention of the scanning tunnelling microscope (STM) in 1981 enabled the first topographical studies of samples with nanoscale resolution, with this achievement was recognised with the 1986 Nobel prize for Physics. While the improvements in instrumentation are not always as profound as the invention of entirely novel technologies, there is a constant drive to improve the performance of scientific instruments, motivated by the potential to investigate phenomena currently inaccessible to established techniques in a given field. This project focuses on the design, assembly and testing of a multimode imaging tool to characterise a wide range of samples on the sub-micron scale. Throughout this thesis, the developed multimode tool will be referred to as the 'instrument' for simplicity

The main goal of this project was to develop a high-spatial-resolution, high sensitivity magnetometer operating in ambient conditions, based on the nitrogen-vacancy (NV) centre in diamond. To realise NV centre magnetometry, a means to read out the magnetically sensitive photoluminescence from the NV centre is required, along with a method to scan the NV centre above a magnetic field source. Commonly, the optical readout is performed using confocal microscopy, while the probe is scanned using an atomic force microscope,

both established techniques for imaging samples on sub-micron length scales in their own right. Therefore, an instrument was designed that could not only operate as a scanning probe magnetometer but also feature multiple imaging modalities that could be operated simultaneously or sequentially for the study of samples on the nanoscale. This project has focused on developing and optimising the constituent components of a scanning probe NV magnetometer, optimising the performance of each imaging mode as a standalone tool while working towards the development of a scanning probe magnetometer.

A key feature of this instrument is flexibility, with the instrument designed to investigate microscopic properties of samples of inherently varied samples, from flakes of 2D materials through to micron-fabricated arrays of conductors with experimental contact structures. In particular, this instrument has been developed to measure the spatial, temporal and spectral characteristics from optically active point-like sources emitting in the 600-750 nm range for NV magnetometry and the study of other sources of localised luminescence. Firstly, the motivation for constructing a high-sensitivity high spatial resolution magnetometer is presented.

1.0.1 Statement of Contributions

This design and construction project was supervised by Dr Christopher Mellor and while I focused on the development of the optical instrumentation and automation of processes, a second PhD student, Russell Vanhouse, led the construction of the atomic force microscope side of the project. Russell Vanhouse also modelled and produced the microwave antenna for the delivery of high-frequency magnetic fields required for magnetometry with NV centres. All data are my own unless otherwise stated.

1.1 Motivation

The investigation of magnetism is an active area of research with a wide range of applications and motivations. On the length scales of $\sim 1\,\mathrm{cm}$ vapour cell magnetometers have

enabled the detection of biological currents associated with neuron action potentials [1]. Magnetic fields associated with currents have also been probed on the nanoscale, through the use of scanning probe techniques. For example, single nitrogen-vacancy (NV) centre magnetometry has enabled non-invasive magnetic imaging of the current density in metallic wires and carbon nanotubes with much greater spatial resolution possible than with conventional resistance-based measurements [2]. This thesis focuses on the development of an instrument to perform scanning probe magnetometry with small numbers of NV centres, motivated by their potential to measure magnetic fields with high spatial resolution. In particular, this instrument has been designed to measure the magnetic fields generated by micron-scale conductors designed to generate magnetic trapping potentials to localise clouds of cold atoms, known as atom chips.

1.2 Atom Chips

The invention of the atom chip was an essential step in 'lab-on-a-chip' type experiments aiming to miniaturise quantum optics experiments both for the study of fundamental physics and metrological applications. To date, clouds of cold atoms on chips have been utilised as inertial sensors, atomic clocks and magnetometers, and have also shown promise for quantum information applications (see the review by Keil *et al.* [3]).

A key component of both atom chip technology and early cold atoms experiments, which utilised macroscopic coils, is the production of a spatially varying magnetic potential generated by current-carrying wires, which acts to spatially confine and manipulate the cold atom clouds. Atoms can only be spatially confined once they have been cooled to ultra-low temperatures and their thermal energy becomes comparable to the interaction energy between the atom and electric, optical or magnetic fields. In general, cold atoms experiments utilise magnetic fields produced by the currents either in macroscopic coils or, in the case of atom chips, microscope wires, to produce magnetic trapping potentials. The condition for spatial confinement of cold atoms using a magnetic field is therefore given by

$$V = -\boldsymbol{\mu} \cdot \mathbf{B} > k_B T \tag{1.1}$$

where $\boldsymbol{\mu}$ is the magnetic moment of the atom, k_B is the Boltzmann constant, $\mathbf{B}$ is the magnetic field and T is the temperature of the atom cloud [4]. Classically, the angle between the magnetic moment of the atom and the external field is constant due to the rapid precession of $\boldsymbol{\mu}$ about the magnetic field axis. In the quantum picture, the energy levels of a particle with quantum number, F, which corresponds to total angular momentum, and g factor, g are given by

$$V = g\mu_B m_F B \tag{1.2}$$

where m_F is the quantum number of the component F along the direction of the external magnetic field [4]. Depending on the orientation of the dipole moment relative to the magnetic field, which is given by the sign of gm_F, an atom either experiences a magnetic force towards minima in the field ($gm_F > 0$, referred to as weak-field seeking states) or towards maxima ($gm_F < 0$, referred to as strong-field seeking states). Since a three-dimensional magnetic maximum can not be produced [5], only weak-field seeking states can be trapped, by producing spatially varying magnetic potentials with local minima.

In addition to producing a strong magnetic field sufficient to trap cold clouds, the gradient and curvature of the potential near the local minimum are also key parameters for devices that produce confining potentials for cold atoms experiments. For example, the magnetic force exerted on atom is proportional to the magnetic field gradient and this must produce sufficient force to compensate for gravity. The curvature of the magnetic field defines the spatial extent of the trapping potential [4], with tight spatial confinement being highly desirable. When potentials can be miniaturised to length scales below 1 µm, arrays of potentials can be utilised for atom interferometry experiments, as the coupling between atoms trapped in adjacent sites in the array is no longer negligible [6].

To summarise, the requirements for a trapping potential for cold atoms experiments are

as follows: a large magnitude field to produce deep traps, a large gradient to produce large magnetic forces which compensate for gravity and a high curvature to tightly confine the atoms. In early cold atoms experiments, such as the first observation of a Bose-Einstein Condensate (BEC), the trapping potential was produced by macroscopically sized coil pairs in an anti-Helmholtz configuration [7]. However, the use of atom chips, which produce trapping potentials, using planar arrangements of microscopically sized conductors, can, at lower electrical power, produce larger fields, gradients and curvatures than macroscopic coils. The principle of atom chip operation can be illustrated by considering the magnetic field produced by an infinitely long thin wire. Such a wire, carrying current, I_0, in the x-direction produces a magnetic field of magnitude, gradient and curvature given by

$$B(z) = \frac{\mu_0}{2\pi}\frac{I_0}{z}, \quad B'(z) = -\frac{\mu_0}{2\pi}\frac{I_0}{z^2}, \quad B''(z) = \frac{\mu_0}{\pi}\frac{I_0}{z^3} \tag{1.3}$$

where z, is the perpendicular distance from the wire axis [4]. The wire produces a field with a strong gradient and curvature but by itself does not produce a local minimum required for trapping atoms. To produce a minimum, a homogeneous external bias field of strength $\widetilde{B}$ is applied perpendicular to the wire axis. The bias field will cancel the field produced by the wire on a line parallel to the wire at a distance z_0 above the wire axis, this principle is graphically represented in Figure 1.1, and the distance of the minimum above the wire given by [4]

$$z_0 = \frac{\mu_0}{2\pi}\frac{I}{\widetilde{B}}. \tag{1.4}$$

In the vicinity of the line above the wire the total field is well approximated by a two dimensional quadrupole with gradient [4]

$$B'(z_0) = -\frac{\mu_0}{2\pi}\frac{\widetilde{B}^2}{I_0} \tag{1.5}$$

The single wire and bias field arrangement discussed so far produces a magnetic po-

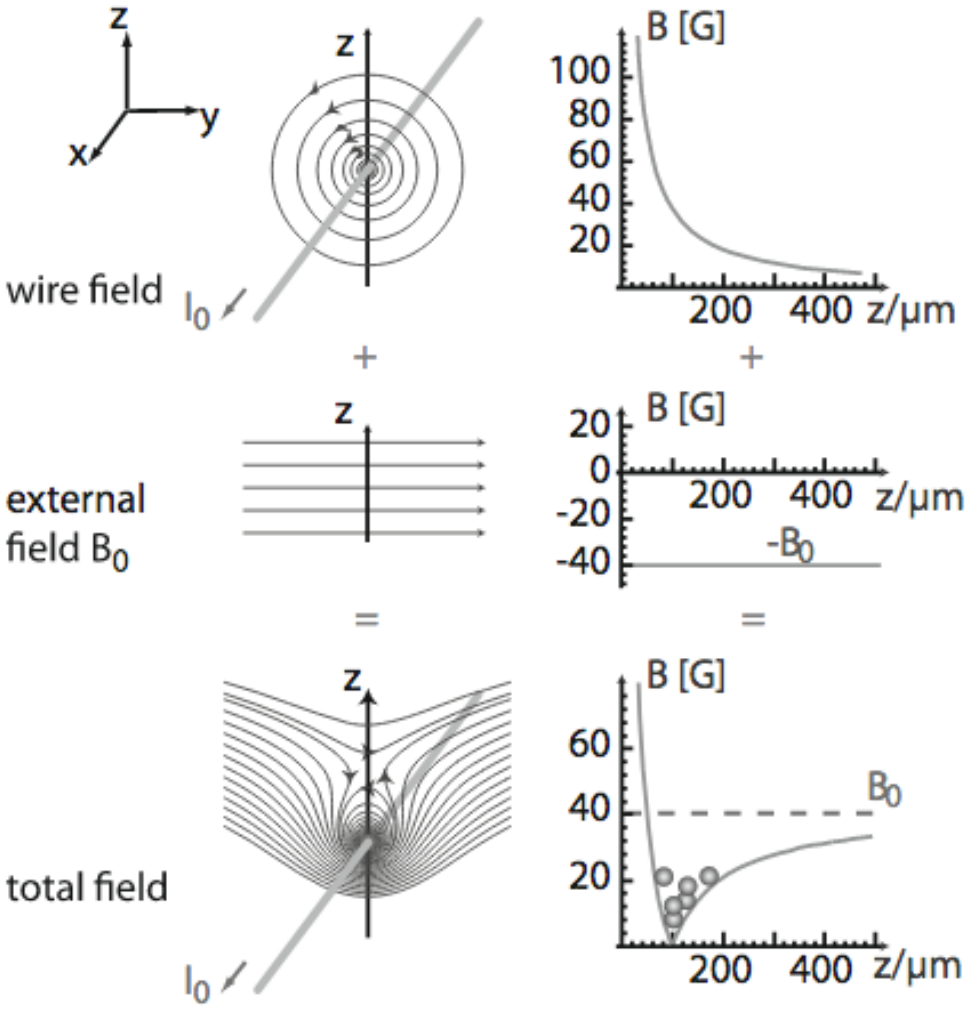

Figure 1.1: Principle of creating a 2D trap using a wire and homogenous bias field. Top: wire, central: bias field, bottom: resulting total field. The left column shows the magnetic field lines while the right column gives the magnitude of the magnetic field for a wire current I = 2 A. Image sourced from [4].

tential that enables the confinement of a cold atom cloud in a plane orthogonal to the current flow, but not along the wire axis. In real devices, which require the capability to confine clouds of cold atoms for sensing applications, the spatial confinement must be in 3 dimensions. To produce 3D confinement, the wire can be bent, with both 'U' and 'Z' shapes commonly used to produce confinement along the trap axis, which corresponds to the x-axis in the simple wire-bias example discussed earlier. Both 'U' and 'Z' shaped wires are approximations of the ideal 'H' shaped wire, which uses the two orthogonal currents in the 'vertical wires' of the H to produce a magnetic potential minimum orthogonal to the minimum produced by the combination of 'horizontal wire' and the bias field perpendicular to this wire, leading to 3D confinement. A complete theoretical description of multiwire layouts to produce potentials enabling 3D spatial confinement, including the 'H', 'Z' and 'U' wires is available in Chapter 2 of the book 'Atom Chips' by Reichel and Vuletic [4].

Whether discussing 3D 'Z' or 'U' traps or single wire 1D traps, to create a tight trap with a given current, I_0, the strength of the bias field, $\widetilde{B}$ must be increased and as shown in equation 1.4, increasing the strength of the bias field decreases the distance between the wire surface and the magnetic field minimum. Therefore, producing trapping potentials with a minimum very close to the wire surface can produce atom chips with very favourable properties, i.e deep traps with large gradients and curvatures. However, there is a lower limit to how close an atom cloud can be brought to the surface of an atom chip to produce tightly confined trapping potentials. When the distance between the atom cloud becomes comparable to the geometry of the wires producing the trapping potential the interaction between the atom chip surface and the atom cloud become significant. The local properties of the wires produce deviations in the current density from the ideal case and this has been shown to produce corrugations in the potential [8, 9]. In real devices, which build on the simple principle illustrated by the wire and bias field to both confine the atoms in 3 dimensions (typical atom chip dimension and component sizes shown in Figure 1.2), and also generate the bias field using on chip currents, the fragmentation effect has led to the use of cold atom clouds as highly sensitive surface probes. As the current density in the wire deviates from the ideal case the cloud of trapped atoms above the chip fragments,

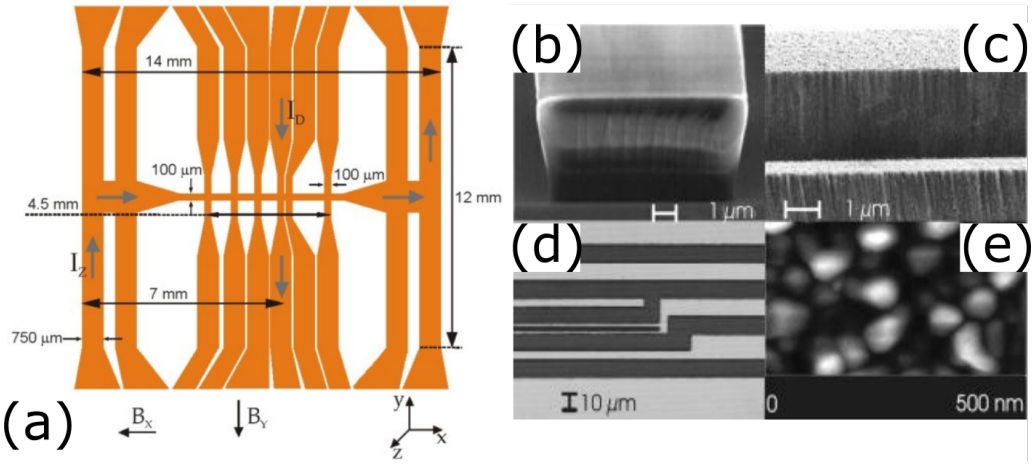

Figure 1.2: (a) Schematic showing typical dimensions of microfabricated current arrays that form atom chips, Image sourced from [11]. Images showing typical feature size in atom chips. (b), (c), (d) show scanning electron microscope (SEM) images showing resist structure used in fabrication, a single wire and the complete atom chip respectively. AFM image showing the granular structure of the gold shown in the devices in (b) and (c) is shown in (e), Imaged source [12].

which can be detected optically through the change in absorption of a probe laser. The modification of the trapping potential produced by a target current placed between an atom chip with a known response and the atom cloud, forms the basis of magnetometry with atom chips, which has been demonstrated with a spatial resolution of 3 µm and sensitivity of 4 nT [10].

While providing a means to detect surface effects, generally, the disordered potential experienced by atoms trapped with short wire-atom distances represents a challenge for manufacturers looking to repeatedly fabricate devices with a known response and provides one of the main obstacles to further miniaturisation of the potential landscape. The origins of the disorder in the potential are the deviations in the local current density in the wire producing the trapping field [8, 9]. It has been suggested that the local deviations in the current density are highly dependent upon the fabrication process involved in producing the wires generating the trapping field and that they arise due to; fabrication inhomogeneities, the roughness of both the surface [13, 14] and the edges of the fabricated wires [15], the

residual roughness of wire borders [16] and the grain structure in polycrystalline metal films [17]. The current deviation from the ideal path produces an inhomogenous component of the magnetic field, ΔB, and a measure of the quality of an atom chip is the ratio of the inhomogenous component, ΔB to the magnetic field produced by the wire at that distance, B, with Figure 1.3 comparing the measured potential roughness measured by a range of research groups fabricating atom chips. One study by Kruger *et al* [18] showed that the magnitude of disorder potentials could be reduced by two orders of magnitude in lithographically fabricated evaporated metals as compared to devices fabricated using an electroplating technique. However, even with the improved fabrication technique the ratio of the inhomogenous component compared to the trapping field was found to be $\Delta B/B = 3$ x 10^{-5}, when measured by probing the optical density of a BEC 10 µm above the wire surface [18]. In general, a requirement for successful atom chip operation is that the potential energy of the confining potential is much greater than associated with the trapped atom and the inhomogenous magnetic field component, which can be expressed as $\hbar\omega >> g\mu_B m_F B$. In this expression, ω is the trap frequency, which is proportional to the curvature of the trapping potential and quantifies the spatial confinement of the trap.

Commonly atom chips are developed using an iterative approach, with each atom chip loaded into a cold atoms setup and the potential disorder measured by probing the optical density of either a thermal cloud of atoms or BEC localised within the trapping potential generated by the device under investigation. Firstly, this approach is time inefficient, as the newly fabricated devices must first be loaded into an ultra-high vacuum and the atoms need to be trapped, cooled and loaded into the trapping potential of the chip, with such an experiment easily taking several weeks. The local deviations in the current densities, introduced by imperfections in the fabrication, can then be detected by probing the optical density of the trapped atoms. While this technique can be highly sensitive, the spatial resolution is limited, theoretically by the diffraction limit (≈ 300 nm), but in practice by the distance between the atoms and the wire generating the potential (typically above 1 µm). An alternative approach to characterising the performance of novel atom chips would be more time-efficient, enabling rapid feedback to fabricators, and have a greater spatial reso-

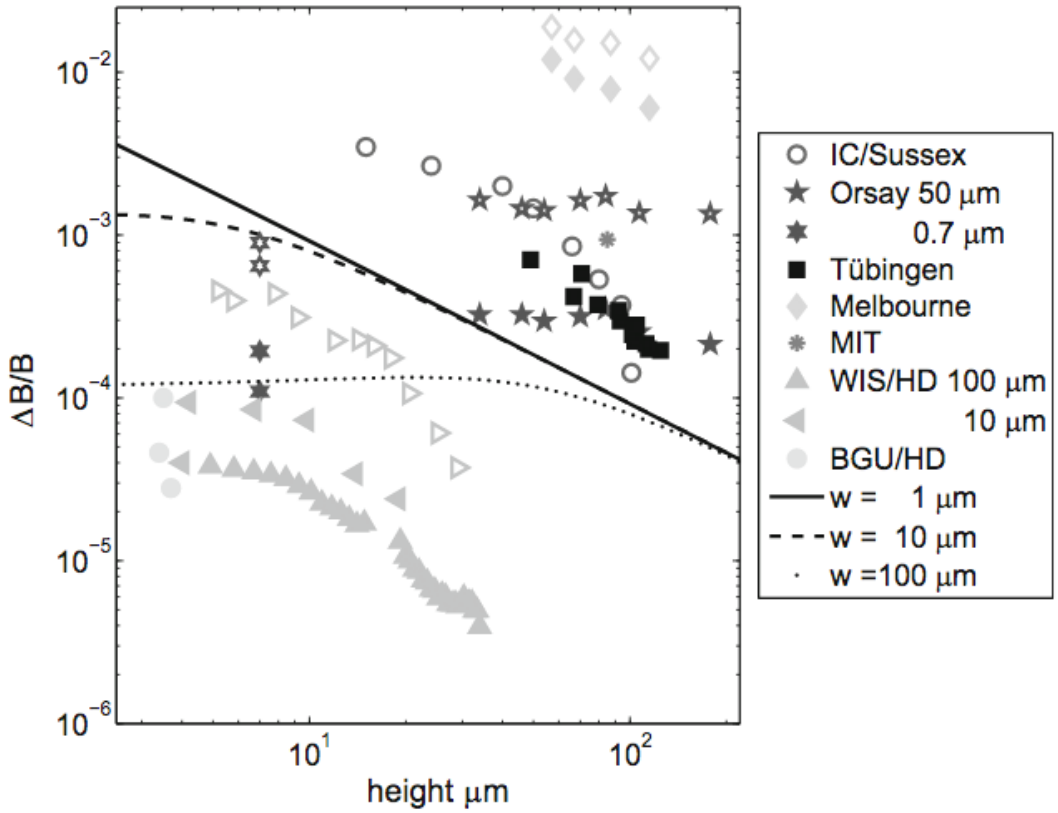

Figure 1.3: Comparison of different atom chip potential roughness measurements with the image sourced from [4], the references to the origin data sources shown in the figure can also be found in [4] . The filled symbols denote rms values and data open symbols peak-to-valley maximum height of the roughness. The dimensions in the legend, where stated, correspond to the width of the wires. MIT denotes Massachusetts Institute of Technology, WIS denotes Wiezmann Institue of Science, BGU denotes Ben-Gurion University and HD denotes Heidelberg University. The dot, dash and solid lines represent the expected scaling of the roughness with distance from the surface for wires with widths of 1 μm, 10 μm and 100 μm respectively.

lution in the magnetic field measurement by locating a probe far closer to the wire surface. Using a magnetic field sensor with a wire-probe distance of less than 1 µm would provide both a stronger measurement signal and also enable the investigation of very short length-scale deviations, which can be averaged out when measuring the potential with trapped atoms at large distances above the conductor [15]. To investigate the modification of the trapping potential introduced by fabrication effects in atom chips, this thesis focuses on the development of a magnetometer with nanoscale probe-source separation and spatial resolution designed to operate in ambient conditions, based on the nitrogen-vacancy (NV) centre in diamond. The spatial resolution a single scanning NV magnetometer can achieve is limited only by the separation between the magnetic field source and the NV centre[19], which is routinely as low as 50 nm. In addition to achieving the desired high-spatial resolution magnetic field measurements required for atom chip investigations, the constituent components of a scanning probe NV magnetometer provide complementary imaging modes for sub-micron-scale sample characterisation. These include high-resolution optical imaging via confocal microscopy and topographical imaging via atomic force microscopy without requiring substantial hardware reconfiguration. The multiple imaging modes developed in this instrument can be used on a single sample either sequentially or simultaneously depending on the application.

1.3 Outline of Thesis

This thesis is divided is divided into 8 chapters:

Chapter 2 - The 2nd chapter of this thesis introduces the NV centre as a magnetic field sensor. The NV centre is first discussed in terms of its optical properties and electronic structure. The influence of external magnetic fields on NV centres is described, and how NV centres can be utilised as highly sensitive magnetometers discussed. The performance of the NV centre magnetometers is discussed and compared to other state-of-the-art magnetic field sensors. Finally, how NV centres can be utilised in combination with scanning probe technology to produce a scanning probe magnetometer, achieving nanoscale resolution in

ambient conditions, is discussed.

Chapter 3 - The third chapter discusses the principle of operation of the optical imaging techniques used in this instrument. The custom design of each component in this instrument and its performance in this instrument is then presented. The primary optical technique discussed is confocal microscopy, developed for the collection of NV centre photoluminescence (PL) for magnetometry. Confocal performance is presented in PL mode but also an additional imaging mode using backscattered. How the confocal microscope has been modified to enable the measurement of spectral and temporal characteristics from diffraction-limited PL sources is discussed and performance demonstrated by presenting results from suitable test samples. The design and performance of a diffraction-limited wide-field microscope is also presented.

Chapter 4 - To produce 2D magnetic field maps using a small number of NV centres, the NVs must be raster-scanned close to the magnetic source. Chapter 4 focuses on the development of a custom atomic force microscope (AFM), both for the control of the AFM probes functionalised with NV centres for scanning probe magnetometry and as a standalone sub-micron imaging tool. The principle of operation of atomic force microscopy is introduced, and how this system has been optimised for combined optical/AFM experiments discussed. Finally, the performance of the AFM is presented as a separate imaging modality of this instrument.

Chapter 5 - The final hardware components required to realise magnetic field sensing using NV centres are introduced in Chapter 5 - a microwave circuit and resonator for NV centre spin state manipulation and a method to generate a bias magnetic field. Optically detected resonances from nanodiamonds are presented to demonstrate this instrument's capability to perform ODMR experiments at the frequencies required for NV centre magnetometry.

Chapter 6 - Chapter 6 demonstrates the progress made with this instrument towards scanning probe NV magnetometry. The principle of operation of a commercially available AFM probe designed specifically for scanning NV magnetometry and its performance in this instrument is discussed. The magnetic field imaging modes available in this instru-

ment are discussed. Finally, test samples are discussed both in terms of fabrication and preparation and the expected response of this instrument.

Chapter 7 - Measurements on localised emitters in hexagonal boron nitride (hBN) are presented, showing this instrument's ability to characterise the spectral, spatial and temporal characteristics of emitters on the sub-micron scale.

Chapter 8 - Summarises this thesis by reviewing the key results and performance of this instrument in a variety of imaging modalities. Finally, future work is considered, both in terms of continued instrumental development and potential applications.

Chapter 2

The Nitrogen Vacancy Centre

2.1 Introduction

Diamond is a wide bandgap material (5.47 eV) that consists purely of carbon atoms and has traditionally been of interest due to its macroscopic properties, such as it's hardness and thermal conductivity [20]. While pure diamond consists entirely of carbon, both diamonds created synthetically and naturally can host a wide range of impurities, such as vacancies or different atoms in place of carbon in the diamond lattice [21]. The existence of defects in solid-state materials, including diamond, can provide an architecture to realise quantum technologies in wide-bandgap materials with some defects introducing isolated electronic spins into the lattice which can be addressed optically. The isolated spin provides a mechanically robust, and when combined with novel fabrication techniques [22], a highly scalable system with potential use for nanoscale sensing and quantum information applications [23]. The nitrogen-vacancy centre, or NV centre, is one such example of a defect centre in diamond that has been the focus of a wide range of research, this defect consists of a substitutional nitrogen atom at one of the carbon sites in the diamond lattice and a vacancy in one of the adjacent sites. There are two prominent charge states of the NV centre, the neutral NV^0 state and the negatively charged NV^- state, with both of these defects exhibiting different spectral properties [24]. In this thesis, NV centre will refer to

the negatively charged state of the nitrogen-vacancy centre as this charge state is of the greatest interest in magnetic field sensing [25]. The wide range of research into the NV centre comes from three key properties; the ability to efficiently spin polarise the centre via optical pumping, the coupling of the centre's spin state to an optical transition facilitating optical readout of the spin state and finally, long coherence times at room temperature.

This chapter focuses on properties of the NV centre that allow it to be utilised as a vector magnetic field sensor. A brief discussion of the NV centre and its optical properties is first presented. The influence of an external magnetic field on the NV centre will be considered and how the resultant behaviour can be used as a magnetic field sensor discussed. The theoretical limits to the magnetic field sensing technique will be presented and how NV centres as magnetic field sensors compared to alternative techniques discussed. Finally, a measurement scheme will be described to enable the use of an NV centre as a probe in a scanning probe approach to magnetometry providing a high-sensitivity nanoscale vector magnetometer.

2.2 Optical Properties

The NV centre is formed of a substitutional nitrogen atom and vacancy pair, with the axis between the sites the intrinsic quantisation axis of the defect, which is labelled as the z-axis. In the diamond lattice, which is shown in Figure 2.1(a), the NV centre quantisaton axis, shown in Figure 2.1(b), can occur aligned along one of four equivalent crystallographic directions; $[1\,1\,1]$, $[1\,\bar{1}\,\bar{1}]$, $[\bar{1}\,1\,\bar{1}]$, $[\bar{1}\,\bar{1}\,1]$. While Figure 2.1(a) shows an NV centre hosted in the diamond lattice 2.1(b) highlights the quantisation axis of an NV centre. The electronic structure of the defect is shown in figure 2.2. The ground state of the NV centre is a spin-triplet state, $|g\rangle$ (S=1), split into three spin sublevels [25, 26]. These sublevels are characterised by the spin projection along the NV centre quantisation axis (z). The $m_s = \pm 1$ sub-levels are degenerate at zero magnetic field with the $m_s = 0$ state at lower energy. The splitting between the $m_s = 0$ and the degenerate $m_s = \pm 1$ sublevels at zero magnetic field is 2.87 GHz [25, 26]. The NV centre can be optically excited to the excited

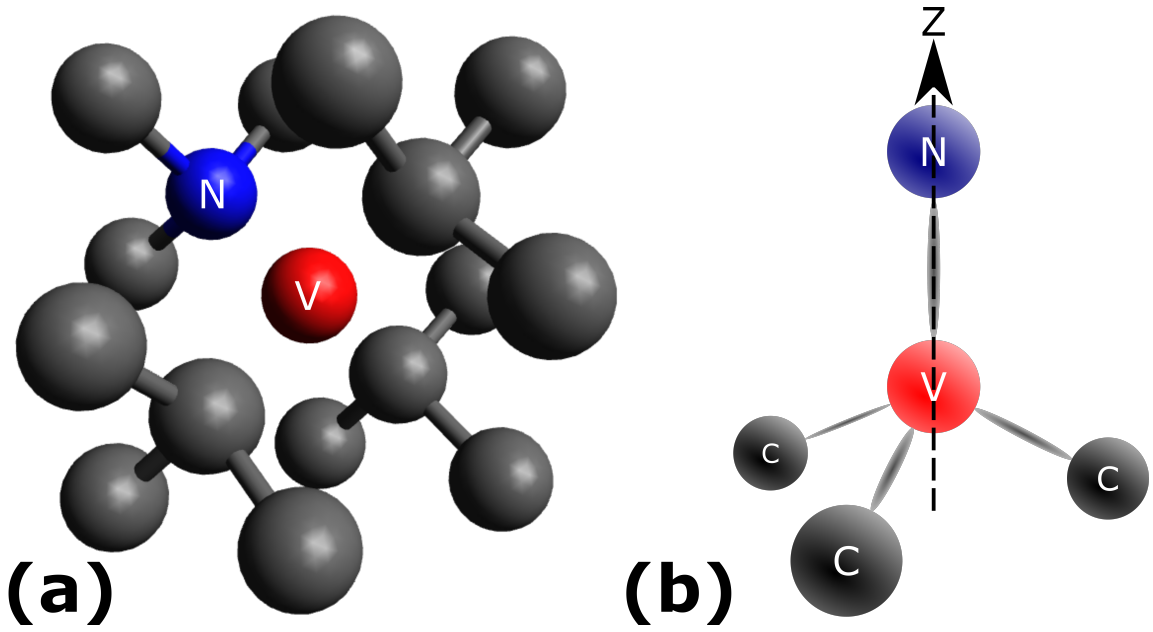

Figure 2.1: (a) NV centre hosted in the diamond lattice, grey represents carbon atoms, blue nitrogen and red a vacancy (image produced by Chris Judd) (b) Shows the co-ordinate axis of the NV centre, the axis (z-axis) joining the two sites is the intrinsic quantisation axis of the NV centre. The z axis defines the measurement axis for magnetic field sensing applications.

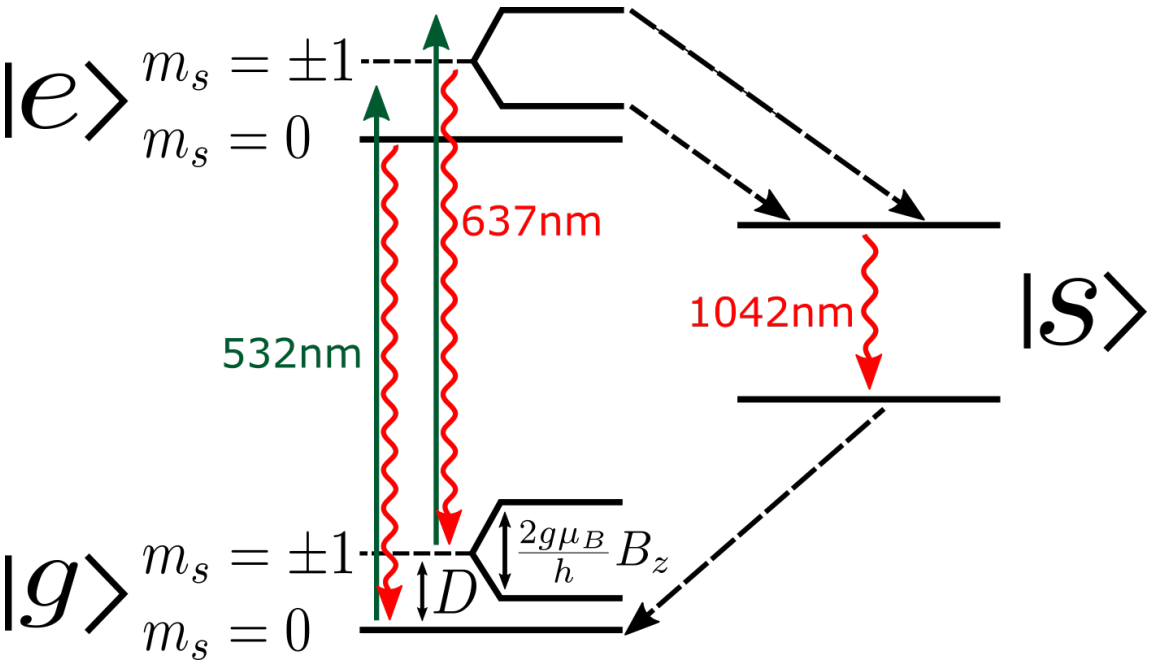

Figure 2.2: Electronic structure of the NV centre. Ground state $|g\rangle$ is a spin-triplet state with m_s denoting spin projection along the NV centre axis. D is the zero-field splitting between the ground state sublevels. The $m_s = \pm 1$ sublevels are degenerate at zero magnetic field and the energy is shown by the dashed line, the solid lines show the lifting of the degeneracy with the application of a field B_z, along the NV centre axis. The excited state, $|e\rangle$ is also a spin-triplet. The additional singlet states are referred to as a single state $|s\rangle$. The green lines represent excitation via green laser and the red lines show relaxation optically. The blacked dash lines denote none radiative decays. Figure adapted from Figure 2 in [28].

state, $|e\rangle$, which is also a spin-triplet state [25, 26]. The optical transitions, between $|g\rangle$ and $|e\rangle$, are largely spin conserving with spin-flip transitions rates less than 2% of the spin conserving transition rate [27]. The lifetime of the excited state varies between the diamond hosting the defect and is typically around 13 ns in bulk diamond and longer in nanodiamonds 20 ns [25]. In addition to the excited state there are also two metastable singlet states with the lower of the states having a lifetime of 300 ns [26], referred to collectively as $|s\rangle$ in figure 2.2.

The metastable singlet states are crucial in the optical dynamics of the NV centre,

allowing the defect to be optically spin polarised through the application of light. The NV centre can be spin polarised using the following procedure. Firstly, the NV centre is excited optically from the ground state with off-resonant light, typically with wavelengths between 450-610 nm via a phonon sideband associated with the excited state [29]. From the excited state, the centre can relax optically, which like excitation is also spin conserving [27], resulting in a broadband photoluminescence (PL) in the 637-850 nm band with a zero phonon line at 637 nm [30]. Alternatively, relaxation back to the ground state can occur via the singlet states, which does not result in emission in the 637-850 nm band [31]. The probability of non-radiative decay via the singlet states is highly dependent on the spin state of the NV centre. The decay into the singlet states is more probable when the spin is initially in $m_s = \pm 1$ sub-level, while the spin also preferentially decays out of the singlet states into the ground state $m_s = 0$ sub-level [27]. Therefore, the NV centre can be optically spin polarised, driving the $|g\rangle$ to $|e\rangle$ transition over many cycles will result in the NV centre being prepared in the $m_s = 0$ sub-level of the ground state. This has been demonstrated in ambient conditions with efficiencies exceeding 90% [27].

As the decay into the singlet states is spin selective, the NV centre can be spin polarised. The decay pathway through the singlet states also enables the optical readout of the spin state by purely optical means. The spin-dependent PL of the NV centre arises from the decay via the singlet states being non-radiative and the probability of decay via this pathway dependent upon the spin projection of the NV centre (high for $m_s = \pm 1$ states, low for $m_s = 0$) [26]. The decay via the singlet states competes with the PL decay and as such the sublevel with the lowest probability of non-radiative decay from the excited state will, therefore, appear the brightest. This provides a means to optically read out the spin state of the NV centre by detecting intensity differences in the PL signal.

To summarise, the optical spin state readout and polarisation with the same off resonant laser, spectrally separated from the measurement signal enables the NV centre to be used as a magnetometer through the optical detection of the Zeeman shift of the NV centre spin states. For example, a single defect is first prepared in the $m_s = 0$ by optical pumping. The defect can then be driven to the ground state $m_s = \pm 1$ states through the application

of a resonant microwave field. When optically excited from these sublevels there is a higher probability the decay is non-radiative (in the 637-850 nm band [31]). Through the application of a range of microwave frequencies, the resonance can be detected by a decrease in PL intensity, characterised by parameter C, which is defined as ratio of the on and off resonance PL intensities. The optical detection of the spin state provides a means to detect Zeeman shifts in spectral positions of the $m_s = \pm 1$ states optically, this is referred to as optically detected magnetic resonance (ODMR) and is the basis of NV centre based magnetic field sensing. An example of this type of ODMR spectra is shown in figure 2.3 (a).

2.3 NV Centres in External Fields

Magnetic field sensing using NV centres can be realised by detecting the Zeeman splitting of the NV centre-ground state. The simplest protocols involve the detection of the spectral shift of the optically detected resonances by recording the PL intensity for a variety of applied microwave frequencies. To provide a quantitative measurement of the magnetic field, the ground state of the NV centre spin Hamiltonian must be considered [32, 33]

$$\mathcal{H} = hDS_z^2 + g\mu_B \boldsymbol{B} \cdot \boldsymbol{S} \tag{2.1}$$

where $\boldsymbol{B}$ is the external magnetic field and $\boldsymbol{S}$ is the dimensionless spin-1 operator. Equation 2.1 is defined in terms of two parameters with units of frequency, D and μ_B. D is the axial zero-field splitting parameter and is equal to 2.87 GHz; the splitting arises from spin-spin interactions between two unpaired electrons that form the defect [25]. Equation 2.1 neglects terms describing the interaction with electric fields and stress in the crystal. At low electric fields and with the application of a bias field $B_0 \approx 1$ mT the contributions of the strain and electric field terms is negligible for all but very high strain diamonds which are not typically used in magnetic field sensing [28, 32, 34]. The interaction with the nuclear spin of the nitrogen has also been neglected in equation 2.1. In the presence of an external

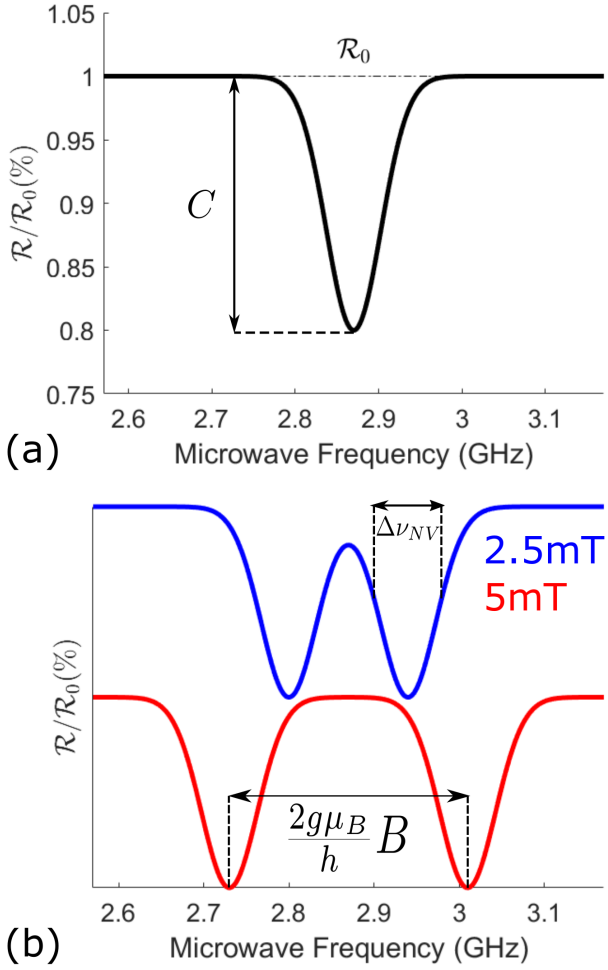

Figure 2.3: (a) A model ODMR spectra from a a single NV centre at zero magnetic field. The PL intensity off resonance is denoted by $\mathcal{R}_0$, when a microwave frequency is applied that drives an NV centre prepared in the ground state $m_s = 0$ state to one of the $m_s = \pm 1$ states, this is observed as in PL intensity. The magnitude of the resonance is characterised the contrast, C, which is the ratio of the off resonance count rate $\mathcal{R}_0$ to the count rate on resonance.(b) A magnetic field, B_z, applied along the NV centre axis, defined as z, leads to the the Zeeman splitting of the optically detected resonances. Two resonances are observed corresponding to each of the $m_s = 0$ to $m_s = \pm 1$ transitions. The resonances are characterised by linewidth $\Delta\nu_{NV}$.

magnetic field orientated along with the NV centre axis $\boldsymbol{B} = (0, 0, B_z)$ equation 2.1, the Hamiltonian that describes each hyperfine state can be written in matrix form [32]

$$\mathcal{H} = \begin{pmatrix} D + \frac{g\mu_B}{h} B_z & 0 & 0 \\ 0 & 0 & 0 \\ 0 & 0 & D - \frac{g\mu_B}{h} B_z \end{pmatrix} \tag{2.2}$$

The energies of the eigenstates, $m_s = 0, \pm 1$ are given by the eigenvalues of 2.2 are linearly dependent upon the magnetic field along the NV centre quantisation axis, defined as the z-axis in this case. As a result, the transition frequencies between the $m_s = 0$ state and the $m_s = \pm 1$ states are given by [32]

$$\nu_{\pm} = D \pm \frac{g\mu_B B_z}{h} \tag{2.3}$$

Equation 2.3 shows the on-axis magnetic field, B_z, can be measured through detection of the transition frequencies and knowledge of fundamental constants, g, μ_B and h, demonstrating the potential use of NV centres for magnetic field sensing. To utilise an NV centre as a magnetic field sensor the intensity of the photoluminescence is measured while sweeping microwave frequencies close to the zero-field transition. When the microwave frequency that satisfies the resonance condition, shown in equation 2.3, for a given value of B_z is applied to the NV centre, this is detected as a decrease in the PL intensity compared to the off-resonance value. A typical NV centre response to a range of microwave frequencies is shown in Figure 2.3. Equation 2.3 also shows that for a weak on-axis field the frequency changes with a simple linear relation only dependent on fundamental constants that are not dependent on the NV centre environment, ensuring reproducibility of measurements. Finally, the large size of the prefactor $\frac{g\mu_B}{h} \approx 28\,\text{kHz}/\mu\text{T}$ enables the detection of very small magnetic fields as the shift of the transition frequencies is substantial when compared to both the precision with which the MW field to drive the sublevel transitions can be generated ($\approx$ mHz) and the typical linewidths of the resonance ($\approx$ 1-10 MHz for pure diamonds used for sensing [35]).

When the external magnetic has non-axial components , i.e $\boldsymbol{B} = (B_x, B_y, B_z)$, the transition frequencies are given up to third order in $(g\mu_B/h)(B/D)$ [32]

$$\nu_{\pm} = D\left[1 \pm \left(\alpha\cos\theta_B + \frac{\alpha^2}{2}3\sin^2\theta_B \pm \alpha^3\left(\frac{1}{8}\sin^3\theta_B\tan\theta_B - \frac{1}{2}\sin^2\theta_B\cos\theta_B\right)\right)\right] \quad (2.4)$$

where $\alpha = \frac{g\mu_B}{h}B/D$ and $\tan\theta_B = \left(\sqrt{B_x^2 + B_y^2}\right)/B_z$. The non-linear dependence of the transition frequencies, when the transverse magnetic field is non-zero facilitates, the measurement of the NV centre orientation in the laboratory reference frame through measurement of the transition frequencies at a range of external magnetic field strengths and orientations at the defect site [36], this is discussed further in Chapter 5. Knowledge of the NV centre orientation facilitates nanoscale vector magnetometry in the weak off-axis magnetic field limit. Equation 2.3 highlights how the NV centre transitions are only dependent upon the axial field; combined with knowledge of the NV centre orientation relative to a magnetic target a single NV centre can be used as a high-sensitivity vector magnetometer with nanoscale spatial resolution.

The sensing applications discussed in this thesis will focus on the limit of a weak off-axis field and the transition frequencies will be assumed to depend linearly on the on-axis magnetic field unless otherwise stated. In the event the on-axis magnetic field isn't significantly larger than the off axis component, i.e when $B_z >> \sqrt{(B_x^2 + B_y^2)}$ is not satisfied, the quantisation axis is fixed by the magnetic field not the defect axis and m_s is no longer a good quantum number [28]. In this case, the eigenstates of the Hamiltonian are given by superpositions of the $m_s = 0, \pm 1$ states [33] and as a result, the optical pumping and detection of the spin state becomes less efficient [33]. The loss of the optical spin readout mechanism represents an upper limit to the magnitude of fields detectable with NV centres. However, the decrease in contrast associated with large transverse fields is also accompanied by an overall decrease in PL intensity even in the absence of MW frequency magnetic field when the transverse component of the magnetic field is large [37]. The decrease in overall intensity can be used to produce qualitative maps of regions with large transverse magnetic fields by monitoring the changes in PL intensity associated with

spatial variations in the transverse fields [38].

2.4 NV Centre Magnetometry

It has been shown that the NV centre can be optically pumped into the $m_s = 0$ sublevel and the spin state read out using the same laser. The linear relationship between the shift of the ODMR resonance under increasing magnetic field of the spin state energies then provides the basis for the use of NV centres as optical magnetometers. Here the state-of-the-art of NV centre based magnetic field sensing is discussed and the fundamental limits to the technique presented. Detecting magnetic fields with both high sensitivity and high spatial resolution is an active area of research across a range of disciplines. To compare NV centre magnetometry to competing technologies the sensitivity of the technique must first be established. The simplest form of magnetometry involves optical detection of the lineshifts of the ODMR resonances due to the Zeeman effect on a single NV centre ground state. It follows that the sensitivity is limited by the smallest resolvable frequency shift in the spectrum, comparing this to the photon shot noise in a measurement time Δt yields the expression for the sensitivity to DC fields for low contrast ODMR [28, 35, 39],

$$\eta_{\mathrm{CW}} = b_{min}\sqrt{\Delta t} \approx \mathcal{P}_{\mathcal{F}} \frac{h}{g\mu_B} \frac{\Delta\nu_{NV}}{C\sqrt{\mathcal{R}}} \tag{2.5}$$

The expression for the sensitivity, η_{CW}, has units $T/\sqrt{\mathrm{Hz}}$ and the minimum resolvable field, b_{min} can be calculated by dividing the sensitivity by the square root of the measurement time Δt. A numerical prefactor, $\mathcal{P}_{\mathcal{F}}$, is introduced that relates to the lineshape of the resonance [35], for a Gaussian profile, $\mathcal{P}_{\mathcal{F}}$ is denoted as $\mathcal{P}_{\mathcal{G}} = \sqrt{e/8ln2} \approx 0.70$. When the lineshape is Lorentzian, $\mathcal{P}_{\mathcal{F}}$ is written as $\mathcal{P}_{\mathcal{L}} = 4/3\sqrt{3} \approx 0.77$. $\mathcal{R}$ is number of PL photons collected per second, with $\Delta\nu_{NV}$ the linewdith of the ODMR resonance, C is the contrast of the ODMR resonance and is defined as the ratio of the on resonance PL intensity decrease compared to the off resonance PL intensity, see figure 2.3.

The count rate $\mathcal{R}$ recorded from an NV centre depends on the collection efficiency

of the optical system and the relaxation of the NV centre spin, with a discussion of the effect of environmental and experimental parameters on the count rate available in the 2011 paper by Dréau *et al* [35]. A fundamental challenge to increasing the count rate for high sensitivity magnetometry is the limit to the optical collection efficiency imposed by the high refractive index of bulk diamond (n=2.4) in which the NV centre is hosted. However, diamond's high refractive index facilitates the development of photonic structures to increase the measured count rate. In 2020, a scanning probe for NV centre magnetometry was fabricated from bulk diamond with a truncated parabolic profile, which yielded a median count rate from a single NV centre of $\mathcal{R} = 2.1 \pm 0.2\,\mathrm{Mcps}$ [40], this corresponds to the highest reported count rate from a single NV centre in a scanning probe geometry. The second parameter that limits the sensitivity is the ODMR contrast and this increases with microwave power, typical ODMR contrasts are around $C \approx 0.2$ [28], a theoretical discussion of the upper limit to the contrast is also discussed in the paper by Dréau *et al* [35]. The final parameter is the linewidth, $\Delta\nu_{NV}$, of the resonance feature, which is fundamentally limited by the spin's inhomogeneous dephasing time T_2^*. In practice, this is not reached as continuous wave application of both the laser and the microwave power introduces power broadening [35]. The parameters are not independent, for example, attempting to increase the sensitivity by increasing the contrast (by increasing microwave power) will also cause power broadening which acts to reduce the sensitivity. Decreasing the linewidth by reducing the excitation power comes at the cost of decreasing the sensitivity by lowering the count rate. It has been shown that for an ODMR spectrum with power broadening introduced by the CW-ODMR, the three parameters can be optimised leading to the best sensitivity of $\approx 1\,\mu\mathrm{T}/\sqrt{\mathrm{Hz}}$ [35].

In addition to the direct measurement of the shift in resonance in the ODMR, measurement schemes based upon detection of phase evolution can utilise the quantum nature of the NV centre resulting in improved sensitivity. This approach eliminates power broadening while preserving the contrast of the ODMR, through the temporal separation of the optical pumping, readout pulse and the microwaves. The sensitivity is optimised while the evolution time is matched with the spins inhomogeneous dephasing time T_2^* [35].

The magnetic sensitivity when the laser and microwaves are applied in short pulses is given by substitution of the fundamental limit to the linewidth $\Delta\nu_{NV} = \frac{2\sqrt{ln2}}{\pi T_2^*}$ into equation 2.5. For an optimised spin procession time $\tau = T_2^*$, the count rate per second can be approximated as $\mathcal{R} \approx \mathcal{R}_0 T_L / T_2^*$ where $\mathcal{R}_0$ is the detected count rate under continous laser excitation and T_L is the length of the readout laser pulse. The sensitivity is then given by [28, 32, 35]

$$\eta_{\text{pulsed}} = 2\sqrt{e}\frac{h}{g\mu_B}\frac{1}{C\sqrt{\mathcal{R}_0 T_L}}\frac{1}{\sqrt{T_2^*}} \tag{2.6}$$

This is fundamentally limited by T_2^*, a factor dependent upon the environment the NV centre, such as dephasing introduced by nitrogen, carbon-13, other NV-centres and finally other paramagnetic impurities [32]. Improving the fabrication to increase purity and achieve long coherence times is an active area of research. In ultrapure diamond $T_2^* \approx 1\,\mu\text{s}$ is routinely observed, with dephasing times as long as $T_2^* \approx 1.5\,\text{ms}$ demonstrated [41]. For example, $T_2^* \approx 1.5\,\text{ms}$ corresponds to a sensitivity as low as $\eta_{\text{pulsed}} = 6\,\text{nT}/\sqrt{\text{Hz}}$.

The sensitivity to AC fields can be orders of magnitude greater than DC sensitivity with the application of dynamic decoupling sequences to increase the spins coherence times [42, 43]. This thesis focuses on DC and slow time varying fields so this is not presented. However, a full discussion of AC field sensing and both AC and DC sensitivity optimisation can be found in [32]

To increase the sensitivity to DC fields using NV centre magnetic field detection the number of NV centres used for sensing can be increased. Ensemble-based approaches can improve the sensitivity by a factor by $\sqrt{N}$ through statistical averaging over a number of spins to increases the signal [32]. Sensitivities as low as $15\,\text{pT}/\sqrt{\text{Hz}}$ to DC magnetic fields has been demonstrated with ensemble NV magnetometers [39], with a corresponding sensing volume of 13 µm x 200 µm x 2000 µm. The increased sensitivity comes at the cost of decreasing the spatial resolution as the point of measurement is no longer well defined. The spatial resolution of a single NV centre magnetometer is given by the precision in the positioning [44] but ensemble magnetometers are fundamentally limited by diffraction

limit [45] or the volume of the sensing ensemble for large high sensitivity magnetometers.

The sensitivity difference between ensembles and single NV centres illustrates the trade-off between spatial resolution and sensitivity experienced by all magnetometers. Figure 2.4 compares the NV centre's sensitivity and spatial resolution to other state of the art magnetometers. The single NV centre's DC theoretical limit is in the nanotesla range which is several orders of magnitude greater than the most sensitive magnetometers, such as spin exchange relaxation free interferometers (SERF) which have a theoretical limit of $0.01\,\mathrm{fT}/\sqrt{\mathrm{Hz}}$ [46]. Where NV centres excel is in offering high sensitivity combined with nanoscale spatial resolution. Figure 2.5 shows NV centres compared to the most promising candidates in high spatial resolution magnetometry. When compared to other magnetometers operating at the high spatial resolution limit, such as Hall probes and SQUIDS (superconducting quantum interference devices) the theoretical limit of NV centre's spatial resolution is an order of magnitude smaller whilst offering comparable sensitivity. The NV centre represents a truly atomic-sized sensor with attempts to improve spatial resolution centred on the implantation of stable NV centres with long coherence times closer to the diamond surface [47], as such the sensing volume remains constant while the probe-source distance is decreased. Attempts to increase the spatial resolution of promising macroscopic detectors can be limited by both the difficulty associated with fabrication and more fundamentally, the decrease in size comes at the cost of decreasing the active area of the sensor. However, recently Hall sensors fabricated from graphene, with a wire width of 85 nm, have demonstrated sensitivities of $59\,\mu\mathrm{T}/\sqrt{\mathrm{Hz}}$ in ambient conditions [48].

While single and ensemble NV centre magnetometers have sensitives orders of magnitude less than the most sensitive magnetometers such as SERFS and SQUIDS, NV based sensors can locate far closer to the source of the signal. In ensemble-based approaches, the fabrication of compact sensors, which due to the nature of diamond are biologically inert and operational at room temperature offers a means for NV centres to compete with bulkier sensors for the detection of magnetic fields associated with bioelectrical currents [51]. However, it is in the limit of sensing with single spins that the advantage of the small probe-sample distance for magnetic field sensing can be best observed. For example,

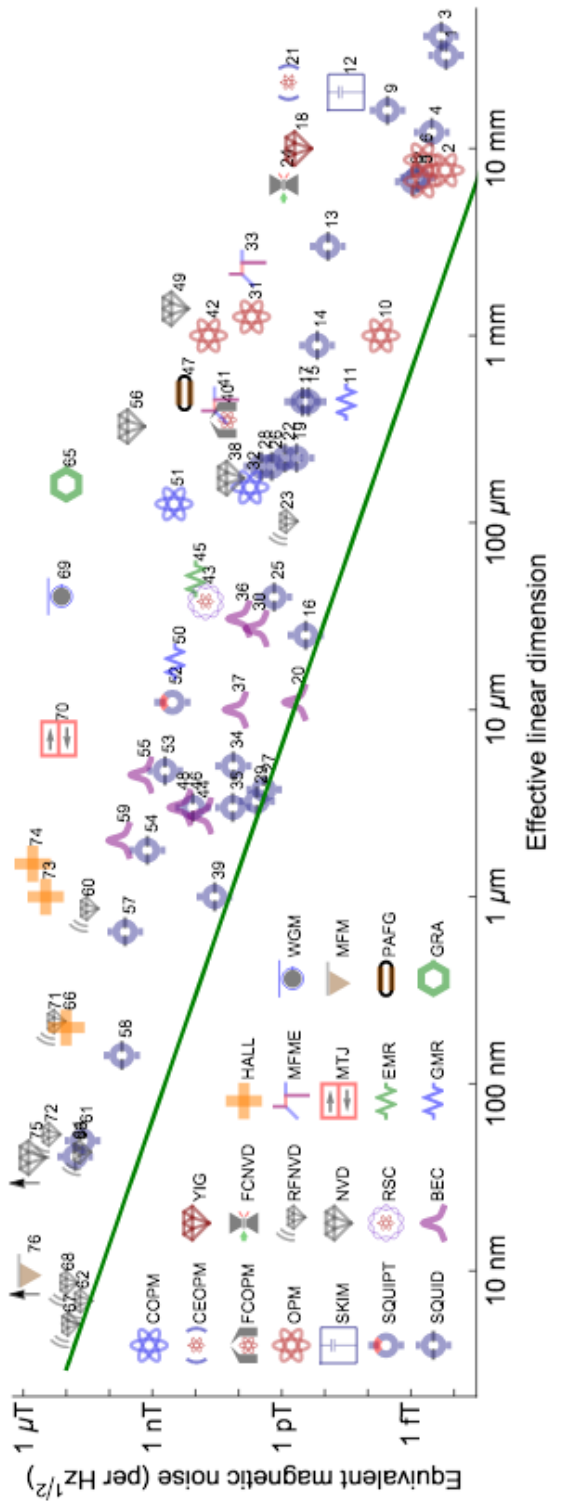

Figure 2.4: Figure from [49] comparing the sensitivity and resolution for promising magnetic field sensors, the corresponding table (Table 1) can also be found in this review. The dimensions shown are an effective linear dimension taking $\sqrt{\text{area}}$ for planar sensors and $\sqrt[3]{\text{volume}}$ for volumetric ones. For point like sensors such as single spins, the effective linear dimension indicates $\sqrt[3]{\text{volume}}$ for a sphere with radius equal to the minimum source-detector distance. Acronyms are defined as follows: SQUID, superconducting quantum interference device; SQUIPT, superconducting quantum interference proximity transistor; SKIM, superconducting kinetic impedance magnetometer; OPM, optically pumped magnetometer; FCOPM, OPM with flux concentrators; CEOPM, cavity-enhanced OPM; COPM, OPM with cold thermal atoms; BEC, Bose-Einstein condensate; RSC, Rydberg Schrödinger cat; NVD, nitrogen-vacancy center in diamond; RFNVD, radio-frequency NVD; FCNVD, NVD with flux concentrators; YIG, yttrium-aluminum-garnet; GMR, giant magnetoresistance; EMR, extraordinary magnetoresistance; MTJ, magnetic tunnel junction; MEMF, magnetoelectric multiferroic; HALL, Hall-effect sensor; GRA, graphene; PAFG, parallel gating fluxgate; MFM, magnetic force microscope, WGM, whispering-gallery mode magnetostrictive. Excepting RFNVD, noise levels are the lowest reported value at measurement frequencies less than 1kHz. An arrow indicates that the value is off the scale.

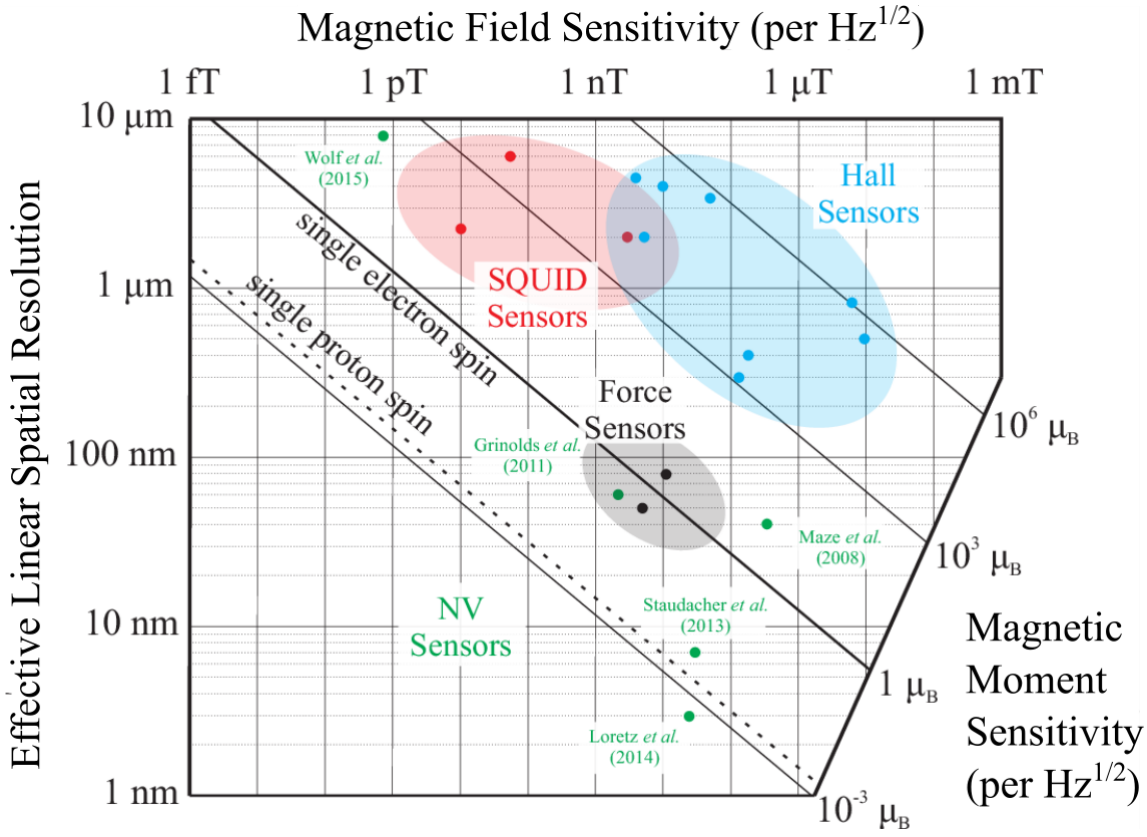

Figure 2.5: Figure adapted from the thesis of Chang [50], comparing high resolution magnetic field sensors comparing NV centres and other candidate sensors for high spatial resolution magnetometry. The dots of differing colours show experimentally recorded sensitivities and spatial resolutions, red represents SQUID sensors, blue Hall sensors, black for force sensors and green NV centre based magnetometers. The diagonal lines represent the stand off required for a given sensitivity to detect magnetic moments in units of the Bohr magneton.

the magnetic field produced by small magnetic particles typically decreases with a $1/r^3$ relationship from the source [52], demonstrating how a modest decrease in probe-sample distances can lead to a large increase in the measurable field from the source, allowing NV centre based sensors to compete with more sensitive magnetometers with greater probe-sample separations. In scanning probe approaches, tip-sample distances as low 10 nm have been demonstrated in cryogenic conditions [53]. While in ambient conditions, standoffs of 50 nm are routinely achieved and limited by the control of the tip-sample separation dependent upon the technique used to scan the probe. The second effect limiting the standoff distance is the depth of the NV centre in the host diamond, with shallow NV centres both in small nanodiamonds or close to bulk single-crystal diamond surfaces experiencing surface effects, which lead to conversion to the neutral charge state, NV^0, or shortened coherence times, rendering shallow defects ill-suited to sensing applications [54, 47]. Attempts to decrease the standoff even further have centred on the improved fabrication of stable defects close to the surface [47]. Additionally, it has been proposed that the standoff could effectively be decreased by using an additional spin system located on the surface coupled to an NV centre in a large nanodiamond [55].

The magnetometer at the centre of this thesis is designed to use a scanning probe approach to position a single spin to capitalise on the most promising region of sensing for NV centres: high sensitivity, high-resolution detection.

2.4.1 Scanning Probe Magnetometer

The use of single spins as high spatial resolution magnetic field probes was first proposed by Chernobrod and Burman in 2005 [56]. The proposed instrument, a scanning magnetic microscope, utilises high-sensitivity magnetic field detection using ODMR to detect the Zeeman splitting of a suitable sensing spin. The use of a single spin results in a nanoscale detection volume with a defined sensing axis, leading to nanoscale spatial resolution. Chernobrod and Burman's proposal outlines using existing scanning probe techniques such as scanning tunnelling microscopy (STM) or atomic force microscopy (AFM) to raster scan

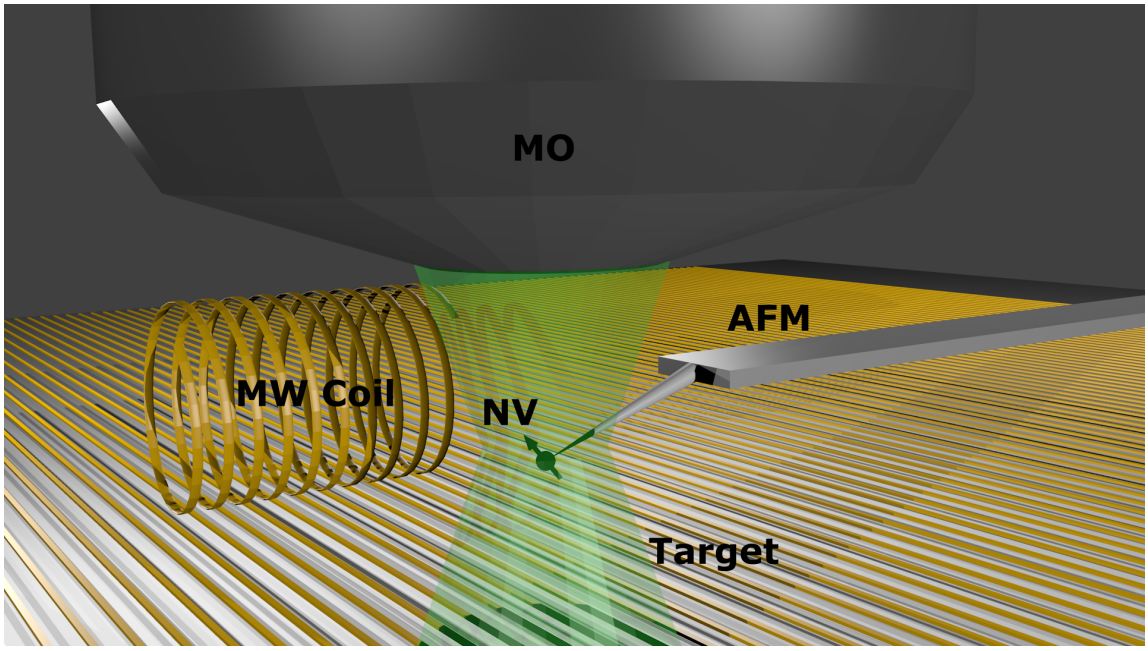

Figure 2.6: The NV centre is placed on a nano-position instrument such as an atomic force microscope (AFM). The NV centre spin is bought close to a magnetic target, here represented by an array of micron-sized gold wires. The Oersted field produced by a current in the array is the field to be probed in this example. The NV centre is located in the confocal spot under the MO of a confocal microscope which provides the means to address and readout the ODMR signal. The technique requires the application of a microwave field, here represented by a microwave coil.

the sensing spin with nanometer precision above a target to map nanoscale magnetic field variations, with nanometer separation of probe and target. Figure 2.6 illustrates the principle in a 3D model. In addition to the AFM for positioning the NV centre, a microscope objective (MO) is used for optical preparation and readout of the magnetic field. A MW coil is also shown, which serves to produce an oscillating magnetic field required to drive transitions between magnetic sublevels of the sensing spin, as is required for the ODMR technique. In 2008 the NV centre was proposed as the measurement spin in this scheme due to the long coherence times and efficient optical polarisation in ambient conditions [57, 58].

The early demonstrations of NV scanning probe microscopes employed nanodiamonds

hosting single or a small number of NV centres grafted on to AFM tips [2, 59, 60], including the first demonstration by Balasubramanian in 2008 [44]. Typically nanodiamonds are deposited onto a substrate for optical characteristics such as silicon/silicon dioxide. A promising nanodiamond can then be attached to the AFM tip using UV curing glue [44] or a polymer with a positive charge such as poly-L-lysine which is electrostatically attracted to the negative surface charges on hydroxyl-terminated nanodiamonds [61].

An alternative approach to producing probes for scanning probe NV magnetometry by functionalising commercial AFM probes with nanodiamonds grafted to the tip consists of fabricating an AFM probe made from a diamond, with a nanoscale scanning pillar hosting a single NV centre acting as the tip of the atomic force microscope [38]. The scanning nanopillar approach offers several advantages over the grafting approach, such as longer coherence times associated with bulk diamond compared to nanodiamonds, enhanced collection efficiency due to the light-guiding properties of the pillar and more accurate control of the NV sample target distance [62]. The success of custom probes for scanning NV magnetometry has lead to their commercial availability, at the time of writing there are two suppliers of NV centre scanning probes, Qnami and Zabre [63, 64]. The probes from both suppliers utilise a quartz tuning fork as the force feedback sensor for controlling tip-sample separation, with multiple or single NV centres housed in a diamond nanopillar.

Scanning probe NV magnetometers have found a wide range of applications including measurement of the magnetic field produced by 2D current networks, facilitating the reconstruction of current densities with nanoscale spatial resolution [2]. Scanning NV centre magnetometers have recently been used to observe order in antiferromagnetic materials [65, 66, 67, 68], a challenging task due to the sensitivity and spatial resolution required due to the net-zero magnetisation of antiferromagnets. However, the small probe-sample distance, resolution and sensitivity of the scanning NV centre enable the detection of stray magnetic fields outside the material associated with the breaking of symmetry at surfaces or domain walls. Finally, while many applications of scanning NV magnetometers focus on operation in ambient conditions, the approach has also yielded results in cryogenic conditions, facilitating the observation of vortices in superconductors with 10 nm spatial

resolution [53].

The most recent developments in technology include the development of commercially available diamond AFM tips cut in the [110] direction [64]. Typically diamond is cut in the [100] direction resulting in the NV axis orientated at 54.7° to the normal defined by the AFM probe. In [110] two of the possible orientations are now orthogonal to the normal with two at 35° enabling sensitivity to in plane fields and increased sensitivity to out of plane fields. In addition to the development of diamond AFM probes for homebuilt instruments two bench top scanning probe magnetometers became commercially available in 2020; the QSM produced by Zabre [69] and the ProteusQ manufactured by Qnami [70]. The QSM produced by Zabre achieves resolutions in the 1-10 $\mu T/\sqrt{Hz}$ region with spatial resolutions between 30-70 nm. The range of sample motion given by the Zabre QSM corresponds to 6 mm x 6 mm for coarse positioning with a scan range of 90 µm x 90 µm x 15 µm in x,y and z respectively. The scan range for the Proteus Q is given by 100 µm by 100 µm by 50 µm, which typical spatial resolutions in magnetic field images and typical sensitivities not quoted.

2.5 Summary

The NV centre has been shown to be a promising candidate in probing both magnetic fields utilising an all-optical sensing scheme. Comparisons have been drawn to competing sensors demonstrating the potential for NV centres in high spatial resolution high sensitivity detection. Spatial resolutions of the order of 10 nm with sensitivities of 1 $\mu T/\sqrt{Hz}$ can be achieved with simple CW-ODMR using single NV centres. The use of pulsed measurement schemes has been discussed, showing the potential for single NV centre senors to achieve sensitivities as low 5 $nT/\sqrt{Hz}$ in high purity diamond. Finally, how a single NV centre can be attached to a scanning probe to produce magnetic field images has been presented. The next chapter discusses the construction of optical instrumentation required to perform high spatial resolution magnetometry with small numbers of NV centres affixed to a scanning probe.

Chapter 3

Optical Instrumentation

3.1 Introduction

The optical components of an instrument designed for NV centre magnetometry are some of the most critical due to the technique's optical nature, with the application of laser light required to spin polarise the NV centre. The readout mechanism is also optical in nature as Zeeman splitting of the NV ground state is detected via changes in the spin-dependent photoluminescence. Therefore, the sensitivity of magnetic field detection with NV is intrinsically linked to the ability to detect the PL intensity decrease on resonance. As a result, the optical collection efficiency of the PL signal defines the minimum magnetic field that can be detected. The NV centre can be efficiently excited, and the PL collected using conventional optical techniques, such as confocal microscopy the method used by the instrument. The use of confocal microscopy confines the excitation and collection volume, offering efficient excitation and detection from point-like emitters with a greater signal to noise ratio than conventional wide-field microscopy. While confocal microscopy confines the excitation volume, this technique is diffraction-limited. As such, the excitation and volume cannot be localised to a spot size smaller than $\sim 250\,\mathrm{nm}$, an order of magnitude larger than a single NV centre. Magnetic field sensing using single NV centres commonly use Hanbury Brown Twiss (HBT) interferometry to determine if an NV centre PL signal

from a diffraction-limited spot contains one or multiple centres through measurement of the second-order correlation function. As this instrument is designed as a single centre NV magnetometer, the additional components required for HBT interferometry are included in this instrument. The final optical component of this instrument is a wide-field microscope. The ability to image in wide-field mode is useful in sample preparation, such as aligning a region of interest (ROI) of a macroscopic sample for both imaging by confocal microscopy and using a home-built atomic force microscope (AFM) system.

This chapter describes the design and construction of the optical instrumentation in the NV magnetometer at the centre of this thesis. The primary focus will be the development of a custom-built confocal microscope, the primary purpose of which is to facilitate optical preparation and readout of NV centres. The additional hardware required to enable the measurement of spectral and temporal properties of emitters, such as NV centres, probed by the confocal microscope will also be presented. The theory of operation of confocal microscopy and the limits to the technique discussed, along with a description of the principle of operation of the additional detection modes. The performance of the optical instrumentation is presented with data from suitable test targets. Finally, the design of a wide-field microscope to provide a complementary imaging method is presented, and the performance evaluated.

3.2 Confocal Microscopy

The sensitivity of an NV centre magnetometer, discussed in Chapter 2, is inversely proportional to the square root of the number of photons collected in the measurement. It follows the most sensitive magnetometer will therefore collect the maximum number of available photons. There are two methods to increase the signal collected: increase the number of NV centres contributing to the signal or increase the collection efficiency of the optical instrumentation. The number of centres addressed is highly dependent on the NV centre fabrication technique and the needs of the application, with this instrument focusing on single NV centre magnetometry for high spatial resolution sensing. To optimise the

sensitivity of any NV magnetometer the collection efficiency of the optical instrumentation must be maximised. There have been a variety of imaging modalities demonstrated to collect NV centre PL for magnetometry purposes with varying efficiencies. For example, common approaches use wide-field [45, 71, 72] or confocal microscopes [2, 44] or more custom arrangements for specific applications, such as doping nanodiamonds hosting NV centres into optical fibres [73]. The efficiency of different imaging modalities will be discussed later in this chapter when evaluating the performance of the optical instrumentation. Ultimately, the goal for all the optical systems used for NV centre magnetometry is to maximise collection efficiency in a way suitable for the design and application for the given sensor geometry. Wide-field microscopes are advantageous when combined with NV ensembles, as an entire microscope field of view can be read out simultaneously. Scanning probe approaches commonly use confocal microscopes as only the diffraction-limited spot containing the nanodiamond with single/few NV centres require illumination and measurement, with the sample typically scanned to form a field map. The use of a confocal microscope suppresses the background contribution by rejecting photons emitted in planes above and below the confocal plane, offering an improved signal-to-noise ratio than in wide-field instruments. In this instrument, a confocal microscope is used, primarily in a sample scanning methodology. This section will now discuss the theory and resolution limit of confocal microscopy both as a means to address NV centres and as an imaging tool in its own right for nanoscale sample characterisation.

The stage scanning confocal microscope was patented by Minsky in 1955 [74] and had become widely available by the 1980s. The ability to optically section thick fluorescent specimens was an important development, particularly for a wide range of biological applications. When compared to conventional wide-field microscopy the primary benefit of confocal microscopy is the rejection of out of plane light, confocal microscopy also offers a modest improvement in lateral resolution, facilitating the formation of high-resolution 3D images of a sample. This section outlines the basic principle of confocal microscopy and the limits to its resolution. The design and performance of the confocal microscope constructed for use in the NV magnetometer will be presented.

3.2.1 Principle of Operation

Confocal microscopy is a well established tool for scientific investigations and with a wealth of literature available describing the key concept and principle of operation. The following description of the optical paths the follows the description in "Confocal Laser Scanning Microscopy" by Shepard and Shotton [75], while the resolution equations follow a review by Webb [76]. A comprehensive review discussing the design, performance and operation of confocal microscopy has also been produced by Pawley et al [77].

Confocal microscopy can be understood by considering the optical paths of the excitation light and the resultant signal, which can either be photoluminescence (PL) from a target emitter or backscattered light from a sample. This description will consider the case for PL confocal microscopy as this will be the main mode of operation for use in an NV magnetometer. The excitation and detection optical paths are the same for PL or reflectance modes where the difference in technique depends only depends on the spectral filtering of the signal. Figure 3.1 demonstrates the basic principle of confocal microscopy, showing rejection of out of plane light and the enhancement of lateral resolution. The light source, such as a laser, originates from a small aperture, ensuring the light source can be considered a point source. The light from the point source is often collimated and directed towards a microscope objective lens (MO) using a dichroic mirror. The reflectance of the mirror depends on the wavelength of the incident light, typically short wavelengths are reflected while longer wavelengths are transmitted through the mirror. The excitation light is focused to a diffraction-limited spot size in the focal plane of the MO. A target illuminated by this spot emits light (PL) and this light is collected by the same objective lens. The collected light from the sample is collimated by the MO and directed towards the dichroic mirror. However, the light emitted by the sample is at a longer wavelength than the illumination light, this allows for the transmission of the collected light through the dichroic mirror but rejection of backscattered light also collected by the MO. The light transmitted through the dichroic mirror is focused to a diffraction-limited spot by a tube lens. The plane in which the spot from the tube lens is focused, the image plane, is con-

jugate to the MO focal plane. As a result, a point in focus in the MO focal plane will therefore be in focus in the image plane. The key feature of confocal microscopy is the addition of a small aperture or pinhole in the image plane. Only light that passes through the pinhole is transmitted to the detector. Consequently, light originating from planes above or below the MO focal plane is out of focus at the pinhole and therefore strongly attenuated at the detector. Furthermore, the pinhole acts as a spatial filter laterally as light originating from points in the focal plane, but not the confocal spot of the MO, are suppressed and do not contribute to the measured signal and eventual image formation.

Thus far an infinitely small source of light focusing to an infinitely small point in the MO focal plane has been considered. However, the image of the source has a finite width described by a point spread function (PSF). When discussing the resolution of confocal microscopes the PSF is often stated in the paraxial approximation (low NA objectives), while this is not the physical case the approximation accurately models the observed behaviour [76]. In the paraxial approximation the point spread function from a MO with a circular aperture has the form $2J_1^2(\rho(r))/\rho(r)^2$ in the MO focal plane, where $\rho(r)$ is defined as $\rho(r) = \frac{2\pi}{\lambda} r\mathrm{NA}$, λ is the wavelength of excitation light, NA is the numerical aperture of the lens and r is the radial distance from the MO centre and J_1 is the Bessel function of the first kind of order one. This in-plane intensity distribution is known as an Airy pattern [76]. The pattern consists of a central intensity maximum surrounded by rings with decreasing intensity from the centre. The central region is known as an Airy disk, with a diameter of 1 Airy unit (AU), which is given by [76]

$$\mathrm{AU} = 1.22\frac{\lambda}{\mathrm{NA}} \tag{3.1}$$

. The resolution of the conventional optical and confocal microscopes are fundamentally related to the spatial distribution of the intensity profile in the focal plane, the resolution can be quantified by considering the Rayleigh criterion. The Rayleigh criterion states the minimum separation in order to resolve two point sources radiating incoherently is 0.5 AU, corresponding to the maximum of an Airy pattern produced by one source is no closer

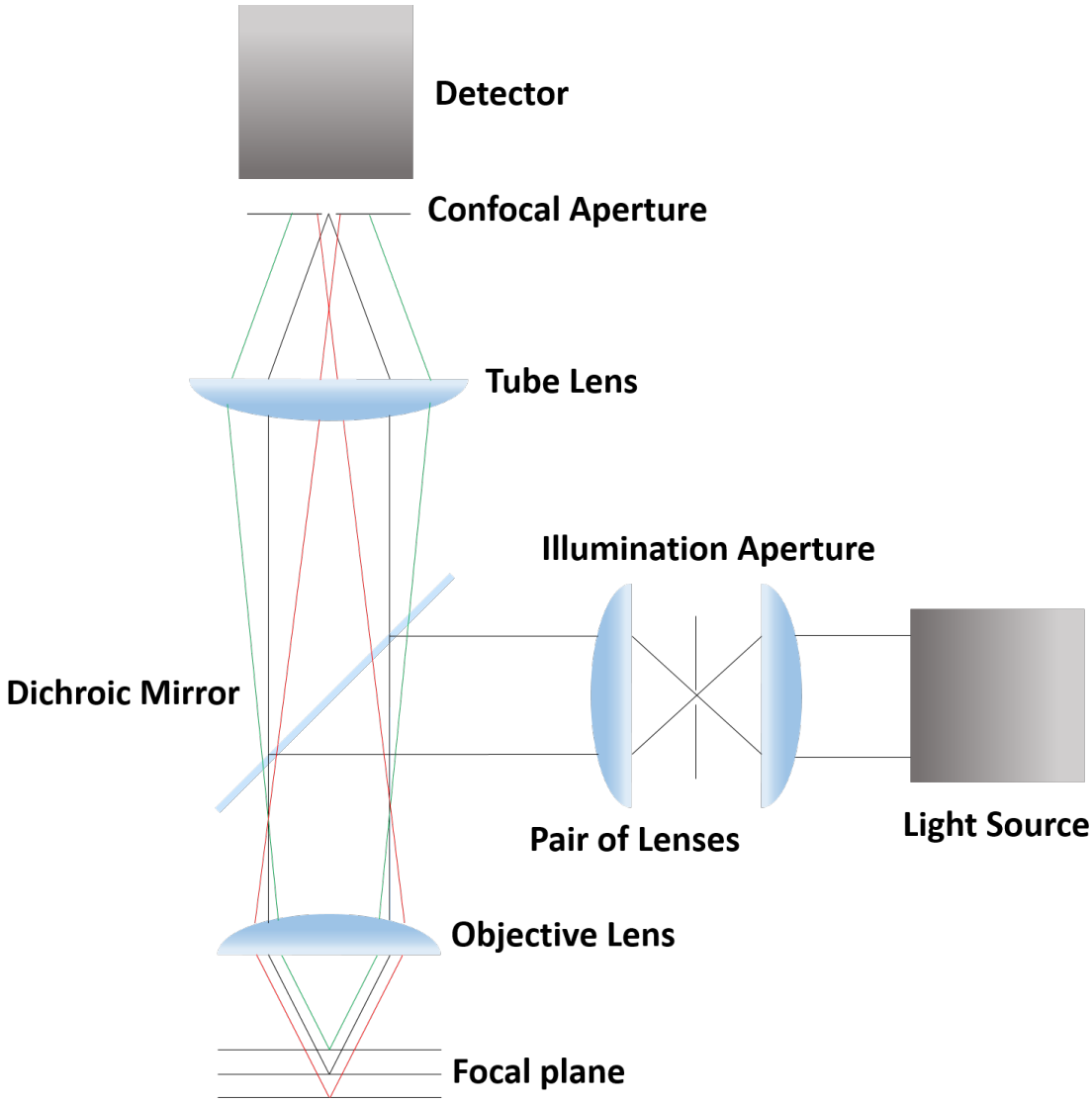

Figure 3.1: Diagram showing the principle of a confocal microscope. A light source is focused onto a small aperture to ensure the light is spatially coherent. The light is reflected by a dichroic mirror into the microscope objective (MO), which focuses the light to a diffraction-limited spot. The same MO collects PL photons from excited species in the focal spot and collimates this light which can now pass through the dichroic mirror. A tube lens focuses the light through the confocal aperture. Light originating from planes above and below the focal plane of the MO is out of focus at the confocal aperture and is therefore strongly attenuated at the detector, making only a small contribution to the detected intensity. The red path shows light originating below the focal plane and green light shows light from a plane closer than the focal plane to the MO.

than the first minimum to the adjacent Airy pattern. Following the Raleigh criterion the lateral resolution for a conventional wide-field microscope is given by [76],

$$\Delta r_{\text{wide}} = 0.61\frac{\lambda}{\text{NA}} \tag{3.2}$$

where λ is the wavelength of the illumination radiation source and NA is the numerical aperture of the microscope objective lens. For a confocal microscope, the lateral resolution is slightly improved due to narrowing of the intensity point spread function compared to the wide-field case. The narrow PSF results from the point scanning nature as the confocal PSF is then given by the product of the illumination and detection PSF. The confocal lateral resolution is given by [76],

$$\Delta r_{\text{confocal}} = 0.44\frac{\lambda}{\text{NA}}. \tag{3.3}$$

The introduction of the confocal pinhole leads to a rejection of out of plane light so that two objects along the optical axis can be resolved. As such, axial resolution can defined as a measure of the separation along the optical axis for which two point sources can be resolved. The resolution along the axial, or z direction [76] is given by

$$\Delta z = 1.5n\frac{\lambda}{(\text{NA})^2}. \tag{3.4}$$

where n is the refractive index of the object medium. The unique ability of the confocal microscope to discriminate sources along the optical axis arises due to the pinhole rejecting light from planes other than the MO focal plane. Therefore, the size of the pinhole is an important consideration in any confocal microscope, too large a pinhole and the ability to depth discriminate will be lost, too small and signal to noise ratio is greatly reduced. The size of the pinhole and the effect on axial and lateral resolution has been evaluated for reflectance [78] and fluorescence microscopes [79]. Generally, the lateral resolution is more sensitive than axial resolution to small variations in size. The diameter chosen

is application dependent with a user choosing to prioritise resolution at the expense of the amount of signal collected. In many commercially available confocal microscopes the pinhole is not fixed but variable using a pinhole wheel to change aperture sizes. Typically diameters of pinholes used are close the size of the size of the image of the Airy disk at the pinhole, given by the Airy disk size in MO focal plane multiplied by the total magnification at the at the pinhole.

Image Formation

The success of confocal microscopy arises from the rejection of light originating from out of the MO focal plane and the confinement of the excitation volume, reducing the measurement volume to a diffraction limited size. As such, to acquire information over a macroscopically sized sample the measured point has to be moved relative to the sample, for which there are two common methods: sample scanning or beam scanning. Sample scanning involves scanning the sample under a stationary imaging point under the MO, typically using piezoelectric scanning stages. Alternatively, there is a finite field of view associated with a MO and scanning the excitation beam in the MO back focal plane translates the measured point in the focal plane. The method of image formation determines the field of view (FOV) of the confocal microscope, with sample scanning limited only by the range of motion of the scanning stage. The FOV in a beam scanning approach is limited by the optics scanning the beam, more fundamentally the FOV is limited by the MO. The field of view for an MO is given by [80]

$$\mathrm{FOV} = \frac{\mathrm{F.N}}{\mathrm{M}} \tag{3.5}$$

M represents the magnification of the MO and F.N describes the field number, a property of a MO. By convention, dividing the field number by the magnification yields the diameter field of view in mm. For example, an MO with a field number of, F.N 26.5, and a magnification, M = x100, has a maximum circular field of view with a diameter of 265 µm. The FOV of a sample scanning confocal microscope is defined only by the range

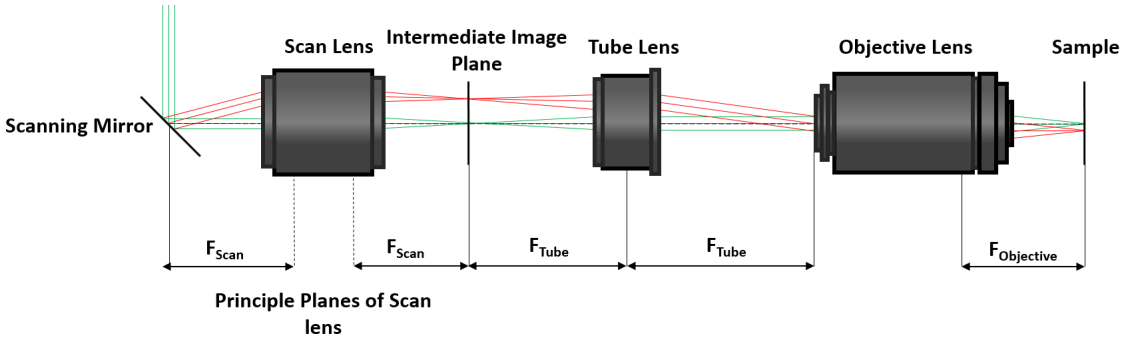

Figure 3.2: 4f scanning arrangement for a beam scanning confocal microscope. A scanning mirror or galvanometric mirror is placed at the back focal plane of a scan lens. The angle of the mirror changes the angle the beam makes to the optical axis, with the optical paths corresponding to two mirror positions shown in red and green. The scanned beam is focused into the focal plane of the scan lens and then relayed to the MO focal plane by the tube lens and the MO. The role of the scan and tube lens in this system is to confine the scanning of the beam to a flat plane under the MO.

of the sample scanning stage, with a stage with a large range and nanometer precision desirable. Piezoelectric flexure stages are commonly employed in nanoscale sample scanning instruments and combine nanoscale accuracy with macroscopic range. Typically, the range of sample scanning microscopes is lower than for beam scanning microscopes, with the precision of the control signal, the size of piezoelectric elements and the large voltages required to produce movement setting a practical upper limit to the design of scan stages.

When compared to beam scanning, sample scanning is often less economical given the relative cost of piezoelectric scanning stages compared to scanning mirrors. Image formation via beam scanning can also be faster than in sample scanning microscopes due to the slower response time of the stages as compared to galvanometers used to produce scanning mirror motion. However, a sample scanning approach reduces the potential to introduce artefacts into the final image, as the beam path remains fixed for the duration of the scan. To reduce artefacts in beam scanning microscopes additional optics are commonly required to restrict the scanning of the beam to the focal plane of the MO. Figure 3.2 shows

a 4f arrangement for a pair of scanning mirrors with the additional optics required.

The position of the measurement point in the MO focal plane is determined by the angle that the beam makes to the optical axis, and thus scanning the angle of the beam will translate the measured point in the focal plane. To scan the angle the beam makes to the MO entrance pupil a pair of mirrors are used, typically one for each orthogonal axis in the MO focal plane. The angle of the scan mirrors is varied by a galvanometer, which produces a deflection of the mirror from a neutral position to deflect the beam. The position of the galvanometer and therefore mirror is in turn controlled by a servo motor, which drives the galvanometer current. To enable accurate control of the measurement point a scan and tube lens pair is inserted between the scanning mirrors and the MO, see figure 3.2. The role of the lens pair is to confine the scanned beam to the focal plane. The beam is scanned in a plane conjugate to the MO focal plane, labelled intermediate image plane in Figure 3.2, and an image of this plane formed in the MO focal plane. Scanning the mirror in an intermediate plane facilitates relatively large mirror motion to produce small changes in the MO focal plane. The scan and tube lens pair also have a secondary function - ensuring that the entrance pupil of the MO is completely filled. In the case where the MO is underfilled, the effective NA of the MO is reduced.

In summary, confocal microscopy offers high lateral resolution optical imaging from a confined excitation volume with out of plane light rejected. For an excitation wavelength of 515 nm with a high numerical aperture lens, e.g NA = 0.8, the lateral resolution is of order $\Delta r \approx 300\,\text{nm}$ with a corresponding axial resolution of $\Delta z \approx 1\,\mu\text{m}$. Confocal microscopy has been identified as a point by point imaging technique with 2D images formed by the sequential acquisition of PL signal from the diffraction-limited measurement volumes. The imaging spot can be scanned via translation of the measurement spot in the MO focal plane by deflecting the beam with scanning mirrors or by scanning the sample under a stationary beam, with each method having relative advantages in different aspects. The out of plane rejection of light and confinement of the excitation volume provides a suitable optical technique to perform optical experiments on atomically sized emitters including optically addressing single NV centres mounted on a scanning probe for magnetometry

applications.

3.2.2 Design of Confocal Microscope

The primary aims of the custom built confocal microscope are to optically prepare and readout the PL signal from single NV centres, both deposited on a substrates and attached to a scanning probe. The following design requirements were identified for the confocal microscope in this instrument:

- An upright microscope geometry as the majority of samples addressed will be opaque. For example, gold nano-wires on a silicon substrate or antiferromagnetic and semiconducting samples.
- High-efficiency collection of photons, as the sensitivity of the optical magnetometer is directly proportional to the count rate. The microscope must use an in air objective lens as high-efficiency oil immersion objectives are this is not compatible with scanning probe techniques.
- Large z range in which the MO focal plane can be varied, facilitating optical detection of magnetic fields several microns above sample surfaces.
- Open system to accommodate both large samples and the insertion of an AFM probe to the focal spot for scanning probe magnetometry and simultaneous AFM/confocal measurement.

A schematic of the custom built confocal microscope is shown in figure 3.3 and the design described below. In the following description of the confocal microscope components, the first entry in the bracket refers to the label in figure 3.3 and the second entry refers to the model and part number. The excitation source is a 515 nm Vortran Stradus diode laser with maximum power output of 60 mW. The laser outputs the light into a single-mode fiber of mode free diameter (MFD) 2.2 µm and a collimating lens (L1, Optosigma FCFC-12.7PC + lens) is form a 2 mm diameter beam. Then the excitation beam is passed

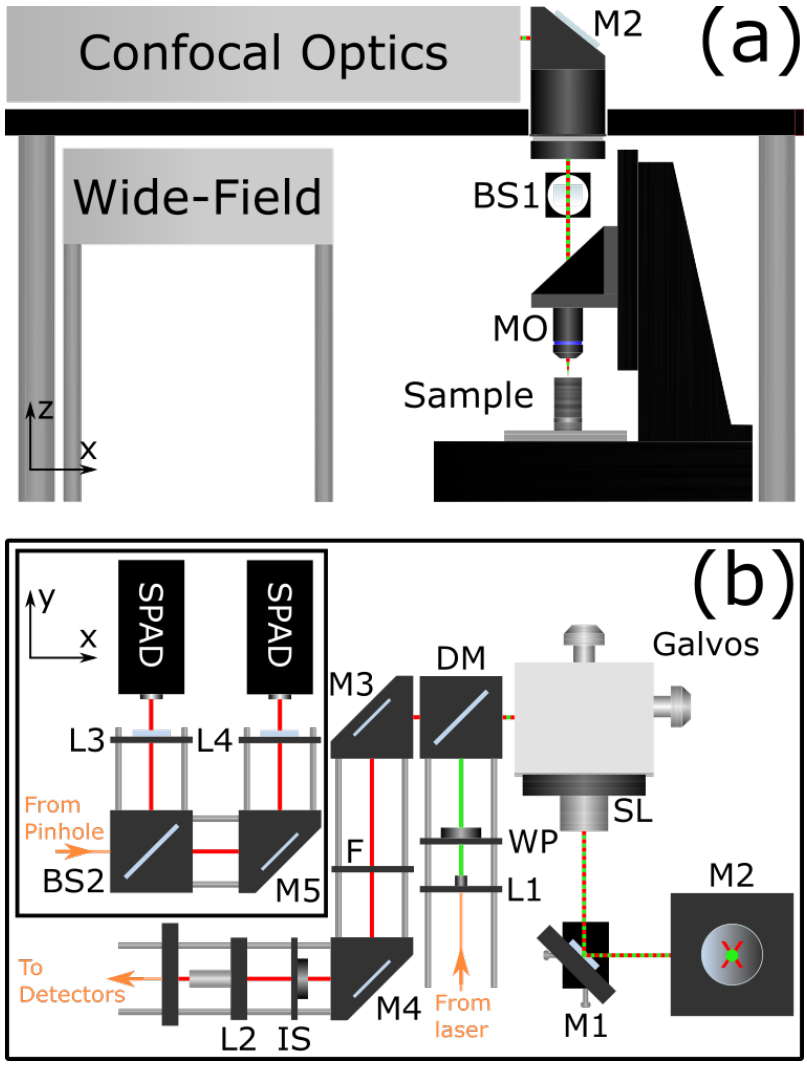

Figure 3.3: (a) Diagram, showing how the wide-field and confocal microscope are combined to image the sample. Light from the confocal optics, which are shown in detail in (b), contained within the black box, is directed down by the mirror then passes through the tube lens into the back focal plane of the MO. The MO can be translated along the optical axis to bring objects of varying heights into focus. The sample can be mounted in a variety of sample holders, depending on the type of sample. The sample holder is mounted on to an xyz piezo stage. Light collected from the sample is collimated and reflected into the confocal optics on the optical breadboard. A beam splitter, BS1, acts to combine the wide-field camera (not shown) into the confocal system. The lower portion of the figure shows the paths of the light from the sample (red line) and the excitation light (green line) through the on board confocal optics.

through a half-wave plate, (WP, Thorlabs WPQ10M-532) for polarisation control. The beam is directed towards a dichroic mirror (DM, Semrock Di02-R514-25x36) which reflects the beam onto a pair of scanning mirrors (Galvos, Scanlab DynaXIs), which facilitate beam scanning in the xy plane. The xy mirrors are in the closely spaced configuration [77], where the centre of the two mirrors is placed at the back focal plane of the scan lens. Following transmission through the galvanometer housing, a scan lens (SL, Thorlabs LSM03-VIS) is placed in the beam path along with a tube lens (TL, Thorlabs ITL200) to form a telescope. The scanning mirrors along with a scan and tube lens telescope are assembled in the 4f configuration. The primary role of the scan-tube telescope is to increase the scan range of the beam while confining the plane that is scanned to the focal plane of the MO, the telescope also expands the beam to fill the MO entrance pupil. Finally, a pair of mirrors (M1/M2, Semrock MaxMirror MM3-311-T6-25.4) are used to direct the beam into the objective back focal plane. Mirror 1 is mounted on a xy dovetail stage (Thorlabs DT12XY/M) to aid in beam alignment.

The objective lens (MO) is produced by Olympus (model number MPLFLN) with x100 magnification and numerical aperture, NA = 0.8. The MO is the most critical component in a confocal microscope, defining the efficiency of photon collection, the spatial resolution and, in the case of beam scanning the FOV. The MPLFLN was chosen due it's combined high in air numerical aperture, NA = 0.8, and long working distance of 3.4 mm, facilitating efficient photon collection while operating with scanning probes positioned at the MO focus. The Olympus MPLFLN has previously been utilised for a range NV centre experiments [81, 40], providing an indicator of good chromatic performance, efficiently exciting at 515 nm and collecting the broadband PL from NV centres at the same working distance.

The detection path begins in the MO focal plane, with light collected and collimated by the MO directed through the scan-tube telescope and the galvanometric mirrors. The detection and laser path are split at the dichroic mirror, which transmits the longer wavelength PL light and reflects the laser. To further isolate the PL signal from the detection signal two filters are placed in the optical path. A long-pass filter (F, Semrock FF01-

593/LP-25) and a notch filter (F, NF03-514E-25) strongly attenuate the 515 nm light of the laser and as result of the spectral filtering the collection window of confocal microscope is 600-900 nm. The filtered signal is directed towards two mirrors (M3/M4, Semrock MaxMirror) which act to vary the position and angle of the collected, to align the light with the confocal aperture. A multimode fiber (Thorlabs, M67L01) with MFD of 25 µm fulfils the role of the confocal aperture. A coupling lens (L2, Thorlabs C230TMD) is used to focus the beam into the fiber acting as the apeture, with the position of the lens controlled by an xy positioner, as part of a fiber launch kit (Thorlabs, KT110/M). Translation of the lens in the xy plane produces a translation of the focused point in the plane of the pinhole for alignment. The fiber is mounted into a component producing translation of the fiber along the optical axis, ensuring the pinhole is placed in the focal plane of the fiber coupling lens. The size of the Airy disk image in the plane of the confocal pinhole is given by the magnification in the tube lens focal plane multiplied by the magnification of the scan lens and fiber coupling lens telescope used to focus to the pinhole aperture. As a result, the 25 µm fibre corresponds to pinhole of $\approx$ 1.4 AU, which is larger than the ideal case for optimal background rejection [78, 79]. However, this size fiber and lens pair was selected as it was the smallest multimode fiber available with the lens NA chosen to match for efficient coupling and a large fibre offers greater photon collection at the slight expense of axial resolution from the true confocal case.

Once the light has been coupled into the fiber for spatial filtering the output is taken to the detection optics. The use of a fiber compared to a fixed aperture allows for flexibility in the positioning and type of detection system. The fibre is coupled into a light-box which is illustrated by a black line in figure 3.3 (b). A beamsplitter (BS2, Thorlabs BPD2545-G) and a mirror (M4, Semrock MaxMirror) are used to direct the beam towards a pair of achromatic lenses (L3 and L4, Thorlabs AC127-030-B) which focuses the signal onto a pair of single photon avalanche diodes or SPADs (SPAD, Excelitas AQRH-14). A pair of short pass filters (Thorlabs FESH0750) are also placed in front of the SPAD sensors to reduce cross-talk, this is discussed later in the chapter. The short pass filters reducing the spectral collection window for the SPAD detection system to 600-750 nm. The use of SPADs to

register the photon events allows for high sensitivity detection while also enabling the collection of temporal data of the PL signal. The output from the SPADS is delivered into a 'time tagger' (Picoharp 300) for time-correlated single-photon counting (TCSPC). Alternatively, for simple PL experiments, the signal is delivered to a pulse counting data acquisition card (National Instruments PCIe-6323). For applications where the spectral composition of the optical signal is of interest, the fiber output can be removed from the box housing the SPADs and directed to a spectrometer (Princeton instruments, SpectraPro 2150 Monochromator with Acton PD473 detector).

Image Formation

As confocal microscopy forms an image on a point-by-point basis a method of scanning the imaged spot is required. In this instrument, two methods are employed; scanning the sample under a fixed beam, and scanning the beam while the sample remains stationary.

Sample Scanning The primary imaging mode for this instrument involves simultaneous measurement from the confocal microscope and a scanning probe, which will utilise sample scanning rather than beam scanning. For NV centre magnetometry the use of sample scanning maintains alignment between confocal microscope and probe as well as playing a vital role in the feedback loops to maintain probe sample separation over a scan.

To perform confocal images via raster scanning the sample piezoelectric flexure stages are used. The scan stages are produced by Piezoconcept with model number LFHS2.50 in the xy directions and the z motion is provided by an accompanying Z-STAGE.50 stage. The precision of the stages is 0.05 nm with a typical noise floor a factor of 10 lower than this. The piezoelectric stages are mounted on a manual scanning stage to produce motion in x and y for coarse sample positioning with a range of 25 mm in each axis, controlled by micrometres with 1 µm vernier scale graduation. The same manufacturer, Piezoconcept, has since produced a new range of scan stages with a far greater scan range in xy, with the same z range. For example, the SPM3LR.300.xx stage offers a smaller noise floor by a

factor of 2 than the stages used in the instrument, with a xy scan range extended to 300 µm. Increasing the scan range represents an easy way to extend the FOV of such an instrument, which may be of interest for some experiments particularly with short integration times. Sample scanning images recorded using this instrument have a range of 50 µm in x and 50 µm in y. The position of the stages is controlled using an analogue signal from 0-10 V for each axis, with 0 V corresponding to the the most retracted position on that axis (0 µm) and 10 V to full extension (50 µm). The control signals are amplified through a manufacturer supplied control unit to a scale of 0-150 V to apply the correct voltage to the piezoelectric elements. The high-resolution achievable results from the closed-loop nature of the stages providing feedback to the controller to correct the position. The position of the stage can be read via an analogue output on the control unit, the output ranges are 0-10 V for each axis.

Beam Scanning The instrument was also designed with beam scanning capability to complement the primary beam scanning approach. The use of a scanning beam system in this instrument would extend the scan range of the confocal microscope beyond the range possible with sample scanning, up to a fundamental limit set by circular image of diameter 265 µm of the MO. The extended FOV in pure confocal mode is of interest for examining large areas of a substrate to characterise nanodiamonds to determine their suitability for magnetic field sensing in a time efficient manner. For scanning probe magnetometry, the ability to scan the beam provides two additional degrees of freedom when aligning the optically active region of the probe with the confocal microscope.

3.2.3 Reflectance Microscopy

The primary imaging mode of the confocal microscope is referred to as PL mode. In this mode of operation, the detected signal is the photoluminescent photons in the range 600-750 nm from emitters excited under 515 nm excitation. In PL mode it is desirable to suppress the contribution from the excitation source to the measured signal to increase the signal-to-noise ratio of the PL measurement. To suppress the contribution the laser signal is

attenuated with wavelength-dependent filters (notch and long pass) and the dichroic mirror, resulting in the optical density (OD) on the path in between the galvanometers and the detectors equal to OD $\approx$ 14. To complement PL mode, the detection of the backscattered 515 nm light can provide an additional imaging mode, referred to as reflectance mode. Images are performed used the same beam/sample scanning method as PL mode, however, now the backscattered laser forms the dominant contribution to the measured signal.

The optical density of the dichroic mirror (OD $\approx$ 2) is low enough that the removal of the long pass and notch filters produce sufficient intensity at the detectors for imaging using the backscattered signal. In this instrument, safe power levels are found by using the wide-field camera to ensure the sample is positioned in the MO focal plane. The SPADs and laser are first turned on with the long pass and notch filters replaced by a large number of ND filters, typically amounting to OD = 8. The high OD experienced by the backscattered signal will attenuate the signal to the extent that the detectors display the dark count. The filters can be removed sequentially until the signal is at a safe power level for the detectors. For example, when imaging silicon/silicon dioxide, a common substrate for nanodiamond deposition, neutral density filters providing a total optical density of 2.3 are required for safe reflectance mode operation under the illumination of several 100 µWs of laser power. In nanodiamond characterisation experiments a substrate with nanodiamonds is typically scanned with a high power laser to bleach emitters which are not photo-stable. Bleaching scans are performed with relatively long duration $\approx$ 1 hour at 5 mW excitation power over the full 50 µm x 50 µm FOV, integrating the reflectance signal over the scan offers a time-efficient approach to building a high-resolution image of the sample surface, providing a reference for later PL images.

The reflectance imaging mode in the confocal microscope increases the functionality of the instrument, facilitating high-resolution imaging of the parts of a sample that do not photoluminesce. Specifically for NV magnetometry applications, the reflectance mode of operation facilitates the observation of reference marks on a substrate. On a macroscopically sized sample reference marks provide a means to align regions of interest with the microscope FOV and the ability to index diffraction-limited PL sources, such as nanodia-

monds.

3.2.4 Synchronisation

The experimental control for confocal microscopy experiments is performed using a multipurpose NI card (PCIe- 6323). The card is equipped with four counting channels and 4 analogue outputs with ±10 V range and 16-bit resolution. One counting channel generates the timing signals, defining the duration for which SPAD TTL pulses are integrated to form a pixel in a confocal image, while a second and third channel record the input SPAD pulses. The card's analogue outputs are used to generate scan signals, to control either the galvanometers (for beam scanning) or the sample scanning stages (for sample scanning). Recording the SPAD pulses and generating the scan signals from the same device simplifies the synchronisation for confocal measurement as compared to multiple devices. The user interface for confocal measurement is provided by Qudi, a modular python suite for home-built confocal microscopes developed at the University of Ulm [82].

While operating the confocal microscope in sample scanning mode, the primary mode of operation, the analogue control voltages for both galvanometric mirrors are held constant. To generate the constant control voltages a home-built 8 channel 16-bit digital to analogue converter (DAC) was constructed. The DAC assembly was based on an open-source design that uses an Arduino microcontroller and an analog devices AD5764 evaluation board. The assembly of a home-built DAC was motivated by the limited number of available outputs on the NI card (4) as a total of 6 was the minimum number required for scan voltages alone (3 for scan stages, 2 for the scanning mirrors). In addition, the open source design is based on the analog devices AD5764 chip which has a relatively low noise level of 45 µV, according to the manufacturers specification [84]. The design uses a single microprocessor to control 2 AD5764 chips, giving a total of 8 analog outputs with a ±10 V range providing additional outputs for future experimental control. The microprocessor code that updates the DAC registers along with a parts list is available online [83]. To pass parameters to the DAC chips via the microprocessor a Python script with a graphical user interface (GUI)

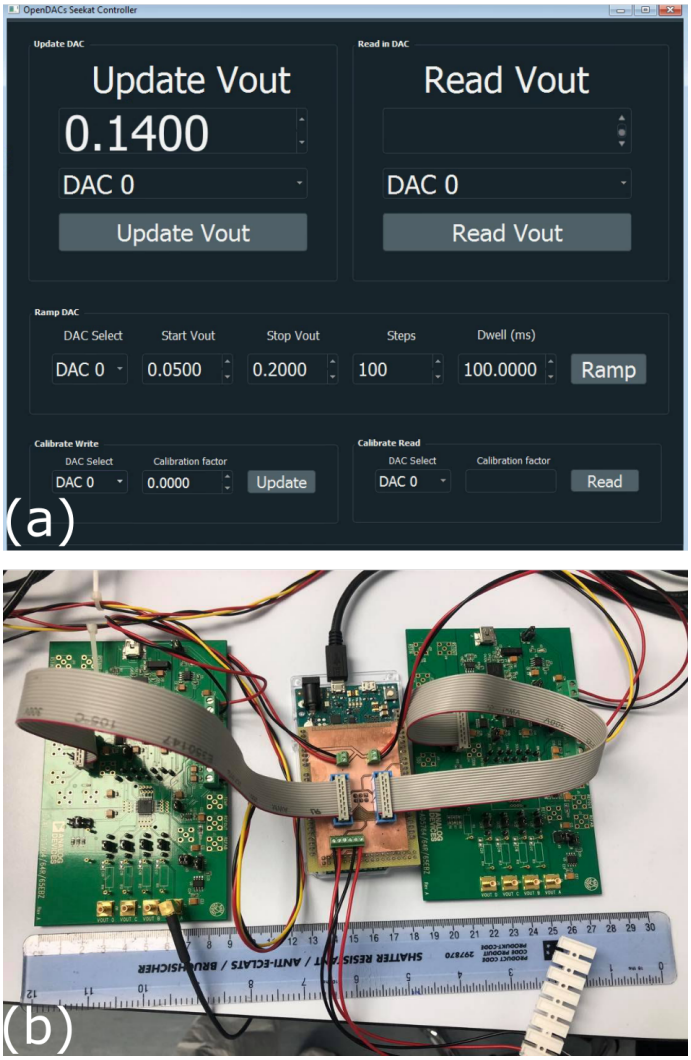

Figure 3.4: Home-built DAC for galvanometric scan mirror control signal generation. (a) Python user Interface used to update DAC registers via microprocessor. (b) Hardware configuration, microprocessor (Arduino DUE) and two AD5764 Analog Device evaluation boards, based on open source design [83].

was developed, see figure 3.4 for the developed user interface and hardware setup.

Optical experiments performed where the confocal microscope generates the measurement signal, such as scanning NV magnetometry can be controlled by range of additional hardware. The specific synchronisation and control sequence will be discussed before each experiment in the relevant section of this thesis. However, a brief overview is included here. The NI counter channels can be configured to accept an external gate signal, an approach well suited for the more complex control sequences involved in NV centre magnetometry, where the synchronisation of a large range of devices including the laser, detectors, and microwave components is required. Complex NV magnetometry sequences not only require the synchronising of a wide range of hardware but also timing precision on the order of nanoseconds, much faster than can be achieved by software control is essential. To achieve hardware control on these short timescales devices are preconfigured with parameters and experience a state change, or enable the output dependent on an input logic pulse. A synchronous digital pattern and arbitrary waveform and generator produced by Swabian instruments (Swabian Instruments Puslestreamer, 8 digital outputs) is used to produce the logic pulses, acting as both the external timing signal for the counter and to control the external hardware in a synchronised manner. As a final method of confocal imaging, the SPAD TTL signal can be integrated by the control unit used to perform AFM measurements. This approach facilitates combined confocal and AFM measurements and is discussed in greater depth in the scanning probe microscopy chapter.

3.2.5 Confocal Performance

The instrument, when assembled, has a footprint of 800 mm by 600 mm by 600 mm excluding the control electronics which are housed on a separate rack. A selection of images showing the instrument size and layout is shown in figure 3.5. The optics are enclosed in a large black anodised aluminium box to optically isolate the instruments from external light sources and limit open beam working, enabling the installation of a laser interlock. To connect the instrument to external devices connections are passed into the box either by

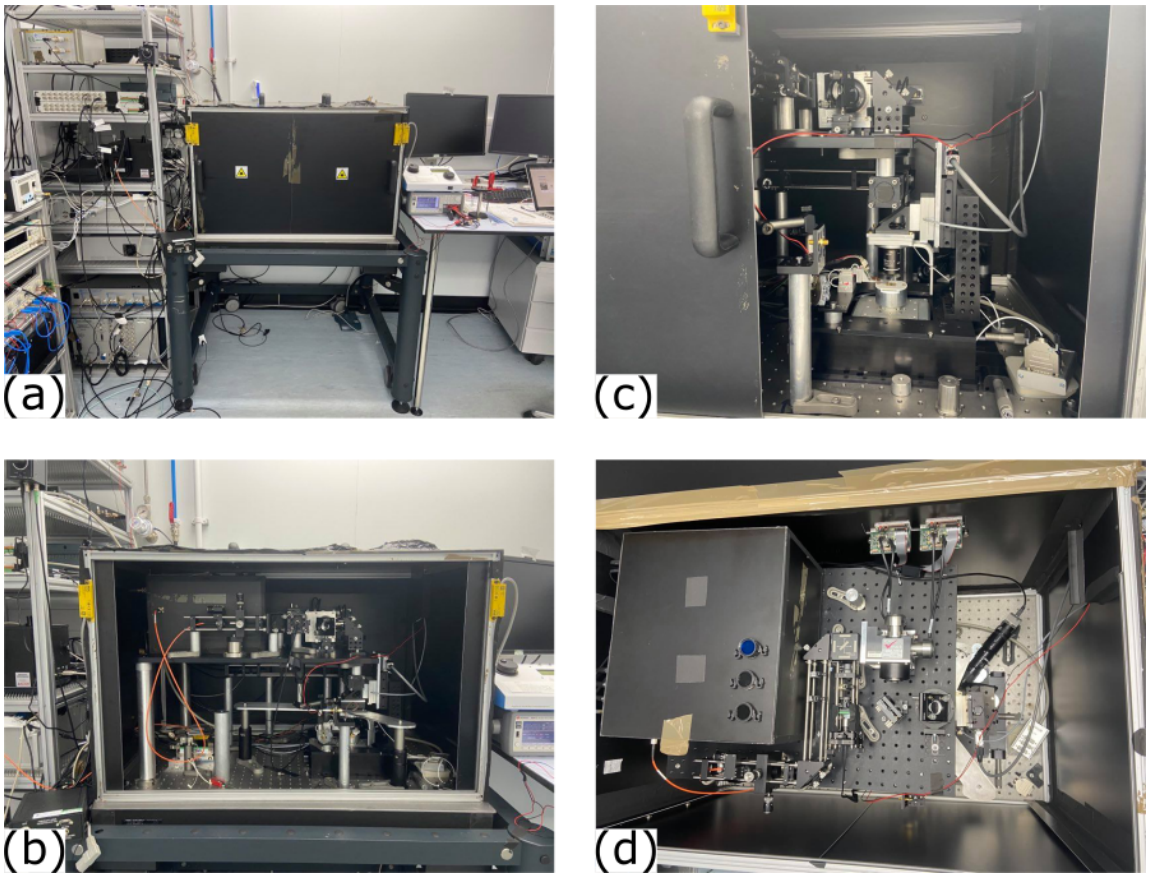

Figure 3.5: Images of the assembled instrument (a) Highlights overall size of the light-tight enclosure housing the optical components, a rack of supporting instruments can be seen on the left. (b) Access panels removed to provide a view of optical components, the MO and sample stages can be seen in the bottom right and confocal optics on the raised breadboard. (c) Sample loading door opened showing MO and sample scanning stages. (d) Top-down view of the raised breadboard showing the confocal optics and secondary detection enclosure.

bulkhead connectors or small holes made into the box. To ensure external light is excluded from the enclosure the connection holes are also fitted with 3D printed covers to ensure there is no line of sight from external sources into the enclosure. In figures 3.5(b) and 3.5(d) a smaller black anodised aluminium box housing the SPADs and focusing optics can be seen. The smaller box is fitted with a black anodised aluminium blanking plate to limit the collection of light originating inside the large box and passing through the tapped holes in the raised breadboard towards the detectors. The nested box approach results in the detectors showing the manufacturer stated dark count (≈ 250 cps) when the large enclosure doors are shut but the room lights remain on.

Reflectance Performance

The optical performance of this instrument is first shown by presenting results from the confocal microscope operated in reflectance mode. Figure 3.6(a) shows a confocal reflectance image of a patterned silicon/silicon dioxide wafer with nanodiamonds deposited on to the surface. The wafer was supplied by Gavin Morley's group at the University of Warwick with the nanodiamonds deposited onto the wafer by Ben Wood. Figure 3.6 (b) and (c) show 2D and 3D projections of the topography of the sample recorded by the AFM component of this instrument, the operation of which is detailed in Chapter 3. To estimate the lateral resolution of the microscope, a smaller range reflectance scan is shown in 3.7(a) with a selection of line profiles shown in figure 3.7(b). Gwyddion, an open-source SPM data analysis package [85] was used to generate figure 3.7(a) and extract the profiles shown in figure 3.7(b). To estimate the spatial resolution the FWHM of small features was estimated by reading off the line profile in Gwydion, with FWHMs ≈ 490 nm, ≈ 470 nm and ≈ 520 nm estimated for line profiles 1, 2 and 3 respectively. The theoretical lateral resolution limit for confocal microscopy is given by equation 3.3, for a MO with NA = 0.8 and an illumination source of 515 nm is equal to 280 nm. The comparison between the theoretical resolution and estimated FWHM here is limited by the physical size of the object probed in image 3.7(b) and the high refractive index of the nanodiamonds. However, routine observation of objects with diameters in the range 400-500 nm provides a rough

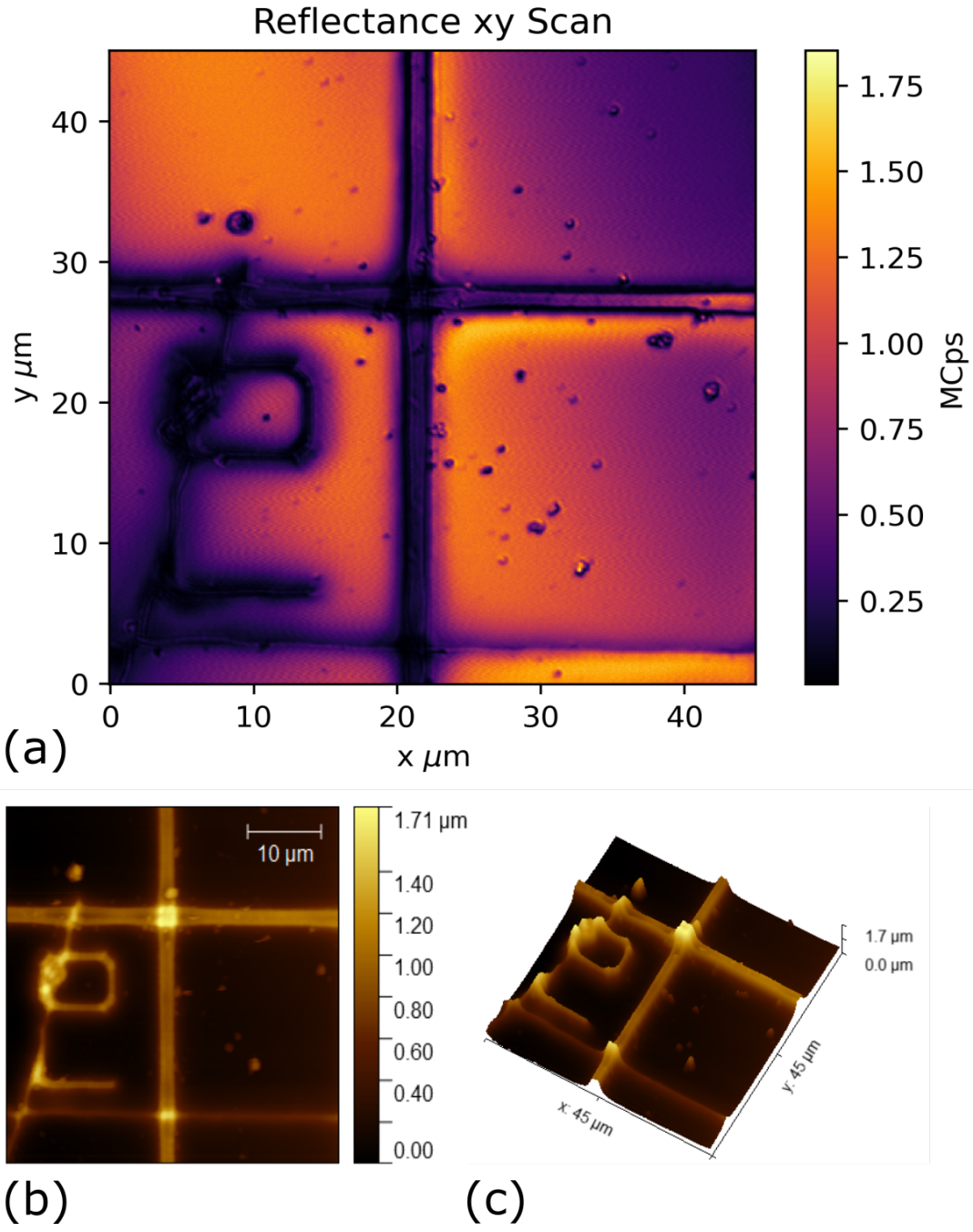

Figure 3.6: Confocal reflectance image of nanodiamonds on Si/SiO_2 substrate (sample prepared by Ben Wood at the University of Warwick). Images (b) and (c) show topographical images recorded using the AFM in this instrument.

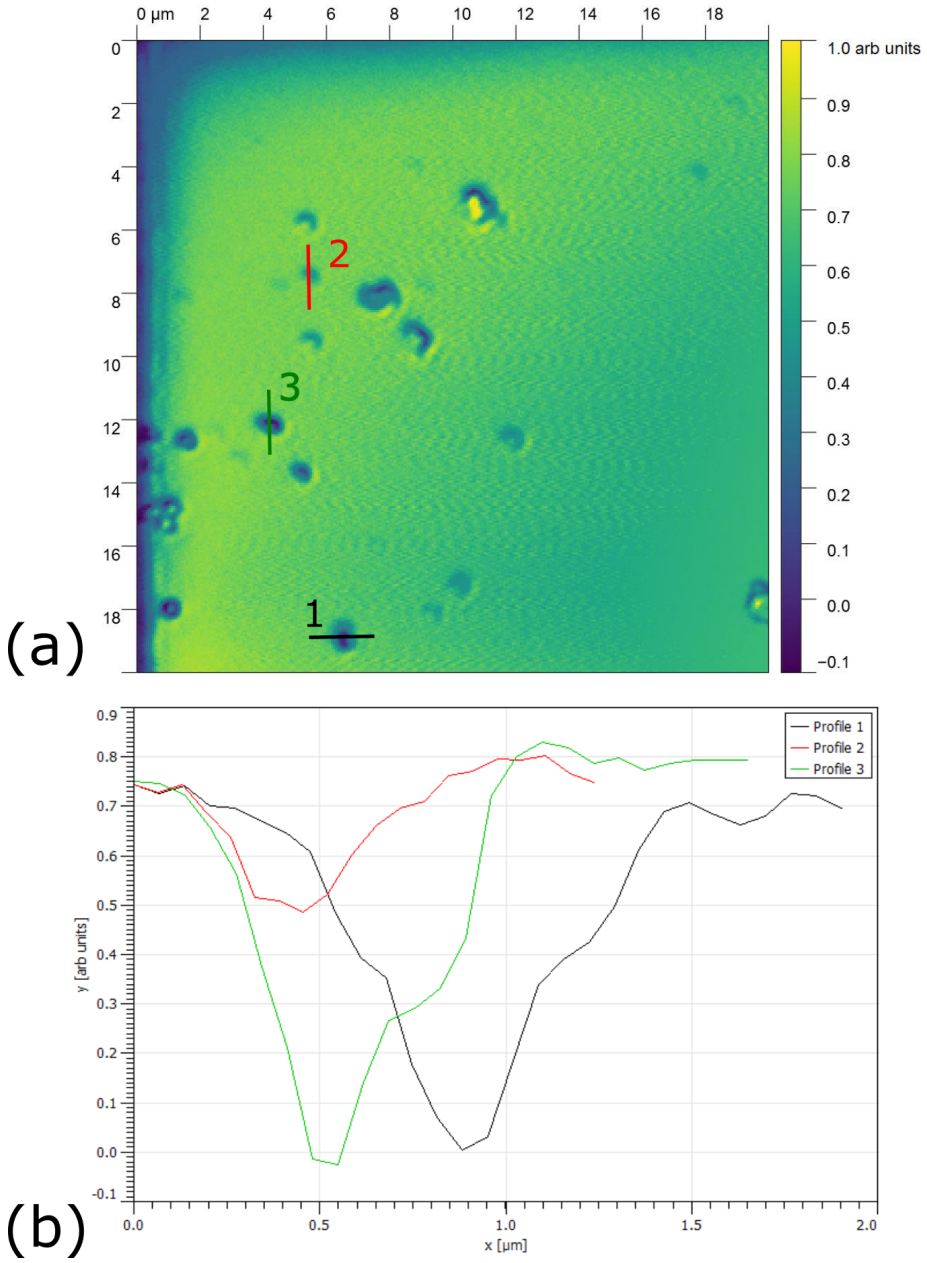

Figure 3.7: Reflectance image of $Si/Si0_2$ wafer with nanodiamond deposition. (a) shows the xy image and (b) a selection of line profiles for a series of random objects in the FOV. Objects with FWHMs of less than 500 nm can routinely be observed.

approximation of the lateral resolution. To more accurately quantify the lateral resolution a test target could be used, with targets of a known size imaged.

The axial resolution was quantified using a method identified by Cogswell et al, scanning a flat object axially and recording the FWHM [86]. Figure 3.8(a) shows a xz confocal scan as a flat mirror was scanned under the stationary beam with a narrowed range xz scan in shown in Figure 3.8(b). A typical line file with Gaussian fit shown in 3.8(c). The FWHM stated corresponds to the average FWHM of Gaussian fit applied to several line z line profiles corresponding to different x positions. The FWHM of the xz scan was found to be 1020±15 nm. The measured FWHM is related to the theoretical axial resolution, Δz, by FWHM = $0.84\Delta z$ [76]. For a 515 nm excitation laser with an MO of NA = 0.8 and the definition of Δz given in equation 3 the theoretically predicted FWHM of the mirror scan is FWHM = 1014 nm, which is in good agreement with the measured 1020±15 nm.

In the works by Cogswell et al [86] the method of scanning a flat mirror and observing the response yielded not only the axial resolution but also identified aberrations in the optical system. In this instrument, it was found that the xz scan could be used to provide feedback on the optical alignment of the scan-tube lens telescope. Following the initial alignment of the microscope, the detection optics remained coupled efficiently when fine adjustments were made to the optical system. To ensure the tube scan-tube lens separation is optimal, small adjustments to the lens positions along the optical axis were made and the xz mirror scan used as a feedback parameter. Figure 3.9 shows two examples of the misaligned case where large sidebands can be seen in the depth scan. The tube lens was translated along the optical axis until the sidebands were minimised and the axial profile symmetric. However, it was found that the sidebands could not be entirely suppressed using this approach. A new mechanism for more accurate tube lens positioning would be required for further improvement.

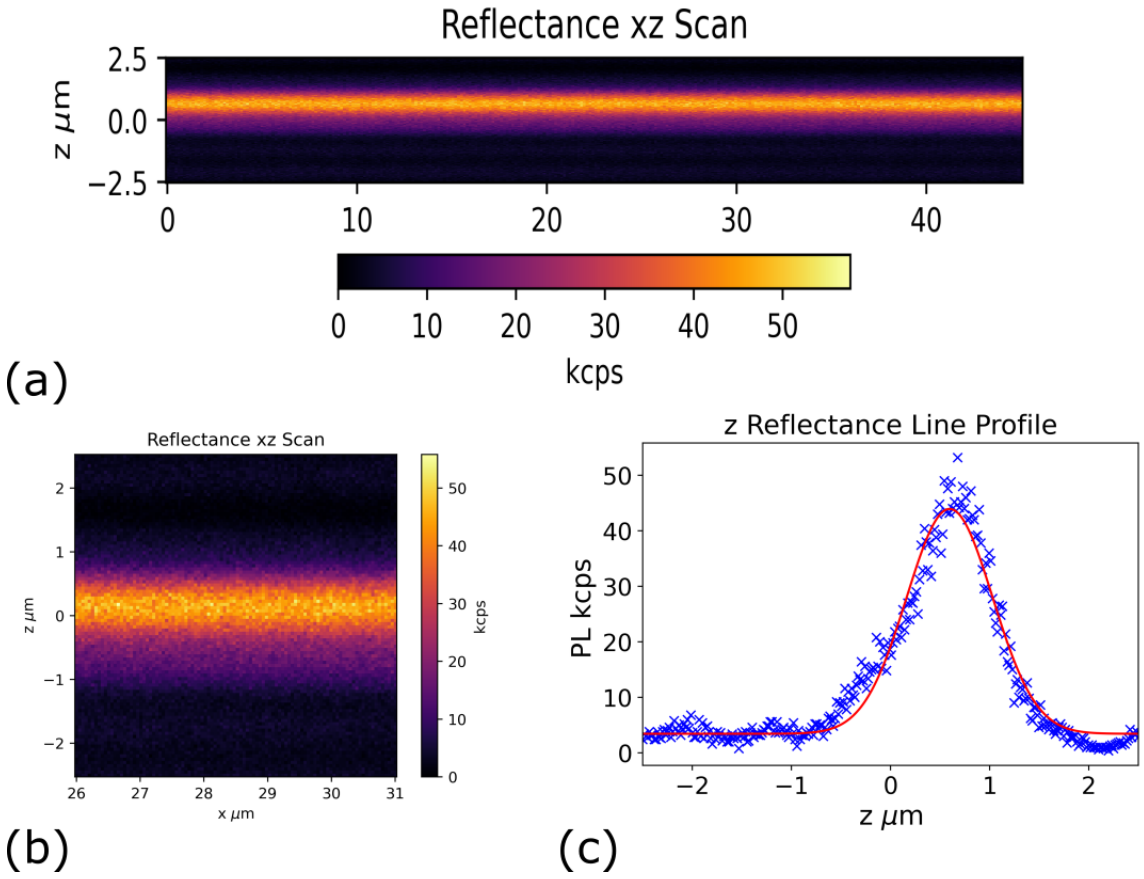

Figure 3.8: (a) Confocal depth scan of flat mirror to provide an estimate of axial resolution. (b) Narrow xz range mirror scan. (c) Line profile from depth scan shown in (b) with Gaussian fit applied to estimate FWHM = 1020±15 nm.

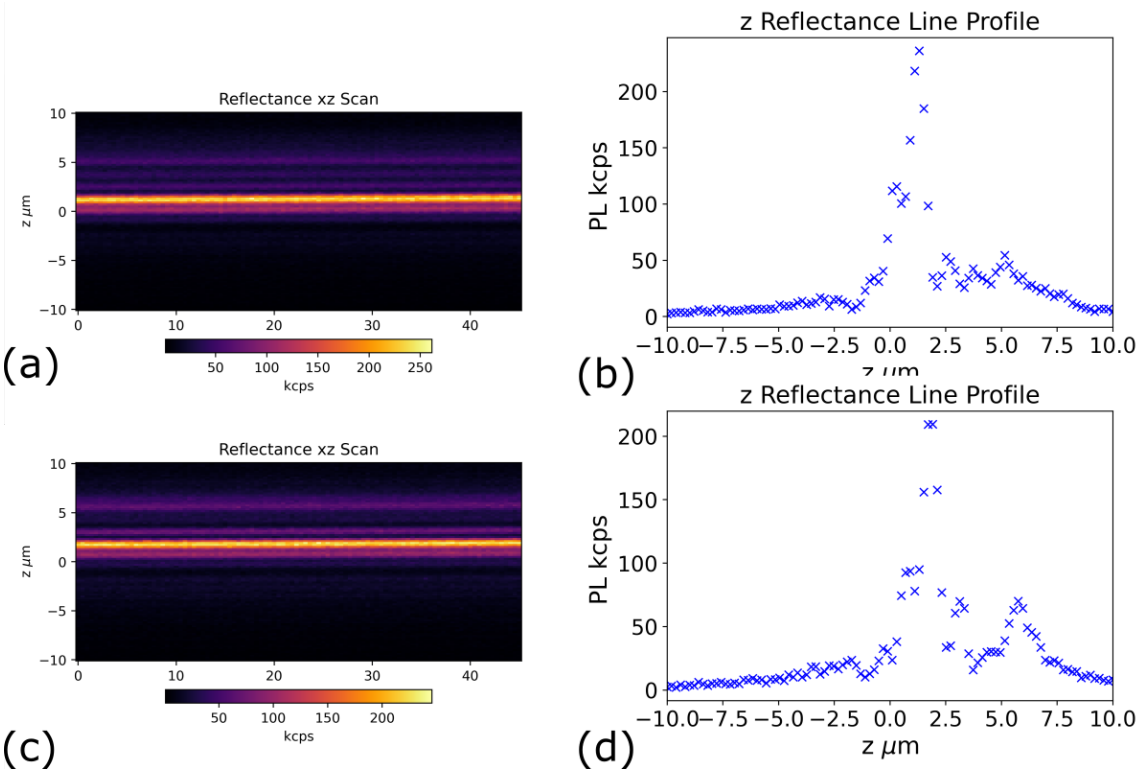

Figure 3.9: Confocal depth scans on flat mirror showing incorrect scan-tube lens separation. (a) and (b) correspond to two different scan tube separations with corresponding line profiles in (b) and (d).

Photoluminescene Performance

The primary motivation for constructing the confocal microscope is to optically pump and then detect PL photons from NV centres. To provide a quantitative measure of confocal performance in photoluminescence mode the lateral and axial resolution were evaluated.

The point spread function of a microscope describes the spatial extent of an image of a point source. In the theory section, the axial and lateral resolutions given assume an infinitely small confocal aperture in the paraxial approximation (low NA lenses). However, in a physical system, the detector has a finite size and high NA lenses are used for efficient photon collection. The ratio of the laser waist to the MO back focal plane also leads to a slight modification of the point spread function from the ideal case [76]. A simple approach to the measurement of the PSF is to calculate the FWHM of the central intensity lobe [77]. The FWHM approach has the experimental advantage of reducing a complex multidimensional PSF to just three numbers which define the PSF along the three axes. In homebuilt confocal microscopes built for NV centre detection, a common approach to evaluating the spatial distribution of the NV centre PL is to fit a Gaussian function to the spatial intensity profile [82, 87].

To estimate the resolution of the confocal microscope a point-like source was scanned in x and y and along the axial direction, z. A nanodiamond of sub-wavelength size can be considered a point source irradiating in to air [87], making an emitter hosted in a nanodiamond a suitable target for measuring the PSF. Figure 3.10 shows typical large range PL scans to identify sub-diffraction limited PL sources for further investigation. Figure 3.11 shows typical xy and xz scans of a nanodiamond fluorescing under illumination by 515 nm light along with line profiles extracted from the scan, corresponding to the line containing the maximum intensity value in each direction. The FWHM in the two in-plane directions (xy) was recorded by fitting 2D Gaussians to a range of objects leading to an x and y FWHM of 515 nm $\pm$ 15 nm and 440 nm $\pm$ 5 nm. The z FWHM was calculated using the same method scanning the same emitters in the xz plane leading to a FWHM 1.7 µm $\pm$ 0.1 µm.

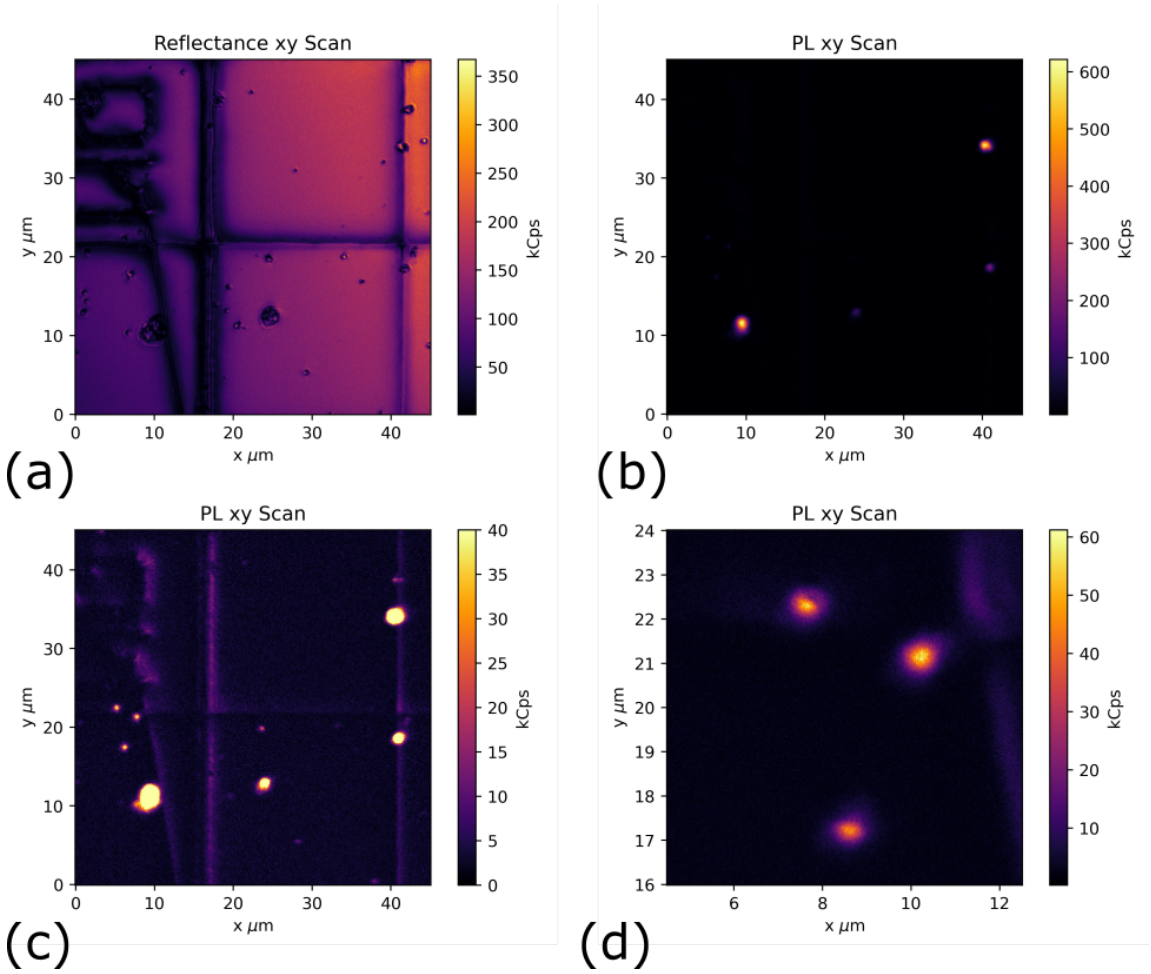

Figure 3.10: Typical scans of diffraction limited emitters on a substrate. (a) Reflectance image taken during sample bleaching serving to identify large emitters (b) PL scan showing large bright emitters. (c) Reduced colour scale image of (b) to identify smaller dim emitters in the FOV. (d) Reduced range scan of small emitters.

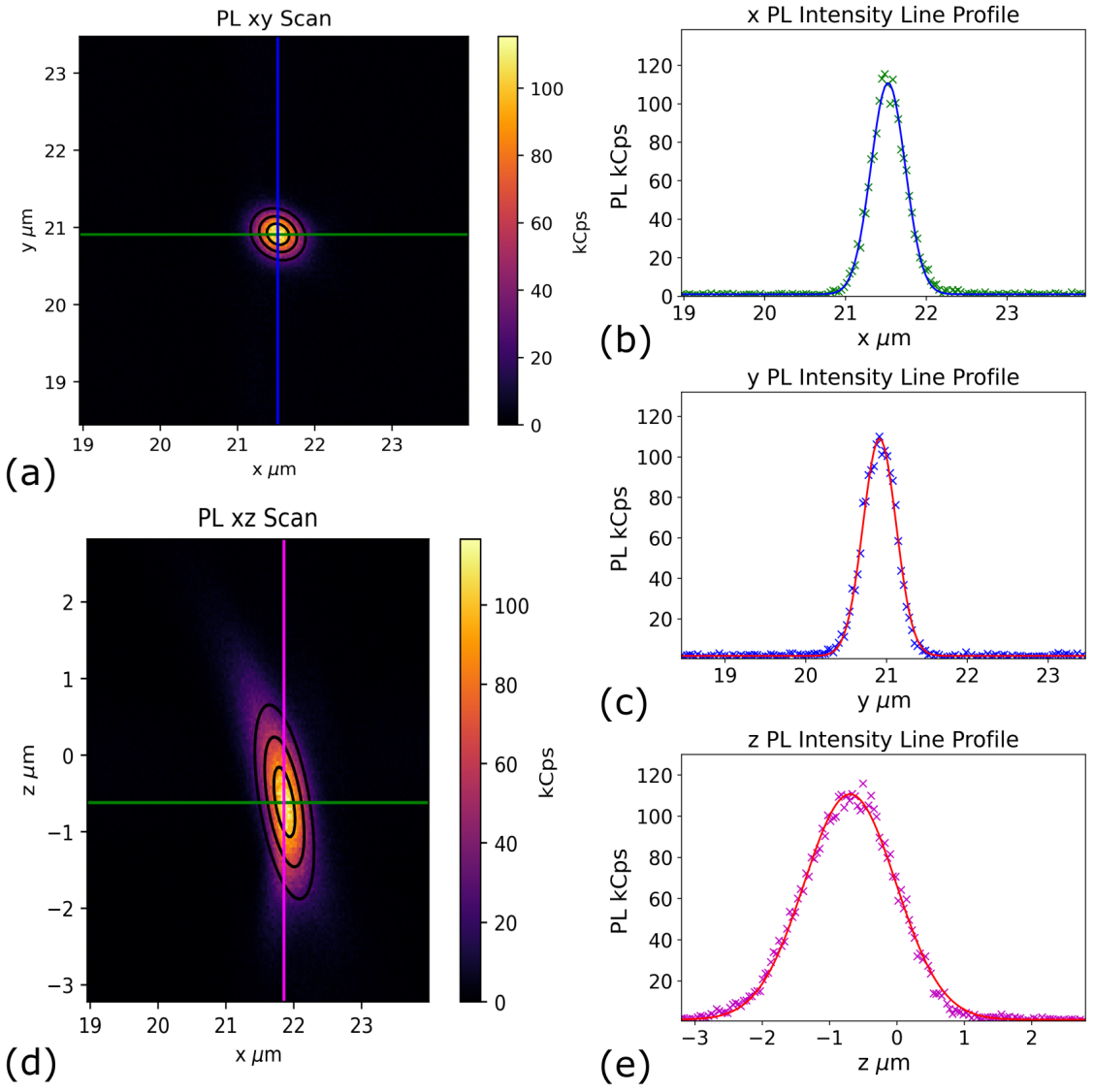

Figure 3.11: Photoluminescence of images of typical nanodiamonds hosting PL sources. (a) shows a typical xy scan with the line profiles of the line with maximum intensity show in (b) and (c). (d) xz of scan of emitter showing extent of PL signal in the axial direction with 2D gaussian fit (e) Line profile corresponding to maximum intensity in z direction.

The difference in the lateral resolutions suggests imperfect optical alignment producing a slightly elliptical laser profile in the sample plane. The theoretical limit to the lateral resolution given in equation 2 is 311 nm assuming the majority of the PL emission occurs at 700 nm. The observed values of 515 nm ± 15 nm and 440 nm ± 5 nm suggest that the resolution is enhanced compared to the conventional wide-field case, corresponding to 475 nm. However, the applicability of this comparison is limited given the high NA lens used, the finite-sized detector and the spatial profile of the illumination source on the MO back focal plane. Experimental effects that may result in a recorded resolution being slightly higher than the true resolution of this instrument include both the validity of the nanodiamond acting as point source emitting into air (n = 1 rather than n = 2.4) and sample drift. The larger lateral resolution of 515 nm ± 15 nm corresponds to the slow scan direction, which is expected to be more susceptible to drift.

Collection Efficiency

To estimate the collection efficiency in the confocal microscope the losses of each optical element between the microscope focus and the detectors (SPADS) have been examined. The losses associated with each element in the band 600-750 nm stated by the manufacturer is shown in Table 3.12. Where the response is not spectrally uniform, such as for the dichroic mirror, the lowest value in the measurement band is stated. The first entry in Table 3.12 refers to the transmission of PL that has been collected by the MO rather than the efficiency in which the MO collects PL, as this is dependent on the orientation of the emitter with respect to the laser, total internal reflection of the medium hosting the emitter and the NA of the MO [97]. For completeness, the collection efficiency of an MO from a point like source can be roughly estimated through the ratio of the MO collection angle to full 4π solid angle for an isotropic emitter [96, 98]. For an MO with NA = 0.8, the simple comparison of the MO collection angle and the full solid angle suggests the MO collection efficiency for a point source emitting into air has an upper limit of $\approx 17\%$ [96] and this is reduced $\approx 5\%$ for an emitter in bulk diamond collected by an air objective [96]. The fiber collection efficiency was estimated during the alignment process using 515 nm

Component label in Figure 3.3 and part number	Efficiency
M0, Objective lens (Olympus LMPLFLN)	**0.85*** [88]
M2, Mirror (Semrock MaxMirror MM3-311-T6-25.4)	0.99 [89]
M1, Mirror (Semrock MaxMirror MM3-311-T6-25.4)	0.99 [89]
DM, Dichroic Mirror (Semrock Di02-R514-25x36)	0.96 [90]
M3, Mirror (Semrock MaxMirror MM3-311-T6-25.4)	0.99 [89]
M4, Mirror (Semrock MaxMirror MM3-311-T6-25.4)	0.99 [89]
NF, Notch Filter (Semrock NF03-514E-25)	0.95 [91]
LP, Long-pass Filter (Semrock FF01-593/LP-25)	0.98 [92]
Fiber Coupling	$\approx$ **0.50**
BS2, Beamsplitter (Thorlabs BPD2545-G))	$\approx$ 0.95 [93]
L3, Achromatic Lens (Thorlabs AC127-030-B)	$\approx$ 0.96 [94]
SPAD, Detector (Excelitas AQRH-14)	$\approx$ **0.65** [95]
Total	$\approx$ 0.2

Figure 3.12: Summary of losses in the confocal microscope, with the figures in bold highlighting the dominant contributions. * The value shown for the MO corresponds to the transmission of light collected by the MO, rather than the efficiency in which the MO collects light from a point like source, which is limited by the NA, the orientation of the emitter and medium to source is emitting into [96, 97].

light reflected from the sample plane. A power meter was placed in front of the fiber and then on the output of fiber to compare the values. To account for the difference between the wavelength of the green light used for alignment and the spectral region of interest in normal operation 600-750 nm the fiber position was varied slightly along the optical axis to maximise the signal when measuring a PL source. Therefore, the fiber coupling is stated as an approximation and the total losses shown in Table 3.12 are intended to introduce the dominant losses in the system (the SPADS, the fiber coupling and the microscope objective).

The second measure of optical collection efficiency is to measure the PL intensity of a source with a known response. In Chapter 6, the operation of a commercially available NV centre AFM probe [63] in this instrument is discussed at length. However, the relationship between the laser power and the PL intensity from this probe is presented here to provide a measure of optical collection efficiency. The probe is supplied with a specification sheet that facilitates a direct comparison between a state of the art system optimised for NV centre PL detection and the confocal microscope described in this chapter. Figure 3.13 shows both laser power - PL intensity relationship recorded using this instrument, (a), compared to the manufacturer-supplied results for the same probe, (b). The laser power shown in Figure 3.13(a) corresponds to the power measured using a power meter placed under the MO prior to the measurement, as the laser power successfully coupled into the probe is not accurately known.

The maximum count rate recorded in this system is ≈ 250 kcps (when both counters are summed), compared to ≈ 1250 kcps in the Qnami data-sheet, note the data displayed corresponds to the PL measured by a single SPAD, which is half the theoretical maximum for this instrument. The comparison between the confocal microscope and the probe specification indicates the confocal microscope is performing with 5 times lower efficiency that than state of the art instrumentation for NV centre PL measurement. The NA of the MO used in the Qnami test set up is not known, with the use of a higher NA MO (than the NA = 0.8 MO in this system) significantly increasing the count rate observed by the manufacturer. It is likely that the manufacturer, Qnami, used a higher NA MO as

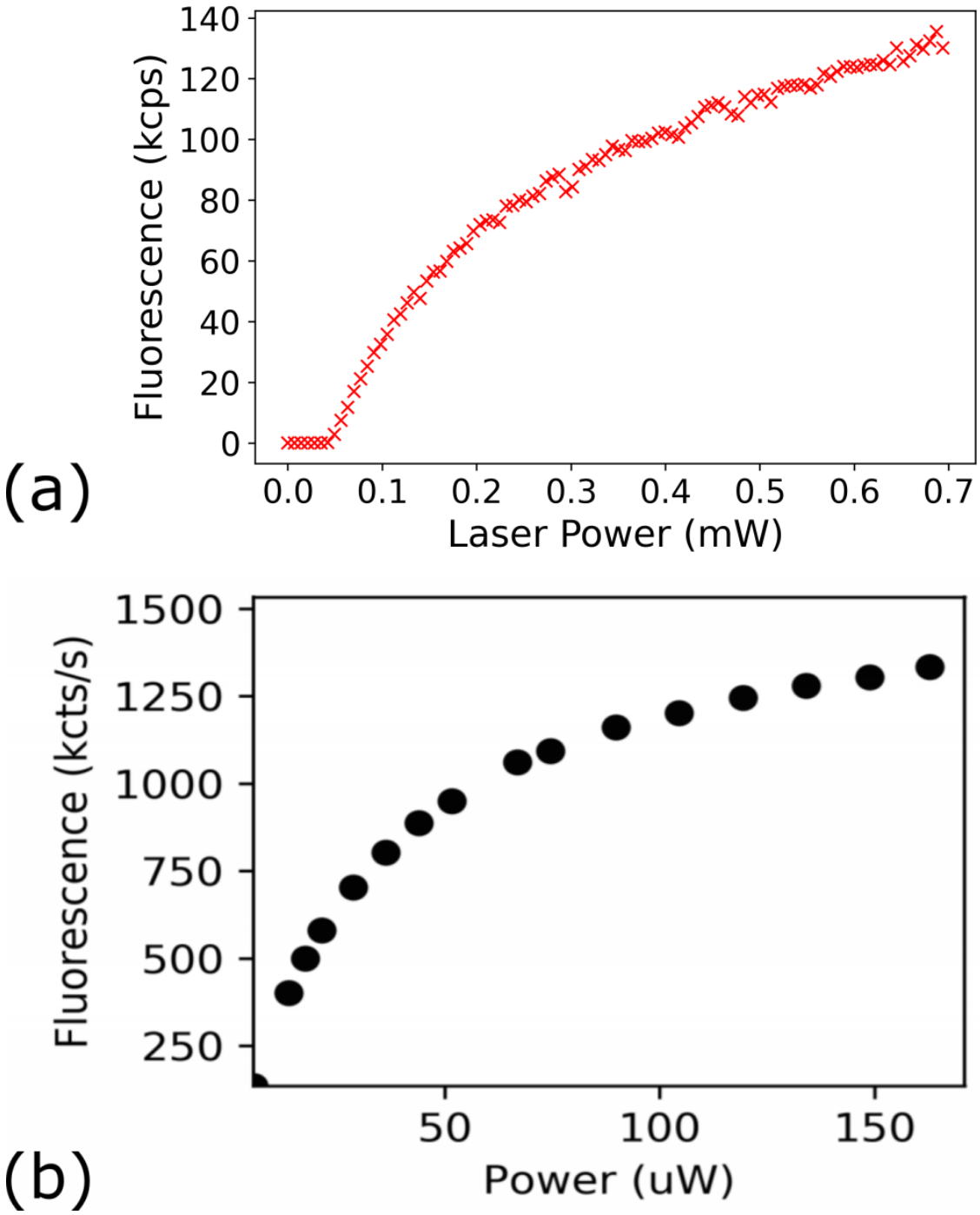

Figure 3.13: (a) Laser power against observed count rate from Qnami probe recorded in this instrument [63], the x axis shows the power recorded directly under the MO using a power meter prior to measurement, as the power coupled into the probe not accurately known, note the count rate shown corresponds to a single detector, which corresponds to half the maximum theoretical detection efficiency. (b) Response from the same probe as stated by the manufacturer (Qnami [63]).

the long working distance needed to operate with a scanning probe mounted into an AFM is not required in a test instrument. For example, the same objective lens series used in this instrument is available with two working distances for each magnification (Olympus MPLFLN or LMPLFLN). This instrument uses the LMPLFLNx100 as the working distance is 3.4 mm [88] as the 1 mm [99] offered by the MPLFLNx100 was judged to be too difficult to with with for operation with a scanning probe mounted in this instrument. However, the increase in working distance is achieved at the cost of a reduced numerical aperture, LMPLFLN NA=0.8 [88] compared to the MPFLNx100 NA = 0.9 [99]. In addition to fundamental differences between the two instruments, the lower count rate can also be explained as the alignment of this instrument could theoretically be improved with higher precision control of the scan-tube lens spacing, see reflectance performance (3.2.7) section for details. The observation of a factor of 5 decrease compared to state of the art system, with the potential for the difference to be decreased with minor alignment improvements suggests this confocal microscope is a competitive device for NV centre PL measurement. A more accurate measurement of optical collection efficiency and the ability to compare to similar instruments could be achieved through the measurement of the laser power against PL intensity relationship for a single NV centre.

Beam Scanning Imaging Performance

The confocal microscope is primarily operated in sample scanning mode, giving a FOV of 50 µm x 50 µm in x and y. Sample scanning is the primary mode of operation given the compatibility with the scanning probe imaging modes of this instrument - AFM and scanning probe magnetometry. The beam scanning imaging method is also not frequently used due to the limited FOV seen in this instrument and as such, all confocal images presented so far have been acquired via sample scanning. For completeness, in this section I will describe the performance in beam scanning mode.

The recorded field of view is approximately 100 µm by 25 µm, see Figure 3.14 for a confocal reflectance image of a patterned wafer formed by beam scanning. The FOV is

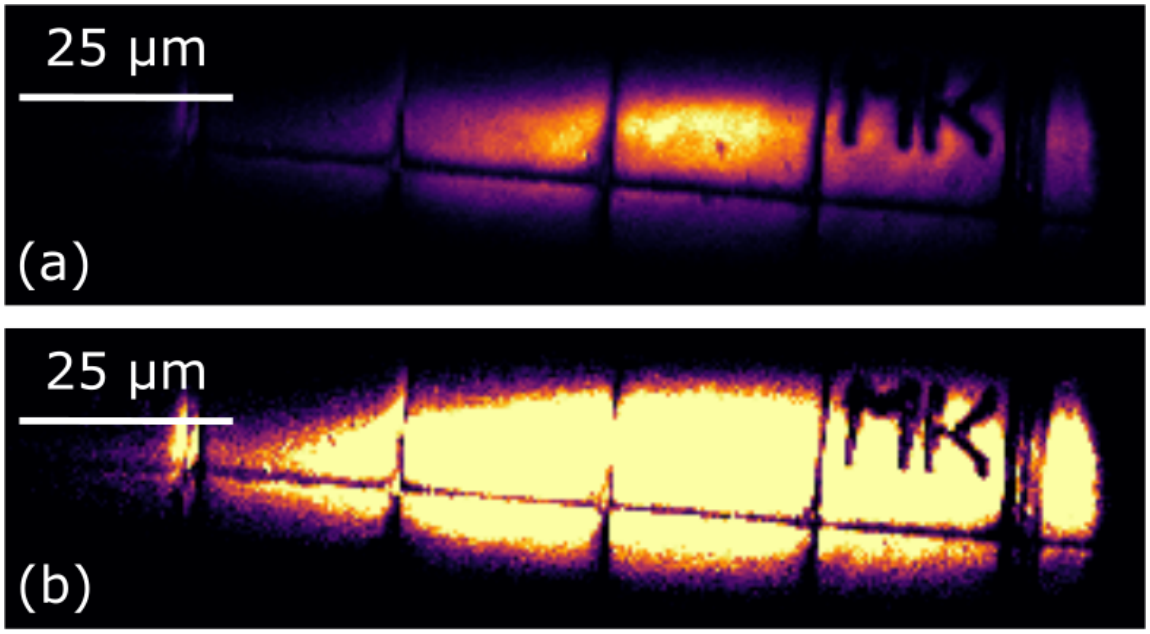

Figure 3.14: Images of patterned silicon/silicon dioxide wafer recorded with the confocal microscope in reflectance mode. The image is formed by beam scanning using the galvanometeric mirrors (a) Variation in signal across flat sample over beam scan attributed to instrument response, maximum efficiency close shown by orange/yellow region in grid next to MK mark (b) Reduced colour image highlighting transmission of the beam to the sample in areas of low efficiency that are observed as dark areas in (a)

substantially lower than the upper limit, set by the MO and given by equation 3.5 that corresponds to a circular FOV with a diameter of 256 µm. The reduced field of view is attributed to two effects: the alignment of the beam at the MO back focal plane and the deviation from the ideal 4f scanning system.

To achieve the maximal field of view in beam scanning mode the beam must be centred on the MO back focal plane and at 0° to the optical axis when the galvanometric mirrors are at their neutral position/centre of the scan range. To ensure the beam is centred on the MO back focal plane iris pairs were inserted into the beam path restricting the angle and position in which the beam can be transmitted through the optical system during alignment. The iris pairs were reliably centred on the optical axis through the use of the Thorlabs cage system, ensuring that the laser is travelling along the optical axis and will ultimately be centred on the back focal plane of the MO at 0° to the optical axis. To align the beam path the apertures of the iris pairs was restricted to their smallest diameter and a power meter fixed to the output of the second iris with the beam position and angle then varied to maximise the transmitted power. The iris pair system was placed along the optical axis in a few locations to ensure the beam remains on and parallel to the axis throughout the instrument. The alignment process maximised the alignment for the variation of the position and angle possible with the fixed optical components in the system. To further improve alignment greater precision in the optical adjustment is required or a change in the position of adjustable components thus changing the spacing of the MO back focal plane and the kinematic mounts.

The non-uniformity seen across the field of view also suggests the scan and tube lens are not functioning optimally, with the beam not confined to the MO focal plane over the FOV. The reduced field of view is also attributed a misalignment of the intermediate optics in the beam scanning system, comprising of the galvanometric mirrors (Galvos) scan lens (SL), tube lens (TL) and the MO, where the brackets refer to the label in 3.3. The tube lens and scan lens are spaced by the sum of their focal lengths, misalignment of these components along the optical axis results in the divergence of either the laser between tube lens and MO and of the collected light between the scan lens the fiber. In addition to the practical

challenge of separating scan and tube lens perfectly by the sum of the focal lengths the positioning of the scan mirrors also slightly differ from their ideal position in a 4f system. In the ideal 4f case the pivot point of the scan mirrors is positioned at the back focal plane of the scan lens, in this instrument the scan lens back focal plane is positioned in between the two closely spaced scanning mirrors to approximate the ideal case. Deviation from the ideal scan mirror - scans lens spacing must be compensated by a change in MO-tube spacing at the other end of the 4f system and vice versa. In this instrument the MO tube lens spacing has varied significantly over the systems development as a range of sample holders and supporting instruments have been placed in the sample plane changing the MO position. In the current configuration the scan lens could not be adjusted accordingly to compensate for this change.

As the main imaging modes require sample scanning further improvements to the beam scanning system were not made. To operate the sample scanning confocal microscope in the region of greatest efficiency, the beam was scanned over a flat mirror in reflectance mode. The mirror is anticipated to be both flat and uniform in response to variation in the single over the beam scan can be attributed to the instrument response. The position of maximum intensity identified and the galvanometers control voltage set to this value for the operation of the instrument in sample scanning mode. The primary application for beam scanning in this instrument is fast, fine alignment between the confocal microscope and AFM probes with affixed NV centres for scanning probe magnetometry. Coarse probe-confocal alignment is performed by scanning the probe using the AFM coarse positioning stages, this is described in Chapter 7, with beam scanning only required for fine adjustments while the probe is on a sample surface. Scanning the probe aligns the optically active region of the AFM probe to with a $\approx 100\,\text{nm}$, therefore the required beam scan range for optimisation is less than $2\,\mu\text{m}$ in x and y. The beam scanning method provides an efficient and uniform response over a $25\,\mu\text{m}$ x $10\,\mu\text{m}$, see figure 3.14. As such beam scanning provides more than sufficient range to optimise NV centre and confocal-probe position, offering a means for optical signal optimisation without withdrawing the probe from the surface, as is required for probe scanning alignment.

3.3 Single Photon Detection

A luminescent target can be considered a single-photon source if, upon excitation, there is a far greater probability of emitting a single photon than multiple photons. To determine if a luminescent target corresponds to single or multiple emitters, a statistical treatment of the luminescent and the expected behaviour in each case must be first be developed and a means to probe the behaviour identified. The photon emission statistics can be quantified by considering the second-order correlation function, denoted by $g^2(\tau)$. In practice, a Hanbury Brown Twiss interferometer is used to measure the second-order correlation function [100].

The development of a reliable single-photon source is key to photon-based communication techniques [101] and an active area of interest in its own right. However, the motivation for single-photon detection in this instrument is to determine the number of dipole like emitters, such as NV centres, contributing to a PL signal from a diffraction-limited spot. The observation of single-photon characteristics from NV centres via HBT interferometry can be used to attribute the PL signal to a single rather than multiple NV centres, ensuring the magnetometer is operating in the high spatial resolution limit. This section first develops a statistical treatment of light by introducing the second-order correlation function and discussing the expected behaviour of a single-photon source. The design of the HBT instrumentation integrated into the instrument will then be presented. Finally, the ability of the instrument to detect single-photon sources will be demonstrated by presenting results from HBT experiments.

3.3.1 Principle of Single Photon Detection

A statistical treatment of the luminescence will be considered by introducing the second-order correlation function which characterises photon number fluctuations. For classical light sources, this is defined as

$$g^2(\tau) = \frac{\langle I(t)I(t+\tau)\rangle}{\langle I(t)\rangle\langle I(t+\tau)\rangle} \tag{3.6}$$

where I(t) is the photon rate at time t and the angular brackets denote a time average by integrating over a long period. Equation 3.6 describes the second-order correlation function in terms of intensity correlations. It can be shown for any classical dependence of intensity function that the value of the second-order correlation function will always be greater than or equal to one, $g^2(t) \geq 1$ [102].

The classical expression for the correlation function can be rewritten to consider the number of photon counts registered on two photon detectors.

$$g^2(\tau) = \frac{\langle n_1(t)n_2(t+\tau)\rangle}{\langle n_1(t)\rangle\langle n_2(t+\tau)\rangle} \tag{3.7}$$

where $n_1(t)$ is the count rate at detector 1 at time t, likewise $n_2(t)$ is the count rate at the second detector at time t. This shows that $g^2(\tau)$ is proportional to the conditional probability of detecting a second photon at time $t = \tau$ if a photon has been detected at time $t = 0$. By considering the case of a photon stream consisting of individual photons with large time intervals between them the probability of detecting one photon immediately after detecting the first one is zero and therefore the second-order correlation function violates the classically expected result. A luminescent object with photon emission that satisfies such criteria ($g^2(0) < 0.5$) is considered to be a single photon source.

The final consideration of the statistical treatment of light is the case the luminescence corresponds to a group of n single photon sources, within the measurement volume of the photon collection optics. For an arbitrary number of emitters , n, the $g_n^2(0)$ value scales n with [103].

$$g_n^2(0) = \frac{n-1}{n} \tag{3.8}$$

for n = 2, this equates to $g_2^2(0) = 0.5$. Therefore if the second order correlation function

of a luminescent target is measured below this threshold value of 0.5, the emitter can be considered a single photon source.

3.3.2 Detection of Single Photon Sources

To measure the second-order correlation function photon detection a Hanbury Brown Twiss configuration is used. Figure 3.15 demonstrates the principle, and the apparatus included in the developed instrument. All of the optics and detectors are contained within a black anodised aluminium box to suppress unwanted light at the detector, this is shown by the black box in this figure. The luminescence photons from a target emitter enters the box via a bulkhead connector from the fiber serving as the confocal pinhole. In figure 3.15 the path the photons take from the fiber to the detectors is denoted by a red line. The photons from the fiber are directed to a 50/50 beam splitter (BS, Thorlabs BPD2545S-G) which divides the photons between the outputs. The photons are then passed through a pair of short-pass filters (F, Thorlabs FESH0750) which act to reduce cross-talk between the detectors. The mechanism for cross-talk and how this manifest in the results of HBT experiments is discussed later in this chapter. Finally, the photons are focused onto the two SPAD sensors using a lens on each arm (L, Thorlabs AC127-030-B). The SPADS produce one TTL pulse per detected photon, this signal is removed from the light-tight box via a BNC bulkhead connector. The SPAD signal is finally delivered to a time-tagger (Picoharp 300) which records the time difference between the pulses from SPADs 1 and 2. Over many emission cycles, a histogram is produced recording the number of events at each time τ between the pulses. As the second-order correlation function is proportional to the probability of measuring a photon at time $t = \tau$ if a photon has been detected at $t = 0$, the produced histogram gives a direct measurement of $g^2(\tau)$ [104]. The data collection for coincidence counting and the $g^2(\tau)$ analysis is performed using QuCoa. The software package is commercially available software produced by PicoQuant for use with PicoQuant time-tagging instruments, with a particular focus on single-photon detection.

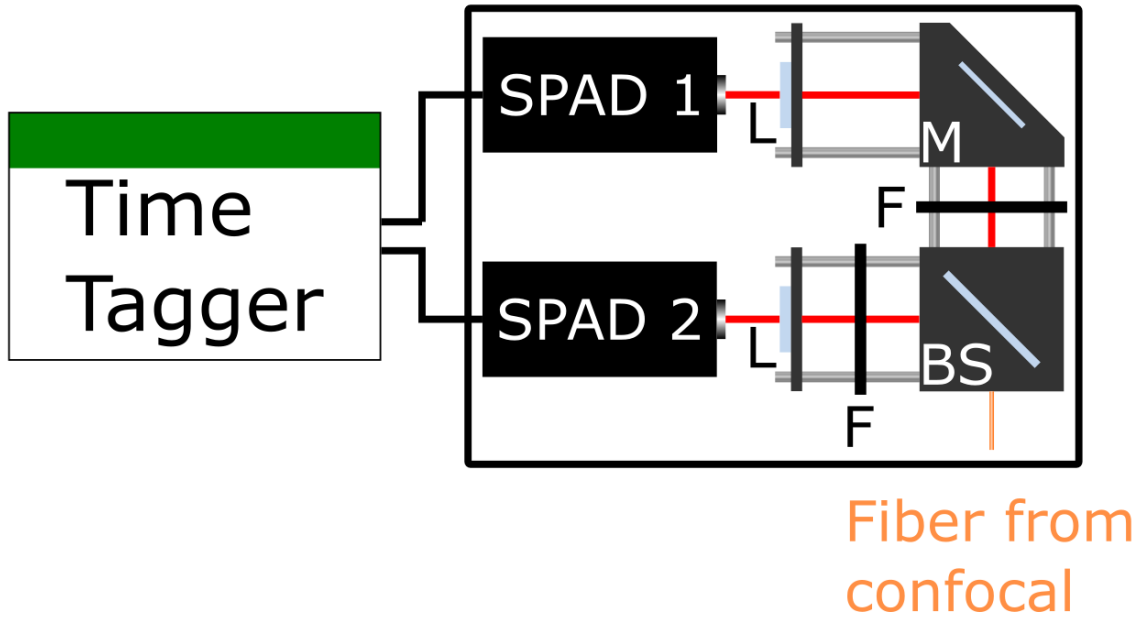

Figure 3.15: Hanbury Brown Twiss configuration incorporated into the instrument. The incident photon stream, shown in red, from the fiber (orange) output from the confocal microscope is split with a 50/50 ratio using a beamsplitter (BS). The resultant pair of beams are first filtered using 750 nm shortpass filters (F) to reduce cross talk and are then directed to two SPADS. The beams are focused onto the SPAD sensors using a pair of lenses (L). The output TTL pulses from the SPADs are delivered to a time-tagger. An additional mirror, M, is used for alignment and due to spatial constraints. The black box represents a black anodised aluminum box housed within the main confocal enclosure to exclude background photons. The fiber and the SPAD signal are extracted/delivered to the box using bulkhead connectors.

3.3.3 Single Photon Detection Performance

The ultimate goal of the single-photon detection instrumentation is to detect photoluminescence from a diffraction-limited spot and confirm that the photons originate from a single NV centre. To test the performance of the single-photon detection apparatus a range of test targets were measured with the aim of measuring the second-order correlation function $g^2(\tau)$ below the single emitter threshold of $g^2(0) = 0.5$, thus confirming single photon source detection. The test samples were nanodiamonds deposited on a silicon/silicon dioxide wafer, prepared by Ben Wood at the University of Warwick. It was anticipated that some of the nanodiamonds on the sample would host single NV centres, and therefore show single-photon source behaviour. The sample was prepared via a long photobleaching scan, as described in the confocal microscope perfomance section. Confocal scans on the bleached scans were performed to identify likely single-photon sources. Photolumiscent targets in the confocal scan from diffraction limted spot, with low PL intensities were then targetted for $g^2(\tau)$ measurements.

The first $g^2(\tau)$ measurements, made without the 750 nm short pass filters inserted before the detectors, showed the characteristic form of emission from a small number of emitters ($g^2(0) < 1$) but also showed sharp central peaks, see figure 3.16. The large peaks are attributed to the cross-talk between the photon detectors. The mechanism for the cross talk is the production of a photon by the SPAD itself following the detection of a photon, an effect called afterpulsing [105]. The SPAD produced photon is then detected by the other SPAD. In the HBT setup in this instrument, the optical path length between the two SPADS is around 30 cm, resulting in a photon travel time between detectors of 1 ns. The detection of an afterpulse produced photon leads to a large increase in coincidence counts close to $\tau = 0$ s in this instrument. To remove the afterpulse counts from the $g^2(\tau)$ measurements a pair of 750 nm shortpass filters were placed just after the beam splitter on each detection arm, a method commonly utilised for $g^2(\tau)$ measurements on NV centres [24, 106].

To determine the minimum of the $g^2(\tau)$ measurement a simple experimental function

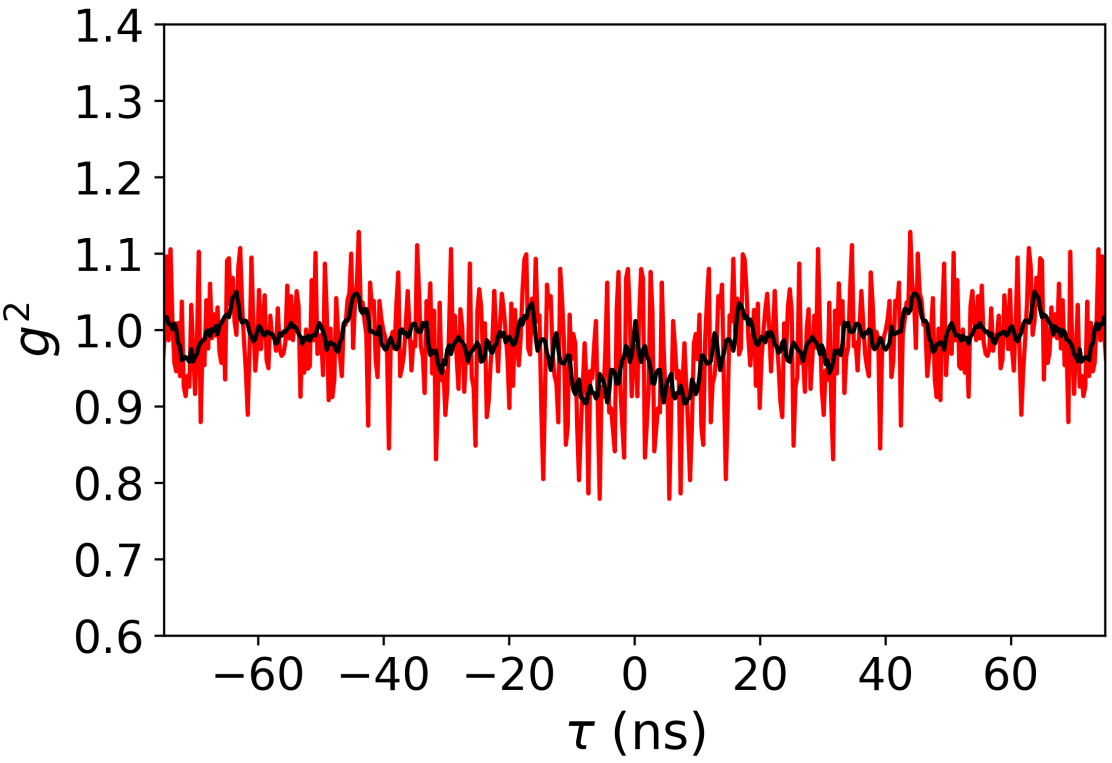

Figure 3.16: Typical $g^2(\tau)$ measurement from a small number of emitters with significant cross-talk between SPAD detectors. The red line shows the $g^2(\tau)$ measurement while the black line shows a 10 point moving average. The cross-talk arises due to the production of a photon by the detector itself. In this instrument with a $\approx 30\,\text{cm}$ distance between the detectors, the cross-talk afterpulse photon leads to an artificial increase of $g^2(\tau)$ when $\tau < 5\,\text{ns}$. The afterpulse artefact obscures the $g^2(0)$ decrease associated with emission from a small number of emitters.

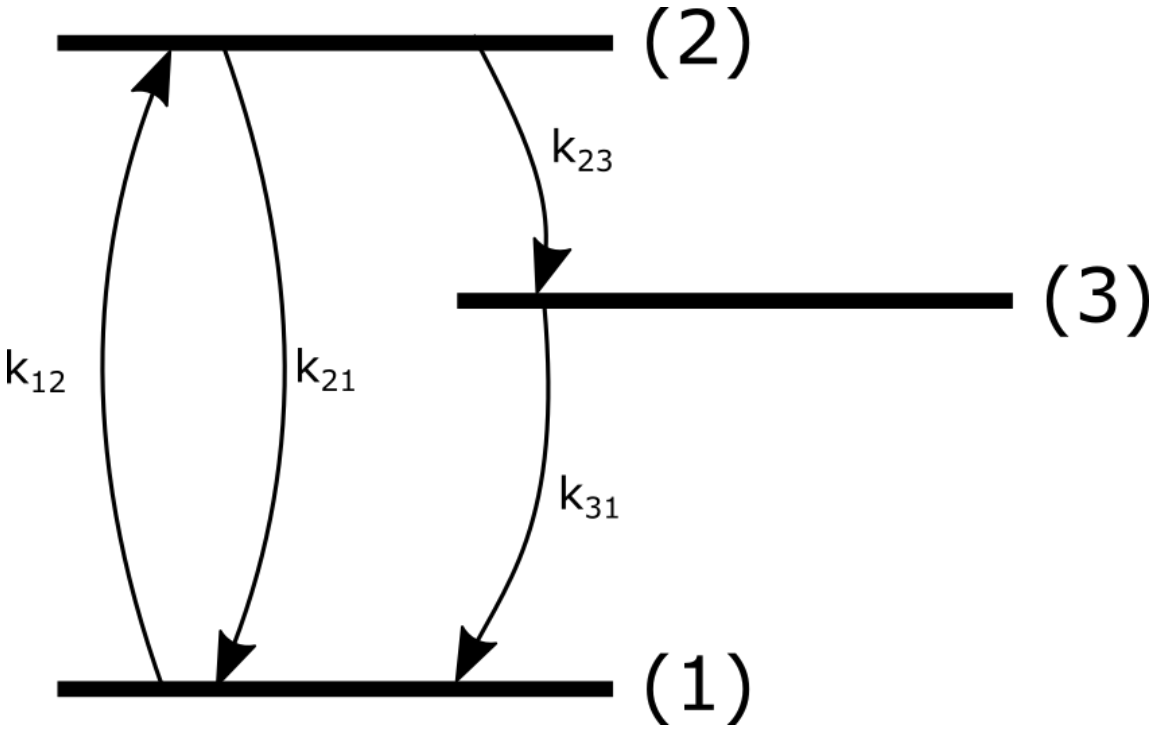

Figure 3.17: Three level model for single NV centre $g^2(\tau)$ measurement. The excited state is represented by (2), the ground state (1) and the metastable state (3). Only allowed transitions are shown by k_{ij}.

based on a three level model is fitted [107, 106, 24].

$$g^2(\tau) = 1 - \beta e^{-\tau/\tau_1} + (\beta - 1)e^{-\tau/\tau_2} \tag{3.9}$$

where the parameters τ_1 and 'tau_2 are defined by

$$\tau_1 \simeq \frac{1}{k_{12} + k_{21}} \tag{3.10}$$

$$\tau_2 \simeq k_{31} + \frac{k_{12}k_{23}}{k_{12} + k_{21}} \tag{3.11}$$

$$\beta \simeq 1 + \frac{k_{12}k_{23}}{k_{31}(k_{12} + k_{23})} \tag{3.12}$$

where k_{ij} refer to the transition rates between the three levels in the model, the levels and allowed transitions are shown in figure 3.17. The three level model, which introduces the metastable singlet to a simple two level model, is needed to account for photon bunching, corresponding to $g^2(\tau) > 1$. However, at lower powers it is found that a simple two level model is adequate to describe the second order correlation function of single NV centres [107]. An example second-order correlation function measurement is shown in Figure 3.18 for a range of laser powers. A two level model was fitted, as $g^2(\tau) > 1$ was not measured for any laser power up to twice the saturation value, suggesting emission does not originate from a single NV centre. The measurement of $g^2(0) = 0.52 \pm 0.05$ corresponds to to the emission from a pair of dipole emitters (n =2 in equation 4.4). The emitter was stable over a period of a week and did not photobleach. Likely candidates for the emitter include one of the other numerous colour centres in diamond. While the signature does not show a single NV centre, which served as the motivation for searching for single photon sourced hosted in diamond, the observation of $g^2(0) = 0.5$ provides a clear demonstration of the instrument's ability to detect single photon sources.

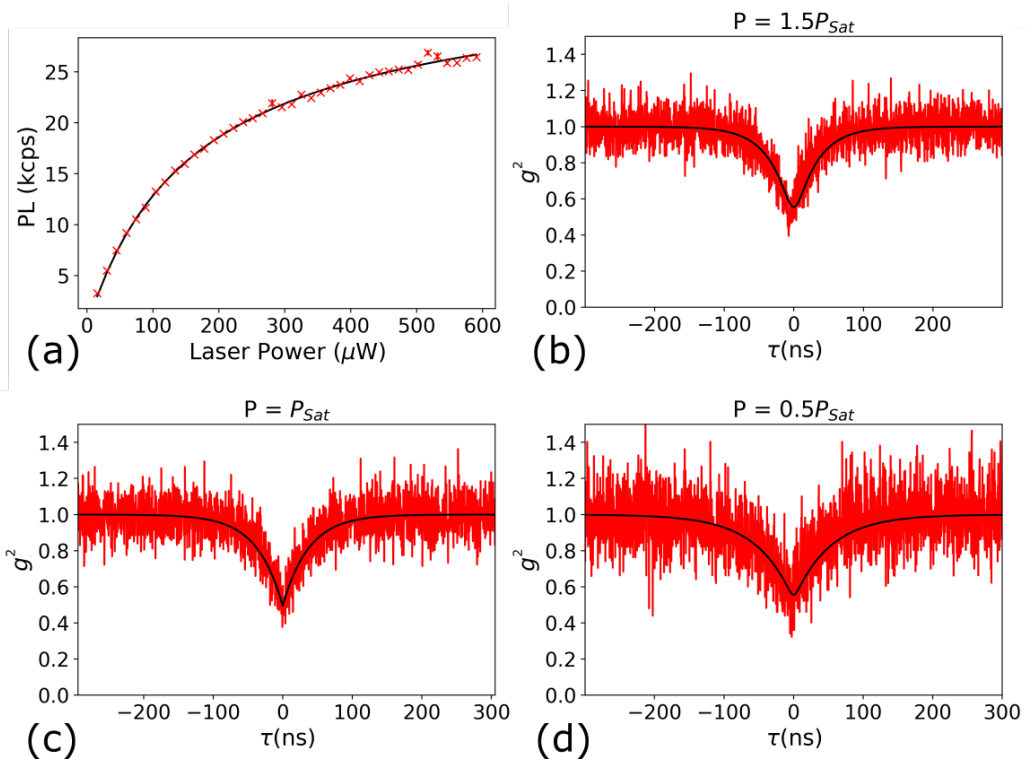

Figure 3.18: (a) PL-laser power relationship from a nanodiamond deposited on a silicon/silicon dioxide substrate suspected to host a small number of dipole emitters. $g^2(\tau) = 0$ measurements (b), (c) and (d) correspond to the same source as shown in (a) at a range of pump powers, expressed relative to the saturation power P_{sat} =, 150 µW ± 5 µW. The $g^2(\tau)$ histogram data is shown in red and a two level model fit using QuCoa's inbuilt fitting is shown in black. The dip at $g^2(0)$ at all three powers shows the characteristic form of an $g^2(0) < 1$ associated with a single photon source. Fitting a two level model yielded $g^2(0) = 0.53 \pm 0.03$, $g^2(0) = 0.56 \pm 0.07$ and $g^2(0) = 0.47 \pm 0.04$ for powers $1.5P_{Sat}$, P_{Sat} and $0.5P_{Sat}$ respectively. The measurements were recorded with integration times of 1000 s, the increased uncertainty is attributed to a decreased averaging in the photon events at lower powers for a constant integration time.

3.4 Emission Spectroscopy

The spectral distribution of a luminescent source can be determined via emission spectroscopy, providing an insight into the composition and structure of the source. In an instrument focused on NV centre magnetometry, the measurement of the emission spectra provides an additional method to confirm a PL source corresponds to emission from NV centres, NV^0 centre or other emitters. For example the NV centre displays a broadband emission with a zero phonon line at 637 nm [108, 24]. The spectral composition of a PL signal can also be used to probe the nature of unknown sources, further extending the functionality of this instrument as a tool for nano-scale sample characterisation.

To record emission spectra using this instrument confocal scans are performed to locate the target, then confocal optimisation routines are used to align diffraction limited targets with the confocal measurement volume. The fiber from the confocal pinhole is removed from the SPAD detection box and connected to a Princeton instruments monochromator (SpectraPro SP-2150). The input light is directed towards a diffraction grating (600g/mm) which disperses the light. Typically for targets investigated by this instrument a diffraction grating with a blaze of 1 µm is used as this corresponds to the greatest sensitivity in the spectral detection window of the confocal microscope. The light is truncated by an exit aperture which defines the spectral width that illuminates the detector, and therefore the wavelength that is measured. The incident angle of the grating is scanned to measure a complete spectrum.

To calibrate the spectrometer a red LED with a known emission profile was used (Nichia NESM026D), with this source placed at the focus of the confocal microscope. The input slit width was minimised to increase the resolution and the position optimised to maximise the available signal. Figure 3.19(a) shows the emission profile from the specification sheet produced by the manufacturer and figure 3.19(b) the spectrum recorded using this instrument. Figure 3.19(c) shows a xy confocal scan of a PL target from a diffraction limited spot size, in this case corresponding to a nanodiamond, and the corresponding emission spectra shown in figure 3.19(d). The black line in 3.19(d) shows the approximate value of

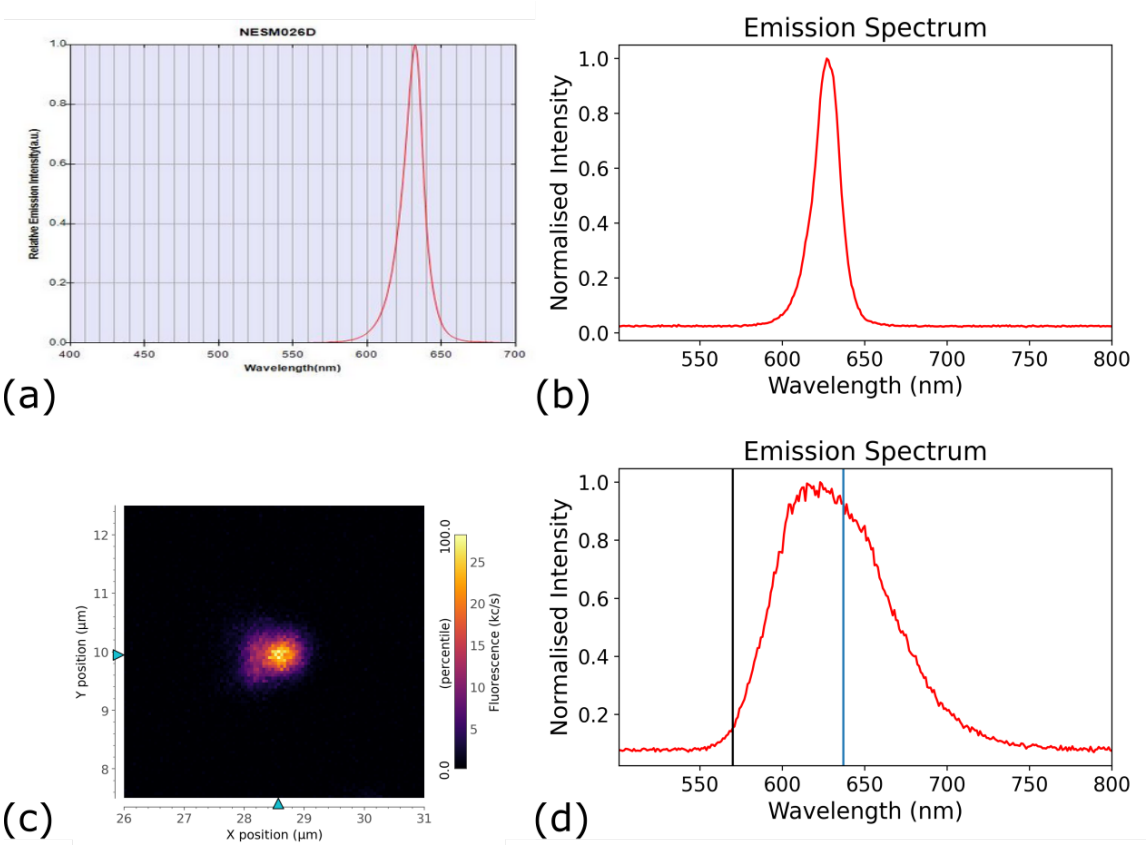

Figure 3.19: (a) Emission profile of calibration LED (NICHIA), sourced from manufactorer [109]. (b) Record emission spectrum of LED recorded using this instrument, integration time of 10 seconds for measurement, with 1 nm resolution. (c) xy confocal scan of nanodiamond used to identified a target. (d) measurement of emission spectra from diffraction limited object shown in (c) measurement time 2000 seconds with 1 nm wide frequency bins. In (d) the blue line denotes the position of the expected zero phonon line for an NV centre 637 nm, while the black line shows the approximate zero phonon line for the observed emitter $\approx$ 570 nm.

the zero phonon line $\approx 570\,\text{nm}$, significantly lower than expected for a NV centre (637 nm). For reference the NV centre zero phonon line is shown in black in Figure 3.19(d).

3.5 Wide-Field Microscope

Confocal image formation is achieved through the sequential collection of fluorescent or reflectance photon counts from a diffraction-limited spot size. As a result, there is an associated acquisition time with a confocal image and the whole field of view can not be imaged instantaneously. The use of a wide-field microscope in combination with an ensemble of NV centres offers a way to increase the temporal resolution of the magnetic field measurement. In a wide-field configuration, the NV centre PL signal from an ensemble can be collected across the whole field of view simultaneously, unlike in the confocal point scanning approach, giving rise to the increase in temporal resolution. There have been numerous demonstrations of NV magnetometers that utilise sensors such as highly sensitive cameras in wide-field microscopes for collection of the NV centre PL [71, 72, 110]. This instrument uses a confocal microscope to address NV centres for magnetometery as the goal of the instrument is to measure the signal from a single NV centre mounted on a probe scanned across a sample. Therefore, the improved signal to noise ratio and spatial resolution of the confocal approach is more advantageous than the increased temporal resolution wide-field microscope can achieve when used with ensembles. Whilst confocal operation is better suited to measuring the PL from a single NV centre mounted on a scanning probe, wide-field imaging can still be a useful component in a confocal based NV magnetometer. One such use is the observation of a large sample to target an area for confocal imaging. Utilising a wide-field microscope, this can be achieved with video frame rates for positioning, as opposed to the longer acquisition time associated with constructing an image on a point by point basis. The increased temporal resolution also facilities the examination of the AFM tip motion for use in attaching a target nanodiamond to the scanning probe. The following sections consider the principle of operation, design and performance of a wide-field microscope built as part of this instrument to support the

main AFM and confocal imaging modes.

3.5.1 Principle of Operation

The principle of operation of a wide-field microscope is comparatively simple when compared to a confocal microscope. There are two main aspects, illuminating the sample and relaying the image produced by a microscope objective lens to a detector such as a camera. A variety of techniques can be employed to illuminate a sample for wide-field microscopy, with Köhler illumination a commonly utilised approach. The Köhler principle is based upon forming an image of a light source in the back focal plane of a condensing lens, resulting in an image of the light source focused to infinity beyond the condensing lens. The collimated beam after the condenser lens produces homogeneous illumination of a sample as any given point in the sample plane is illuminated by every point of the illuminating source. A standard configuration for wide-field microscopes, particularly for biological applications, is the inverted microscope, in which a transparent sample is placed in the collimated beam produced by the condenser lens. A microscope objective (MO) and additional optics are then used to direct an image of the sample to an eyepiece or camera. In the case where samples are not transparent, such as the majority to be addressed by the instrument discussed here, the role of the condenser lens can be fulfilled by the imaging objective lens with additional relaying optics. Imaging and illumination using the same MO is referred to as epi-illumination.

A diagram of the principle of wide-field microscopy using Köhler illumination is shown in figure 3.20, with the optical path from the illumination source represented in green and the imaging path in red. A light source, such as an LED, is collimated to ensure efficient collection. An imaging lens (Lens 1) is then used to produce an image of the light source in the back focal plane of the MO, which produces an image of the light source focused to infinity in the MO focal plane. The same MO also collects light backscattered by the sample for the final image formation. If the MO is infinity corrected, as shown here, the MO produces an image of the sample focused to infinity in the back focal plane of the MO.

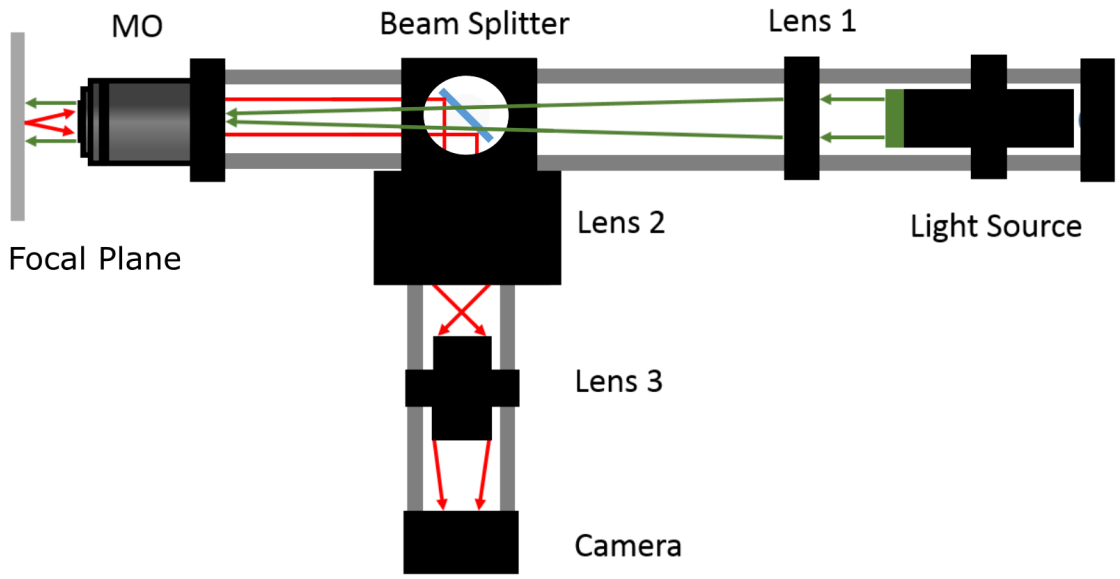

Figure 3.20: Diagram showing the principle of Köhler illumination and wide-field imaging. The illumination path is shown in green and the red represents the imaging light path. A collimated beam from a light source is focused by a lens (Lens 1) into the back focal plane of the objective lens (MO), forming an image of the light source focused to infinity in the focal plane. An image of a sample in the MO focal plane is focused to infinity by the MO and directed towards a tube lens (Lens 2) by a beam splitter. The tube lens produced image can then be resized using additional optics, such as an achromatic doublet pair, Lens 3) to form an image on the camera sensor.

The light collected by the MO for image formation is separated from the illumination path using a beam splitter, which directs the light towards a tube lens. The tube lens (Lens 2) produces an image of the sample which can be resized using additional relay lenses (Lens 3) to the correct size for the camera sensor.

3.5.2 Design of the Wide-Field Microscope

The motivation for the addition of a wide-field microscope is to assist in sample loading and alignment for confocal and AFM operation, rather than high sensitivity detection of

the NV centre PL signal. To achieve these goals the following design requirements for the wide-field microscope were identified:

- Limited impact on the confocal system, so as to not reduce the NV centre count rate and ultimately magnetic field sensitivity.
- A compact system so that it does not limit the placement of additional components, such as bias magnets and AFM components.

A 3D diagram of the wide-field instrumentation is shown in figure 3.21. A high power LED (Light source, Thorlabs M530L3) acts as the light source. The light is collimated by an aspheric condenser (Light source, Thorlabs ACL25020U-A) to ensure efficient collection from the LED. An imaging lens (Lens 1, Thorlabs LA1461-A) is used to form an image of the LED in the back focal plane of the MO (MO, Olympus MPLFLN100x). After Lens 1, the illuminating light is reflected using a polarizing beamsplitter (BS1, Thorlabs CCM1-PBS251/M), which acts to separate the returning imaging light from the illumination path. A second beamsplitter cube, with a changeable filter (BS2,Thorlabs CM1-DCH/M + optic), is then used to direct the light source image down into the back focal plane of the MO. The light backscattered from the sample is collected by the same MO and focused to infinity. The imaging light is first reflected by BS2 and split from the illumination path by transmission through BS1. Using a tube lens (Lens 2, Thorlabs ITL200), an image of the sample is produced. Finally, the image produced by the tube lens is relayed and resized using an achromatic doublet (Lens 3, Thorlabs MAP1030100-A) onto a CMOS camera (Thorlabs DCC1545M).

To add the wide-field microscope to the confocal path without lowering the confocal collection efficiency a compact filter cube (BS2, Thorlabs CM1-DCH/M) was inserted between the confocal tube lens and the MO. The filter cube can house a variety of rectangular optics up to 36 mm wide, 26 mm tall, and 3 mm thick using an integrated clamp. The optic housed in the filter cube sets the ratio in which signal is split between wide-field and confocal detection. The base of the filter cube easily detaches allowing quick and easy switching

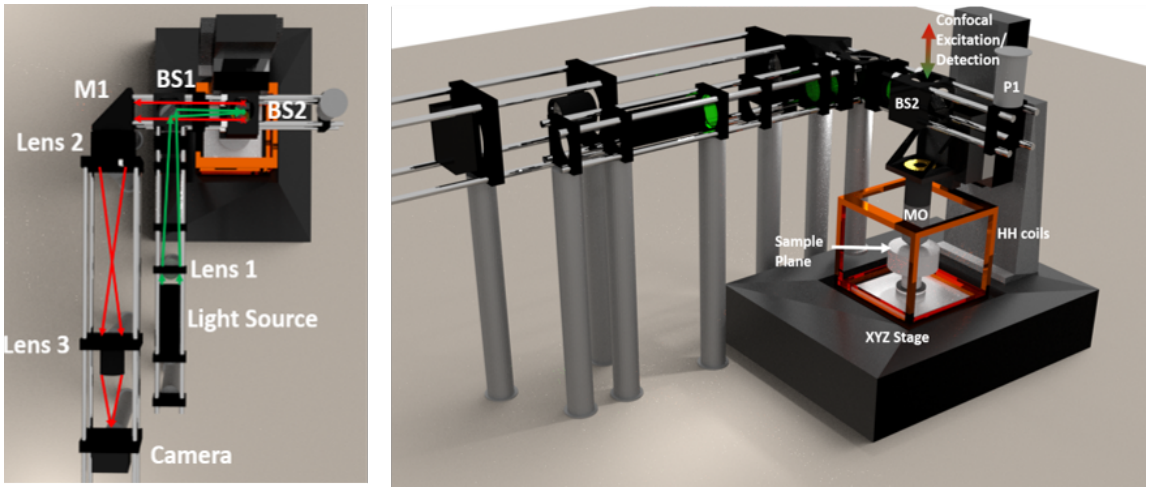

Figure 3.21: 3D diagram showing the placement of components in the wide-field microscope utilising Köhler illumination. The illumination and imaging light paths are shown by green and red lines respectively. The wide-field optics shown here are situated below an optical board housing the confocal optics (see figure 3.3) and the optical paths are combined using a range of optics denoted by BS2.

of this optical component without impacting confocal alignment, facilitating quick modification of the wide-field/confocal ratio. In pure AFM experiments, a mirror is placed in the filter cube giving 100% wide-field collection and 0% confocal collection. In confocal operation, the filter is removed preventing loss of the confocal signal (0% wide-field collection, 100% confocal collection). Where simultaneous wide-field/confocal operation is required a beamsplitter with a suitable ratio can be inserted into the filter cube. The approach of combining the wide-field and confocal path with an easily changeable optical component ensures that no confocal signal is lost during high sensitivity magnetic field measurements. In addition, it ensures a high-quality wide-field image is available when required, rather than using a permanent optic leading to compromise of both confocal and wide-field performance.

3.5.3 Wide-Field Performance

To test the performance of the wide-field microscope an AFM calibration standard was used as a test target. The known pitch of the features allowed the magnification and the field of view (FOV) to be determined. The field of view was determined to be 135 µm x 105 µm with a magnification of x52 times. Figure 3.22 demonstrates the field of view and magnification achieved with the microscope. Figure 3.22(a) shows the dimensions of an Akiyama AFM probe in an image produced by the supplier [111], figure 3.22(b) shows the image taken by the wide-field microscope of a damaged probe. Figures 3.22(c and e) show a diagram of the silicon/silicon dioxide AFM calibration standard, with the area shown in the wide-field images (d and e) denoted by red and blue the coloured boxes respectively.

As can be seen from figure 3.22, there is a dark ring surrounding the images, this is an effect referred to as vignetting. The effect occurs when the image is smaller than the sensor on the camera. To consider the origin of the vignetting and the performance of the wide-field microscope the maximum field of view in the focal plane must be considered, which is fundamentally limited by the MO. In the confocal microscope section, the field of view for an MO was given in equation 3.5. The MO in this microscope (Olympus MPFLN x100) has a magnification of 100 with a field number of 26.5, giving a circular field of view in the focal plane with diameter 265 µm, this represents the maximum achievable FOV. The FOV that is actually observed is also dependent on the size of the camera sensor and the image size in the plane that the camera sensor is placed. The tube lens produces an image of the sample that is $\approx$ 30 mm in diameter, while in this microscope, the camera sensor has dimensions of 6.66 mm x 5.32 mm. To reduce the size of the image to better match the sensor and increase the FOV, a relay lens pair, with a ratio of focal lengths (1:3.33), was placed a focal length away from the camera and tube lens image. The anticipated effect was a reduction of the magnification by a factor of x33 resulting in a wide-field FOV is $\approx$ 200 µm by $\approx$ 160 µm. However, this is not observed. The reduction in FOV is attributed to the entrance aperture of the lens pair used to relay the image produced by the tube lens. The entrance aperture is 22 mm in diameter and the diameter of the image produced

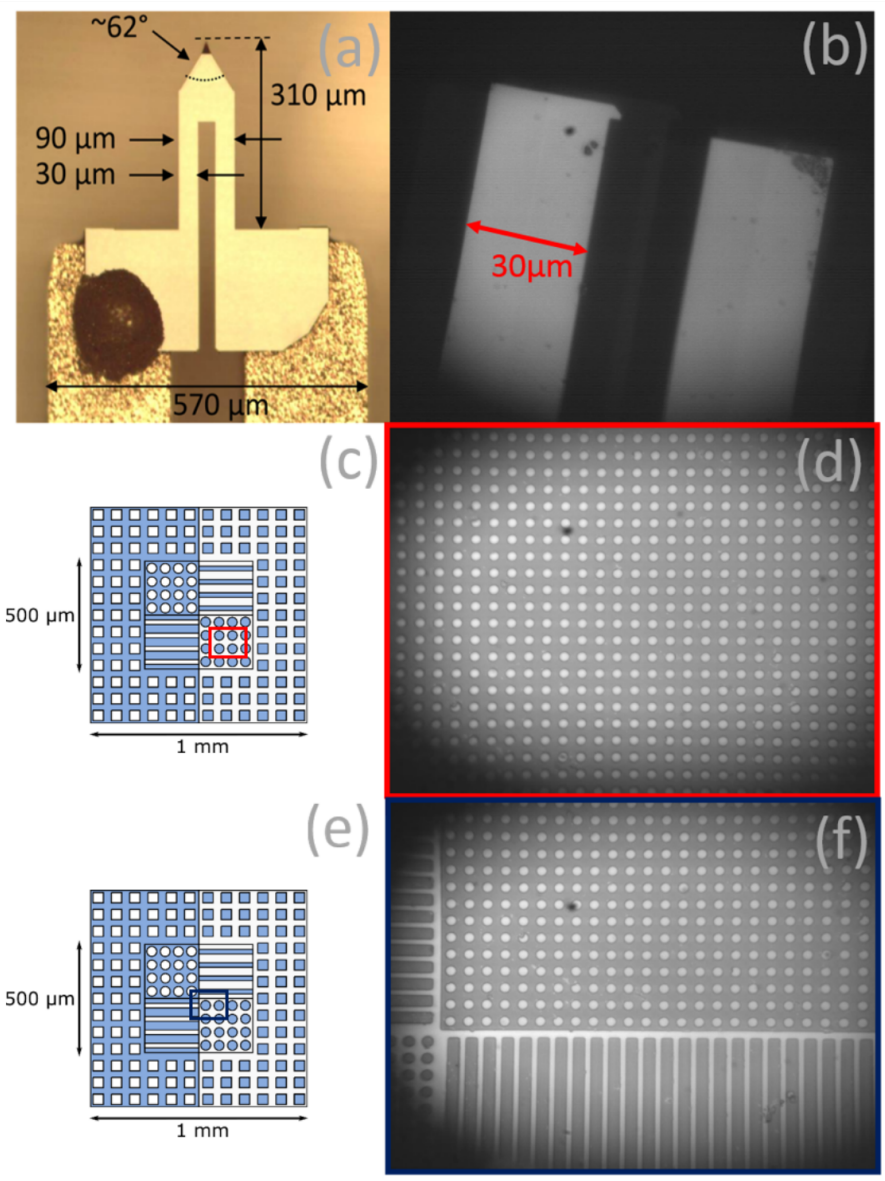

Figure 3.22: Images taken using the wide-field microscope, and dimensions of samples for scale. (a) shows the dimensions for an Akiyama probe [111], and (b) the image captured. Images (c) and (e) show the scale and features of an AFM calibration grid. The central region features have a pitch of 5 µm. The height of the features in both regions is 100 nm. The coloured rectangles on images (c) and (e) show approximately the area imaged by the microscope in images (d) and (f) respectively.

by the tube lens in this plane is 30 mm. As a result, it expected that the FOV will be reduced by a factor of (22/30) from the expected ($\approx$ 200 µm x $\approx$ 160 µm) to ($\approx$ 155 µm x $\approx$ 126 µm) with the sensor now under-filled so vignetting will be present. Accounting for the physical aperture size the observed observed FOV, 135 µm x 105 µm, is close to the expected value. The slight difference is attributed to misalignment.

To quantify the resolution of the wide-field microscope, the size of small features seen in the images were estimated by extracting lines profiles from a wide-field image of nanodiamonds deposited on to patterned silicon/silicon dioxide wafer with nanodiamond deposition, using Gwyddion [85]. Figure 3.23 (a) shows the wide-field image and the locations in which line profiles are shown in figure 3.23(b). The physical size of the image is calculated by measuring the calibration sample used to estimate the field of view shown in 3.22. To estimate the resolution of the wide-field microscope the FWHM of the line profiles shown in 3.23(b) was estimated by reading off the line profiles. The typical FWHM observed corresponds to $\approx$ 500 nm, suggesting the wide-field microscope achieves close to the diffraction-limited resolution, given by equation 3.1 and equivalent to 400 nm for this MO (NA = 0.8) under illumination by 530 nm using the Thorlabs M530L3 LED. The resolution is stated as $\approx$ 500 nm as uncertainty is introduced by conversion between feature size in pixels and the physical dimensions. To improve the accuracy of the pixel to physical dimension conversion a calibration sample with smaller feature sizes could be used, such as a grating with spacing on the order of 0.5-1 µm. However, for high-resolution optical imaging, this instrument is operated in confocal reflectance mode, in which the physical image size is accurate. As a more qualitative demonstration of resolution figure 3.24 shows a wide-field microscope image post processed using ImageJ [112], an open source java based tool for optical image analysis. The image in 3.24 shows a false colour image processed using the ImageJ background subtraction, 'sharpen' and enhance 'contrast' routines to highlight the smallest features on the substrate.

The functionality of the wide-field microscope, to provide an imaging mode with a greater temporal resolution and larger FOV than sample scanning modes is best illustrated in figure 3.25. A wide-field microscope image is shown in figure 3.25(a) that was captured

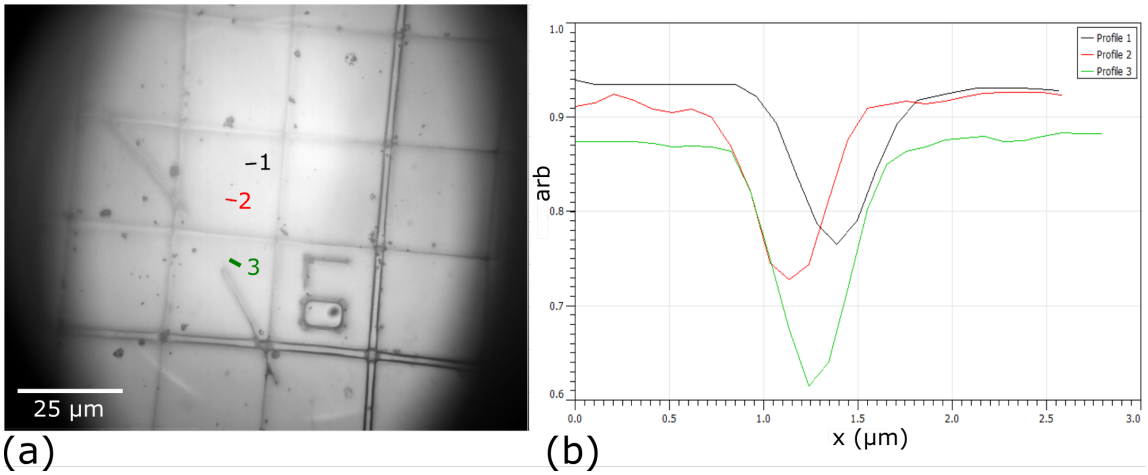

Figure 3.23: (a) Wide-field image of patterned silicon/silicon dioxide wafer with nanodiamonds deposited on to the surface. The lines 1,2,3 show the location of line profiles shown in (b) corresponding to small diamonds.

during atomic force microscope (AFM) imaging (AFM operation discussed in Chapter 4). The position of the AFM tip can clearly be seen relative to the sample, which in this figure is a component (grating coupler) of a silicon photonic integrated circuit, designed by Dr Yaping Zhang and fabricated by Dr Richard Cousins and Dr Chris Mellor. The corresponding AFM image is shown in figure 3.25(b). The AFM scan shown has 30 µm x 30 µm while the max range corresponds to 500 µm x 50 µm.

To summarise a wide-field microscope has been developed that achieves near to diffraction limited performance and provides a larger field of view at a greater temporal resolution than sample scanning imaging modes. The wide-field imaging lenses chosen lead to an expected magnification of x33 with a FOV of $\approx$ 155 µm by $\approx$ 126 µm with an under-filled sensor and vignetting present. The observed FOV of $\approx$ 135 µm by $\approx$ 105 µm and magnification of x52 is attributed to imperfect alignment. The alignment errors arise due to the incorrect positioning of the lens pair relative to both the tube lens and sensor. However, the observed field of view is sufficient when compared to the range of the scanning stages of the microscope (50 µm x 50 µm). To increase the FOV and reduce the vignetting a lens pair with a larger entrance aperture could be used, or a camera with sensor that is better matched to the tube lens image used.

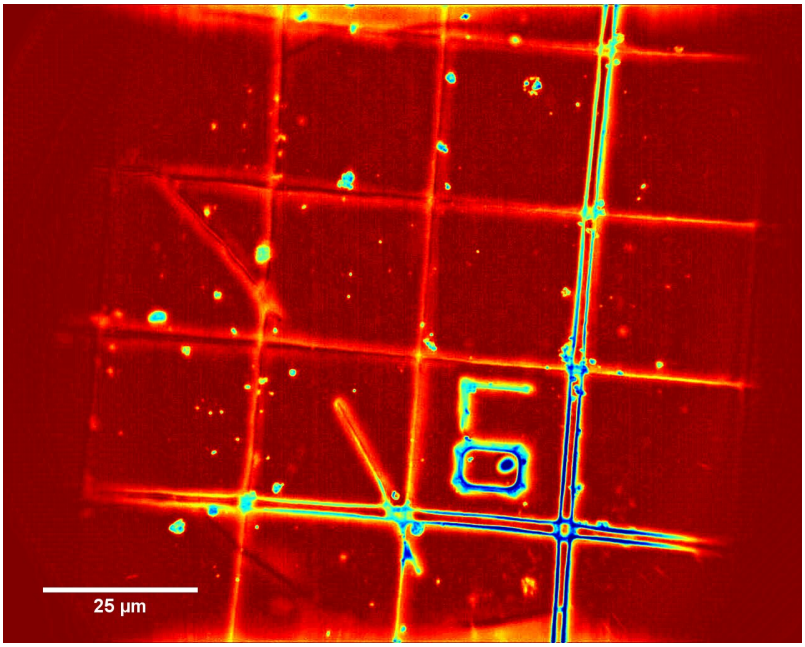

Figure 3.24: Post processed image of patterned silicon/silicon dioxide wafer with nanodiamond deposition producing using ImageJ [112]. The contrast has been enhanced to highlight small features on the wafer.

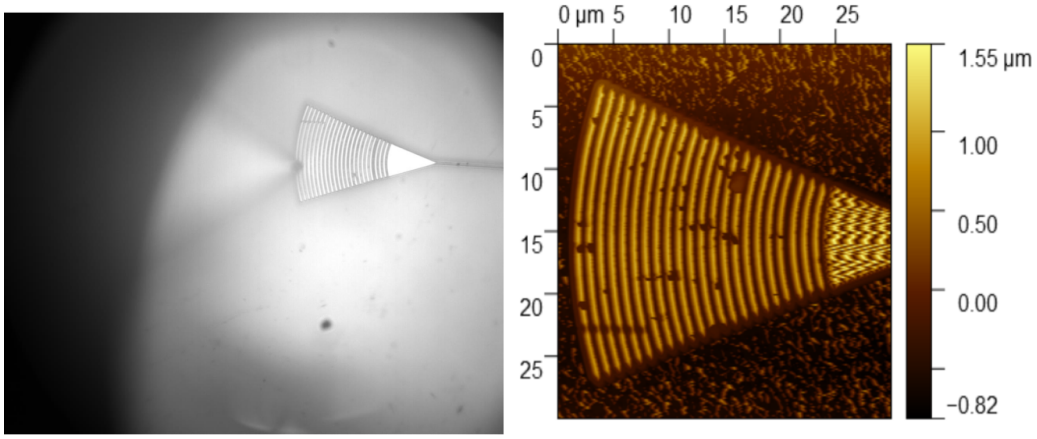

Figure 3.25: (a) Wide-field image captured during atomic force microscopy (AFM) imaging. The AFM probe enters the image from the left with AFM tip, corresponding to the point addressed by the AFM, is clearly visible. (b) Large range (60% of maximum AFM scan range in both x and y) AFM image, showing the relative size of the wide-field camera FOV and scanning probe measurements in this instrument.

3.6 Summary

To summarise a versatile optical instrument capable of characterising samples on the nanoscale has been produced with a variety of imaging modalities. The primary focus was the development of a confocal microscope to excite NV centres and efficiently collect the PL signal for optical magnetometry.

3.6.1 Confocal Microscopy

A custom built confocal microscope has been constructed with a 515 nm laser as the illumination source, primarily to excite NV centres and measure the resultant photoluminescence. The high power of the laser and sensitivity of the SPADs enable the use of a backscattered confocal imaging mode, referred to as reflectance mode, to complement the observation of targets that undergo photoluminescence under the application of 515 nm. The lateral resolution in reflectance mode was shown to be $\leq$490 nm by scanning nanodiamonds deposited onto a wafer. A flat mirror was scanned and the FWHM of the axial profile measured as 1020 ± 15 nm, which is in good agreement with the theoretically predicted 1014 nm. The performance in photoluminescence mode was characterised by performing confocal scans on a photoluminescent nanodiamond. The xy resolution was measured as 515 ± 15 nm and 440 ± 5 nm via a 2D Gaussian fit to approximate the point spread function. The difference in the x and y resolutions is attributed to a slightly elliptical laser profile in the MO focal plane.

The optical efficiency was considering by evaluating the losses in the detection system between the MO and the detectors, and is estimated to ≈ 0.2. A second measurement of the optical collection efficiency compared the count rate from a small group of NV centres with a known response in state of the art instrument. This instrument was shown to be a factor of 5 worse, which could be partially compensated with improved alignment. In addition, the exact hardware configuration of the reference instrument is not known, therefore the difference could be explained through hardware choices. The comparison

provides an order of magnitude estimate and shows that instrument is competitive tool for experiments involving NV centre PL measurement.

Future work includes a more accurate measurement of the point spread function using suitable test targets. The resolution in reflectance mode could be quantified using test targets with features of a range of sizes, typically gratings, and the smallest size that can be resolved stated as the resolution. An alternative test target for confocal alignment and optical sectioning capability are test slides containing stained microspheres in a range of sizes designed for fluorescence microscope calibration, such as the F36909 FocalCheck™ fluorescence microscope test slide #1, manufactured by Invitrogen [113].

The FOV achieved in beam scanning, 100 µm by 25 µm, is substantially less than theoretical limit of a 265 µm circle. To increase the FOV a more accurate means of scan tube lens separation could be developed, along with a method to translate a fixed scan-tube lens telescope between the galvanometric mirrors and the MO back focal plane, if the sample height is changed. To extend the beam scanning FOV the laser needs to be aligned to the MO back focal plane with greater precision than is currently possible with the fixed components in the system. One method of increasing the alignment precision would be through positioning a kinematically mounted mirror closer to MO back focal plane. The main experiments performed with the confocal microscope, including HBT intferometry for single photon emitter detection, emission spectroscopy and eventually NV magnetometry utilising a scanning probe integrate the PL signal from a diffraction limited spot size for relatively long periods. As such sample scanning provides a sufficient range and scan speed, therefore the restrictions on beam scanning do not have serious implications for the scientific goals of the project.

The observation of PL from diffraction limited objects provides a clear demonstration of the custom built confocal microscope's ability to integration the signal from NV centres for ODMR experiments and eventually NV centre based magnetometry.

3.6.2 Single Photon Detection

The single-photon detection experiment has been used to measure a single/small numbers of point-like emitters contained within the diffraction-limited measurement volume of the confocal microscope. The measurement of $g_2(0) = 0.50 \pm 0.05$ is a clear demonstration of the capability to identify single-photon sources and small groups of dipole emitters using this instrument.

Future work includes detection of a single photon source corresponding to a single NV centre. The confirmation of single NV centre emission would be confirmed again by the observation of $g_2(0$ below the single emitter threshold of 0.5 and the observation of $(g_2(0) > 1)$ at high excitation power, associated with the shelving of the spin state into the metastable singlet spin states. To confirm a single photon source corresponds to an NV centre, not just a 3 level system with a dark state, the ODMR spectrum or the emission spectrum could be evaluated for the same source. The observation of a 2.87 GHz zero-field ODMR resonance and a 637 nm zero phonon line being the distinct NV centre signature in ODMR and emission spectra measurements respectively. As this instrument has observed $g_2(0) = 0.50 \pm 0.05$ from an unknown emitter hosted in nanodiamond, it suggests that the instrument would be capable of such a measurement providing the correct sample was addressed.

3.6.3 Spectroscopy

A spectrometer has been integrated into the system capable of identifying the spectral composition of a photoluminescent signal from point-like emitters. The performance of the spectrometer has been demonstrated in this chapter, firstly, by the reconstruction of the emission profile of a known sample - a red LED [109], then the presentation of a broadband spectrum from PL originating from a nanodiamond.

There are two main avenues of further development for the spectroscopic instrumentation in this instrument. The first development is the development of an imaging modality

that allows for the simultaneous acquisition of emission spectra and 2D intensity maps. The dual imaging mode can be realised by splitting the collected signal from the confocal microscope between the SPADs and the spectrometer input, which can be achieved via a beamsplitter in the optical path, a fiber splitter between two outputs (which can often be too narrow bandwidth) and the use of a separate fibre coupler/switch. An ideal method would limit the loss of signal and be easily customisable allow the ratio of the signal to be modified, for example, in magnetic field sensing a loss of optical signal would degrade the sensitivity while the spectral data from the NV centre would not provide further information. The second improvement relates to an increase in the sensitivity and shortening of acquisition time in spectroscopic measurements. The replacement of the photomultiplier tube with a charge coupled device (CCD) as the photodetector in the spectrometer would vastly shorten integration times as multiple frequency bins can be measured simultaneously, with a pixel in the CCD corresponding to a frequency bin. The use of a cooled CCD would also reduce the dark count, enabling the spectral profiling of weak emitters.

3.6.4 Wide-Field Microscope

The wide-field microscope constructed has a FOV of 135 µm by 105 µm. The use of an easily changeable beamsplitter facilitates easy switching between confocal and wide-field mode and a variation in the ratio in which the signal is split. The large field of view relative to the (50 µm x 50 µm) sample scanning range combined with video frame rates provides both a complementary imaging tool and a useful image for sample loading and alignment.

A sample, such as a grating, with features close to the theoretical resolution (≈ 400 nm) could be imaged to increase the accuracy of the pixel to physical size conversion. Imaging a sample with small features of a known size would also increase the accuracy in which the resolution is known. However, the primary mode of producing high-resolution imaging of the light back samples is the confocal microscope operated in reflecnatnce mode. Therefore the current resolution estimate and pixel to distance conversion is sufficiently accurate for the wide-field microscope primary application of sample loading and alignment.

Currently, the wide-field camera uses a green led for illumination and a monochromatic camera for detection. The use of a green light ensures that the wide-field signal is well filtered from the confocal signal facilitating simultaneous operation without saturating the sensitive confocal optics. However, the microscope could be used to generate a true colour image through changing the green LED for a 'white' LED, for example, the Thorlabs MWWHL3, and using a colour camera. The field of view could also be extended up to the maximum diameter of 265 µm set by the MO. To increase the FOV an alternative camera, relay lens or both would be required to better match the image produced by the tube lens and a given camera sensor.

Chapter 4

Scanning Probe Microscopy

4.1 Introduction

The first scanning probe microscope was demonstrated in 1981 by Binnig, Gerber and Weibel [114] using a technique called scanning tunnelling microscopy (STM). The principle of operation consists of bringing an atomically sharp tip towards a conductive sample with a bias voltage applied between the tip and sample. When the separation is on the angstrom length scale there is a measurable tunnelling current between the tip and the sample. This tunnelling current is exponentially dependent on the tip-sample separation and so the topography of a sample can be measured utilising this effect. If a sample is raster scanned under the tip, or the tip scanned above the sample, the tunnel current can be used as part of a feedback loop which alters the sample z position using a piezostage to keep the tunnel current constant. The variation in the piezostage drive voltage over a scan then yields a topographical image of the surface. The unprecedented spatial resolution stems from the exponential dependence of the tunnelling current on the tip-sample separation and the production of atomically sharp tips, limiting the influence of the sample not directly under the tip.

In the first demonstration in 1981 by Binning et al, lateral and vertical resolutions as low as 10 Å and 6 Å were demonstrated [114]. The invention of STM generated a wide

range of research activity into a variety of scanning probe techniques with one of the most widely used being the atomic force microscope or AFM. The working principle of atomic force microscopy (AFM) is based upon a similar principle to STM - interrogating a sample through the local measurement of the tip-sample interaction. However, AFM measures the forces between the tip and sample using a force-sensing cantilever, rather than the tunneling current as is the case for STM. As a result, the AFM can measure both insulating and conductive samples, making the AFM a far more versatile tool than the STM. The first AFM was demonstrated by Binnig et al in 1986 [115] with a lateral and vertical resolution of 30 Å and 1 Å respectively.

In a scanning probe NV magnetometer, a crucial component is the scanning probe itself which controls the motion of the probing NV centre spin. The precision of the scanning probe element sets the spatial resolution of the magnetic field measurement [19], demonstrating the need for a stable and precise positioning tool on the nanoscale. The atomic force microscope was chosen to provide the scanning probe component in this instrument due to it's nanoscale resolution, even in ambient conditions. Previous works on scanning probe magnetometry have utilised an AFM to control the NV centre positioning, including the first demonstration by Balasubramanian et al in 2008 [44] and as of 2020 in the first commercially available scanning probe NV magnetometers [70, 69]. This chapter focuses on the construction of a homebuilt atomic force microscope both as a complementary imaging tool in its own right, and as a means to position a probe spin close to a magnetic target. Firstly, the principle of atomic force microscopy is presented including a discussion of the different AFM modes and their respective merits. The design of the AFM integrated into this instrument at the centre of this thesis will then be discussed. The operation of the AFM will be discussed, considering software control, tip approach procedures and alignment with the optical instrumentation. Finally, the results produced by the AFM on a range of test samples will be presented, as a measure of performance and demonstration of simultaneous confocal-AFM operation.

4.2 Principle of operation

4.2.1 Tip-Sample Forces

The first scanning probe microscope, the STM, probed the tunnelling current between the tip and sample. The tunnelling current is highly dependent on the tip-sample separation and the bias voltage applied, making this interaction both relatively easy to both control and interpret the result. Atomic force microscopy extends the range of samples that can be characterised to include insulating samples, as the technique probes the cumulative forces between the tip and sample using a force-sensing cantilever. The force acting on tip, positioned at the free end of sensing cantilever is both sample and environment-dependent, making the interpretation of the force-distance relation and the recovery of physical parameters such as topography more complex. As with STM, the high lateral and vertical resolution of the AFM technique stems from the atomically sharp tip, limiting the interaction ideally between a single atom in the tip and a single atom in the sample. To interpret the result produced by AFM most models describing the tip-sample potential, V_{ts}, start by summing the forces between a single tip and sample atom. The potential V_{ts} between the tip atom and the sample produces a z component of the tip-sample force, $F_{ts} \propto -\partial V_{ts}/\partial z$. In a vacuum, the tip-sample force, F_{ts}, can be described by considering the chemical bonding forces, which considers the contributions of attractive van der Waals (vdW) forces and a repulsive term due to Pauli repulsion. One simple model commonly used to describe the chemical bonding forces is the Lennard-Jones potential [116],

$$V_{LJ}(z) = 4\epsilon \left[\left(\frac{\sigma}{z}\right)^{12} - \left(\frac{\sigma}{z}\right)^{6} \right] \tag{4.1}$$

ϵ describes the bonding energy between the atoms in the tip and sample, while σ describes an equilibrium separation. The z^{-12} term arises due to Pauli repulsion and dominates at smaller spacings. The second term, z^{-6} term describes the long range attractive van der Waals forces due to induced dipoles. The form of the Lennard-Jones potential over the

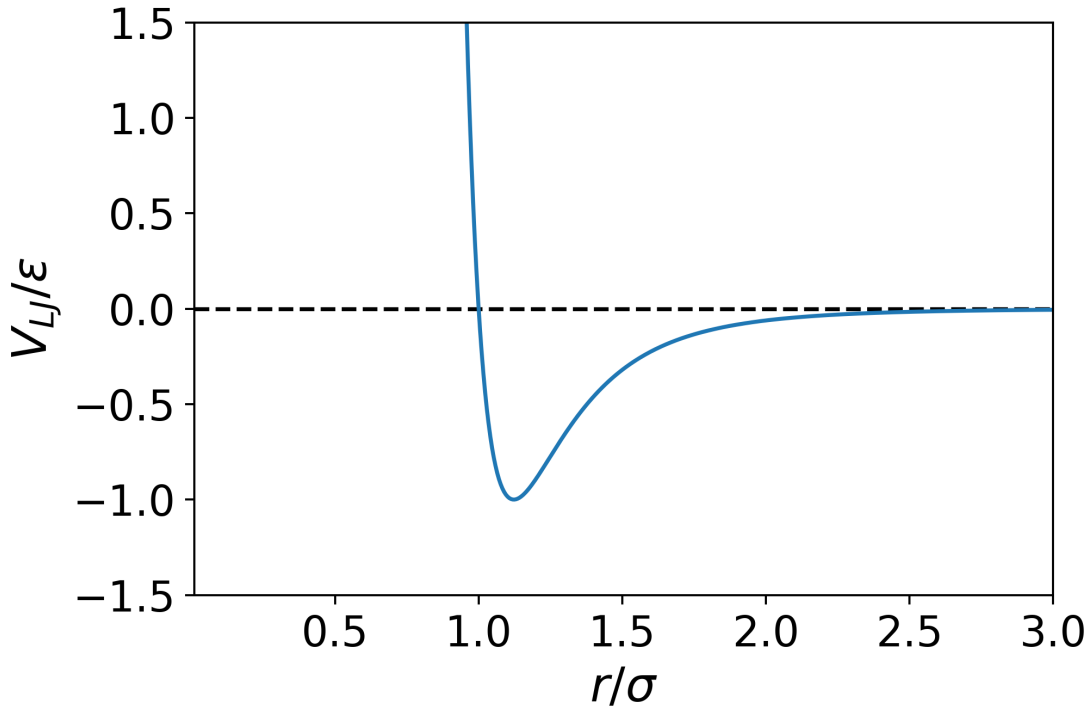

Figure 4.1: Form of the Lennard-Jones potential as a function of the separation between the sample and an atom on the end of an AFM cantilever. Dimensionless units are used as the length scales, characterised by σ, and bonding strengths, described by ϵ, depend on both the tip atom and the sample. In the Lennard-Jones potential shown here, the general form of the potential consists of long-range attractive van der Waals forces for large tip-sample separations, r. At decreased separations, the repulsive force due to Pauli repulsion dominates the potential. The change in sign of the gradient represents a change in the force direction experienced by the cantilever. Knowledge of the form of the potential allows a user the choice as to which region to probe by choosing an appropriate cantilever-surface separation and AFM mode.

length scales probed in AFM is shown in figure 4.1.

The Lennard-Jones potential is one model of the potential that produces tip-sample forces detected in atomic force microscopy and introduces the dominant contributions in a vacuum, the long-range van der Waals component and the comparatively short range Pauli term. In ambient conditions, terms arising from meniscus forces formed by adhesion layers on both the tip and sample must also be considered in the potential model [116]. There's a wide range of models aiming to provide a more quantitative understanding of the tip-sample interaction, with the Stillinger-Weber potential and the Tersoff potential being notable examples, these models, along with others are discussed extensively in the review by Bazant *et al* [117].

AFM tips can be modified with functional materials to tune the forces to which the tip is sensitive, this has lead to the emergence of a variety of subdivisions of AFM. One such example is magnetic force microscopy (MFM) that utilises a cantilever with a magnetised tip to introduce a term associated with the magnetic force between the tip and the sample. A disadvantage associated with this technique are the tip-sample forces probed in MFM are not solely from the desired magnetic interaction and so modelling is required to isolate the magnetic contribution from contributions from other forces.

In addition to functionalising probes to introduce desired contributions to the tip-sample forces, terms can be introduced by the measurement environment. For example, in air thin layers of water coat both tip and sample leading to a force contribution arising from capillary action. The impact of this effect will be discussed when considering the operating modes of the AFM later in this chapter.

4.2.2 Contact AFM

Contact mode or static mode AFM is one of the simplest operating modes to physically interpret the result. The tip is held on the surface and the deflection of the force-sensing cantilever, which is characterised by a spring constant, k, provides a measure of the tip-

sample interaction. The relationship between the deflection and the tip-sample force F_{ts} is given by

$$F_{ts} = -kq \tag{4.2}$$

where q, is the deflection from the equilibrium position. The force acting on a cantilever with a known effective force constant, k, can be calculated by measuring the deflection and the above relation. Furthermore, a topographical image can be generated by maintaining a chosen deflection of the cantilever using a z feedback loop which controls the sample position while raster scanning the tip across the sample. Scanning and maintaining the deflection leads to a constant force on the tip, this is referred to as constant force AFM. Alternatively, a constant sample height can be maintained and the tip deflection is measured to provide topographical information. Contact mode operated in constant height mode can be useful for applications where the variation in the force is small. Samples where real-time information is required, such as in biological samples, also benefit from the shortened measurement time of constant height mode.

Contact mode AFM provides a simple interpretation of the results and has been shown to demonstrate true atomic resolution in certain conditions [118]. However, there are some limitations due to the nature of the contact between the tip and sample. It can be seen that from equation 4.2 that for a given a tip-sample force, F_{ts}, the deflection q, will be maximised when k is small. Therefore the higher sensitivity contact AFM can be achieved through soft cantilevers (low k). However, there is a practical lower limit to stiffness of the cantilever. If the maximum force gradient exceeds the stiffness of the cantilever then the tip jumps into contact with sample. The condition on k can be expressed as [116]

$$k > \max\left(-\frac{\partial^2 V_{ts}}{\partial z^2}\right) \tag{4.3}$$

The contact between the tip and the sample leads to large lateral forces which can be damaging to soft samples; with harder samples, the tip itself can quickly become damaged

adversely affecting performance.

4.2.3 Dynamic AFM

To address some of the problems experienced by contact AFM, such as noise, jump to contact and the large forces on the tip and sample, dynamic AFM can be utilised. In dynamic modes the tip is retracted from the sample and is subject to an oscillating driving force, applied to the cantilever via an actuator such as a piezoelectric crystal. The changes in the oscillation parameters, such as amplitude, A, resonant frequency, f, and the phase relative to the drive signal, ϕ ,are used to control the feedback loops and create images of the sample. For example, a set point in amplitude or frequency can be chosen and a feedback loop used to maintain this parameter by altering the sample height over the course of a scan. The parameter controlled by the feedback loop leads to a subdivision of dynamic atomic force microscopy into two operating modes.

The oscillating cantilever can be modelled as a driven, damped, harmonic oscillator, with a resonant frequency f_0 and quality factor, Q, with an additional time dependent sample force, F_{ts}. This is considered in many textbooks, one such review has been provided by Giessibl [116]. The model is used to explain the frequency and amplitude behaviour under the action of tip-sample forces which will be discussed when considering two dynamic modes of operation. The following discussion of AM-AFM and FM-AFM below consider the harmonic oscillator model in the limit of small amplitude oscillation relative to the range of the tip-sample interaction. This model provides simple analytic expression and introduces the key concepts of dynamic AFM. However, they do not provide a complete quantitative description of the experimental behaviour.

Amplitude Modulation AFM

In amplitude modulation mode (AM-AFM) the cantilever is driven by a fixed drive amplitude, A, at a fixed drive frequency, f_{drive}, typically just below the free space resonance

frequency f_0 ensuring stable operation. As the cantilever is brought towards the sample the tip is subject to a force gradient, firstly due to the attractive van der Waals force changing the effective spring constant of the cantilever, resulting in a decrease in the resonant frequency, f from the free space value of f_0. At a fixed driving frequency, f_{drive}, this will be detected in a change of cantilever oscillation amplitude. Once the Pauli term begins to dominate, the frequency shift is positive due to the repulsive nature of this force. The shift in frequency due to the interaction is detected as a change in cantilever oscillation amplitude as the drive amplitude and frequency is fixed. A feedback loop changes the z position of the sample to keep the amplitude at a preset value. A problem with this technique is the change in amplitude can be attributed to the change in resonance from changing the tip-sample force gradient over the course of a scan or due to other dissipative forces making the quantitative interpretation of data complex. A limitation to this technique is the action of the force between the tip and sample cannot be measured instantaneously but on a timescale of $\tau_{AM} \approx 2Q/f_0$ [116], this is particularly limiting in an ultra-high vacuum where dissipation is low and Q is high. This represents a limit to the scan speed for this mode of AFM operation.

Frequency Modulation AFM

AM-AFM was demonstrated in 1987 by Martin et al [119] and four years later Albrecht et al [120] proposed a second form of dynamic AFM, frequency-modulated AFM (FM-AFM). The frequency modulated approach aimed to improve the signal-to-noise ratio that can be achieved by using a high Q cantilever, but without the limitation to the bandwidth seen in AM-AFM. Albrecht et al demonstrated the change in the frequency due to the tip-sample interaction occurred on a far shorter timescale, with a single oscillation cycle, given by $\tau_{FM} = 1/f_0$ [120, 116].

In FM-AFM the drive frequency is adjusted to ensure that the cantilever is always driven on resonance, the frequency of which changes due to variance of tip-sample interactions over the course of a scan. The change in resonant frequency, $\Delta f = f + f_0$ of

the cantilever by the interaction can be evaluated by modelling the cantilever as a driven damped harmonic oscillator. This leads to the following relation,

$$\Delta f = \frac{f_0}{2k}\langle k_s \rangle \tag{4.4}$$

$\langle k_s \rangle = \langle \partial F_{ts}/\partial z \rangle$ denotes the force gradient of the tip-sample interaction [121, 122]. This relation depends on the oscillation amplitude of the cantilever and the force gradient the tip experiences. The full analytic descriptions which allow for conversion from Δf to force are beyond the scope of this thesis [123, 124]. In this simple form, the expression serves to demonstrate a change in tip-sample separation can manifests itself as a measurable frequency shift from the free space resonance.

In FM-AFM, the frequency difference between between the free space resonant frequency, f_0 and the shifted frequency, f , via tip-sample interaction acts as the feedback parameter. A phase locked loop (PLL) loop is used to keep the cantilever at the setpoint by monitoring the the phase lag, ϕ between the driving and measured oscillation, which is defined as

$$\phi = \tan^{-1}\left(\frac{f_{drive}}{Qf(1 - f_{drive}^2/f^2)}\right) \tag{4.5}$$

where Q is the Q factor of the resonance and f_{drive} is the frequency of the drive signal [116]. When the cantilever is driven on resonance, e.g $f_{drive} = f$, the argument of equation 4.5 tends to infinity resulting in phase lag of $\phi = 90°$. Therefore the PLL enables the modulation of drive frequency to maintain a phase set point and frequency difference setpoint is then maintained through altering the tip-sample separation.

In FM-AFM, the magnitude of the drive signal can be kept constant, referred to as constant drive FM-AFM or the amplitude of oscillation can be kept constant, referred to as constant amplitude FM-AFM. As the cantilever oscillates, energy is dissipated in a number of ways, including intrinsic dissipation in the cantilever itself, energy lost to the surrounding medium, or through interaction with the sample itself [116]. Operating the

cantilever in constant excitation mode utilises an additional feedback loop to maintain the oscillation amplitude which changes over the course of a scan due to variable dissipation.

4.2.4 Limitations of Dynamic Mode AFM

These days FM-AFM routinely achieves atomic resolution in ultra-high vacuum. However, there are limitations to the technique. In ambient conditions, most samples develop a fluid layer and as a consequence the oscillating cantilever can become trapped in this layer, making dynamic AFM hard to implement with micro-machined silicon cantilevers ($k \approx 1\,N\,m^{-1}$). Even in ultra-high vacuum cantilevers with high force constants ($k \approx 1000\,N\,m^{-1}$) such as quartz tuning forks are often used to achieve the highest resolution.

4.2.5 Tapping mode

Tapping mode AFM is a dynamic mode where the oscillating cantilever makes intermittent contact with the sample at the extreme of the oscillation cycle. This tapping approach was developed to utilise the benefits of both contact and dynamic AFM [125, 126]. The sample and tip are not subject to the lateral forces of contact mode AFM, protecting soft samples and the tip. An advantage over other dynamic modes is the larger amplitude oscillation associated with the technique, typically slightly lower than the free space amplitude (e.g 0.7x). The large amplitude ensures that the tip can penetrate covering layers, such as fluid layers that can accumulate on samples in ambient conditions. The amplitude decreases partly due to the repulsive force gradient increasing the resonant frequency but mainly due to the increased dissipation during contact with the sample. A z feedback loop acts to maintain a chosen amplitude which controls how hard the sample its 'tapped'.

4.3 Design of AFM system

The primary function of the homebuilt AFM integrated into the instrument is to position NV centres, affixed to a cantilever tip, close to a magnetic field source with nanometer precision. For the AFM to be suitable for scanning probe NV magnetometry, the following design requirements were identified:

- A large z range is required to both accommodate samples of varying sizes. For example, atom chips consisting of arrays of gold wires 2 µm thick, with the region several microns above the wire of interest for scanning NV centre magnetometry.
- Non-optical detection of cantilever motion, avoiding collection of light in the NV centre emission spectra and removing the need for additional optical components.
- A compact system to allow for the addition of microwave and optical components required for the measurement of the NV centre.

4.3.1 Akiyama Probe

The choice of probe for any AFM is dependent upon the type of sample used and the conditions of operation, for this instrument Akiyama probes were chosen as the primary AFM sensor. The motivation for choosing Akiyama probes relates to the first design requirement identified for our instrument, non-optical detection of cantilever motion. A common method for monitoring cantilever motion is through the application of a laser to the cantilever tip. The laser is reflected from the surface of the cantilever towards a sensitive quadrant photodiode, with the position on the quadrant diode used to detect the motion of the cantilever. The photodiode then provides the feedback signal for the chosen AFM mode. Optically detected cantilever motion for scanning probe NV centre experiments presents two problems. The first problem considers the spectral overlap of the AFM laser and the NV PL signal, leading to the coupling of the laser to the NV PL detection instrumentation. In addition to direct detection of the deflection laser itself, the

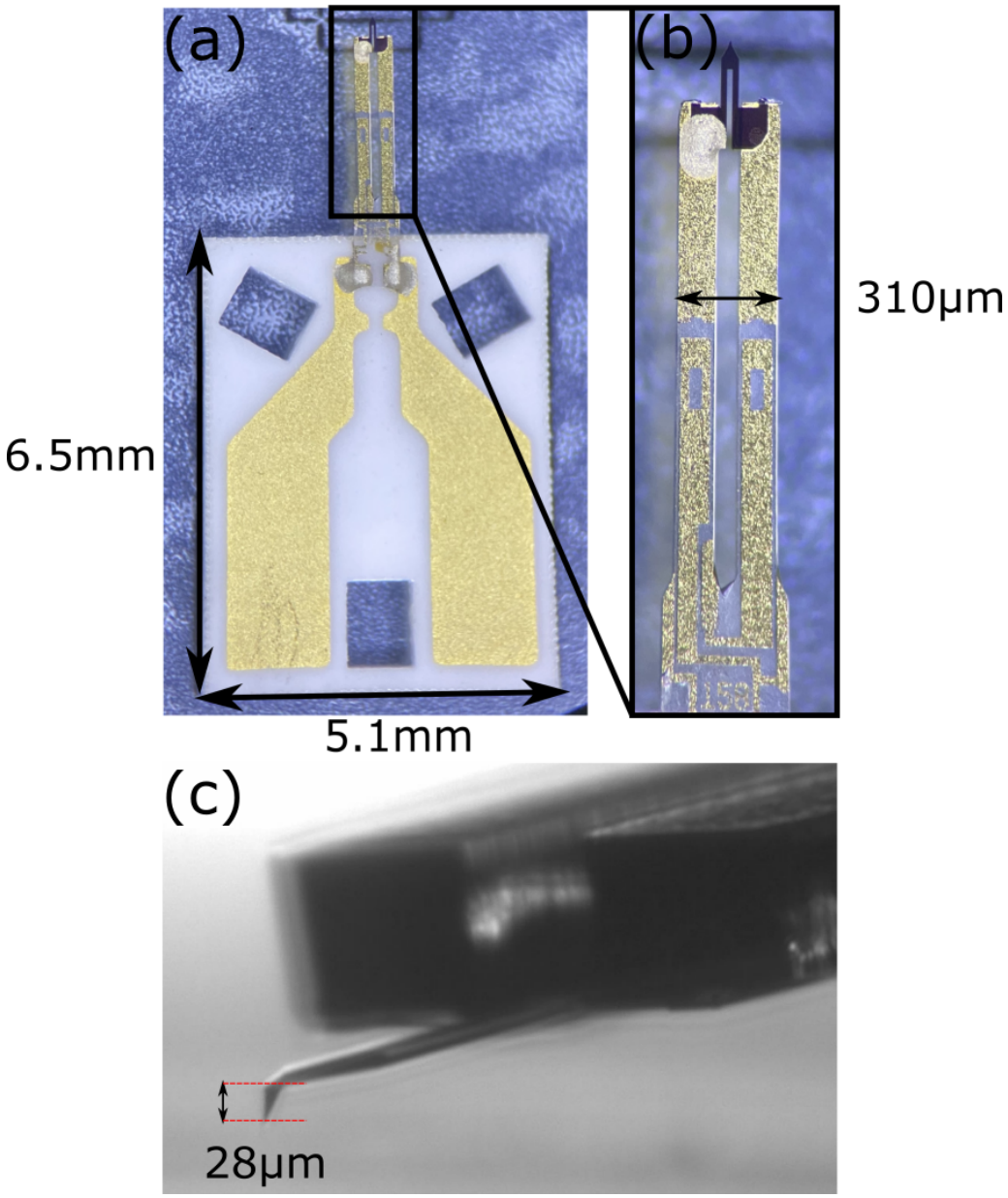

Figure 4.2: Image of Akiyama probes taken under an optical microscope. (a) shows the dimensions of the Akiyama ceramic probe holder, the probe is held onto the preamplifier board via clips onto the contacts, also providing the electrical connection. The tuning fork can be seen at the top of the image (b) Shows the end of the tuning fork and how the tines of the fork are coupled by the silicon cantilever, the tip points up and towards from the camera. (c) Image (captured using a camera integrated into the instrument) showing the tip extending down towards a sample from the free end of the cantilever.

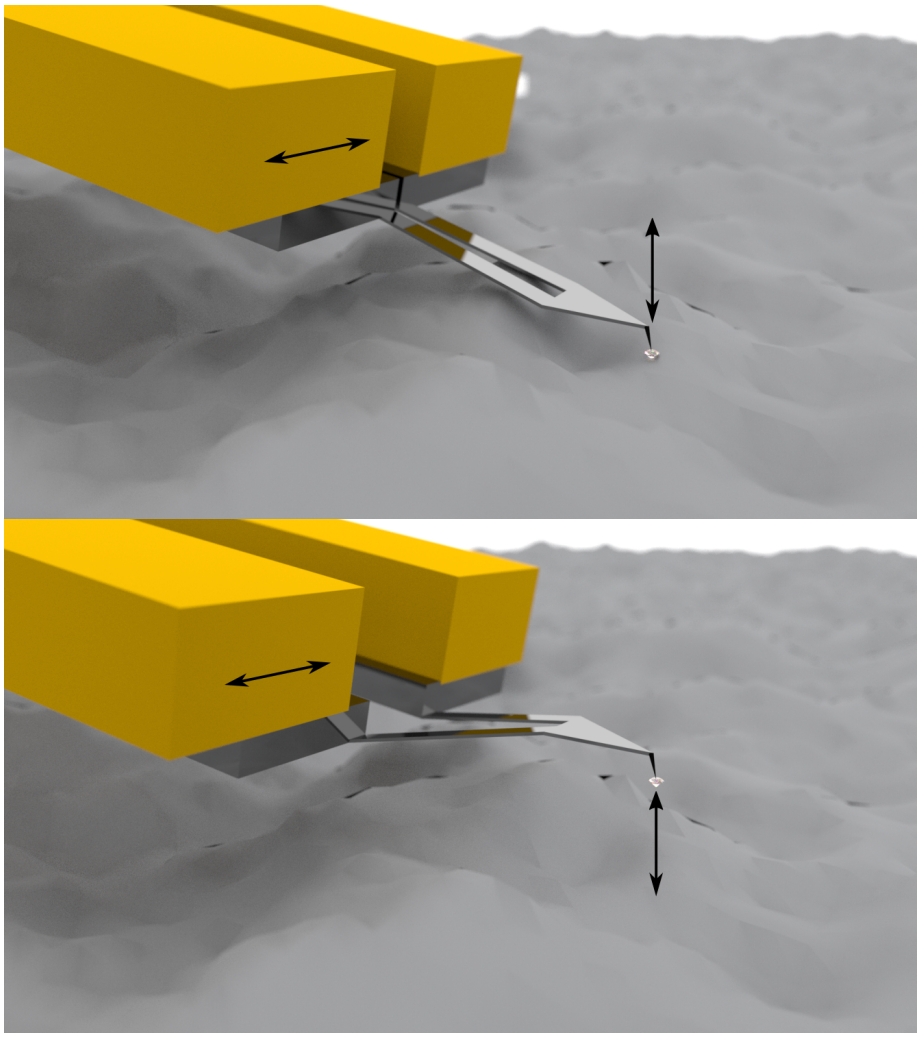

Figure 4.3: 3D representation of the working principle of the Akiyama probe showing how in-plane motion of the tuning fork is translated to vertical motion of the cantilever. The application of the drive signal causes the tuning fork, shown in gold, to oscillate in antiphase. When the tines are close together the cantilever is close to the surface, as shown by the top image. As the tines move apart the cantilever is withdrawn. Figure based on slide 4 of Akiyama technote [127].

deflection signal can also induce unwanted fluorescence at wavelengths which can not be easily filtered from the desired NV PL. The standard beam deflection approach can also be bulky with the addition of the laser and photodiode positioned close to the cantilever. The physical space required for the laser and photodiode can be restrictive when positioning the other elements vital for NV centre experiments, including the MO for optical addressing, MW components for coherent control of the spin, and the addition of a magnet for bias fields. To avoid an AFM based on a beam deflection approach Akiyama probes were identified for this instrument. The probe consists of a quartz tuning fork with a silicon cantilever affixed to both tines at the free end of the fork . The motion of the cantilever is both actuated and detected electrically, through the detection and driving of the tuning fork using the piezoelectric effect. Therefore no optical detection of the cantilever is required [128]. In addition, the Akiyama probe geometry, with 3 mm between the cantilever and mounting point allow for easy integration into the confocal setup. A picture of an Akiyama probe is shown in figure 4.2. A key feature of the Akiyama probe is that the cantilever is attached to both tines of the tuning fork therefore tuning fork is symmetric, with no mass imbalance between the tines, resulting a high Q. It has previously been shown that tuning fork based force sensors with a mass difference between the tines have a lower Q and sensitivity than the unloaded case [129].

The principle of operation of an Akiyama probe is graphically represented in figure 4.3. A silicon cantilever is glued to the free end of a quartz tuning fork with each cantilever leg attached to a tuning fork tine, with the probe tip at the free end. The tip is orientated to point in the z-direction, which is perpendicular to the xy plane defined by the tuning fork. In operation, the prongs of the tuning fork vibrate in the xy plane in antiphase. The movement of the tines induces a periodically changing mechanical stress in the cantilever resulting in oscillatory motion of the tip in the z-direction. The tip-sample interaction changes the amplitude and frequency of the cantilever oscillation which can then be read out electronically, via the tuning fork [128]. Applying an AC voltage between the two electrodes oscillates the tuning fork and cantilever via the piezoelectric effect. Inversely, monitoring the current which has a frequency nominally identical to the cantilever oscillation frequency,

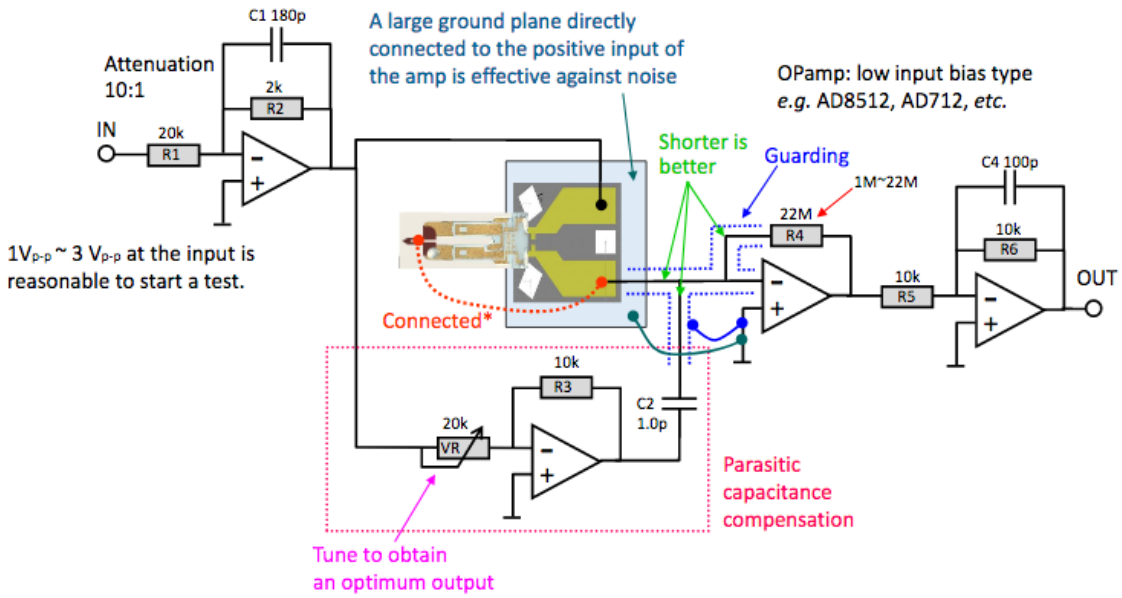

Figure 4.4: Circuit diagram of the preamplifier board. Image sourced from manufacturer [111]

produced by the tuning fork motion facilitates the readout of the mechanical motion and therefore the tip-sample interaction. The key parameters that define the Akiyama probe are a tip radius less than 15 nm, a free space resonant frequency $f_0 \approx 50\,\text{kHz}$ and an effective cantilever force constant $5\,\text{N}\,\text{m}^{-1}$ [127].

The Akiyama probe is mounted onto a 6.5 mm x 5.1 mm x 0.4 mm ceramic holder (see figure 4.2a), the function of which is to provide contacts for the drive and measurement signal. The relatively large size of the ceramic also reduces the skill required to load the probe into the AFM instrumentation. In this instrument, the Akiyama probe is mounted onto a small preamplifier board using clips, which are also used to make electrical contact between the board and probe. The preamplifier board is commercially available and produced by Nanosensors specifically for operation with Akiyama probes, circuit diagram shown in Figure 4.4. The preamplifier board supplies the drive signal to the probe, this is stepped down by a factor of 10 to be at a safe level at the probe. The drive input signal is supplied to the preamplifier board in the region 0-1 V_{pp}, a common standard for many AFM controllers. The second function of the preamplifier board is to amplify the measure-

ment current and convert the signal to a voltage. A transimpedance amplifier with a gain of $22\,\mathrm{V}\,\mu\mathrm{A}^{-1}$ is used to convert the measurement current to a detectable voltage. Finally, the board features an additional circuit to prevent the coupling of the drive signal to the measurement line through parasitic capacitance. A key element of this circuit is a variable resistor, this is adjusted each time a new probe is loaded onto the preamp PCB. The parasitic capacitance manifests as an asymmetry of the Lorentzian response of the probe to the drive signal limiting the ability to demodulate frequency and amplitude changes. To reduce parasitic capacitance the drive signal frequency is varied close to the resonant frequency and the response of the tuning fork examined after adjustment of the variable resistor in the compensation circuit. When the resonance of the measurement signal is symmetric and the amplitude is low away from the resonance the resistor is determined to be in the correct position for capacitance compensation, with only the piezoelectric current amplified by the detection circuit. The response of a typical Akiyama probe, with the parasitic capacitance circuit well adjusted, is shown in Figure 4.5.

A mount was constructed from aluminium alloy to connect the preamp PCB and probe to AFM coarse positioning stages, produced by Smaract, the operation and purpose of the stages will be discussed in greater detail later in this chapter. The design requirements for the mount were as follows, lightweight, non-magnetic and rigid. The mount was machined so that the probe and therefore cantilever had an 11° offset from the sample plane, resulting in the cantilever tip being perpendicular to the sample. The AFM mount is shown in Figure 4.6.

4.3.2 Scan Stages

In all of the AFM modes performed by this instrument the probe and therefore, the cantilever position is stationary. The raster scanning is performed by using piezoelectric flexure stages. The scan stages are the same stages as described in the confocal microscopy chapter, produced by Piezoconcept with model number LFHS2.50 in the xy directions and the z motion is provided by an accompanying Z-STAGE.50. The full scan range of the AFM is

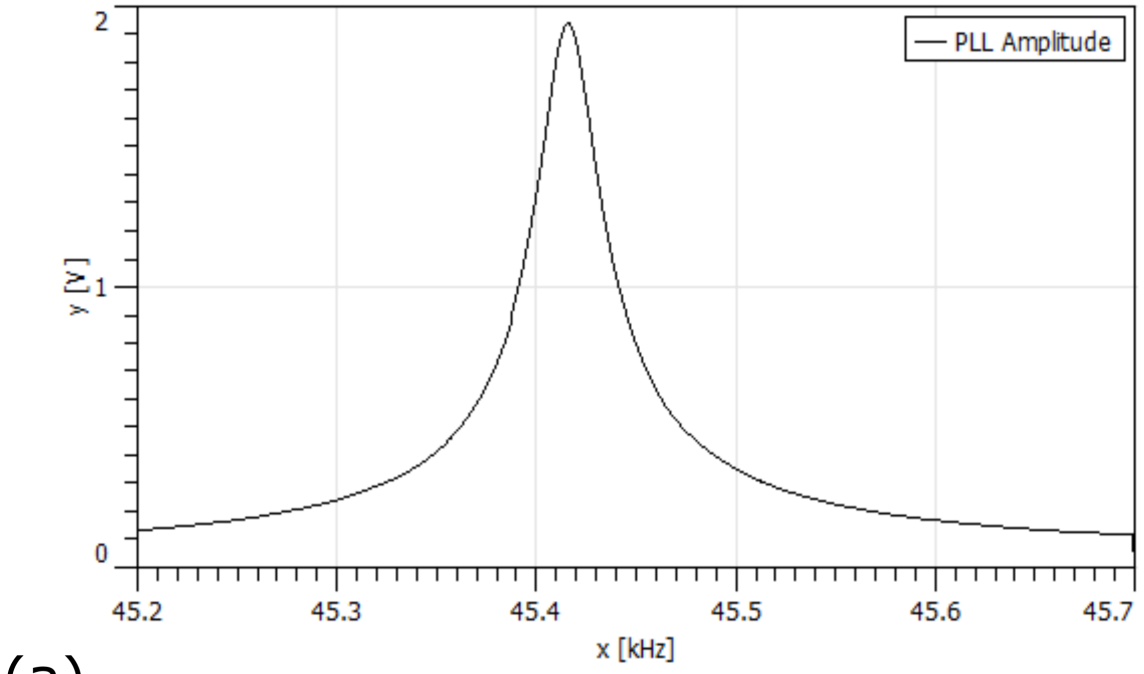

(a)

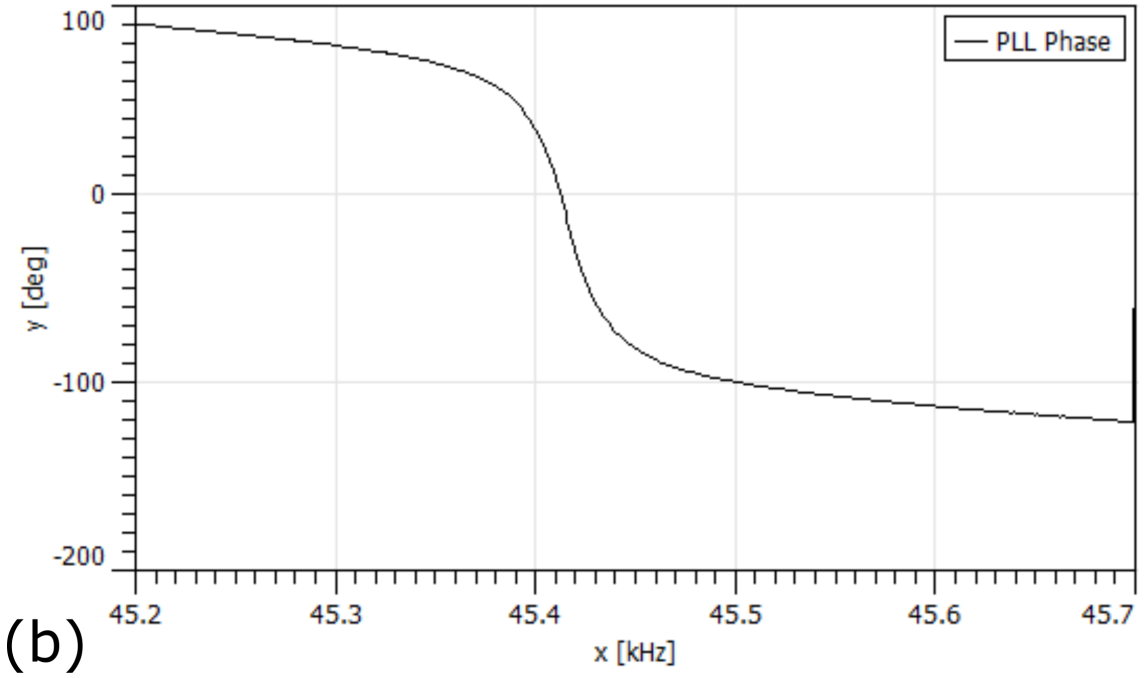

(b)

Figure 4.5: (a) Typical response of an Akiyama probe at drive frequencies close to the resonant value, the y-axis is shown in volts and is proportional to the piezoelectric current in the tuning fork, and therefore, the physical oscillation amplitude of the Akiyama probe. (b) shows the corresponding phase relation between the drive signal and the probe oscillation.

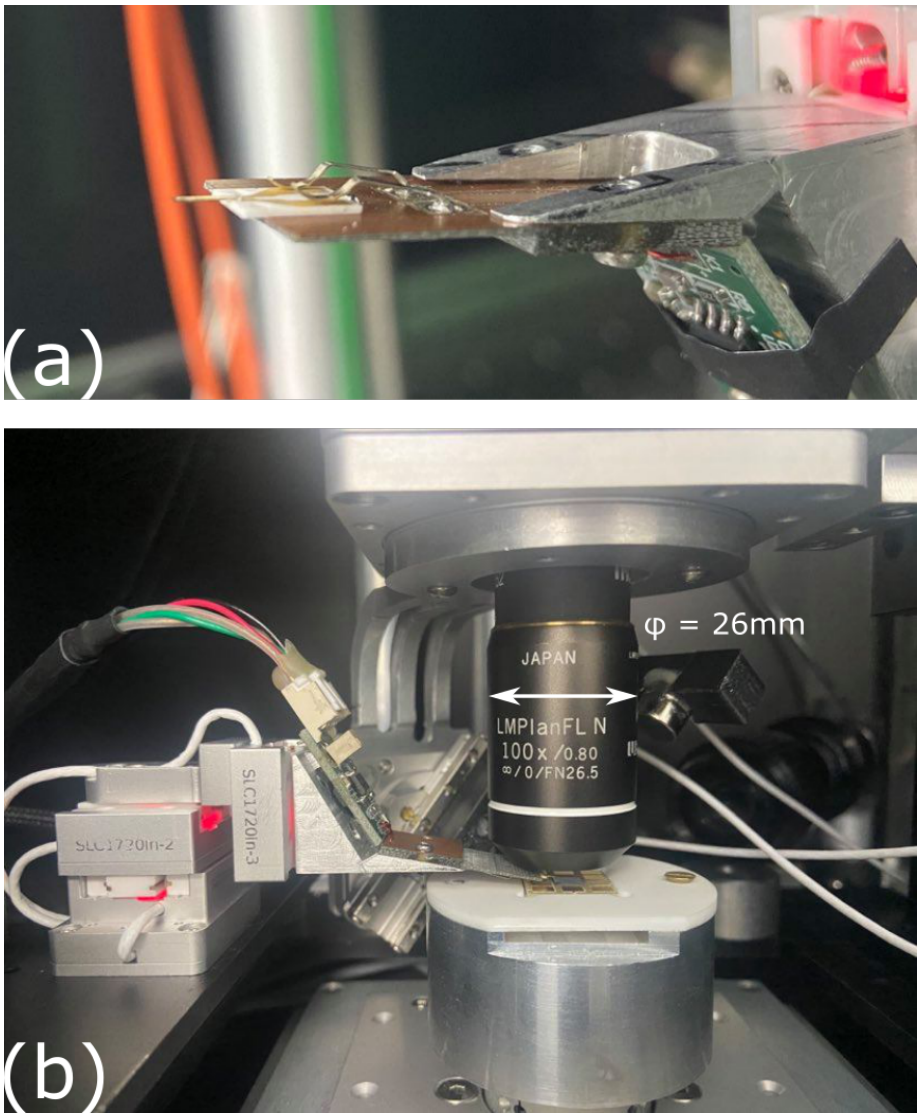

Figure 4.6: (a) Image of Akiyama probe mounted on to preamp PCB, with the PCB and positioning stages removed from confocal microscope to the probe loading position. The A-probe is connected both physically and electrically to the PCB via a pair of clips. (b) Image of home-built mount connected to coarse approach z stage (SLC1720ln-3), the PCB with preamplifiers for the probe is shown affixed to the constructed mount. The tuning fork with cantilever on the end can be seen positioned above a sample under the objective lens. The wires at the top deliver the drive and measurement signals as well as the power for the preamplifiers.

set by the range of the stages and corresponds to 50 µm x 50 µm x 50 µm in x, y and z respectively. According to the manufacturer's specifications the resolution the stages in each direction is 0.05 nm with a typical noise floor of 0.005 nm. While the resonant frequencies each of the three axes greater than 2 kHz [130, 131].

4.3.3 AFM Control

The control of the homebuilt AFM system can be considered in terms of two distinct challenges. Firstly, approaching the sample in a time-efficient manner that does not crash the tip into the sample, potentially damaging the AFM probe or sample. The second challenge relates to the control of the oscillating cantilever close to the surface, this includes scanning the sample, maintaining the feedback loops for the chosen AFM mode and the acquisition and processing of the imaging signal.

4.3.4 Coarse Z control

The instrument was designed to be versatile in the type of samples that can be investigated. The main motivation for the development of this instrument is to characterise atom chips which consist of arrays of wires typically 2 µm thick, the region several microns above this surface is also of interest for scanning probe NV magnetometry measurements. Likewise the instrument is suited to characterising very flat samples, such as scanning NV magnetometry on antiferromagnetic layers or the investigation of single photon emitters in 2D materials such as hexagonal boron nitride. The samples probed by this instrument are inherently varied in size demonstrating the need to reliably change the sample plane. Many of the samples investigated are fixed to the sample scanning stages with custom built sample holders, including devices with electrical contacts, and the ability to change the plane in which measurements are conducted is important given the sample holders and contact structures can change between investigations. To offer the ability to change the sample plane easily the PCB with the AFM probe was mounted to a piezo closed-loop slip-stick stage (Smaract, 1720). The stage consists of a piezoelectric actuator which is

coupled to a sliding element via friction. The speed in which the piezoelectric element is expanded or contracted determines whether the sliding component moves with the piezo expansion/contraction (sticks) or remains stationary (slips). The slip-stick principle enables the stage to move with nanometer precision over a macroscopic range at mm/s speeds. The precision of the Smaract 1720 facilitates cantilever positioning with 1 nm accuracy anywhere within the 12 mm range. The combination of the 50 µm range of the z scan stage and Smaract z stage, enables imaging of samples with large variations in topography over the scan range about a setpoint anywhere in the 12 mm range.

The Smaract stage is used to perform the z approach of the probe to the sample in a quick, yet controllable manner. When the tip of the cantilever is close to the sample the feedback mechanism for the chosen AFM mode is activated and the sample stage brought towards the cantilever until the setpoint for the feedback parameter is reached. The stage is centred in its range before the approach procedure and the coarse approach Smaract stage is used to bring the tip to a few micrometres above the sample. Setting the stage to the middle of the range before approach ensures the scan is centred close to the middle of the z range and this is not a limiting factor during measurement. The coarse approach z stage is controlled using Python with a GUI, giving the user an easy means to control the size, speed and direction of motion. To allow the user to safely bring the tip a few micrometers above the surface a side-view camera was integrated into the instrument to observe tip motion in real-time.

The side-view camera consists of two main components, the illumination source and a CMOS camera with an imaging lens. A green LED array acts as the illumination source and is placed opposite the probe to a CMOS camera (Thorlabs, DCC3240M). The array is powered by a benchtop power supply at around 20 V drawing around 30 mA. The camera is fitted with a variable zoom lens (Thorlabs, MVL6X12Z), that allows for changing the magnification and refocusing as the tip is brought close to the surface. Figure 4.7 demonstrates the position of the quartz tuning fork and cantilever tip position during the approach procedure. In figure 4.7(a) the tip is withdrawn and figure 4.7(b) it has been approached by a distance of 25 µm. The user can easily observe micron-scale motion of the

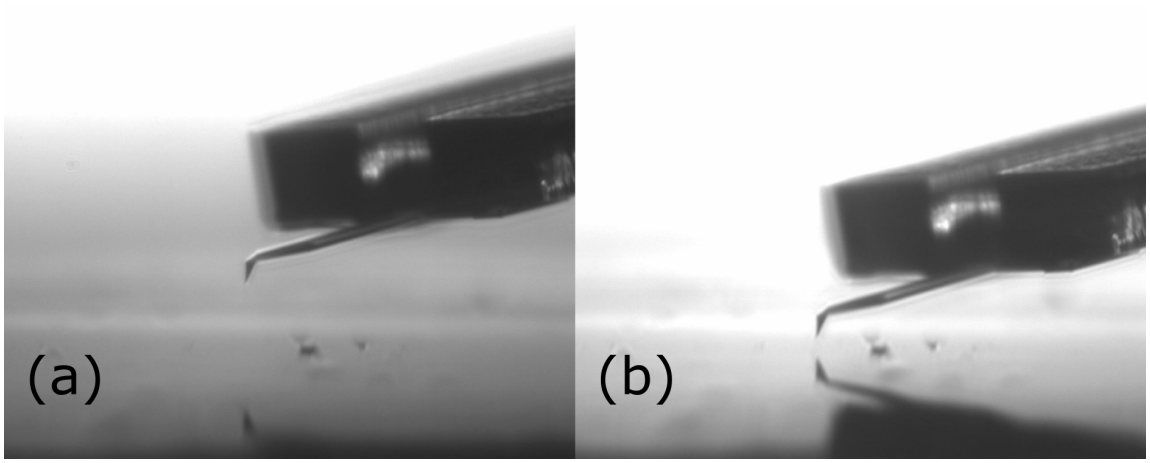

Figure 4.7: Images captured using the side-view camera used during the z coarse approach procedure. (a) the tip is shown slightly retracted, the reflection of the tip can clearly be seen on the sample, in this case a silicon calibration sample coated with silicon dioxide. (b) the tip has been advanced toward the sample by 25 µm demonstrating the ease in which the user can safely and quickly approach tip to sample before activating feedback loops for the final approach.

tip with respect to the sample using the side-view camera. The illumination angle and the nature of the samples addressed so far produces a reflection of the tip on the sample, the separation between reflection and tip aids in the knowledge of the tip position assisting the user in the approach procedure.

AFM Interface

The AFM positioning and control of the feedback loops is performed using a commercially available SPM controller, the R9 produced by RHK Technologies. The controller produces the scan signals for scanning the piezostages under the sample, the cantilever drive signal and control of the feedback loops. The software was delivered with programs for the imaging modes suited to our application and chosen probe. The modes include dynamic AFM modes (AM-AFM or FM-AFM) and tapping mode.

The R9 software is icon-based and allows the user to easily customise the setup without

requiring intricate knowledge of the base code. In addition to the user-friendly software interface, the use of a single unit to control the drive signals, the feedback loops and the scan signals simplifies synchronisation with scanning and data acquisition. One benefit of the R9 is the entirely digital phase locked loop (PLL), which facilitates fast feedback enabling modulation of the drive frequency for FM-AFM.

4.3.5 Combining AFM and confocal imaging

Theoretically an AFM scan, with full 50 µm x 50 µm range, can be performed anywhere on the sample plane the region addressed just depends on the initial xy position of the AFM tip. In a multimode imaging instrument, such as the one considered here, it is important to align the FOVs for the different techniques. In this instrument, the FOVs that must be aligned correspond to the AFM and the microscope objective for wide-field and confocal microscopy. There are three primary motivations for aligning the FOV of the AFM with the optical instruments all with slightly different alignment protocols and motivations. In pure AFM, the optical measurements provided by the confocal microscope are not required. However, the alignment of the AFM FOV with the wide-field microscope aids in the alignment of a region of interest of a sample and the AFM tip prior to measurement. The use of the CMOS camera in the wide-field microscope allows an area to be previewed before scanning with the substantially longer acquisition times associated with AFM imaging. In scanning probe NV magnetometry it is vital the confocal measurement volume is accurately aligned with the NV centre or centres on the probe to collect the NV PL for magnetic field readout. In this imaging mode, the oscillating AFM tip will be held stationary with the sample scanned underneath with the very tip of the cantilever in the focus of the diffraction-limited spot of the confocal microscope for optical preparation and readout from the NV centre. Finally, the AFM and confocal field of view can be aligned to acquire data from the two imaging modes on the same region of a sample, either sequentially or simultaneously. In this section an overview of the general alignment between optical and AFM FOV for pure AFM measurement is presented with the fine alignment procedures for scanning NV magnetometry and simultaneous AFM/confocal measurement

discussed in more detail in the relevant section.

The scan stages have a range of 50 µm x 50 µm and the instrument is designed to accommodate large samples, potentially several centimetres wide. A large sample could potentially host many 50 µm x 50 µm areas for characterisation, demonstrating the need to accurately position the AFM tip in the sample plane. The in-plane (xy) motion of the AFM probe is controlled using two additional Smaract 1720 closed-loop slip-stick stages, the same type used for coarse z control with 12 mm range and 1 nm precision. Figure 4.8(a) shows the degrees of freedom and the motion control a user has over the AFM tip position for choosing a region to address and the scan stage motion.

The task of aligning the FOVs between microscope and AFM was one of the main motivations for the integration of the wide-field microscope into the instrumentation. A detailed discussion of the design and performance of the wide-field microscope is included in Chapter 3 (optical instrumentation). To align a sample for imaging the coarse positioners on the sample scanning piezo-stages are used to centre the region of interest in the wide-field microscope. The wide field of view of the microscope, 130 µm by 105 µm, combined with the real-time view of the CMOS camera facilitates quick and accurate FOV alignment. Once a sample region has been selected and centred under the wide-field MO the AFM tip can then be centred on the same area. The wide-field microscope again plays an important role in this process.

The protocol for aligning the AFM field of view with the confocal is defined as follows. Firstly, the MO is withdrawn slightly to account for the cantilever being above the sample surface and the 1 µm depth of focus of the MO. The xy Smaract stages are used to scan the tip around the sample until some part of the tuning fork or cantilever is observed on the wide-field microscope. The cantilever tip can then easily be moved to the centre of the wide-field FOV using the Smaract stages. As the tuning fork and cantilever are moved to the centre the MO must be refocused to keep the fork, cantilever and finally tip in focus. The greatest challenge in the alignment process is observing any part of the cantilever and fork in the wide-field microscope when first scanning in x and y. To address

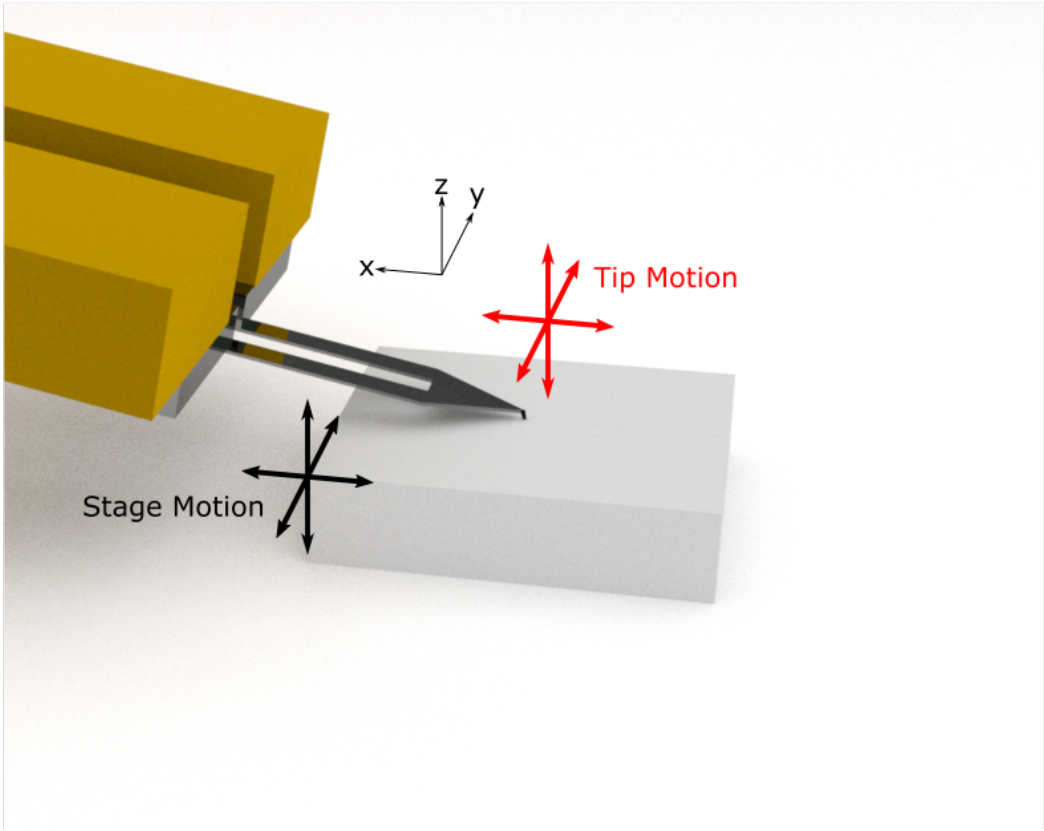

Figure 4.8: (a) 3D representation of the motion control of the AFM. The thick black arrows show the stage motion and are used to control the scanning of the AFM, these signals are generated by the R9 with the z motion part of the feedback loop for imaging. The red arrows show the motion for the Smaract stages, the Smaract z motion is used to bring the tip close to the sample before the feedback loops control the approach. The xy tip motion allow the selection of a FOV for the AFM, including aligning the AFM tip with the confocal FOV. The x,y, z in the co-ordinate system of the lab reference frame is shown in thin black lines.

this challenge a user can physically observe the microscope to see if the tuning fork is in the region illuminated by the wide-field microscope. Additionally, the side view camera can assist in the initial alignment as the illumination from the wide-field microscope can be seen on the tuning fork or cantilever. Observation of the microscope illumination spot on the tuning fork or cantilever in this camera this informs a user that part of the tuning fork or cantilever can be focused on the wide-field camera by adjusting the MO position. Once part of the fork or cantilever is in focus, the Smaract stages can be moved and the MO refocused to find the tip of the cantilever as described above.

4.4 Simultaneous Confocal AFM

The procedure for coarse alignment between AFM and the objective lens as described above can be extended to align the smaller confocal microscope FOV with the AFM FOV. Firstly the confocal laser is turned on at low power and the confocal spot is detected on the sample as a small saturated spot in the wide-field microscope. Neutral density filters are added to the confocal laser path, even for the lowest operating power, as this reduces the size of the spot on the camera by reducing the number of saturated pixels, giving a more accurate position of the confocal spot. Figure 4.9 shows images captured in the wide-field microscope during the alignment procedure. The four images show the cantilever tip centred in the wide-field camera positioned just above an AFM calibration sample. From 4.9(a)-4.9(d), the MO is brought closer to the surface showing the sample and tip gradually come into focus. In the final image, 4.9(d), the laser spot can be seen aligned with the tip. In scanning probe magnetometry, the confocal microscope and the AFM can be accurately aligned with nanometer precision, as the NV centre PL intensity provides feedback on the degree of alignment, this is discussed in the scanning probe magnetometry chapter.

The visual alignment of the confocal measurement spot and the AFM tip represents the first stage in aligning the optically active probes for NV centre magnetometry. The second motivation for aligning confocal and AFM field of views is the two complementary imaging techniques can be used to image the same area of a sample, however now with the

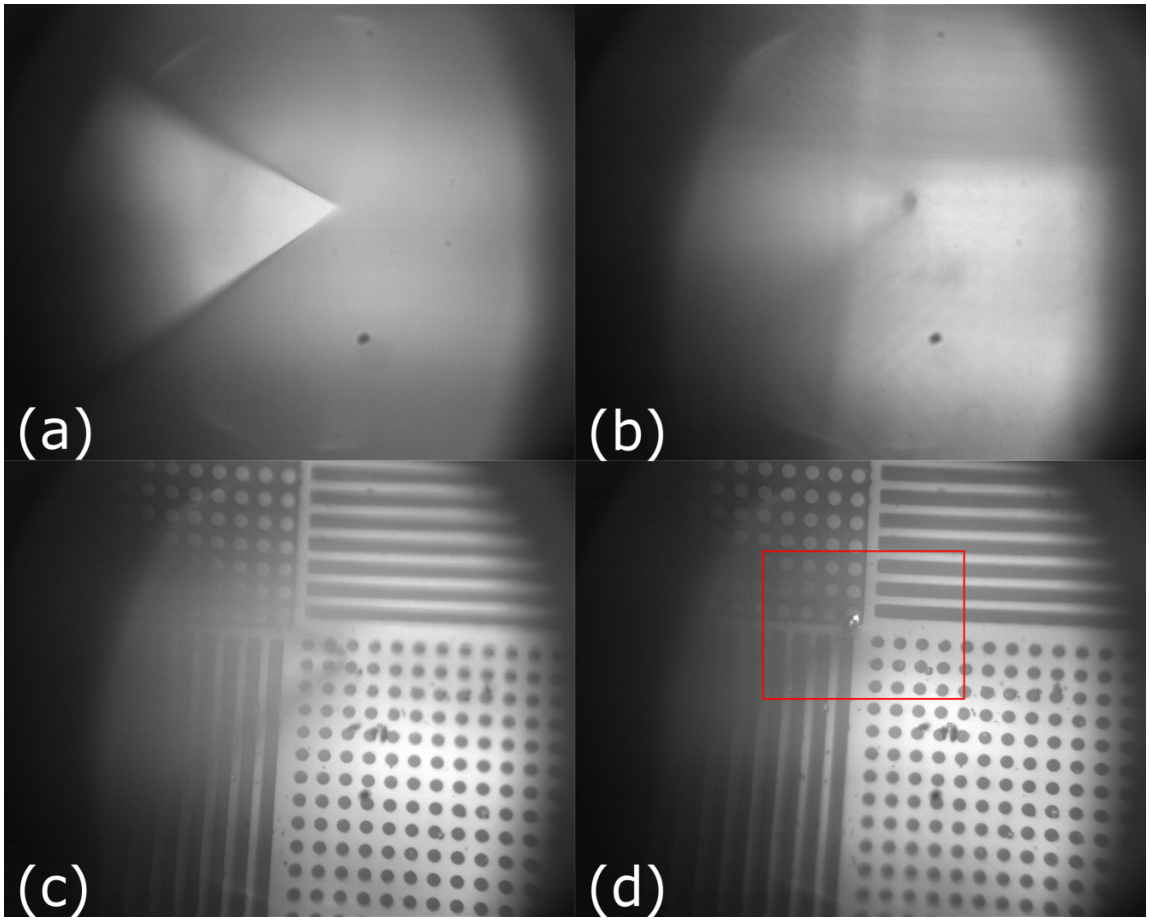

Figure 4.9: (a) Image from wide-field microscope showing retracted cantilever in focus just above a sample surface this is useful for coarsely aligning AFM and confocal FOV. The MO is shown advanced towards the surface in (b) and then advanced further still in (c), with the sample surface coming into focus. In (d) the confocal spot can be seen, shown within the red box, aiding fine xy adjustments to align the area on the AFM to be optically addressed by the confocal microscope.

confocal microscope focused on the sample rather than the tip, which is the case for NV magnetometry. Once the two FOVs are aligned data can be acquired sequentially with the confocal microscope and AFM with independently operated to produced accurately aligned images. However, in this instrument, a dual imaging mode has been developed allowing the operation of the confocal microscope and the AFM simultaneously. Simultaneous AFM and confocal measurement is of interest to a range of optically active devices on the nanoscale. A particular benefit is to this imaging modality is addressing the difficulty associated with aligning a microscopic region of interest on separate AFMs and optical instrument. An additional advantage of the simultaneous confocal AFM mode is the focal point of the confocal microscope is always in focus on the sample regardless of the sample topography. The z feedback loop of the AFM maintains the tip-sample force and therefore separation with nanoscale precision. As a result, even if the topography changes by over 1 µm the sample remains in focus as sample height is adjusted relative to the AFM cantilever, which has a fixed position relative to the MO.

In NV centre magnetometry the probe and confocal microscope are precisely aligned by maximising the optical signal from the NV centres affixed to the probe. More generally when the AFM and confocal microscope are aligned visually by inspecting tip and laser spot position on the wide-field camera there is an offset associated with the two imaging modes, this is represented in Figure 4.10. The offset is tuneable and controlled by the AFM tip coarse positioning stages, measurement of the offset in simultaneous AFM/confocal measurements is discussed in greater depth in the AFM performance section.

To perform simultaneous confocal-AFM measurement the confocal spot and the AFM tip are aligned using the procedure outlined in the section above. The feedback loop is activated and the stage moved towards the AFM tip. To bring the MO into focus on the sample the lasers/detectors are powered on and the confocal microscope operated in reflectance mode. The backscattered signal intensity is monitored as the MO is moved towards the sample; when the maximum signal is detected the MO position fixed. The confocal microscope can be operated in PL or reflectance when performing simultaneous AFM confocal measurements, however, reflectance mode is always used initially to ensure

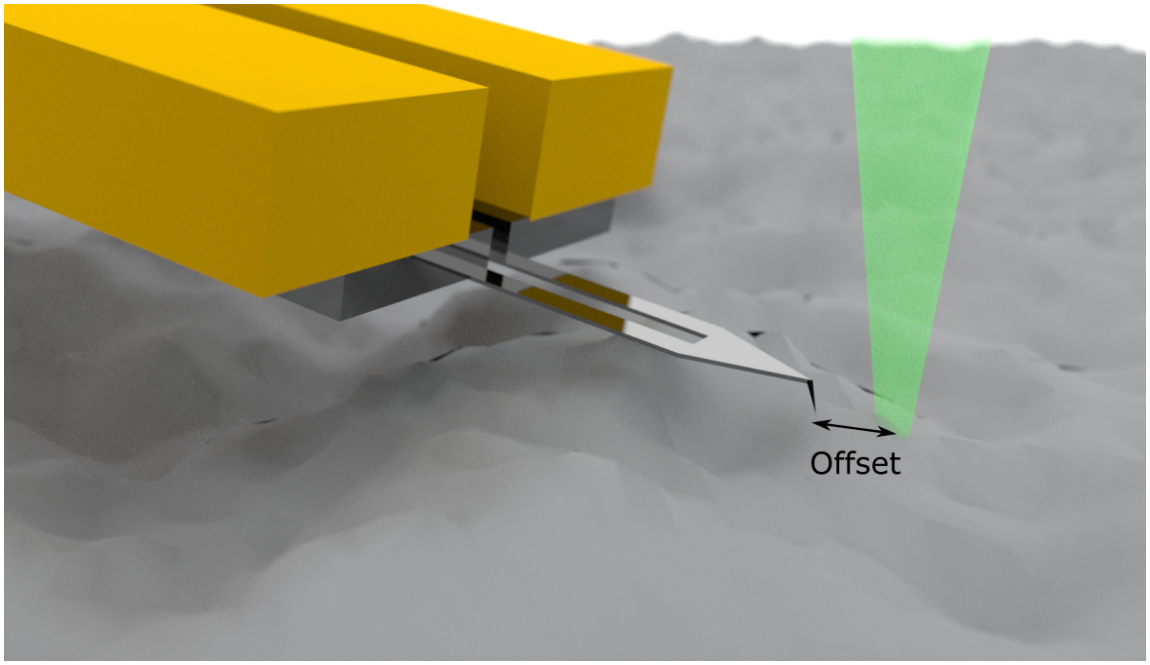

Figure 4.10: Simultaneous AFM and confocal measurements are subject to a small offset associated with the degree in which the tip and confocal microscope are aligned. The confocal measurement volume is represented by the green cone.

a large signal for focusing. The SPAD signals for confocal microscopy is delivered to a pair of pulse counting inputs on the RHK R9 SPM controller used for AFM control. The AFM signal and optical signal are easily synchronised using the R9 software as the AFM control circuity and pulse counters run on the same FPGA chip with the same underlying clock.

4.5 AFM performance

To provide a measure of the performance of the homebuilt AFM a range of test samples were scanned. Firstly, an AFM calibration grid was scanned to demonstrate the AFMs ability to accurately resolve features in the z-direction. Typically an AFM calibration sample consists of a grid of features of known size and topography. In the calibration grid used here, the features have a 5 µm period with a feature height of 113 ± 2.5 nm above the background. Figure 4.11 shows a topography image recorded in FM-AFM mode with a frequency difference setpoint of 3 Hz, this image has been post-processed to remove the

effect of sample tilt. The lower half of figure 4.11 shows a 3D projection of the topography. To analyse the height of the features a combination of Gywddion [85] and Python were used to post-process the data. Figure 4.12 (a) shows the FM-AFM image displayed in Python, with three horizontal lines showing the location of line profiles used to estimate feature height. The line profiles across a 20 µm section are shown in figure 4.12(b). The final plot figure 4.12(c), shows the line profiles from (b) in a reduced range to highlight a single feature. The profiles have been corrected for tilt by the subtraction of a linear background with the base offset to z = 0 µm. In figure 4.12(c), the line profiles have been offset by 20 µm for clarity. The blue, orange and green line profiles showed a feature height of 112 ± 3 nm, 112 ± 2 nm and 115 ± 2 nm respectively. The sample is contaminated with objects several 100 nm tall, restricting the range in which line profiles can be evaluated. However, the recorded height of around 113 ± 3 nm is in good agreement with the expected feature height and suggests the noise floor of the AFM is 3 nm in the z-direction.

The 3 nm noise level in the z signal is higher than many commercially available AFMs, even operating at ambient conditions. State of the art AFMs such as the Park Systems NX10 demonstrate noise levels down to 0.02 nm in the z detection signal, with 15 µm total range [132]. The resolution of the AFM developed here could potentially improve performance through increased vibration isolation or through using a lower noise transimpedance amplifier, both acting to decrease noise on the measurement signal. An upper limit to the achievable z resolution is set by the noise floor in the piezo scanning stage which forms an important part of the z feedback loop. The stage was chosen so that samples up several centimetres can be accommodated and the magnetic field can be characterised over a range of several microns above a target. A consequence of a large scan (50 µm) range is the output resolution of the AFM controller for z feedback signal corresponds to a larger z motion than on a stage with a reduced range. As the main aim of the AFM in this instrument is positioning target spins and not operating at the limit of AFM resolution this is not considered a major limitation.

The resolution is largely set by the scan speed and the P and I controls for a given frequency sweep and the tuning of the PLL. Future work on performance improvement

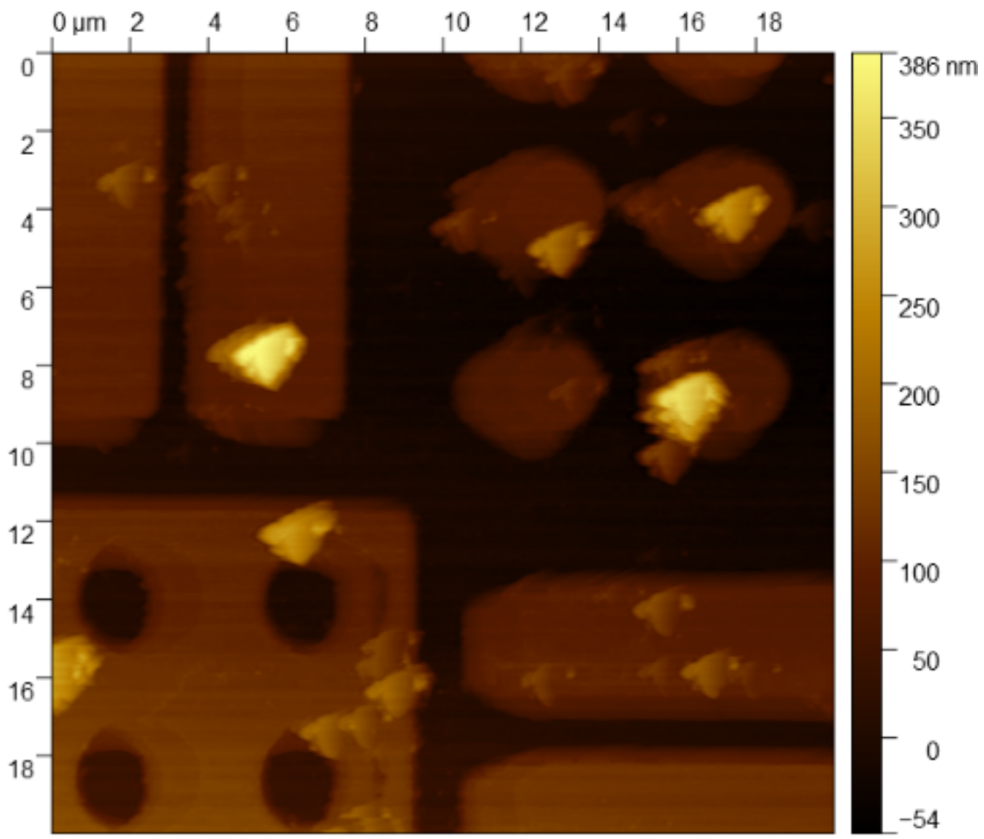

(a)

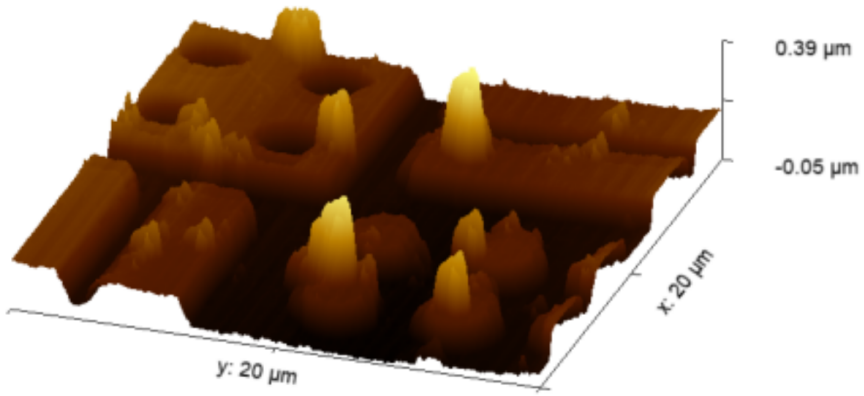

(b)

Figure 4.11: (a) Post processed image topographical image of AFM calibration recorded in FM-AFM mode with a $\Delta f = 3\,\mathrm{Hz}$ setpoint. The calibration grid shows some additional features due to contamination. (b) lower image shows a 3D projection of the image shown in (a).

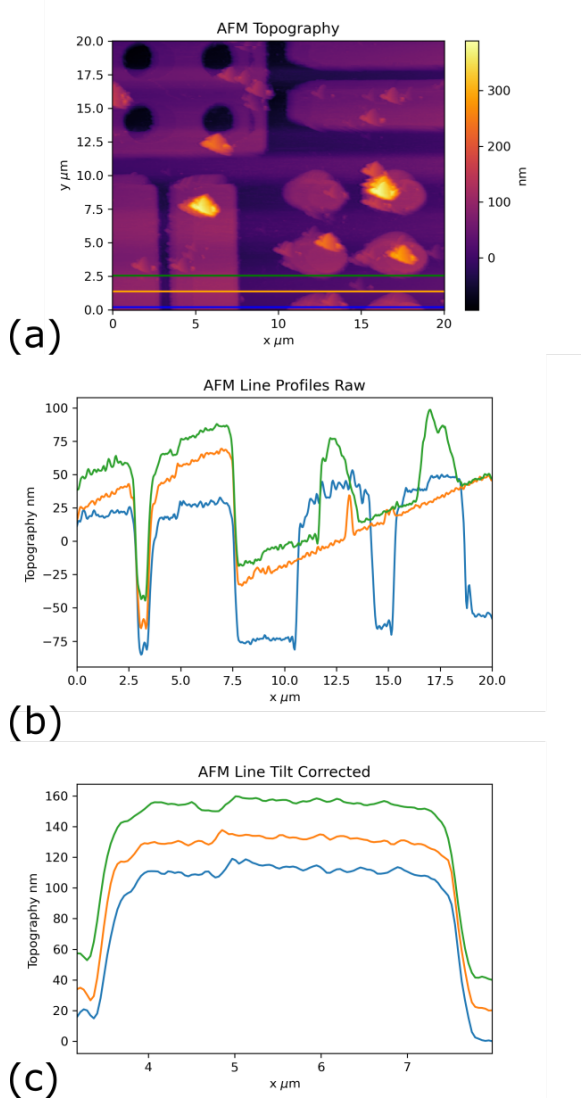

Figure 4.12: Python analysis of FM-AFM recorded topography on calibration sample, same data as displayed in figure 4.11. (a) shows the image imported from Gywddion displayed in Python with three lines showing the locations were line profiles have been evaluated. (b) the raw data from the FM-AFM on three lines. (c) reduced lines profile from the full range shown in (b), the profiles have been corrected for a constant sample and offset to zero. Each line profile has been then been offset by 20 µm for clarity. The blue, orange and green line profiles showed a feature height of 112 ± 3 nm, 112 ± 2 nm and 115 ± 2 nm respectively.

focuses on a more detailed characterisation of the noise floor, identifying and reducing the noise sources.

4.5.1 Simultaneous AFM and Confocal Performance

To perform a simultaneous AFM/confocal measurement the offset between the AFM tip and the confocal measurement volume must be measured. The offset is quantified by performing a large area scan with the confocal microscope operated in reflectance mode. The offset between the two images is then estimated by visual inspection of features present in both the subsequent topography and reflectance images identified by visual inspection. Figure 4.13 shows an AFM topography image with the simultaneously recorded reflectance image overlaid (green). The open-source software package Gwyddion [85] was used to produce a mask using the simultaneously recorded confocal reflectance image and overlay the mask on the AFM recorded topography image and measure the offsets. The offset is measured by calculating the distance between features seen in both imaging modes, in figure 4.13 , the offset was determined to be $\Delta x \approx 2\,\mu m$ and $\Delta y \approx 11\,\mu m$. In figure 4.13, x and y are the slow and fast scan axis respectively and a positive value of offset denotes the confocal image leads the AFM image on a given axis, this convention is applied to all simultaneous AFM/confocal images unless otherwise stated. The accuracy in calculating the offset using the approach of overlaid images is set by the resolution in the scans and the size and response of the reference feature common to both images. The smallest offset that has been achieved in proof of principle tests corresponds to less than 1 µm along each scan axis and the image is shown in figure 4.14. Figure 4.14(a) and 4.14(b) correspond to low resolution images showing topography and confocal reflectance respectively and the topography with reference mask showing the offset shown in 4.14(c) . The offset could be more accurately determined with a higher resolution scan for this particular offset, however, the AFM developed a fault preventing the acquisition of a high resolution scan for offset calculation following the initial low resolution scan used to visually estimate the offset. The topography image and simultaneous confocal PL image are shown in 4.14(d) and 4.14(c) respectively, providing the first demonstration of a small offset AFM/confocal

image highlighting the probe does not prevent the acquisition of optical data and that this instrument can produce and AFM image and measure luminescence from exactly the same area.

The dual imaging mode in this instrument has been demonstrated in tapping and FM-AFM mode shown in figures 4.15 and 4.16 respectively. In the full range scan shown in figure 4.15 topographical images are shown on the left and the simultaneously recorded optical image on the right, 4.15(c) shows the reflectance image used to calculate the AFM/confocal offset, while PL image recorded immediately after the reflectance scan is shown in 4.15(d). In figure 4.15(b) and (d) the background count rate is more uniform than seen in pure confocal measurements, which can be affected by sample tilts or large changes in topography over a large area scan. The uniformity of the background in dual imaging mode demonstrates how maintaining a constant AFM-sample interaction acts to refocus the confocal microscope over the FOV. Figure 4.16 shows a small range simultaneous AFM/confocal image highlighting the range of information available while performing a single raster using this instrument to characterise samples on the nanoscale. (a) Shows the topography, (b) reflecatance confocal image, (c) df and (d) the PLL amplitude which corresponds to the amplitude of the tuning fork current.

Currently, the AFM coarse positioners are operated in open-loop mode however the stages themselves are fitted with sensors enabling closed-loop operation. In future work operating the AFM tip using the stages in closed loop mode will provide a 3 axis co-ordinate of the AFM tip. Performing a high-resolution scan of a test sample will then provide an accurate measurement of the offset for a given tip co-ordinate. The separation between beam and tip can then be accurately controlled even after a sample is changed. The effect of the cantilever attenuating the optical signal for the smallest achievable offsets has also not yet been characterised. In future, this could be investigated by performing confocal scans of a sample with a known response in dual imaging mode and comparing the signal intensity with the AFM probe withdrawn from the MO FOV.

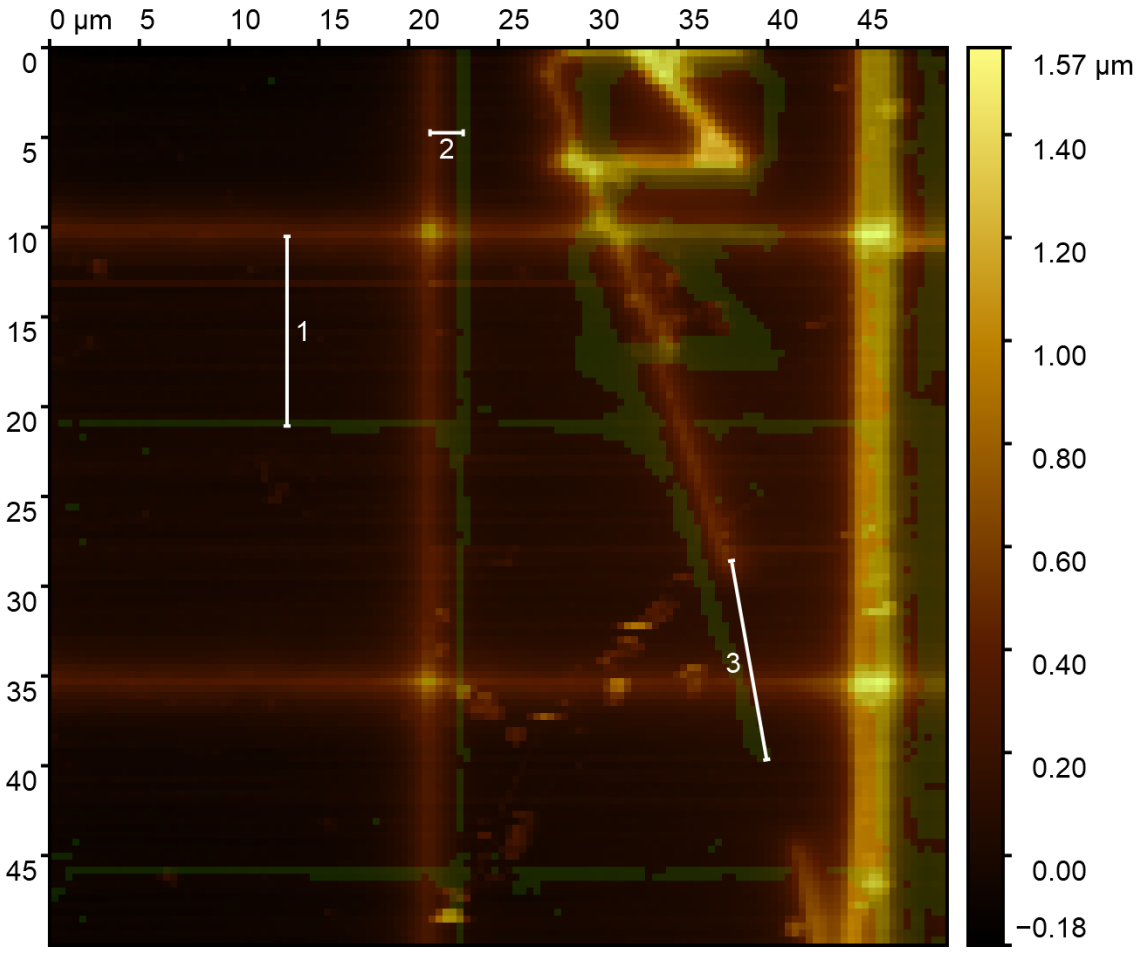

AFM Confocal Offset		
Line Number	Δx	Δy
1	0 µm	10.6 µm
2	1.9 µm	0 µm
3	2.0 µm	11.1 µm

Figure 4.13: Topography image and overlaid reflectance image (green) record simultaneously. Numbered lines show distance between features seen in topography scan and reflectance mask to estimate AFM/Confocal offset.

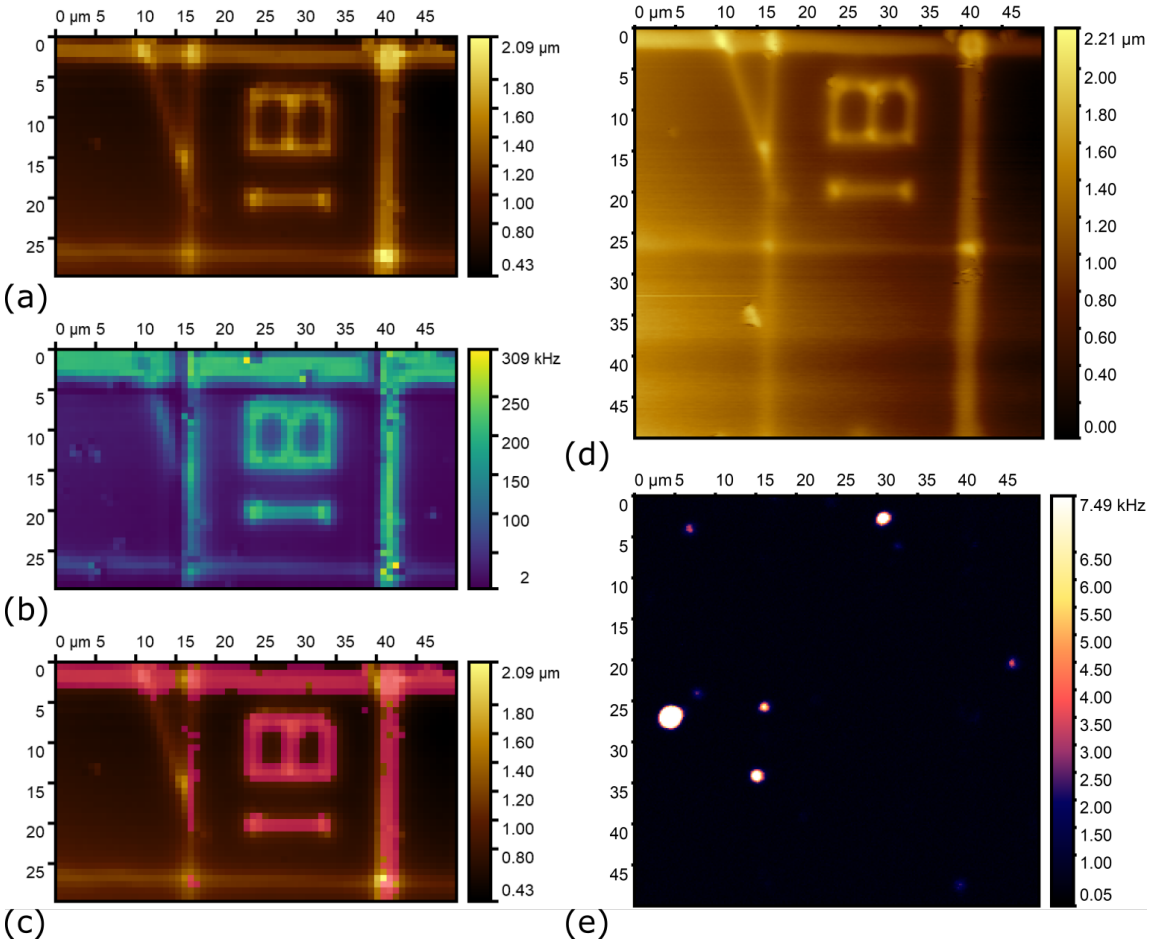

Figure 4.14: (a) Topography image of patterned silicon samples with nanodiamond deposition, (b) simultaneously recorded confocal reflectance measurement. (c) Mask produced from (b) overlaid on (a) showing offset off confocal and AFM measurement, $\Delta x \leq 1\,\mu\text{m}$, $\Delta y \leq 1\,\mu\text{m}$. (d) and (e) show simultaneously recorded topography and confocal PL measurement with offset shown in (a)-(c).

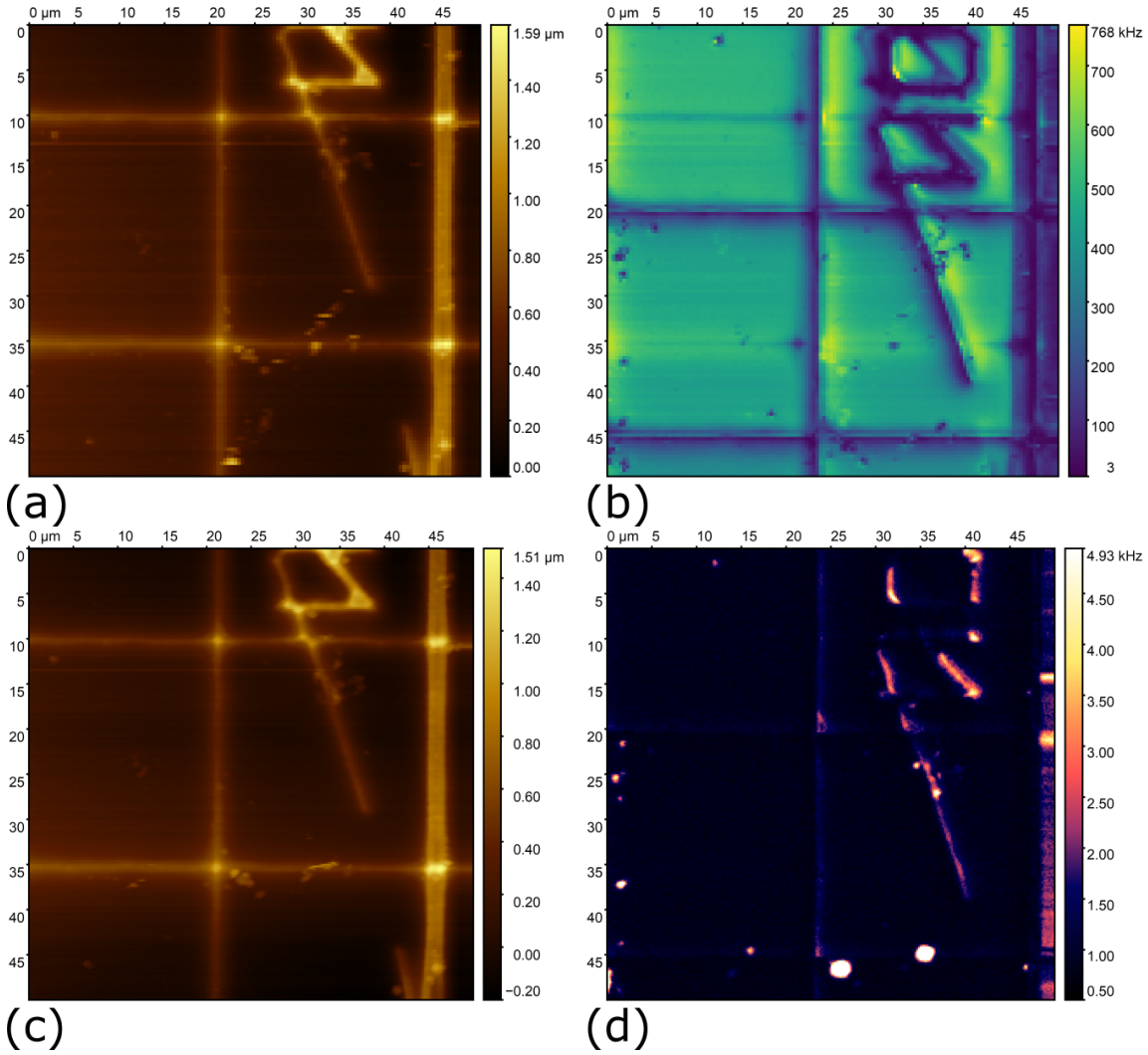

Figure 4.15: Tapping mode AFM images with offset confocal microscope images recorded simultaneously, sample is silicon/silicon dioxide with nanodiamonds deposited on the surface (offset: $\Delta x \approx 2\,\mu\text{m}$ and $\Delta y \approx 11\,\mu\text{m}$) (a) Topography image in same measurement integral time as confocal reflectance image (b). The reflectance image is used to calculate the offset between the confocal and AFM measurements. (c) topography image recorded while recording PL confocal image, shown in (d).

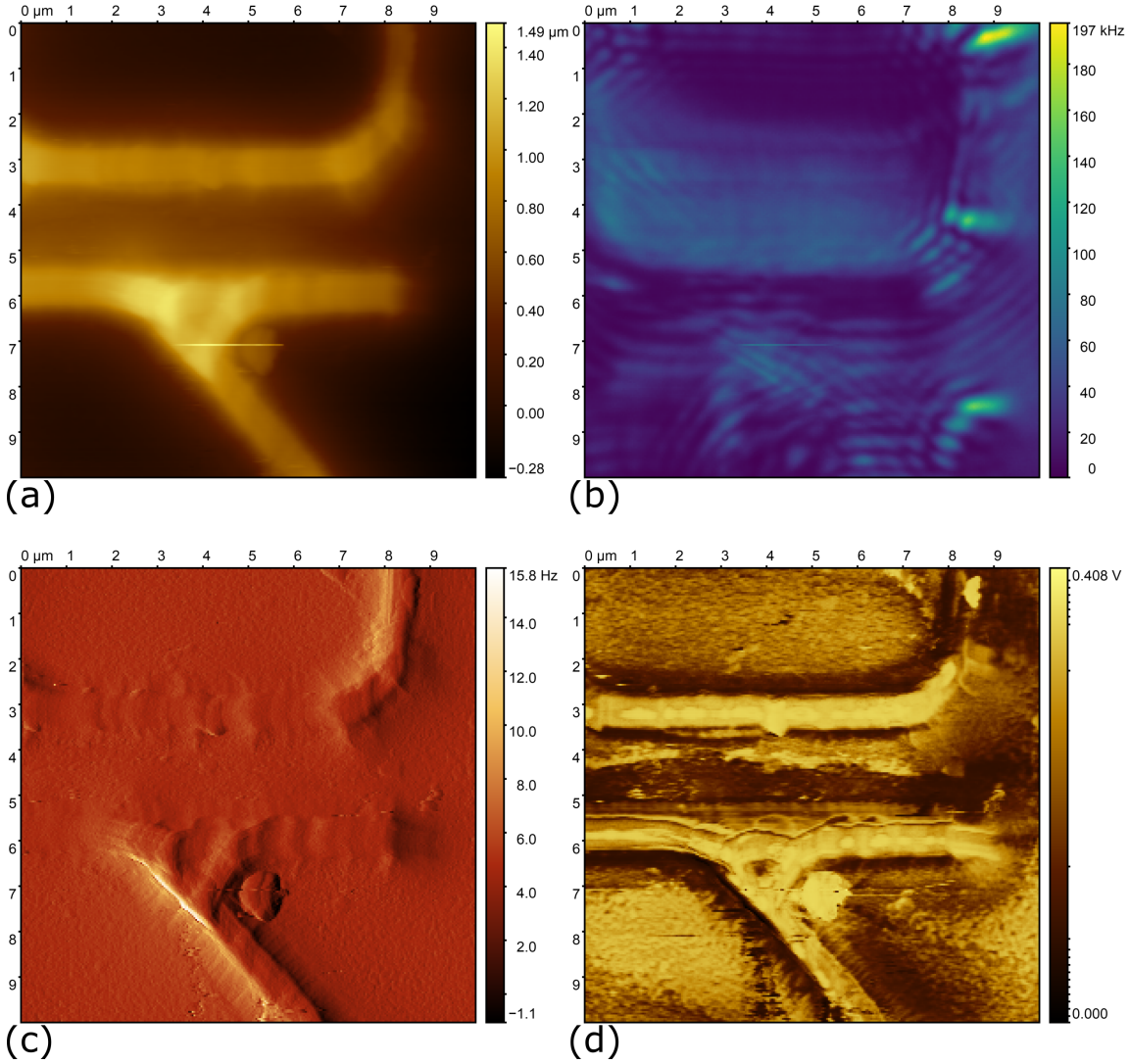

Figure 4.16: Simultaneous AFM/confocal images of patterned silicon/silion dioxide wafer with AFM/confocal (offset $\Delta x \approx$ -1 µm and $\Delta x \approx 3$ µm) with AFM operated in FM-AFM mode with constant drive (a) FM-AFM topography image, (b) reflectance mode confocal image (c) df, which corresponds to how far the frequency is shifted from the set point upon arrival at the pixel (d) PLL amplitude, corresponding to probe oscillation amplitude.

4.6 Summary

To summarise an AFM has been constructed to use Akiyama probes for dynamic AFM measurement which has been shown to record topographical measurements in ambient conditions with a z resolution of 3 nm. The AFM coarse positioning stages enable accurate positioning of the 50 µm by 50 µm by 50 µm scan range at any position within the 12 mm travel range of each axis in the positioning stages. The nanoscale vertical resolution shown demonstrates the ability to image even atomically thin samples characterisation of samples on the nanoscale, even if the performance is not at the cutting edge of AFM performance. The resolution demonstrated highlights the suitability of the constructed AFM for use as the scanning probe element in the NV magnetometer, giving nanoscale xyz resolution and a substantial vertical range of measurement. The large 50 µm z range will facilitate the measurement of magnetic fields above targets to produce 3D magnetic field maps. The z range of the scanning stages enables larger z range scans for magnetic field imaging than would be possible with the shorter range seen in commercially available AFMs.

A dual imaging mode has been presented showing the simultaneous AFM and confocal microscope operation with a tunable offset between the imaging modalities. The development of a dual AFM/confocal mode enables the investigation of samples with localised luminescence regions as well as producing an autofocus effect maximising optical collection efficiency over wide range of confocal scans. The dual imaging mode circumvents the challenge of aligning a nanoscale region of interest on a macroscopically sized sample on two separate instruments. The final advantage associated with the dual imaging mode is the timing separation is significantly lower than using independent instruments enabling the measurement of changes of topography and structure in unstable optical devices.

The immediate future work for the scanning probe instrument is to implement the AFM system to raster scan an NV centre with nanometer separation above a magnetic field source for scanning probe magnetometry. The scanning NV probe can either be a functionalised Akiyama probe with nanodiamond grafted to the tip [44] or commercially available probes with an Akiyama footprint [63]. The resolution limit could be investigated more thoroughly,

isolating the dominate components to the z noise and implement hardware changes if necessary. The development of a dual AFM/confocal mode enables the investigation of new samples displaying regions of localised luminescence. To improve the simultaneous imaging mode the offset needs to be more accurately measured and set using the closed-loop stages as discussed above. Future works also include the investigation of samples that would be of interest for the dual imaging mode. To conclude a custom AFM has been constructed showing compatibility with optical measurements, representing the ability to perform scanning probe NV magnetometry with a suitable probe. The final stage in instrumental development to perform scanning probe magnetometry is developed the final instrumentation required to observe optically detected magnetic resonance, e.g the application of an oscillating magnetic field for spin state manipulation and a bias field, this is discussed in the following chapter.

Chapter 5

Optically Detected Magnetic Resonance

5.1 Introduction

Chapter 3 demonstrated that the instrument can selectively excite optically active defects in nanodiamonds and then detect the subsequent photoluminescence photons. Chapter 4 then showed the functionality of the scanning probe component of this instrument, demonstrating the ability to scan a probe with nanometer precision while simultaneously recording confocal data. The final hardware components to realise a scanning probe NV magnetometer are a means to deliver a high-frequency oscillating magnetic field, referred to as microwave magnetic field, for coherent control of the NV centre spin state and a method of applying a static bias field. The delivery of precisely controlled microwave radiation to an NV centre combined with the optical preparation/readout provided by the confocal microscope completes the instrumental requirements to simply optically detect magnetic resonances (ODMR) from the NV centres. The static bias field enables high-sensitivity magnetic field detection while the application of a bias field with variable strength and orientation facilitates the identification of an arbitrarily orientated NV centre axis hosted in bulk or nanodiamonds.

This chapter demonstrates the functionality of the instrument for its intended purpose - optical detection of magnetically sensitive spin resonances. Firstly, instrumentation to deliver the MW radiation to NV centres addressed by the confocal microscope will be presented. The performance of the microwave instrumentation will be shown later in the chapter by presenting continuous-wave ODMR spectra (CW-ODMR) from photoluminescent nanodiamonds. The design of a magnet mount is then presented, facilitating the application of a magnetic bias field along an arbitrarily chosen radial direction (with respect to the confocal microscope focus) at a range of strengths. Following the assembly of MW and bias field instrumentation, the first recorded ODMR spectra from this instrument are shown from emitters in nanodiamonds.

5.2 Design of the Microwave Circuit

To perform magnetic field sensing with NV centres an oscillating magnetic field is required to drive the transitions between the $m_s = 0$ and $m_s = \pm 1$ ground state sublevels. In the low crystal stress diamonds used for magnetometry the frequency that drives both the $m_s = 0$ to $m_s = \pm 1$ sublevel transitions is given by D, corresponding to 2.87 GHz when there is no magnetic field along the NV centre axis ($B_z = 0\,\mathrm{mT}$). To generate this magnetic field, referred to as MW magnetic field, a microwave circuit was produced to address the following design requirements:

- Produce large amplitude ($\sim$0.1-1 mT [2]) oscillating magnetic fields close to the zero magnetic field resonance of NV centres, $D = 2.87\,\mathrm{GHz}$.
- Capability for fast switching with phase control for the pulsed application of microwaves for high-sensitivity detection.

The circuitry for the synthesis of high-frequency currents for the MW magnetic field generation is common to many instruments investigating NV centres, typically consisting of a synthesiser, high power amplifier and fast switches for timing control. However,

the resonator structures attached to the output of the high power amplifier generating the MW magnetic field at the location of a target NV centre varies greatly; with single wires [133], small loops [134] and double split-ring resonators [135] commonly used. The choice of structure is set by the application, with common goals of easy fabrication and implementation, while maximising the available power in the MW magnetic field at the NV centre position. The necessity of high power in the MW field for magnetometry can be demonstrated by considering the MW power dependency of the magnetic field sensitivity. For example, in CW-ODMR, the sensitivity is maximised by increasing the contrast of the resonances while reducing the linewidth of the ODMR resonances, with both parameters highly dependent on the power of the microwave field [35]. While in magnetic field sensing protocols using pulsed measurements, a high power magnetic field can reduce the duration of pulses required for spin state manipulation. The spatial profile of the produced MW field must also be considered, when sensing with single NV centres, the spatial profile is related to the power consideration and sets the accuracy in which the MW source and the NV centres must be positioned relative to each other. When sensing with multiple NV centres inhomogeneity in the MW field can increase the dephasing of the spin and therefore decrease the sensitivity of large ensemble detectors which average the signal over many NV centres [136]. However, MW field inhomogeneity is less of a consideration for scanning probe techniques utilising few spins. A more complete discussion of different resonator structures can be found in the following references [137, 138].

It is common for many instruments centred on NV centre scanning probe magnetometry to use small wires to generate the MW frequency oscillating field, including in one of the first commercially available instruments manufactured by Qnami [70]. The advantage of thin wires structures to generate the MW field relates to their ease of fabrication and implementation. The thin wire approach can generate high power MW fields in close proximity to the wire, however, the power of the field falls off rapidly with increasing distance from the wire. As a result, the wire needs to be positioned relative to the NV centre with micron-scale precision, presenting an experimental challenge for scanning probe techniques and a limit to the area in which ODMR can be observed from dispersed NV

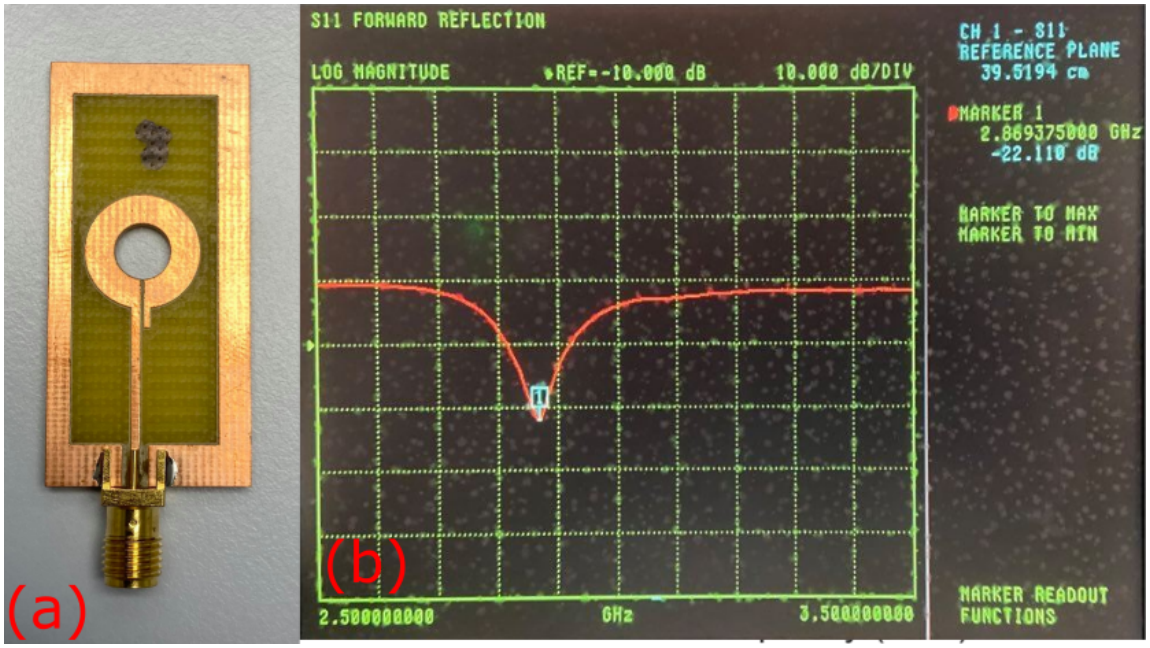

Figure 5.1: (a) Picture of planar microwave antenna used to produce the microwave frequency magnetic field at the focus of the confocal microscope. (b) The power transmission of the microwave antenna at a range of frequencies centred on the zero-field resonance of the NV centre ground state. The Q factor is equal to ≈ 10 and the bandwidth $\approx 250\,\text{MHz}$, with the peak response centred on the zero field resonance 2.87 GHz

centres on a substrate. Additional disadvantages associated with the use of thin wires include unwanted sample heating and a high risk of disconnection from the MW source [139]. An alternative structure to thin wires is a planar antenna, which compared to simple coil and wire-based structures have been demonstrated to produce stronger fields over larger areas for efficient coupling to NV centres [135, 139]. This instrument uses a planar antenna to produce the MW magnetic field as the antenna is mechanically robust and produces high power magnetic fields over large areas, removing the need for an additional microscale positioning element to accurately locate a wire close to the scanning probe.

The antenna was produced to have a peak response at 2.87 GHz, with a quality factor, $Q \approx 10$ and bandwidth of $\approx 250\,\text{MHz}$. The Q factor of 10 represents a trade-off between the maximum power available and the bandwidth. For example in a study by Bayat et al, a resonator with a $Q = 70$ was found to increase the power output, however, the

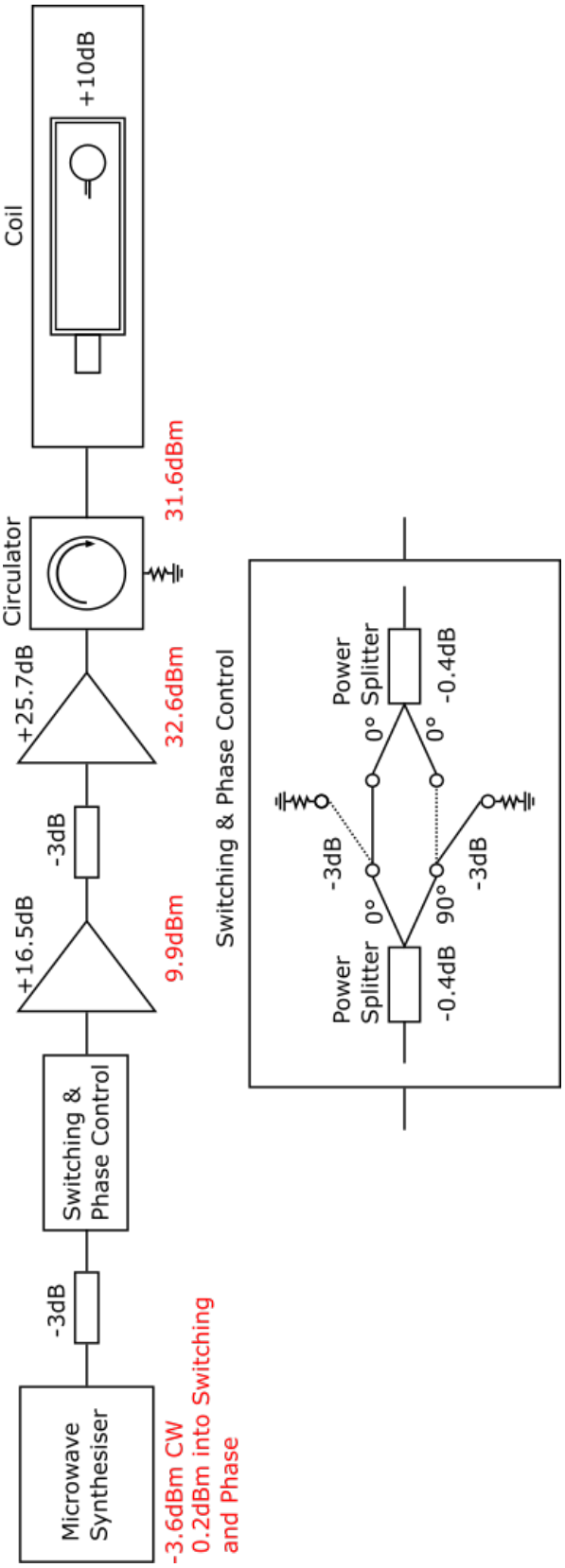

Figure 5.2: MW synthesiser signal is first delivered to the switching and phase control circuit, which is shown in a separate diagram below. In the switching and phase control circuit, power splitters and fast microwave switches are used to control the phase of the transmitted signal either at 0° or 90° to the input signal. The phase and switching circuit is shown separately as this circuit is removed from CW-ODMR experiments for simplicity. The maximum power at the output of key components is shown in red. A series of 3dB attenuators are used to minimise the risk of reflections in the circuit without limiting maximum power output.

corresponding bandwidth, BW = 40 MHz, resulted in only one of the two NV centre resonances observable at once. However, the frequency of the peak response could be varied via tunning the response of the resonator using copper tape [135]. The 250 MHz bandwidth of the antenna used in this instrument is equivalent to Zeeman shift of the NV centre resonances due to on-axis magnetic field of 4.2 mT. The central aperture of the antenna is 6 mm, with the magnetic field produced designed to be spatially uniform within this region. A picture of the antenna is shown in figure 5.1, along with the S_{11} parameter, which characterises the insertion loss, at a range of frequencies close to the zero-field resonance value, D = 2.87 GHz. The S_{11} parameter parameter was measured using a Wiltron 37217B vector network analyser (VNA).

The diagram of the microwave circuit used for ODMR experiments is shown in figure 5.2, with gain and max output power at each component stated. The MW signal is first synthesised by a Berkeley Nucleonics synthesiser (model number: 835), with an output frequency resolution of 1 mHz. The signal from the synthesiser is directed into a switching and phase control circuit consisting of a series of switches (Mini_Circuits ZASWA-2-50DRA+) and power splitters (Mini_Circuits ZAPDQ-4+ and ZAPD-4-S+) to enable short phase-controlled MW pulses at the output. The phase control circuits produce an output either 0° or 90° relative to the input to be transmitted, with the output controlled by switches (Mini_Circuits ZASWA-2-50DRA+) toggled with a TTL control signal with a 20 ns switching time. The switching and phase control circuit is shown as a subsection in figure 5.2 as this circuit is removed for CW-ODMR experiments, to simplify both the circuit and the experimental control, removing the need to generate the switch TTL signals. The output of the switching and phase circuit, or simply the synthesiser for CW-ODMR then provides the input for two amplifiers, acting to maximise the strength of the MW field at the scanning probe position. The first amplifier (Mini-Circuits ZX60-4016E-S+, gain 16.5 dB) ensures that the maximum power is always available at the input of the high power amplifier (Mini-Circuits ZHL-4W-422, gain 25.7 dB). The signal from the high-power amplifier is delivered via an isolator, to a planar ring antenna. The isolator prevents reflections from returning to the amplifier. A series of 3 dB attenuators are also placed between compo-

nents in the circuit to minimise reflections. The power produced by the planar antenna is limited by the output of the high power amplifier, 32.6 dBm. Assuming a 1 dB insertion associated with the isolator, and negligible losses due to the antenna, the max input power to the coil is 31.6 dBm. The Q factor of the antenna amplifies the signal by a factor of 10, giving an effective maximum power in the antenna of 41.6 dBm or 14.45 W. The planar antenna offers a high power oscillating field over a large area. However, the antenna can easily be swapped for a thin wire should this appropriate for the application. A thin wire approach may be beneficial when the magnetic field produced by micron-scale conductors is the target of the measurement as there is no longer the challenge of locating the sensing NV centres close to both the MW source and the target.

5.2.1 Sample Holder

The planar antenna produces the strongest magnetic field just above the surface of the central aperture. To ensure the maximum available MW field strength at the microscope focus/NV centre a sample holder was produced to locate the sample, the antenna and the MO in the optimal position relative to each other. The following design considerations for the sample holder were identified; the sample must be held rigidly in microscope objective (MO) focal plane and located at the centre of the antenna aperture, maximising both the MW field strength and the size of the area imaged with efficient microwave NV coupling. The holder was also designed to locate the sample as close to the antenna surface as possible, also with the aim of maximising the available magnetic field strength. The final design consideration was to limit the impact of the sample holder on the antenna operation, either by modifying the response of the coil or screening the produced magnetic field.

A 3D representation of the sample holder and how the constituent parts are assembled is shown in figure 5.3(a) and 5.3(b). The holder consists of two components; An aluminium post to fix the antenna to the sample stages, facilitating the positioning of the antenna relative to the confocal microscope and the second component a macor® disk which secures to the aluminium post. The disk holds the antenna in place on the post and locates the

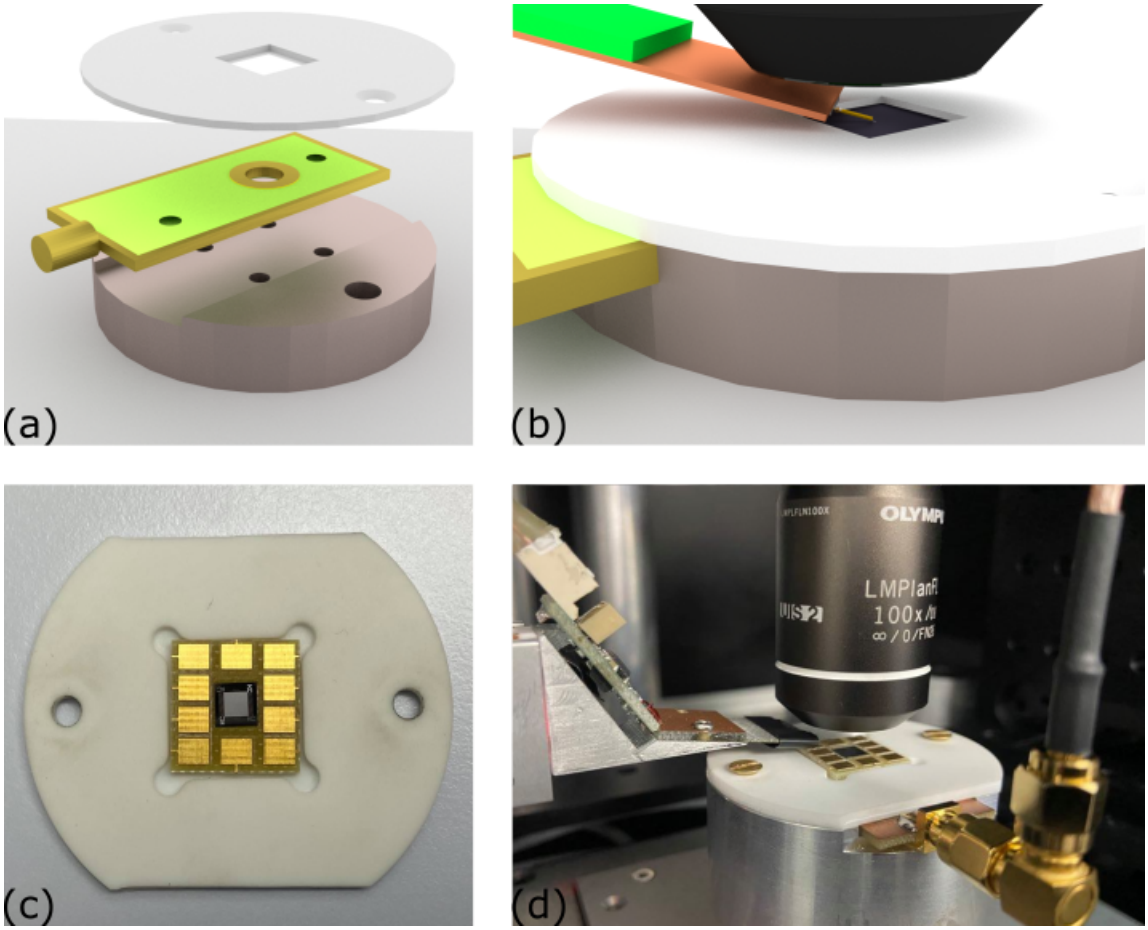

Figure 5.3: (a) 3D design showing components of microwave coil sample holder. An aluminium post is milled so the antenna can sit flush to the surface with the aperture centred on the post. Finally, a macor® disk screws on to post to secure antenna in place. A recess is milled into the centre of the disk to secure a sample directly above the antenna aperture with minimal sample-antenna distance. (b) 3D model showing assembled sample holder underneath the confocal objective lens with the AFM probe at to the focus (c) Picture of the macor® disk with sample, in this case 15 mm by 15 mm PCB designed for samples with electrical connections. (d) Image of assembled sample holder.

sample above the antenna aperture via a central recess milled into the disk. Macor®, a machinable glass ceramic, was chosen as for the disk material due to the ease of machining and low conductivity [140], limiting the effect of the holder on the resonant frequency of the antenna and reducing the potential for screening of the MW field. The recess is milled (from 2 mm thickness down to 0.1 mm) into the centre of the disk to hold the sample, with a further 6 mm diameter aperture cut to further limit the area of the antenna covered by the disk, with the aim of reducing screening. A range of disks with differently sized recesses to accommodate sample of common sizes, e.g 15 mm by 15 mm, were produced. The disk with a sample located in the recess is shown in figure 5.3(c), the assembled sample holder is shown in figure 5.3(d).

5.3 Magnetic Bias Field

Static magnetic bias fields are often applied during NV centre experiments for two main purposes. In NV centre magnetometry, the application of a bias field allows the Zeeman term to dominate the ground state Hamiltonian so that the strain and electric field terms can be neglected [34] thus simplifying data analysis. The application of a bias field also allows small Zeeman shifts to be detected that would otherwise not be resolvable due to the close spacing of the resonances associated with the both $m_s = 0$ to $m_s = \pm 1$ ground state transitions at low magnetic fields. The spectral separation of the resonances allows a single transition to be addressed with the application of a given MW frequency.

The application of a static magnetic field is also crucial in enabling vector magnetometry, facilitating the calculation of the NV centre quantisation axis, and therefore the sensing axis, in the laboratory reference frame. The orientation can be determined through the sequential application of a range of static magnetic field strengths and orientations to the NV centre axis, inferring the orientation from the change of the ODMR frequencies [36, 44].

With the goal of determining the NV centre quantisation axis and the application of

a static field for high-sensitivity magnetometry, the following design requirements for bias field instrumentation were identified:

- Produce stable magnetic fields in the few mT range.
- Produce a variable field strength at the confocal microscope focus.
- Produce a variable orientation of the bias field at confocal microscope focus.

To produce the bias magnetic fields two methods are commonly employed, generating magnetic fields with current-carrying wires and by positioning a rare earth magnet close to a region of interest. To control the direction of the applied bias field using current-carrying wires a variety of coil geometries can be used, including a 3 axis Helmholtz configuration [38, 141]. The advantage of using coils over permanent magnets is associated with the ease in which the field direction and strength can be changed - simply by changing the current magnitude and direction within each coil pair. However, the magnitudes of the fields required for NV centre bias fields, in the few mT range, can require large currents for the large open coil systems required for AFM/optical axis. In addition to the physical constraints, a more fundamental limit to bias fields produced by wires is associated with the AC noise on the currents [142], limiting the precision in the produced bias field. Permanent magnets offer a more stable approach to producing bias fields, with the strength and orientation of the field at a target controlled by physical translation and rotation of the magnet. In this instrument bias fields are applied to NV centres via permanent magnets attached to a home-built rotational mount. The magnet can be rotated about the confocal microscope focus to produce a range of field orientations at the focus. The magnitude of the bias field can be varied at any given orientation via radial translation of the magnet using a linear component in the mount.

5.3.1 Bias Magnet Mount

This following section describes the design and construction process of a 3D permanent magnet mount. The magnet mount was designed to maximise the range of magnetic

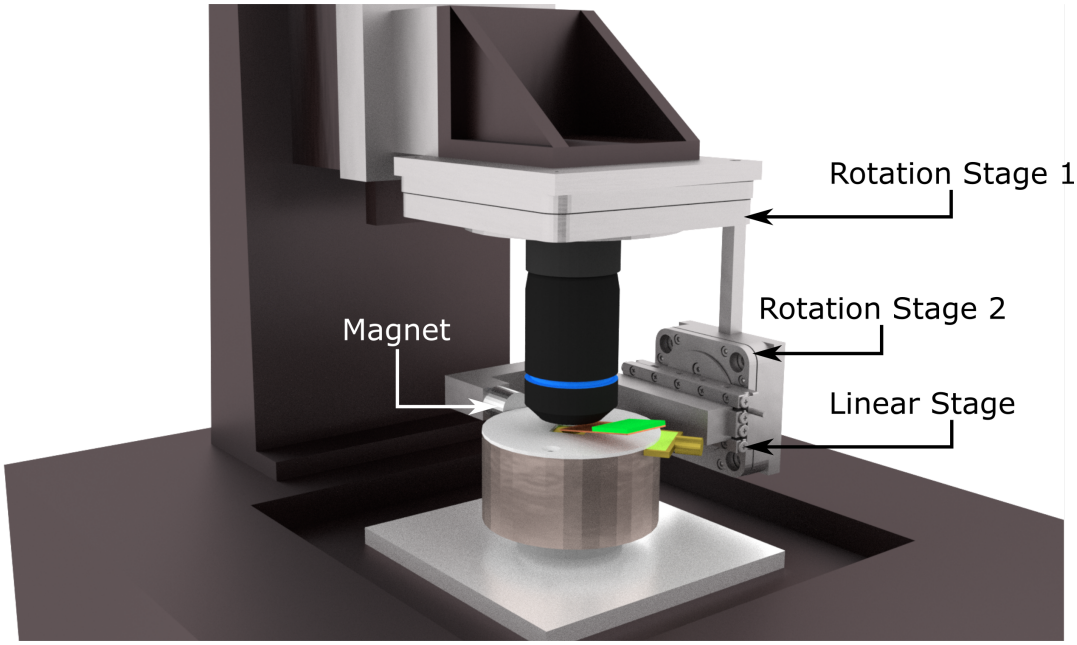

Figure 5.4: 3D model of magnet rotation mount mounted to the microscope supporting structure. The green and copper represents part of the AFM circuitry (preamplifer PCB) - the supporting structure of these elements is omitted for clarity.

field orientations, produced by rotation of a permanent magnet, and to maximise the range of field strengths, produced by magnet translation, at the microscope focus/NV centre position. In the following description of the rotational instrumentation the axis of motion refers to the lab reference frame, with the axes labelled as x', y', z' along with the corresponding polar and azimuthal angles θ', ϕ' to differentiate between NV centre axis labelling. In this coordinate system, the origin is at the microscope focus/NV centre.

The rotational components of the mount are provided by two slip-stick stages. The first rotation stage (Smaract SR-7012), labelled Rotation Stage 1 in figure 5.4, has a central aperture to allow the objective lens to pass through to reach the required position for imaging. This first stage provides the rotation, ϕ', around the z'-axis with a closed-loop resolution of 15 µ°. A second rotation stage (Smaract SR-4011), labelled Rotation Stage 2 in figure 5.4, rotates around the x'-axis and provides the variation in the polar angle, θ', also with a closed-loop resolution of 15 µ°. A linear stage (Smaract SLC-1750), labelled as Linear stage in figure 5.4, is used to translate the magnet along a chosen axis with a range

of 31 mm with a closed-loop resolution of 50 nm.

A 3D model was produced to estimate the range of motion possible when rotating and translating a permanent magnet without fouling on other instrumentation. The model also aided in the design of brackets to connect the components of the rotation mount. Figure 5.5 demonstrates the rotation of the magnet produced by the two rotational stages. The rotation around the z' axis is limited by the AFM support structure, with ϕ' variable over a 180° range. Rotation θ' around the x' axis is limited by the objective lens and can be varied over the range 40°-90°.

The permanent magnet attached to the mount to produce the bias field can easily be added and removed to change the dynamic range of the magnetic field produced. The closest the magnet can be positioned is set by the width of the sample holder, 25 mm, with the furthest distance then given by the range of the linear stage corresponding to31 mm. The magnet position can therefore be accurately controlled with a minimum magnet face - microscope focus separation of 25 mm and a maximum separation of 56 mm. The magnetic field along the axis of symmetry (referred to as the u-axis to avoid labelling this axis in the lab co-ordinate system) of a cylindrical magnet is given by

$$B_u = \frac{B_r}{2}\left[\frac{u}{\sqrt{(u^2+R^2)}} - \frac{u-L}{\sqrt{((u-L)^2+R^2)}})\right] \tag{5.1}$$

where B_r is the residual magnetisation, a material property and u is the axial direction, joining the centre of the magnet face to the microscope focus [144]. Finally, L and R are geometric parameters defining the length and radius of the magnet respectively. The parameters L, R and the axial direction, u, are shown figure 5.7(a). This expression was evaluated for a variety of commercially available N42 Neodymium Iron Boron (NdFeB) magnets with the known sample-magnet separation provided by the mount (u = 25-56 mm). Figure 5.7(b) shows the fields produced from a selection of magnets chosen to produce bias field strengths in the few mT range.

As shown in the 3D model, figures 5.4, 5.5 and 5.6, the supporting brackets connecting

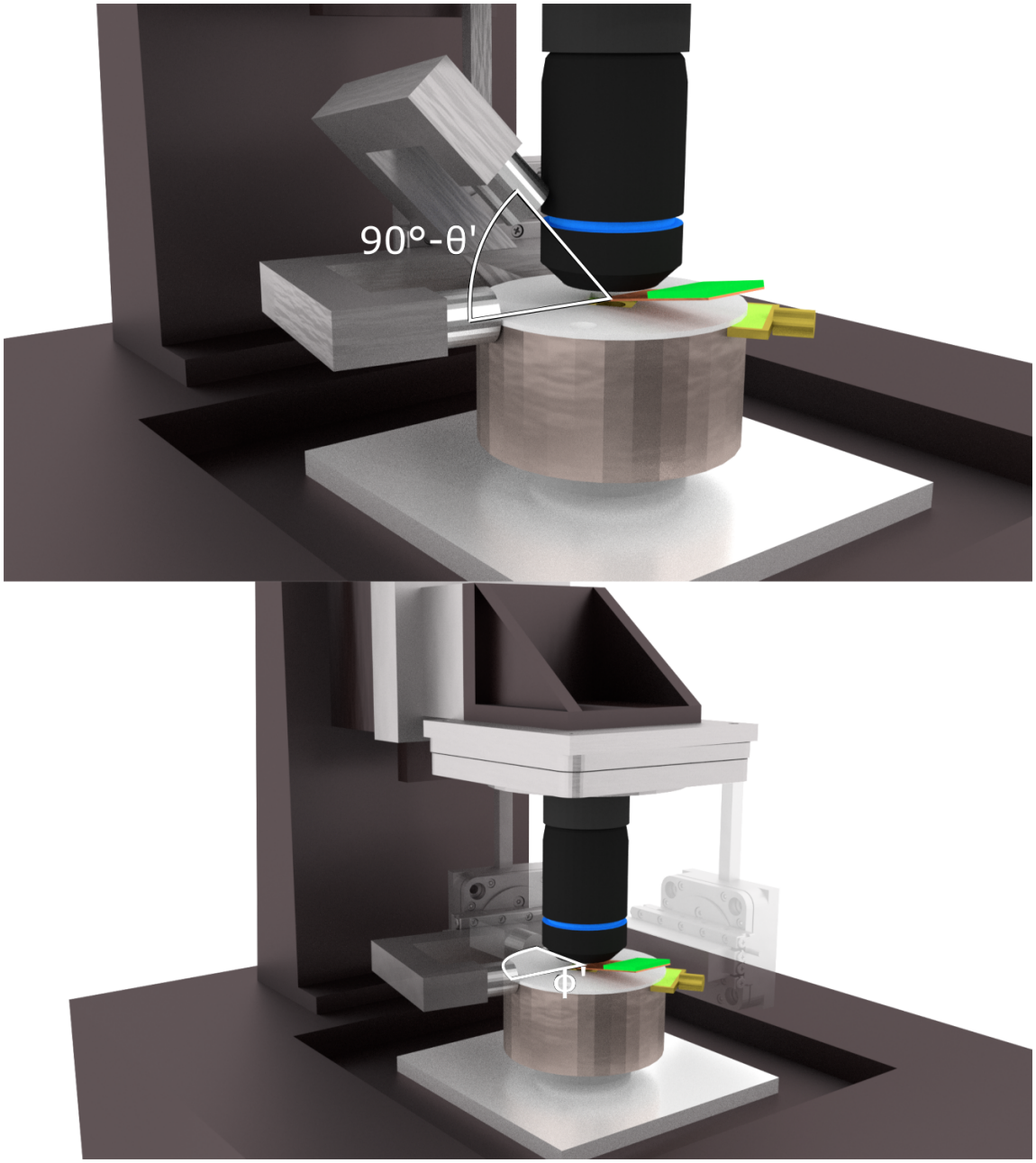

Figure 5.5: 3D model demonstrating the rotation of a permanent magnet provided by rotational stages one and two. (a) Rotation around the x'-axis, described by angle $\theta^{'}$ is generated by rotational stage 2. (b) Rotation stage 1 produces rotation around the z'-axis with angle $\phi^{'}$. The rotational angles ϕ' and θ' are limited by the AFM support structure and by contact with the objective respectively.

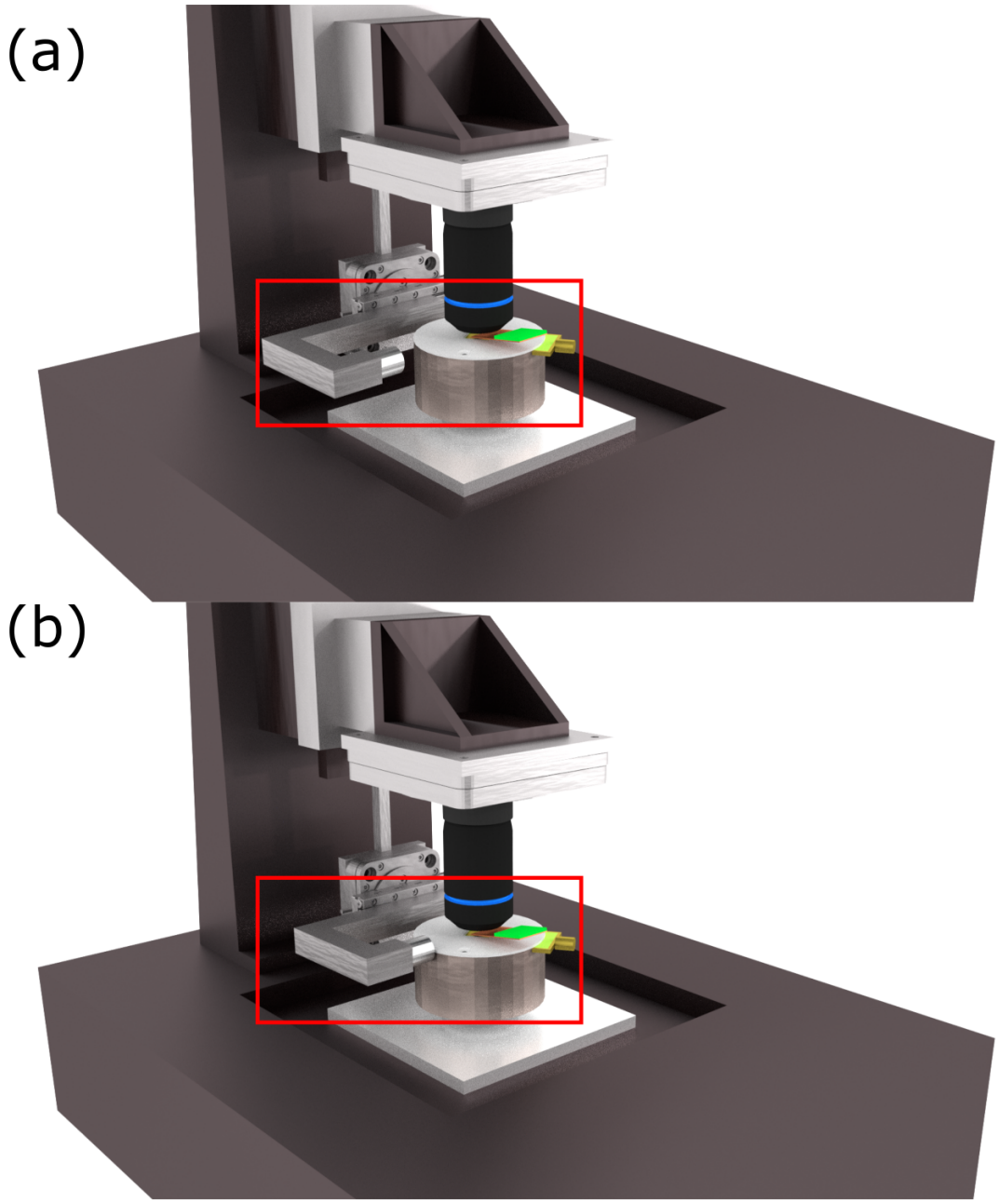

Figure 5.6: 3D model showing linear translation along a chosen axis. The translation provides an accurate means of changing the field strength for a chosen orientation. (a) The magnet is pulled back along the same axis to demonstrate the lowest magnetic field strength. (b) Shows magnet as close as possible to confocal focus, representing the strongest field.

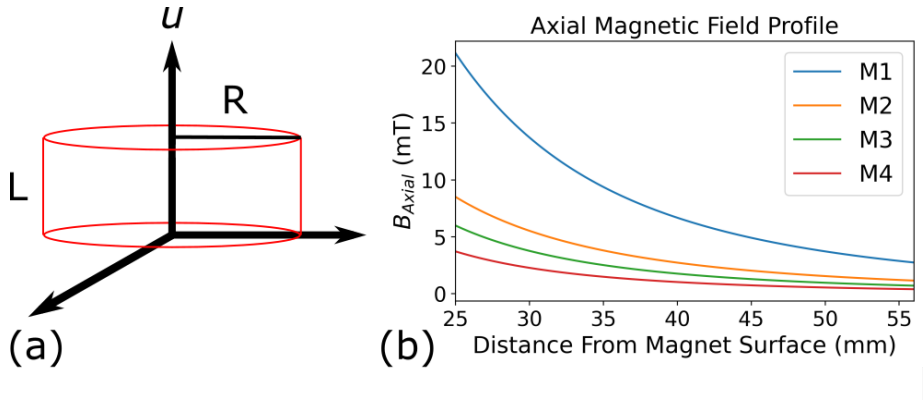

Figure 5.7: (a) Geometric parameters associated with a cylindrical permanent magnet. (b) The axial magnetic field produced by the magnet between the minimum and maximum separation offered by the mount. All magnetic line profiles are from commercially available magnets N42 NdFeB magnets [143].

NdFeB Magnets					
Figure 5.7 label	B_r(mT)	Diameter, 2R (mm)	Length, L (mm)	B_z(25mm) (mT)	B_z(56mm) (mT)
M1	1280	20	10	21.15	2.74
M2	1280	10	20	8.51	1.16
M3	1280	10	10	6.00	0.71
M4	1280	10	5	3.71	0.40

Figure 5.8: Properties of cylindrical magnets to produce bias magnetic fields at 25 mm ad 56 mm from the magnet surface in the axial direction.

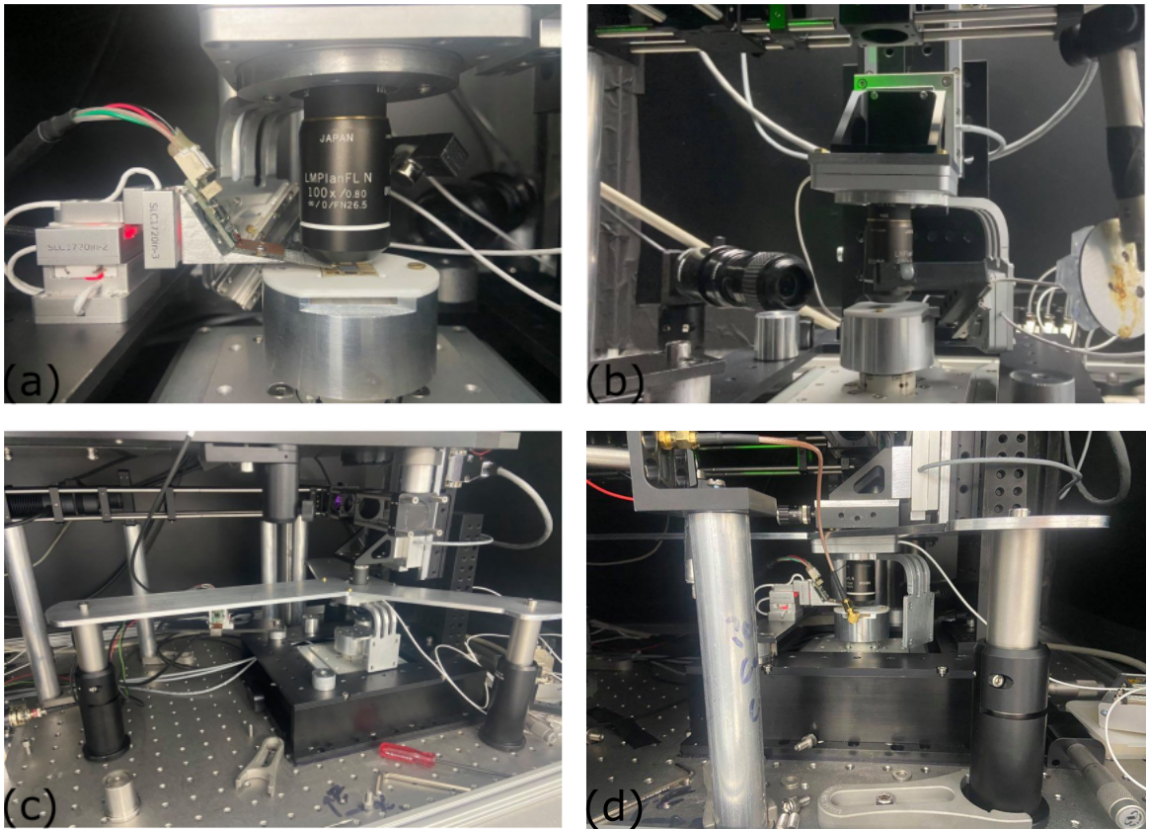

Figure 5.9: Pictures of the constructed magnet mount. (a) and (b) shows the initial configuration with the magnet mount supported on MO stage. (c) and (d) show the final configuration with the mount now supported by a custom plate. The plate was used as the confocal alignment was affected by motion of the mount supported on the MO stage.

the magnets and the slip-stick stages are mounted to the same right angle bracket that connects the MO to the microscope focusing stage. With the magnet mount and MO fixed to the same linear stage the magnet is translated with the MO and the magnet rotation origin always remains at the working distance of the MO. A picture of the rotation mount secured to the MO stage is shown in figure 5.9 (a) and (b). It was found, by monitoring the intensity of reflected light from a mirror placed at the microscope focus, that the rotation of the magnet translated the MO pupil position, causing the confocal microscope to become misaligned. To mechanically isolate the magnet rotation mount from the MO a separate plate was constructed fixing the rotation mount to the optical bench. The origin of rotation is translated along the optical axis using three variable height posts (Thorlabs model number: RSH4/M). The rotation mount with the separate mounting plate is shown in figure 5.9.

5.4 CW-ODMR

5.4.1 Nanodiamonds

The first demonstration of CW-ODMR using this instrument focused upon examining photoluminescent nanodiamonds deposited on a silicon wafer substrate, this sample was prepared by Ben Wood at the University of Warwick. In addition to the targeted NV centres, nanodiamonds can host a wide range of optically active defects [21]. To distinguish between NV centres and other PL sources the sample is first scanned at high laser power ($P \approx 5\,\mathrm{mW}$). The high power scan aims to photobleach other PL sources while NV centres are largely expected to remain unaffected by the process due to their photostability [145]. The PL or reflectance signal can also be recorded during the long ($t_{scan} \approx 1\mathrm{hr}$ for $50\,\mu\mathrm{m}$ by $50\,\mu\mathrm{m}$) bleaching scan to provide complementary information on the sample. The sample is then imaged at a moderate laser power ($P \approx 250\,\mu\mathrm{W}$) to identify PL sources from the nanodiamonds on the sample, an example image is shown in figure 5.10(a), with reduced xy range images showing emitters that were investigated further in figure 5.10(b),(c) and

(d). Once an emitter was identified the excitation power - PL relationship was evaluated by applying a range of laser powers and monitoring the PL. The saturation power was determined by fitting the following relation

$$N_{ph} = \frac{N_{sat}}{1 + P_{Sat}/P} + mP \tag{5.2}$$

where N_{ph} is the photon count for at excitation power P. The saturation flux is denoted by N_{Sat} and m is a factor that accounts for background emission [106]. Figure 5.10(e) shows the saturation curve for the PL sources shown in confocal images 5.10(b), (c) and (d).

To perform CW-ODMR measurements on target emitters data acquisition was synchronised with the MW application via a multi-function NI card (PCI 6323), which was used to record the SPAD count rate and generate timing signals for MW application. To interface with the NI card a Python suite, Qudi, produced by the University of Ulm [82] was used, in particular the ODMR sequence.

The Qudi package is modular in nature allowing simple integration of different hardware components for complex experimental sequences without changing the base code. A simple experiment in the Qudi package has a script that defines the sequence of commands for an experiment, which referred to in the Qudi package as a logic file, a script to generate a graphical user interface (GUI) for to parameters to any hardware and finally a separate script for each hardware component used in an experiment. The package provides a template for a hardware file of a given type, e.g 'Microwave generator' that consists of the functions that must be defined for a users hardware to be compatible with the experimental logic and GUI. Due to time constraints, a hardware file was not written for the microwave generator. However, Qudi ODMR routine was utilised for ODMR experiments by directing the counting gate signal produced by the NI PCIe-6323 card to an output terminal. The output signal was used to trigger a digital pulse generator (Swabain Pulse Streamer), which was programmed to generate digital triggers for the microwave circuit control. The trigger signal was used to increment the frequency generated by the microwave synthesiser

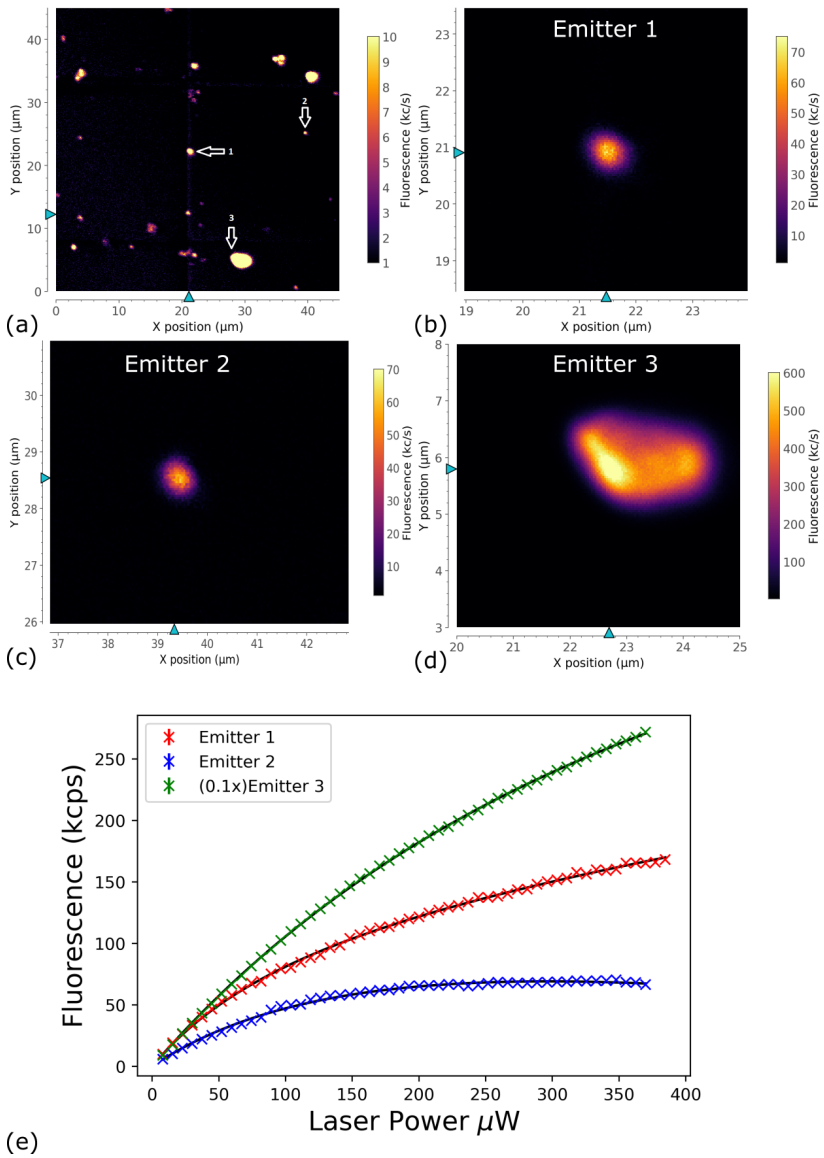

Figure 5.10: Confocal PL scan of nanodiamonds on silicon/silicon dioxide substrate to identify target emitters for ODMR experiments. (b),(c) and (d) show Emitters 1, 2 and 3 respectively in higher resolution images used to optimise the position of the diffraction limited measurement volume prior to ODMR experiments. (e) shows the change of the PL signal with laser power for the emitters shown in (b), (c) and (e). The crosses show the recorded data and the black lines are a fit based on equation (5.2), with saturation values $P_{sat1} = 130 \pm 10\,\mu W$, $P_{sat2} = 260 \pm 25\,\mu W$, and $P_{sat3} = 600 \pm 40\,\mu W$ respectively. Note: Emitter 3 signal in (e) is a shown factor of ten lower than the true value as a ND = 1.0 filter was inserted into detection path to avoid saturation of the detector.

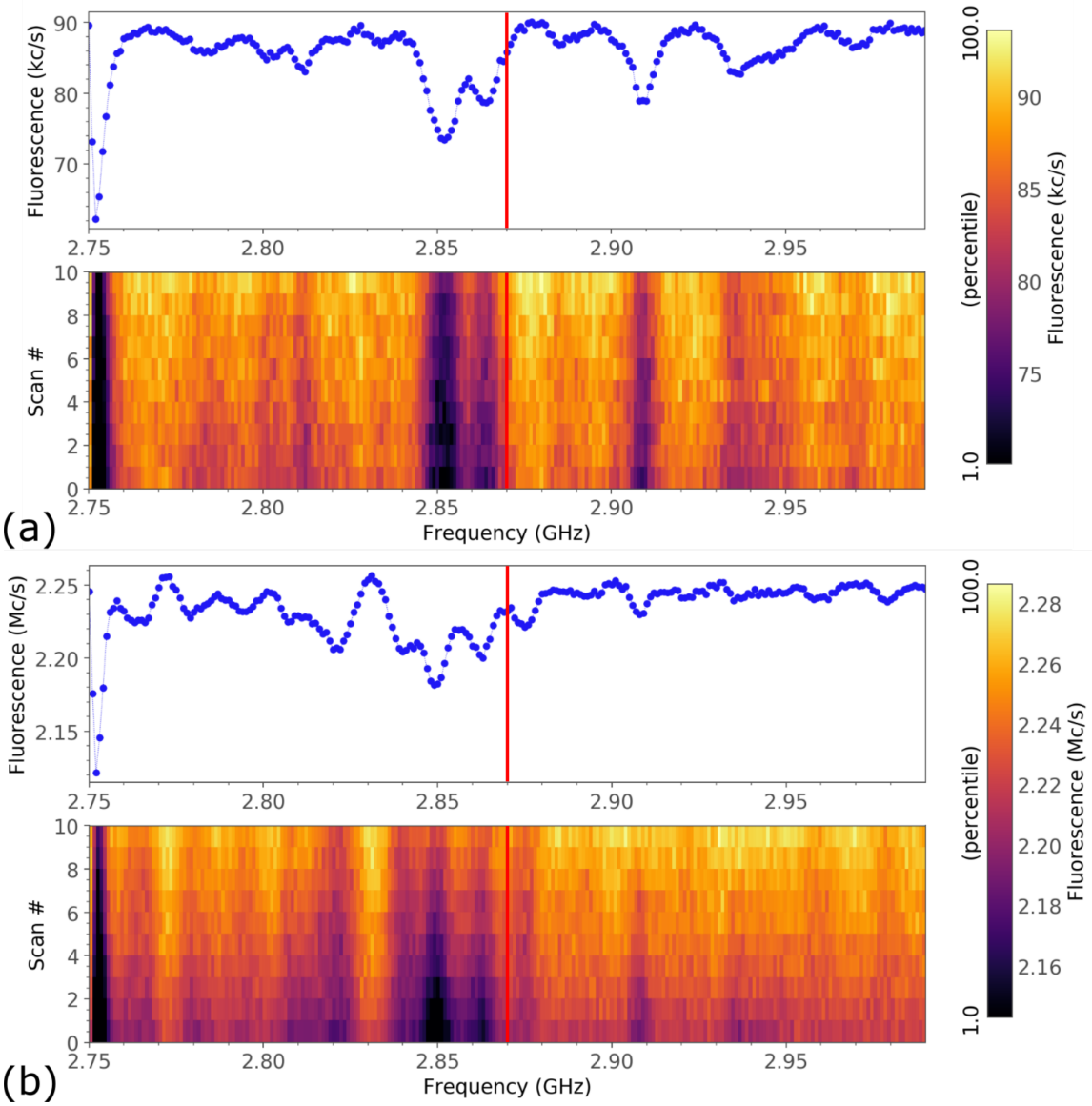

Figure 5.11: (a) CW-ODMR from nanodiamond emitter 1, $P_{Laser} = P_{sat}$, the input power to the antenna $P_{MW} = 1.32\,\mathrm{W}$. The line graph shows the average of ten frequency sweeps, with each sweep contributed to the average measurement shown below the line graph. (b) CW-ODMR from nanodiamond emitter 3, $P_{Laser} = P_{sat}$, $P_{MW} = 1.32\,\mathrm{W}$. Figures (a) and (b) were both recorded with zero bias field applied. The scans are centred on 2.87 GHz, shown in red, which corresponds value for both the $m_s = 0$ to $m_s = \pm 1$ transitions of the NV centre ground state at very low magnetic fields..

over a range set via the front panel. Using the Qudi ODMR sequence facilitates the use of the Qudi's confocal routines to optimise the x, y and z position of an emitter relative to the MO immediately before ODMR measurements. The routing of the NI counting gate signal to digital pulse generator control a pre-programmed MW synthesiser represents a time-efficient and easily customisable approach to ODMR experiments, benefiting from Qudi's experimental logic and compatibility with confocal optimisation routines without having to write an interface for a microwave synthesizer.

Figure 5.11 shows typical ODMR spectra from PL sources deposited onto the silicon/silicon wafer, corresponding to emitter 1 and 3 shown in Figure 5.10. The expected response for single or multiple NV centres is a decrease in PL intensity centred 2.87 GHz when there is zero bias field applied ($B_z = 0\,\mathrm{mT}$) and this behaviour was not observed in any emitters characterised. To confirm that the ODMR response was dependent on the sample, and not an artefact introduced by the response of the instrument, the effect of the microwave power was investigated by measuring the nanodiamond ODMR spectrum at a range of microwave powers. A typical ODMR response from a nanodiamond emitter is shown in Figure 5.12.

To extract the centre frequencies, line widths (FWHM) and contrasts (the PL intensity at a given frequency normalised to the off-resonance value) for each resonance observed in Figure 5.12(a), a Gaussian fit was applied, with both the fit and the raw data is shown Figure 5.12(b). The response was modelled as the sum of several Gaussians, one associated with each resonance. Therefore, to produce a model for a given emitter, the ODMR spectrum was first visually inspected to determine the number of resonances. For the typical nanodiamond spectra shown in Figure 5.12(a), five resonances were identified, and so the sum of 5 Gaussians was fitted to the data set using the MATLAB curve fitting toolbox with the Levenburg-Marquardt algorithm. Five resonances were identified with frequencies $2.8017 \pm 0.0003\,\mathrm{GHz}$, $2.827 \pm 0.002\,\mathrm{GHz}$, $2.883 \pm 0.003\,\mathrm{GHz}$, $2.8823 \pm 0.001\,\mathrm{GHz}$, $2.9227 \pm 0.0004\,\mathrm{GHz}$. The corresponding contrast of each resonance against antenna input power is shown in Figure 5.13. The increase in contrast with MW power demonstrates the suitability of the MW circuit and antenna for generating magnetic fields in the 2.75-2.99 GHz

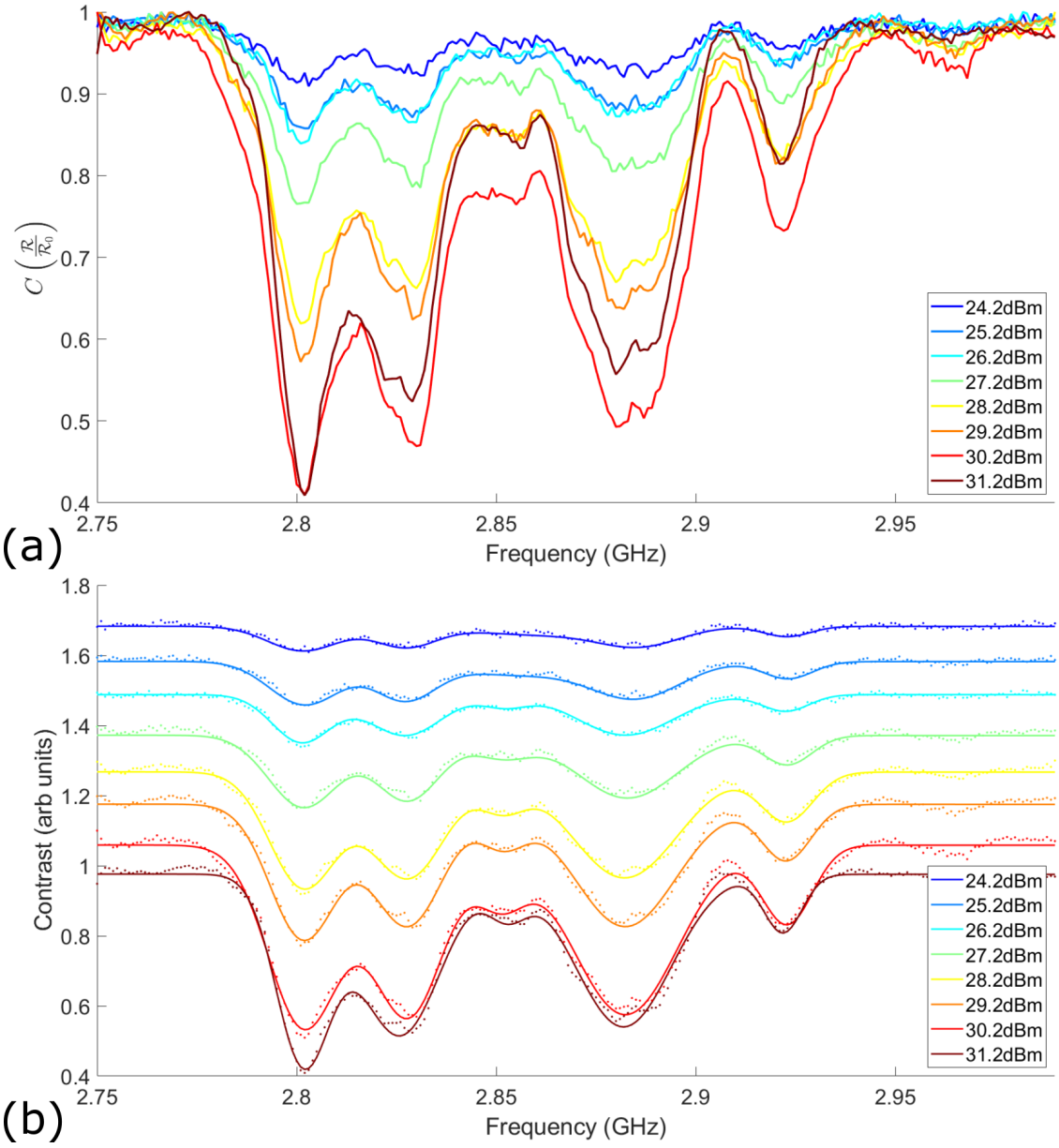

Figure 5.12: (a) Typical ODMR spectra from nanodiamonds deposited on Si/Si0_2 wafer. The contrast (the count rate $\mathcal{R}$ normalised with respect to the off resonance count rate $\mathcal{R}_0$) is shown for a range microwave powers, the power for each spectrum is quoted as the power at the input of the coil. (b) Normalised data with 5 Gaussian peak fit applied, each trace has been offset by 0.1 for clarity. Raw data is shown as points while the solid line represents the fitting result.

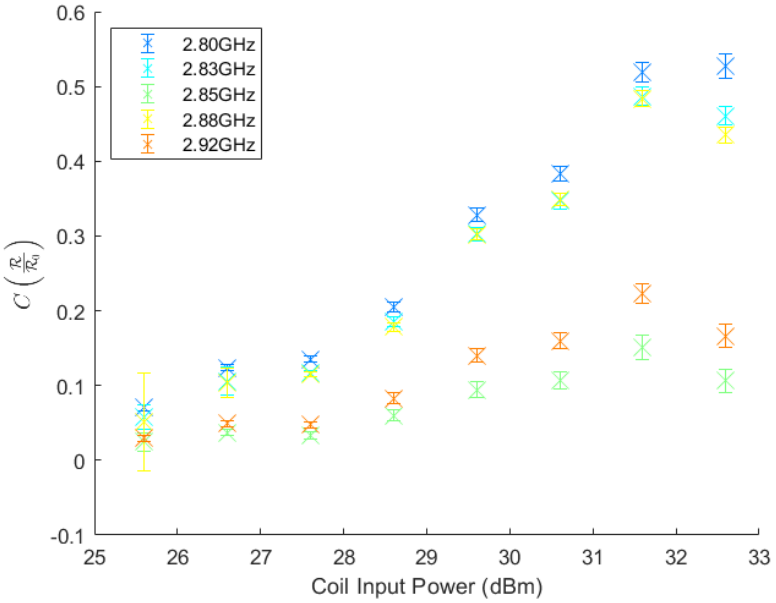

Figure 5.13: Graph of the contrasts of the resonances observed in Figure 5.12 against the input power to the antenna.

region for ODMR experiments.

The contrasts of the resonances shown in Figure 5.12 are significantly higher than expected for NV centres, which are typically reported at around 30% [35]. For example, commercially available NV AFM probes, fabricated by Qnami, are stated to have a contrast $C > 0.15$ [63]. The high contrast, along with the spectral positions of the resonances shown in Figure 5.12 suggest that this PL source does not correspond to emission from single or even multiple NV centres. In the absence of a bias field, single and multiple NV resonances are anticipated to be degenerate, resulting in a single resonance in the ODMR spectra at 2.87 GHz. When a bias field is applied the degeneracy of the $m_s = \pm 1$ levels is lifted and two resonances are seen when a single centre is addressed. The ODMR spectra from multiple NV centres is more complex with multiple resonances as the projection of the local magnetic field along the NV centre axis varies for each different orientation. The observation of multiple spin resonances in the spectra could suggest that the magnetic field is non-zero at the emitter position during the measurement shown in Figure 5.12. However, the magnetic field was measured using a Gauss meter and found to be $B_{\text{residual}} < 1\,\text{mT}$,

which is insufficient to suggest the emitter shown in Figure 5.12 corresponds to multiple NV centres at a non zero magnetic field. A local magnetic field of $B_z = 2.43\,\mathrm{mT}$ would be required for an NV centre to be shifted from 2.87 GHz to 2.80 GHz, which corresponds to the lowest frequency resonance shown in Figure 5.12. The strain parameter is also capable of changing the frequency of an NV centre zero-field resonance by the order MHz [28, 32]. As a result, the resonances shown in Figure 5.12 could correspond to multiple NV centres in a highly strained lattice. Finally, nearby paramagnetic defects in the diamond lattice have been shown to modify the ODMR response of NV centre when compared to a lone centre [146], and this could also be contributing to the complex nanodiamond spectra observed.

While the complex spectra typical of nanodiamonds observed from this sample is not well understood, a very high contrast NV centre resonance would enable highly sensitivity magnetometry. Therefore, this sample will be investigated further following the demonstrating of expected behaviour from verified NV centres. However, the observation of ODMR from nanodiamonds in the range 2.75-2.99 GHz provides a clear demonstration of the functionality of the microwave delivery system, with the potential to be utilised for NV centre magnetometry.

Applying a Bias

To demonstrate the functionality of the bias magnet hardware, and to demonstrate the capability of this instrument to measure ODMR spectra from point-like sources with a controllable bias field, ODMR spectra were measured from the same PL source hosted in a nanodiamond at two different bias strengths. Figure 5.14 shows two ODMR spectra from the same nanodiamond source at the same laser ($P_{Laser} = P_{sat}$) and microwave power ($P_{MW} = 1.32\,\mathrm{W}$), with Figure 5.14 (a) showing the ODMR spectra with the magnet fully withdrawn, representing the field at the PL source at the ambient value. While Figure 5.14 (b) shows the magnet approached towards the sample, along an arbitrary direction.

For a single NV centre, with the approach of the bias magnet aligned with the NV centre axis, a linear shift of the resonances corresponding to each of $m_s = 0$ to $m_s = \pm 1$ would

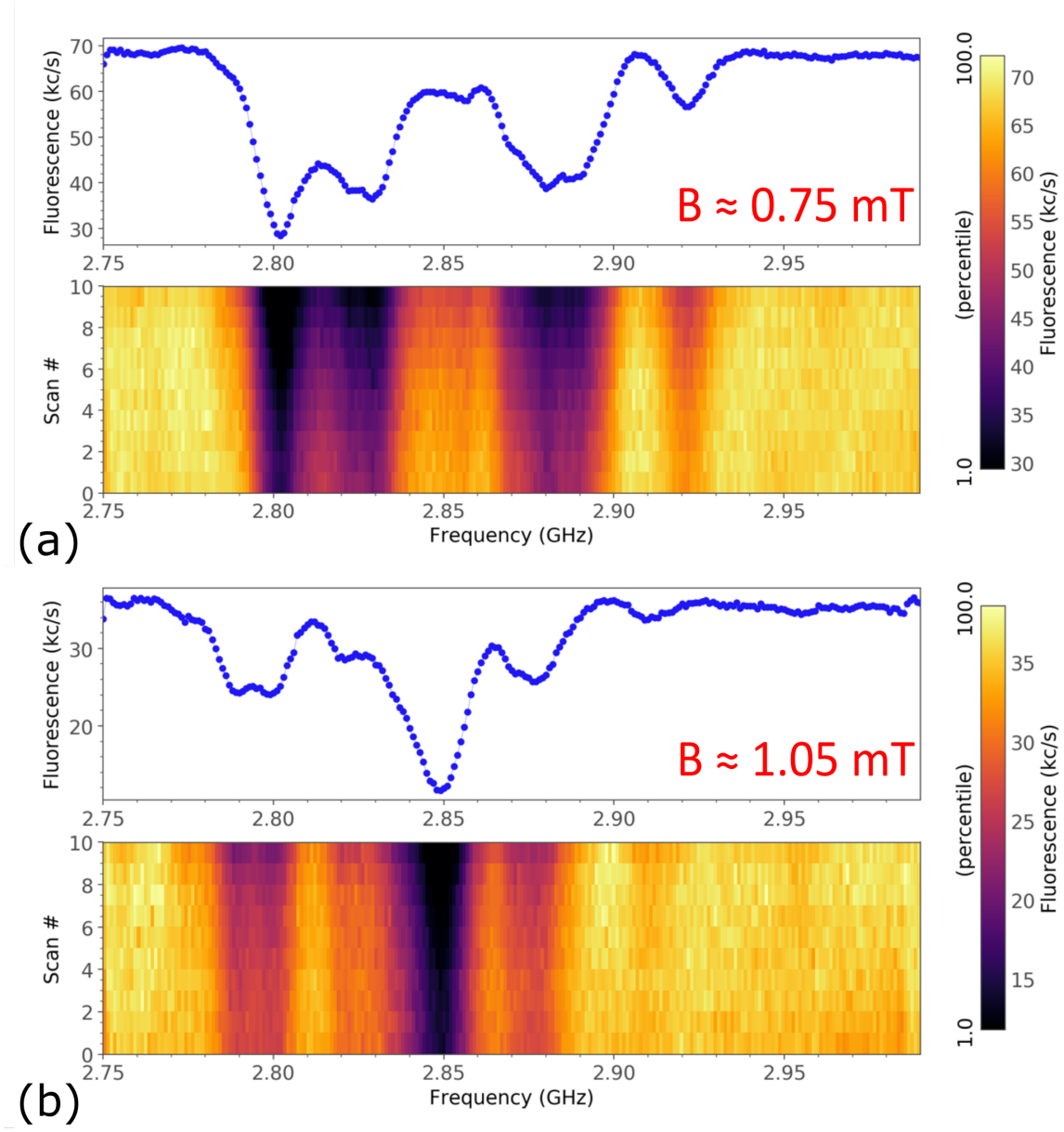

Figure 5.14: ODMR of PL source hosted in a nanodiamond at different magnetic bias strengths. (a) ODMR spectrum with magnet fully with drawn equivalent, with magnetic field at the PL source given by the ambient magnetic field ($B \approx 0.75\,\mathrm{mT}$). (b) Bias magnet approached towards MO along and arbitrary direction, with the bias strength at the focus estimated to be $B \approx 1.05\,\mathrm{mT}$.

be expected. In the case that an ensemble of NV centres, featuring a range of orientations is addressed, the bias field will not be aligned with every orientation, resulting in a more complex change in the ODMR spectrum as the strength of the bias field along any given axis is increased. NV centres well aligned with the bias field will display the simple linear splitting of the ODMR resonances as the strength of the bias field is increased. The ODMR features of poorly aligned NV centres will change in a non-linear manner, depending on the projection of the bias along the NV centre axis. In the limit that the bias field is applied perpendicular to the NV axis, the contrast of the resonances is anticipated to decrease as mixing of the spin-states occurs [33]. Knowledge of the orientation of the bias field relative to the defect axis is crucial to interpreting the change in the ODMR spectra as the bias field is increased in strength. However, in Figure 5.14 it is the unknown nature of the PL source that presents the main challenge in quantitatively interpreting the change in the ODMR spectrum. The ODMR spectra presented in Figure 5.14 are recorded from the same PL source shown in Figure 5.12 and 5.13. As discussed in the 'Nanodiamond' section above, the emitting species is unknown, with the frequencies and contrasts inconsistent with the expected values for a single, or ensemble of NV centres. However, Figure 5.14 provides the first demonstration of this instrument to observe ODMR that is dependent on the bias field, which can be accurately controlled at the microscope focus, as shown by both the change in contrast and central frequencies of the ODMR resonances as the strength of the bias field is increased. The bias magnet instrumentation will be calibrated following the confirmed observation of a single NV centre, which will allow accurate determination of the bias strength at the focus.

Referenced ODMR

An experimental problem associated with sample scanning experiments of long duration is drift associated with the piezoelectric scanning stages. When measuring a sample in a diffraction limited spot size $\approx 300\,\text{nm}$ the effect of drift can significantly degrade the signal as the emitter drifts out of the confocal volume. When drift is significant there are two mechanisms acting to decrease the PL intensity, the drift and the intensity decrease

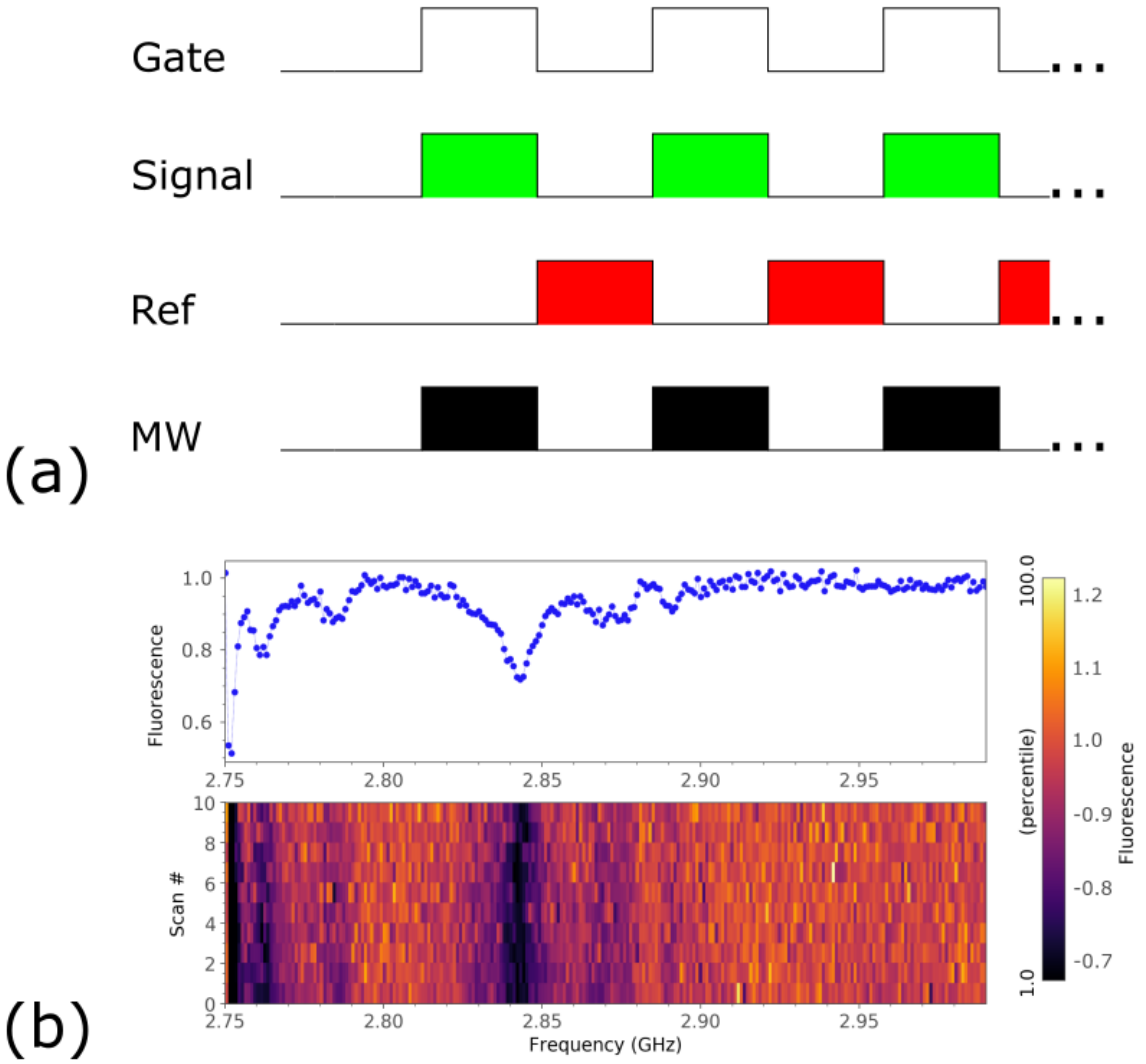

Figure 5.15: (a) Experimental control signals for a referenced CW-ODMR measurement. The gate is a timing signal generated with by the National Instruments card and internally routed to the counting channels. Signal shows a counting period when the MW output is applied to the NV centre. The Ref signal shows the counting period for the reference signal (laser on, MW off) which occurs in the low period of the gate signal. For each frequency in the sweep a single signal and reference is made. (b) Shows a referenced ODMR measurement from a PL source hosted in a nanodiamond.

associated with the ODMR resonance. To account for the drift two PL measurements are made at each frequency in the CW-ODMR sweep, one prior to the application of the MW field and one with the MW output enabled. The PL change between the bright reference and the MW on the signal can then be entirely attributed to the MW induced resonance and not drift.

The Qudi NI card counting routine for ODMR utilises 'semi-period counting'. In this method, the NI counter records the incoming pulses on the counting at intervals defined by a gate signal, also generated by the NI card. In the 'semi-period' method used by the Qudi ODMR routine, the signal is recorded during both the high of the gate signal and the low. To isolate the effect of drift and performed a bright referenced measurement the Qudi NI hardware file was adapted to count the signal in the gate high and record the bright reference in the following gate low, see figure 5.15. The 'semi-period counting' method is time-efficient as signal and reference are acquired for 100% of the experimental sequence. At very low fields, which require longer measurement times, the timing of the acquisition sequence can limit the fields that can be measured, demonstrating the value of a time-efficient referenced measurement sequence.

5.5 Summary

To summarise, a range of supporting instrumentation has been produced to work in conjunction with the optical components and scanning probe components in the development of a scanning probe NV magnetometer. An MW delivery system consisting of a planar ring antenna has been shown to produce oscillating magnetic fields required to observe optically detected magnetic resonances in nanodiamonds. A custom-built sample holder was produced to rigidly secure samples for scanning and locate them in the region of greatest microwave field strength for scanning probe magnetometry. The design of a rotational mount to produce bias fields along an arbitrarily orientated NV centre axis was presented. Finally, referenced ODMR measurements from PL sources in nanodiamonds are presented, facilitating the direct comparison between a source PL intensity in two experimental states,

in this case with microwave power enabled and disabled.

Chapter 6

Scanning Probe Magnetometry

6.1 Introduction

The previous chapter focusing on ODMR demonstrated the ability of the instrument to optically detect resonances associated with the application of high-frequency magnetic fields. To utilise this capability to produce nanoscale maps of the local magnetic field above a sample, a probe hosting an NV centre or centres must be raster-scanned across the sample while simultaneously recording the optical signal. This chapter presents the progress made towards operating this instrument as a scanning probe magnetometer. Firstly, test measurements from a Quantilever™ [63] probe, manufactured by Qnami, are presented. The test measurements characterise the probe's performance in this instrument, both as a scanning probe and as an optical sensor for eventual magnetic field readout. Optical alignment procedures are presented, describing the alignment of the optically active region of the probe and the confocal/MW instrumentation with the nanoscale precision. The different magnetic field imaging modalities of a scanning probe NV magnetometer are discussed, with a focus on the development of protocols for their eventual implementation in this instrument. Finally, the progress made in the design and fabrication of test targets is presented.

6.2 Qnami Quantilever™

The optical scanning probe used in this instrument is the Qnami Quantilever™ [63], one of two functionalised AFM probes designed for use in scanning probe NV magnetometry that recently became commercially available. The Quantilever™ probe consists of a quartz tuning fork which acts as a force sensor for the control of probe-sample separation and measurement of the sample topography. The interaction between the probe and sample is mediated through a 200 nm diameter diamond nanopillar protruding from a diamond cantilever which is affixed to one tine of the tuning fork via a quartz rod, see Figures 6.1 and 6.2 for the working principle and dimensions respectively. The probe is designed to be operated dynamically in lateral force mode, with the asymmetric motion of the tuning fork tines producing motion of the diamond cantilever and nanopillar in a plane parallel to the sample, with the directions of motion shown Figure 6.1 (a). The tuning fork is driven either electrically or mechanically, resulting in the motion of the driven tuning fork tines in-plane, which produces the lateral motion of the diamond cantilever. The 200 nm diameter nanopillar both limits the interaction area for AFM operation and acts as a waveguide to increase the optical collection efficiency of the NV centre PL from the NV centres, which are typically implanted in the range 10-30 nm from the tip apex [62, 63]. Figure 6.1 (b) demonstrates the principle of the Quantilever™ probe operating as a scanning probe magnetometer. The application of the MW magnetic field to drive the ground state sublevel transitions is represented by a resized coil in Figure 6.1 (b), while a small wire represents a sample. The typical flying distance of the NV centre or centres implanted into the probe is 50 nm [62] enabling high sensitivity optical magnetometry when the sample is scanned under the probe while the pillar is positioned in the optical collection/excitation volume of a confocal microscope.

The recommended mode of operation for the Quantilever™ probe control is frequency modulated AFM (FM-AFM), where the resonance frequency shift acts as the feedback parameter for probe control and imaging. The tuning fork oscillation is electrically driven in this instrument, using the same drive circuit as discussed for Akiyama probe operation

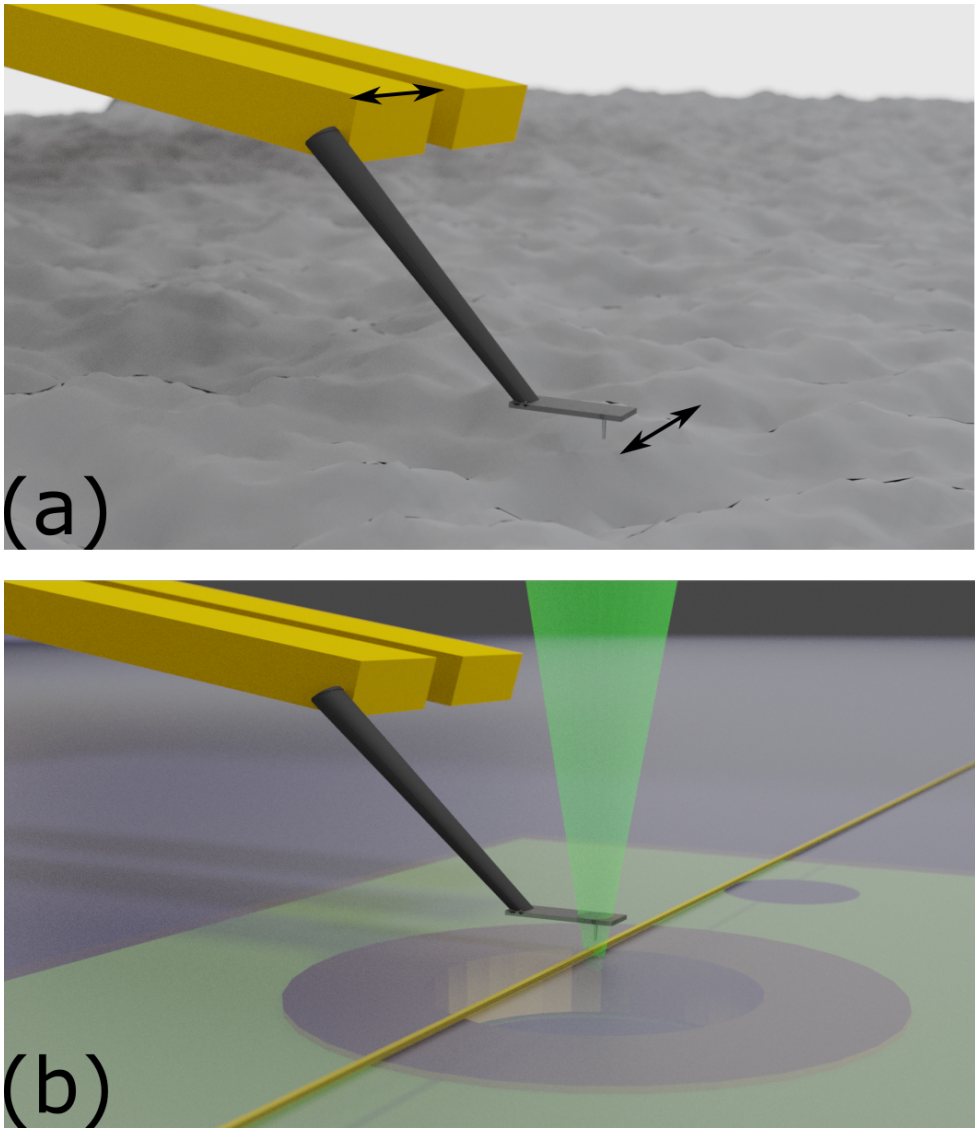

Figure 6.1: 3D representation of the working principle of the Qnami Quantilever™ . Gold represents the tuning fork which vibrates in the xy plane of the fork. A small diamond cantilever with 200 nm diameter nanopillar is affixed via a quartz rod to the tuning fork. (a) Shows principle of the probe as a dynamic AFM probe for topographic measurements and tip-sample separation control, the in-plane motion of a tine of the fork produces motion of the nanopillar above the sample. (b) The working principle as an optical magnetic field sensor. The NV centres are addressed via the confocal MO shown by a green light cone. The gold wire represents a magnetic target. The MW coil is resized and shown under the sample to illustrate the application of the MW magnetic field.

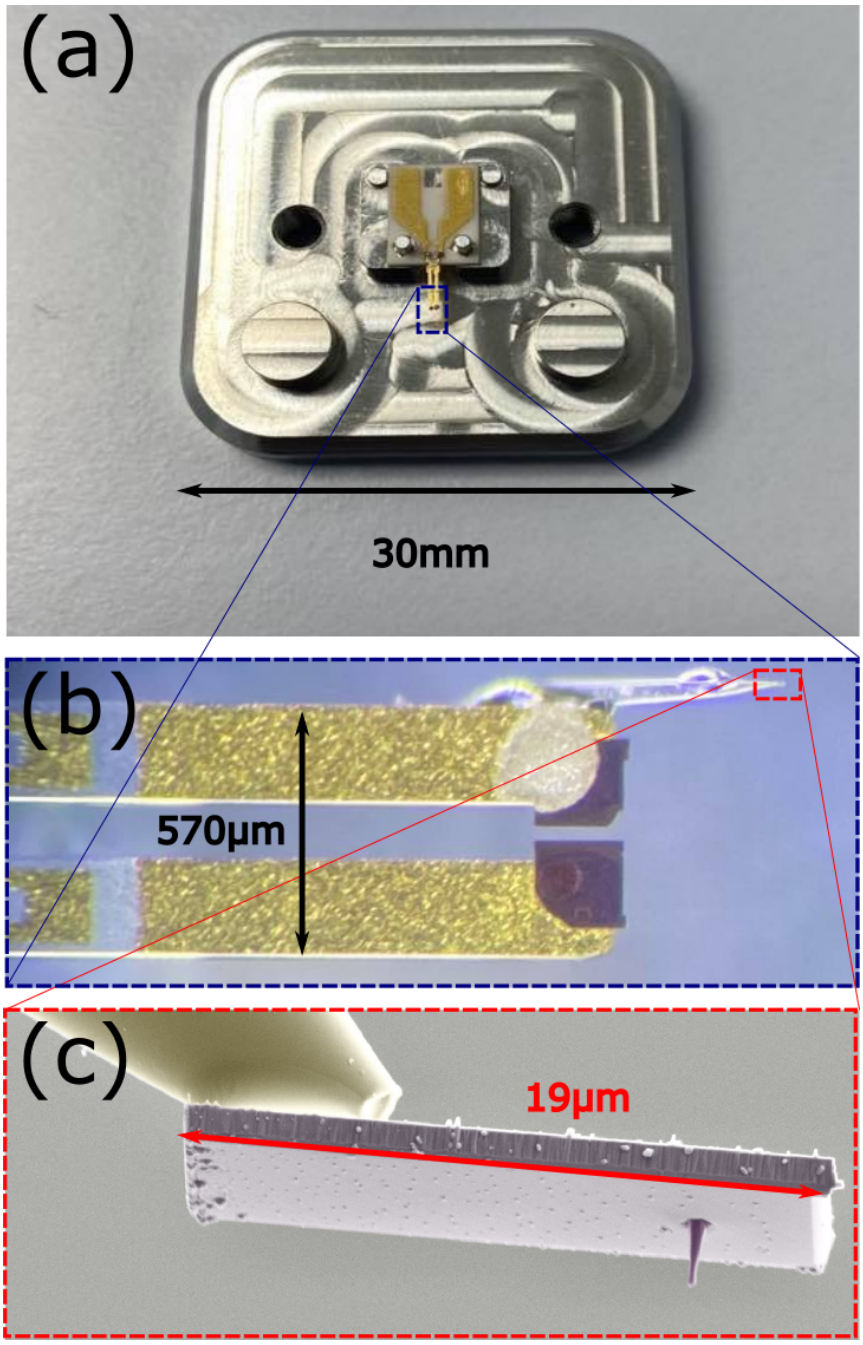

Figure 6.2: (a) Quantilever™ probe in housing prior to loading into the AFM, the ceramic has the same footprint as an Akiyama probe, with dimensions of 6.5 mm by 5.1 mm (b) Optical microscope image of tuning fork tip with quartz rod support rod visible and diamond cantilever shown in the red box. (c) Image from manufacturer [63], showing diamond nanopillar on sample facing side of the cantilever.

in Chapter 4, see figure 4.3 for the circuit diagram. The oscillation of the tuning fork is driven by the application of a drive voltage in the range 0 - 1 V which is generated by the RHK R9 scanning probe controller. The voltage applied to the probe is stepped down by a factor of 10 on the preamp board before application to the probe. The motion of the tuning fork is measured electronically and recorded by the R9 controller following the amplification of the measurement signal by a transimpedence amplifier with a gain of $22\,\mathrm{V}\,\mu\mathrm{A}^{-1}$, with the R9 controller controls the feedback loops using a digital PLL and generates the stage/sample scanning voltages.

A typical response of the Quantilever™ probe mounted in this instrument as the frequency of the drive signal is varied is shown in Figure 6.3(a). Two resonances are observed in the range 28-32 kHz, with the higher frequency resonance and the associated phase lag between the drive signal and probe response used to control the feedback loops in FM-AFM mode. The two resonances in figure 6.3(a) correspond to two eigenfrequencies of the coupled oscillator system that describes the behaviour of the two tines that comprise the tuning fork. The lower frequency corresponds to in-plane motion of the tines in-phase and the higher frequency oscillation in anti-phase [129]. The expected quality factor, Q, of the high-frequency resonance is greater than 1000 ($Q > 1000$) when the Quantilever™ probe is mechanically driven in the scanning probe instrument produced by the same supplier [70]. The Q factor in this instrument was determined by the RHK R9 software and estimated be Q $\approx$ 80 with the probe ceramic loaded into the clips used to secure the Akiyama probes, see Chapter 4 Figure 4.5(b). Firstly, the low Q factor seen in this instrument is attributed to a mass imbalance between the tines of the tuning fork associated with the mass of the quartz support rod when compared to balanced tines, such as the for the Akiyama probe [129]. The lower Q compared to the manufacturer's specification is also due to the probe ceramic being poorly fixed to the AFM support structure in this instrument. Figure 6.3(b) shows the response of the probe against the drive signal frequency after the probe ceramic was secured using a gel adhesive (Pritt Glue dot). The Q factor of the higher frequency resonance was estimated to be Q $\approx$ 120, an improvement by a factor of 1.5. The asymmetry of the resonance seen in figure 6.3(b) suggests Q can be increased further with the

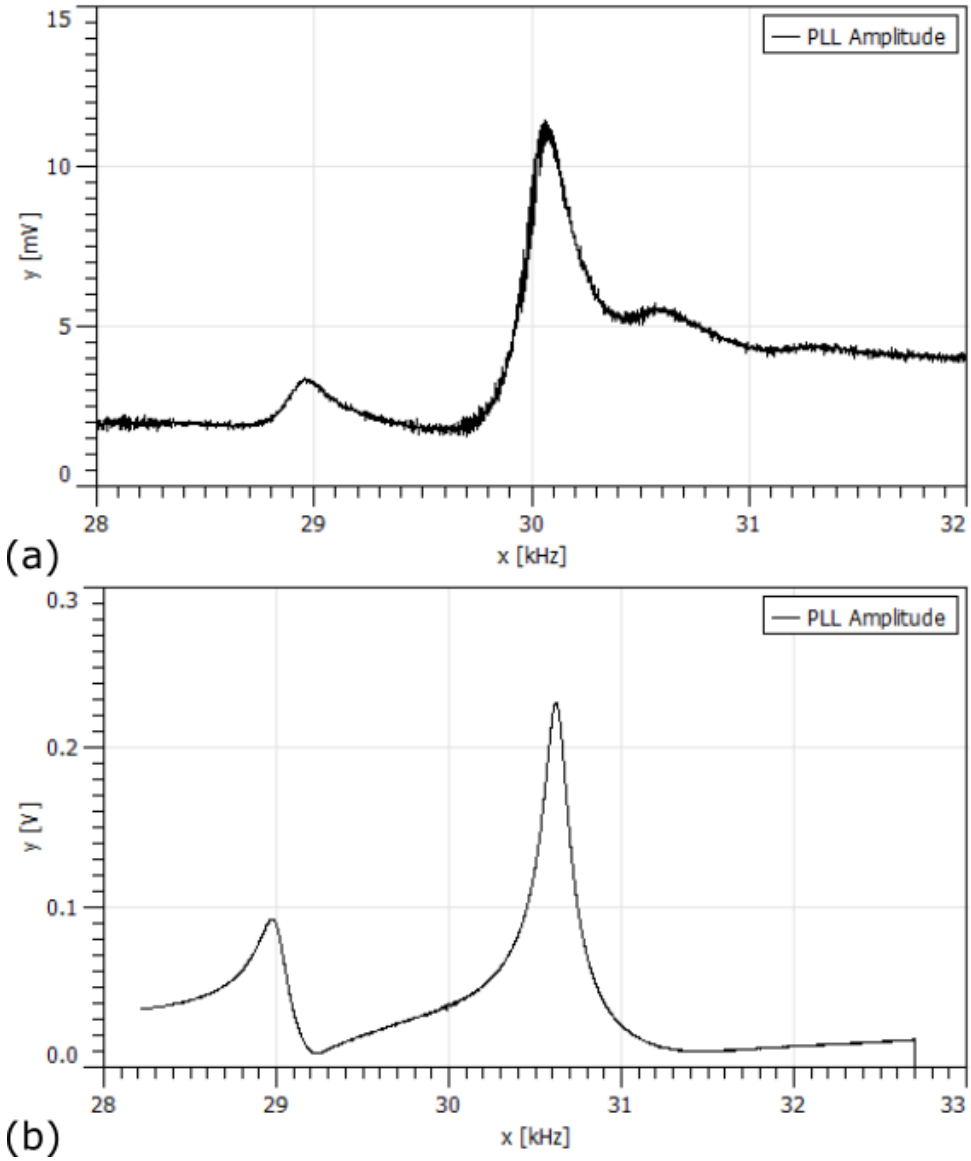

Figure 6.3: (a) Qnami probe response to varying drive frequency, Q ≈ 80. (b) Resonance of Qnami probe with the ceramic secured with gel adhesive, Q ≈ 120, an improvement by a factor of 1.5 when compared to the unsecured resonances shown in (a). In both (a) and (b) the drive level is set to 0.8V, corresponding to The asymmetry of the resonance in (b) suggests Q can be further increased with improved parasitic capacitance compensation. More fundamentally, the Q could be increased through the addition of a mass on the tine without the quartz rod and diamond cantilever, re-balancing the tines [129].

improvement of capacitance compensation. In addition, the tines of the probe could be re-balanced with the addition of mass of the tine without the quartz rod attached [129].

The Quantilever™ probe is available with either single (MX series) or multiple NV centres (DX series) implanted in the nanopillar tip of the probe [63]. A multi NV centre probe offers a larger optical signal than a single NV centre probe at the expense of spatial resolution. However, the larger optical signal can improve the sensitivity making a multi NV probe ideal for test measurements on an instrument or sample of unknown response. A common approach, when imaging using Quantilever™ probes, is to perform a measurement with a multiple NV centre probe (DX series) and repeat the measurement achieving higher spatial resolution using a single NV centre probe (MX series). The results presented in the following section on optical alignment are from a Quantilever™ DX series probe [63], which contain multiple NV centres.

6.2.1 Optical Alignment

Scanning probes for NV centre magnetometry, including the Quantilever™ probe, require precise alignment of the excitation and readout optics and the optically active region of the probe case, in this case, the diamond nanopillar. The nanodiamond pillar is 200 nm in diameter and is approximately a factor of two smaller than the diffraction limit for high NA lenses, demonstrating the nanometer precision of the optical alignment required. In this instrument, scanning probe magnetometry will be performed with a stationary tip and beam with the sample scanned to form an image. To align the probe and optics for magnetometry the probe is moved relative to the stationary optics.

Coarse Alignment

The wide-field microscope is used to provide a visual reference for coarse alignment due to the greater temporal resolution than available with the confocal microscope. The wide-field microscope is combined with the confocal path using a mirror, resulting in the optical

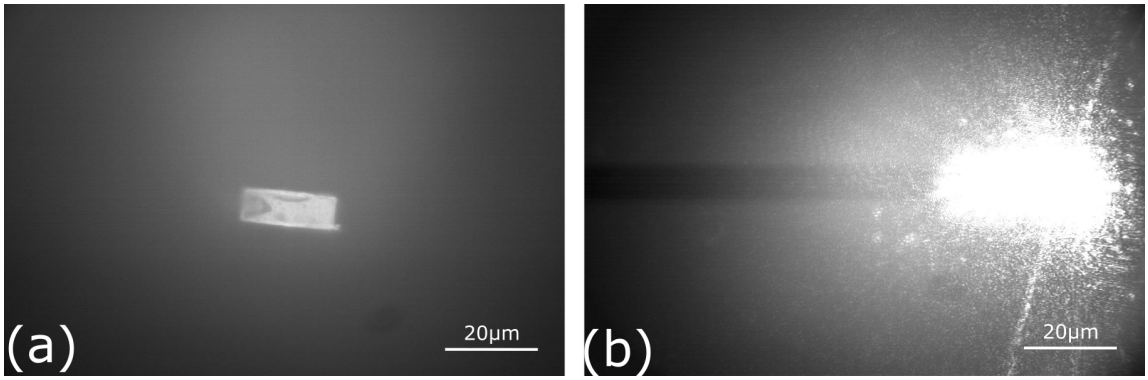

Figure 6.4: Wide-field images of Qnami probe taken during coarse alignment. (a) Show microscope configured in 100% wide-field mode. (b) Shows wide-field image with microscope configured with the optical signal split 50/50 between wide-field and confocal detectors. The confocal laser can be seen on the cantilever as a saturated area.

signal from the MO being directed entirely towards the wide-field camera (100% wide-field, 0% confocal mode). The use of the mirror ensures there is a large signal at the wide-field microscope maximising the contrast and ensure maximum visibility during coarse alignment and focusing of the relatively thin ($\sim 1\,\mu m$) and translucent cantilever. An example image of the cantilever in the wide-field microscope is shown in 6.4(a). The cantilever is coarsely aligned in the centre of the MO FOV using the AFM coarse positioning stages controlled using Python. Following coarse xyz alignment of the cantilever and MO field of view, the mirror coupling the wide-field and confocal optical paths is replaced by a beamsplitter (50% wide-field, 50% confocal operation). The contrast of the wide-field image is reduced. However, the confocal laser is now transmitted through the beamsplitter and focused onto the cantilever. Fine adjustments to the cantilever's alignment with the MO can be made in this configuration as the cantilever's position can be adjusted while monitoring the confocal signal with the microscope configured in reflectance mode. Simultaneously operating the wide-field camera while monitoring the confocal signal provides a visual confirming that the large confocal reflectance signal corresponds to the cantilever.

Once the probe is positioned under the confocal microscope with a large reflectance signal from the cantilever, the confocal microscope is then reconfigured into PL mode by replacing the filters on the signal path. The beam splitter is then also removed so the

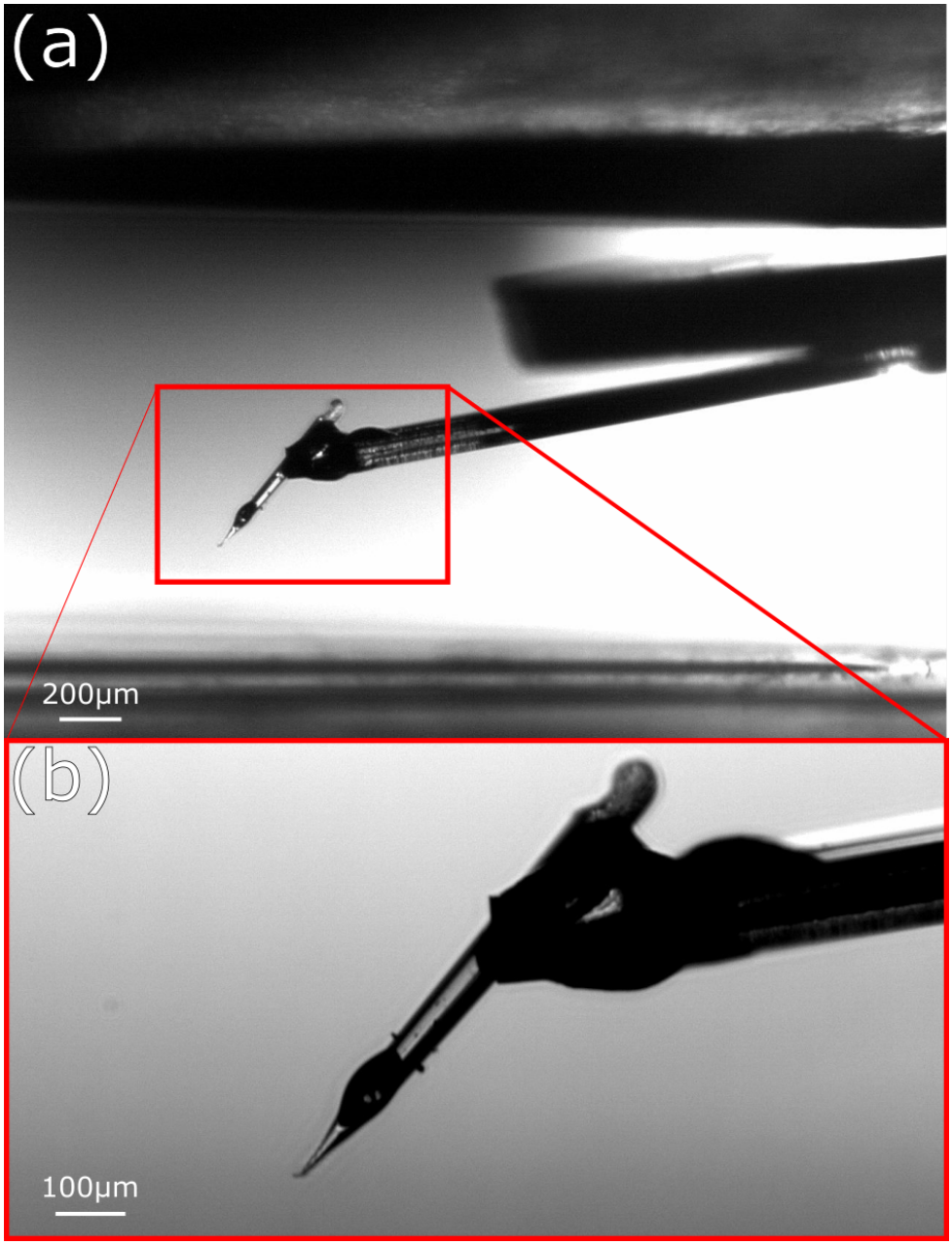

Figure 6.5: Side-camera images used to observe relative tip-sample separation during coarse optical/probe/sample alignment. (a) wide-view with (b) showing a larger magnification image focusing on the quartz rod/cantilever.

microscope operating in 100% confocal mode (0% wide-field) to avoid attenuation of the NV PL. The confocal microscope then provides the feedback signal for fine alignment, utilising the NV centre PL rather than the wide-field image used for coarse alignment.

To approach the probe towards the sample plane the side-view camera is used to provide a visual reference. Typical side view camera images are shown in Figure 6.5.

Fine Alignment

To align the NV centres in the scanning probe with the confocal microscope to within $\sim$ 100 nm, this instrument uses confocal scanning routines to adjust the probe position on the MO. The x and y motion of the probe is controlled using the AFM coarse positioning stages; see Chapter 4 for hardware details. A custom Python routine was developed to synchronise the acquisition of confocal measurements, using a NI PCIe-6323 multifunction DAQ card with probe scanning.

A 10 µm x 10 µm scan can be performed either in reflectance mode or in PL mode to give an approximate coordinate for the diamond nanopillar. However, Visual inspection in the wide-field camera is often sufficient that a confocal scan of the probe in reflectance mode is not required. Figure 6.6(a) shows a typical wide range PL scan used recorded during probe alignment with the x and y coordinates of the actual value of x and y positioning stage positions.

After a 10 µm x 10 µm confocal scan, the probe is set to the xy coordinates of best NV-confocal alignment identified in the long-range scan. A reduced range (1 µm x 1 µm), reduced-resolution (10 pixels) scan can then be performed about the updated position. The optimum probe xy position can be determined from this smaller scan and the probe xy coordinate subsequently updated. Figure 6.6(b) shows a typical small range scan with the x and coordinates shown independent of the scanning probe coordinates.

To optimise the position of the MO relative to NV centres along the optical axis, the MO is scanned in the z-direction using a piezoelectric stage (ASI MS-2000). The MO is

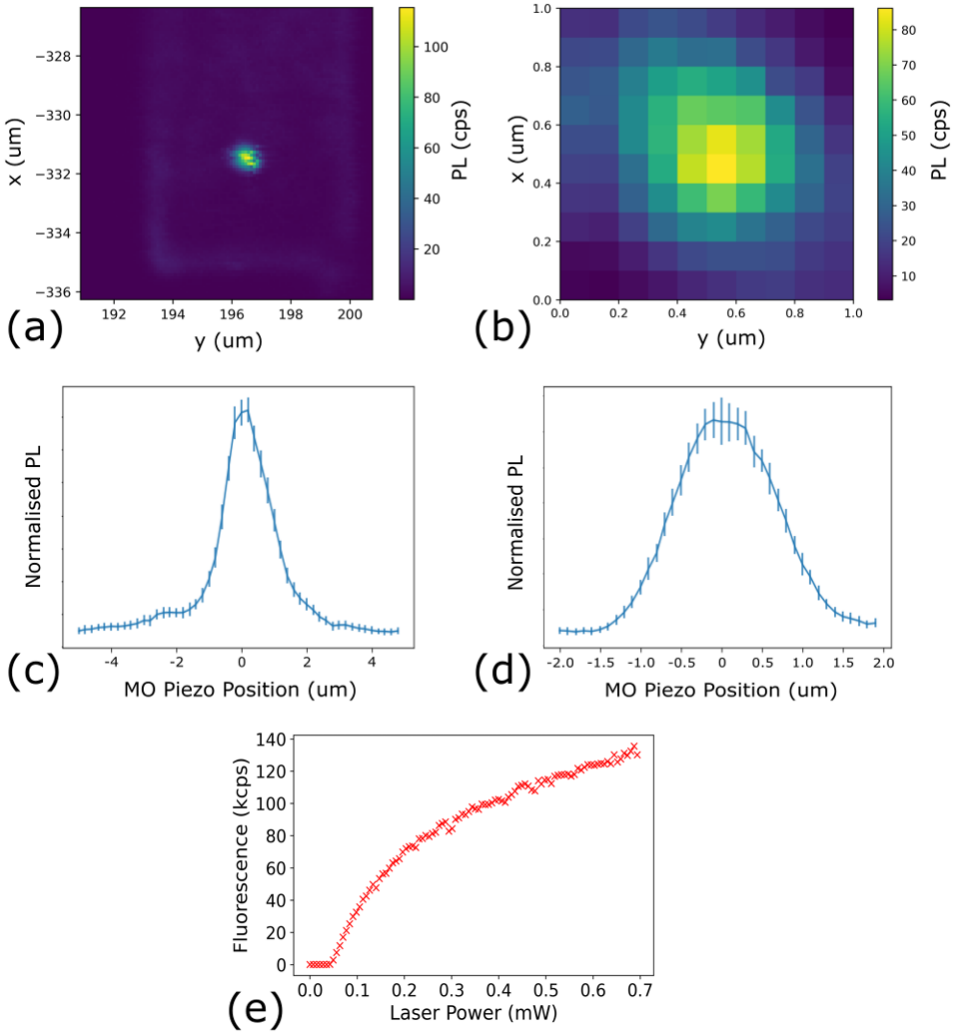

Figure 6.6: Confocal microscope measurements of Quantilever™ recording during optical alignment, in images shown the PL count rate corresponds to data acquired by one of the two counters. (a) 10 µm x 10 µm confocal PL scan produced by scanning the probe (b) 1 µm x 1 µm confocal scan used to optimise xy alignment of confocal microscope (c) Confocal depth scan centre on NV centres in recorded during autofocus routine, the count rate is shown against the microscope objective position. (d) Reduced range depth scan. (e) Typical saturation curves, the count rate is shown against the laser excitation power.

scanned as opposed to the probe to prevent unwanted xy motion of the cantilever during focusing. A Python routine was developed to scan the MO 5 µm above and below the cantilever position identified via focusing with the microscope operating in wide-field mode, while synchronously recording confocal data using the NI PCIe-6323 card. A smaller 2 µm scan is performed about the maximum identified in the long-range MO scan to ensure the MO is set the position of with maximum PL detection from the NV centres in the probe. Figure 6.6(c) and 6.6(c) show the 10 µm and 4 µm MO scans of the probe recorded during aligment.

Prior to scanning, the response of the NV centre PL intensity to laser power is measured to determine a safe level of operation to avoid photobleaching. The ratio of the applied power to the saturation power significantly alters the ODMR response [35], and therefore the magnetic sensitivity [35, 32]. Figure 6.6(e) shows a saturation curve recorded following xyz alignment. The laser power is shown as a control voltage in Figure 6.6(e) as the value of an external control voltage as the laser power coupled into the waveguide of the probe is not known.

6.3 Qualitative Imaging Modalities

One of the key appeals of NV centre based magnetometry is the quantitative and vectorial nature of measurement, which can be performed in ambient conditions. This section introduces two simple qualitative imaging modalities for scanning NV centre magnetometers. The first mode, referred to as contour imaging, is a simplification of the full ODMR sequence. The second qualitative imaging mode, referred to as PL quenching, provides a means to image a sample when the off-axis magnetic field is large, and the mechanism for ODMR sweep imaging becomes inefficient.

6.3.1 Contour Imaging

There are two primary motivations for developing contour imaging mode capability in a scanning NV centre magnetometer. Firstly, contour mode provides a demonstration of a scanning probe magnetometer's functionality with a relatively simple experimental control sequence, with only a single microwave frequency applied at each spatial location. In contour imaging mode, only a single optical measurement needs to be recorded at each pixel, while the single MW frequency is applied to the coil for the total acquisition time. In addition to the experimental simplicity of contour imaging mode, making it an ideal first operating mode for the developed instrument, contour imaging mode also has practical implications as the acquisition time compared to a full ODMR sweep is greatly reduced. The comparatively short acquisition times of the contour field mode allow it to be used to probe the frequency limits, setting the range for a full ODMR scan and therefore setting the dynamic range for a given 2D scan. The contour imaging modality also represents a time-efficient way to characterise samples where the exact magnitude and direction of the local magnetic field is required while still benefiting from the NV centre's high spatial resolution. Targets of interest for contour mode imaging include ferromagnetic domains where the direction and precise strength are not required to be measured.

To perform a contour scan, the NV PL intensity is recorded at the probe is scanned above a region of interest. As the probe is scanned across the sample, the NV centre resonance frequency varies spatially due to the Zeeman shift of the NV centre-ground state levels caused by local variations in the magnetic field over the 2D scan. When the local magnetic field induces a Zeeman shift equal to the single MW frequency, ν_{contour}, applied for the duration of the raster scan, the PL intensity decreases. The choice of the single applied MW frequency sets the magnitude of the magnetic field that is probed, B_{contour}, which is given by

$$B_{\text{contour}} = \frac{h\nu_{\text{contour}} - hD}{g\mu_B} \tag{6.1}$$

where h is Planck's constant, $D = 2.87\,\text{GHz}$ the zero field splitting parameter, $g = 2.000$ the Lande g factor and μ_B the Bohr magneton [32].

The decrease in the PL intensity in the contour image is related to the lineshape of the transition, which has a Lorentzian shape [147],

$$\frac{\mathcal{R}(\nu)}{\mathcal{R}_0} = 1 - \frac{C}{[(\nu - \nu_{contour})/\gamma_{NV}]^2 + 1} \tag{6.2}$$

where γ_{NV} is the linewidth parameter and is related to the full width half maxima (FWHM), $\Delta\nu_{NV}$, by $\Delta\nu_{NV} = \gamma_{NV}/\pi$.

To perform a contour scan in this instrument, a region of interest of a sample is aligned with the microwave coil using the wide-field camera. The probe is also aligned with the confocal microscope using the procedure outlined above. The probe control will be performed using the RHK R9, with the probe to be operated in FM-AFM mode with a constant drive signal. In contour mode, the laser and microwave application are constant in signal level and frequency throughout the entire scan, and therefore these instruments do not have to be synchronised with the sample scanning and photon counting procedures. The synchronisation of sample scanning, probe control and probe control will all be performed using the RHK R9, using the procedure developed for simultaneous confocal/AFM, as discussed in Chapter 4. However, with no offset between the optical and AFM image as the confocal microscope will be aligned with the NV centre/centre prior to scanning.

In addition to performing xy scans utilising the RHK R9 a prebuilt routine referred to as 'lift mode' can be utilised, where a single topographic line is scanned at a given distance above the sample plane. The measurement is then repeated at a range of preset heights, enabling magnetic profiling in the vertical direction.

6.3.2 NV PL Quenching

The most promising region of NV sensing is the weak off-axis field limit, resulting in simple linear splitting for an on-axis magnetic field. When there is a large transverse component the change of the resonance frequency becomes more complex, this was discussed in Chapter 2. When the magnitude of the transverse magnetic field is much greater than the on-axis magnetic field, i.e when $\sqrt{(B_x^2 + B_y^2)} >> B_z$, mixing of the spin states occur and the optical readout of the spin states becomes inefficient [33]. However, the loss of ODMR contrast is also accompanied by an overall decrease in PL [37]. While ODMR based magnetic field sensing is inefficient where there are large transverse magnetic fields, the overall loss of PL provides a qualitative means to map the transverse magnetic field onto the PL signal [38]. Therefore monitoring the decrease in the PL signal, referred to as quenching, the local variation of large transverse magnetic fields can be imaged.

To image a sample in PL quenching mode in this instrument, the RHK R9 will be used for probe control, sample scanning and acquisition of the optical signal. NV PL quenching mode does not require the application of the high-frequency magnetic field generated by the synthesiser, and so the experimental control will be performed using the same routine as for developed for simultaneous confocal/AFM measurement, as discussed in Chapter 4.

6.4 Quantitative Imaging Mode

It was discussed in Chapter 2 how the on-axis magnetic field for an NV centre can be determined using a CW-ODMR measurement scheme, with this measurement protocol demonstrated on nanodiamonds in Chapter 5. The frequency of the MW magnetic field is varied and the frequency that satisfies the local resonance condition is detected by a drop in PL intensity. The measured resonance frequency can be converted to the magnetic field projected along the NV centre axis, using equation 2 discussed in Chapter 2. To produce a full 2D map of the local magnetic field variation, the probe is scanned and the MW frequency swept across a wide range and the resonance frequency, and therefore magnetic

field at each location determined. The magnetic field along the NV centre axis, in the presence of a bias field is given by

$$B_z + B_{bias} = h\frac{(\nu_{\pm} - D)}{g\mu_B} \tag{6.3}$$

To first measure the bias field strength, B_{bias} the sample is withdrawn vertically by 25 µm using the sample scanning stages to reduce the target magnetic field strength, B_z. A full ODMR sweep is then perfomed to accurately measure the bias strength, B_{bias}. In the case the source field is a current, the bias field can be measured with the AFM feedback engaged and the NV centres at the actual probe separation over the coarse of the measurement when there the device is grounded.

A full B field image can be measured in a variety of ways, firstly a full ODMR sweep can be recorded at each pixel, this is the approach taken the ProteusQ, manufactured by Qnami [70]. Alternatively, when the dynamic range is low, the MW frequency can be fixed on the slope of the ODMR dip and linear changes in on axis field produce linear changes in the PL intensity.

The first full ODMR sweep scan performed with this instrument utilises the RHK R9 scanning probe software to control the probe scanning. The probe is scanned using a 'pixel scan' procedure where the dwell time at each pixel is set using the R9 software. The timing of the optics and microwave application will be controlled using a digital pulse generator (Swabian Instruments, Pulsestreamer) and preprogramming of the MW synthesiser via the front panel. The optical signal will be measured by counting the SPAD produced TTL pulses using a NI PCIe-6323 card with the optical signal binning defined by the digital signal generator, the position of each optical measurement is recorded using an analogue input of the same NI card, with an input for each axis. The input to the NI card will be taken from the scanning stages which produce an analogue output signal relative to the position on each axis. The scaling of the output signal is the same as the input control signal, with 0 V corresponding to 0 µm on each axis and 10 V full extension, or 50 µm.

6.5 Test Samples

This section presents the proposed test samples for this instrument. The first test sample is a magnetic hard disk, chosen due to its magnetic stability and simplicity in sample preparation. The second type of test targets are sets of micron-sized wires with simple geometries. The simple wires will provide a model system to demonstrate the capability of this instrument to measure magnetic fields produced by currents, representing a key step towards the goal of measuring the magnetic fields produced by atom chips.

6.5.1 Magnetic Hard Disk

The use of a magnetic hard disk has previously been proposed as a test target for a range of magnetometers operating in the high-spatial-resolution regime [148]. While showing general potential as test targets for magnetometers, the stray field associated with hard disks has previously been shown to be a suitable test target for scanning NV magnetometers [38].

To simulate the expected response of this instrument operated in contour mode, a simple model of a hard disk test sample was produced. The magnetic domains, which produce the stray field detected by the NV centre above the hard disk, were modelled as small current loops in the sample plane, with the loops equal to the size of the bits on the disk drive. The small current loop model is based on a study by Maletinksy et al, which demonstrated that this simple model could recreate the response of an NV centre probe scanned above a hard disk [38]. To calculate the local magnetic field above the disk the BSmag toolbox [149] for MATLAB was used, which provides a simple method of numerical integration of the Biot-Savart law for arbitrary current-carrying filaments in the magnetostatic approximation. As a demonstration of this model, the current loop sizes were set to 200 nm x 125 nm squares to match typical domain sizes of the bits, while the tracks were modelled as square loops of 50 nm x 125 nm. The magnitude of the current was set to 1 mA in both the track and bit current loops.

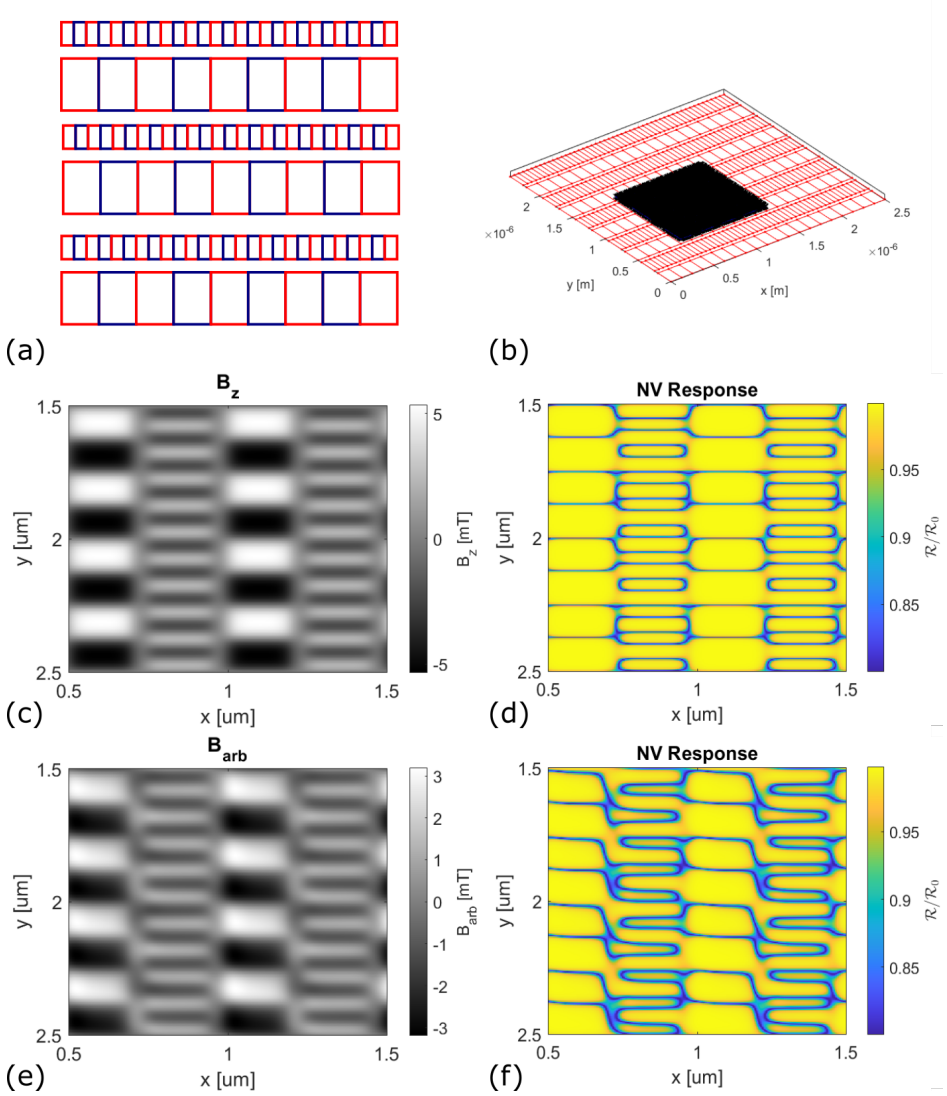

Figure 6.7: a) Hard drive model of current loops with dimensions matching the domain size, red and blue show clockwise and counterclockwise currents respectively. (b) The Black area shows the region for which the local magnetic field was evaluated, while red rectangles show current loops evaluated in the simulation. The magnetic field projection on the z-axis is shown in (c) and in an arbitrary direction, $(\sqrt{2}\sin(\phi), \sqrt{2}\cos(\phi), 1)1/\sqrt{5}$, with $\phi = \pi 162/180$, in (e). The expected NV centre response when a contour image is recorded with the NV centre orientated along the z-axis is shown in (d) and orientated along the same arbitrary direction described above in (f). In both (d) and (f) the NV response is shown for a MW detuning equal to 10 MHz and therefore, the resonance condition is satisfied when on NV-axis magnetic field $B_{\text{contour}} = 0.36\,\text{mT}$.

The local magnetic field was calculated in a plane 50 nm above the current loops to approximate typical NV-sample distances. To convert the magnetic field calculated from the Biort-Savart law to the NV centre response in contour imaging mode, the local magnetic field was inserted into equations 6.1 and 6.2, giving the optical signal at each spatial location. The ODMR resonance was assumed a typical response, with contrast, $C = 0.2$, and a linewidth $\Delta\nu_{NV} = 10\,\text{MHz}$. In Figure 6.7 the magnetic field projection on a given axis and the response of NV centre orientated in the same direction are shown with MW detuningof 10 MHz, which corresponds to the local magnetic field induced a Zeeman shift of 0.36 mT. The magnetic field component in the z-direction is shown in Figure 6.7 (c) and the response of an NV centre orientated on the z-axis shown in Figure 6.7 (d). In Figure 6.7 (e) shows the magnetic field projected onto an NV centre with an arbitrary orientation, in this case corresponding to $(\sqrt{2}\sin(\phi), \sqrt{2}\cos(\phi), 1)1/\sqrt{(}5)$ with $\phi = \pi 162/180$ and the predicted response of an NV centre oriented along this axis shown in Figure 6.7 (f).

The model shown can easily be adapted to a hard disk with a different geometry by changing the current loop size, which can be estimated via AFM measurement.

6.5.2 Current-Carrying Test Samples

The design and construction of this instrument was primarily motivated by the application of measuring the magnetic fields produced by currents in ambient conditions. The current-carrying devices, atom chips, consist of arrays of micron and nanoscale wires designed to produce a range of trapping potentials for on-device experiments. The fabrication of such devices is beyond this thesis's scope but is discussed at length in a review by Folman et al. [150]. To provide a proof of principle experiment to demonstrate this instrument's ability to detect surface currents, test samples have been designed. The test samples allow simple geometries with known current distributions to be measured by the instrument before progressing towards the measurement from more complex devices. This section discusses the progress made in the fabrication of test samples and the supporting components to connect the microscopic devices to benchtop current sources.

Test wires were designed to have similar dimensions to the wires that form atom chips, however, with simpler geometries. Therefore, a contact structure was designed with two purposes: to aid in the location of a wire several microns long and potentially hundreds of nanometers wide and also provide robust electrical contacts. Figure 6.8 shows the layout of the contact structure, with Figure 6.8(a) showing a 2 x 2 array of the contact structure for fabrication on a 5 mm x 5 mm Si/SiO_2 wafer. Figure 6.8(b) shows a single contact structure in more detail. Each contact structure can host four devices connected to a central ground contact. A range of features have been included on the central ground contact to aid the alignment of the sample using the wide-field microscope. Each wire will be connected to a large 400 µm x 400 µm pad, which facilitates bonding a wire which can then be directed to a current source. The designs were produced in gds format for writing with electron beam lithography. A combination of Python, KLayout - a 2D open-source CAD package [151] and open-source software package enabling the development of scripted lithography patterns [152] were used to generate the designs.

To provide a connection between the micron-scale contacts on the device arrays and a benchtop source measure unit (Keysight B2901A), PCB samples holders were produced. The PCB was produced in a 15 mm by 15 mm square to locate in the central recess of the macor sample holders produced for NV magnetometry, ensuring the PCB is centred on the MW antenna aperture. The PCB sample holders were produced from single-sided PCB, to reduce the screening effect on the magnetic field produced by the planar antenna. The top plane was written to remove the majority of the surface copper except for eight copper pads to provide electrical contacts between the devices on the sample and the source measure unit used to drive the current. A central region was milled into the PCB to locate the sample as close to the MW antenna's surface as possible. The recess also centres the 5 mm by 5 mm wafers in the PCB and, therefore the antenna. Finally, the PCB was gold plated to improve the electrical contact between the device, the PCB and eventually a source measure unit. A picture of the PCB sample holder is shown in figure 6.9.

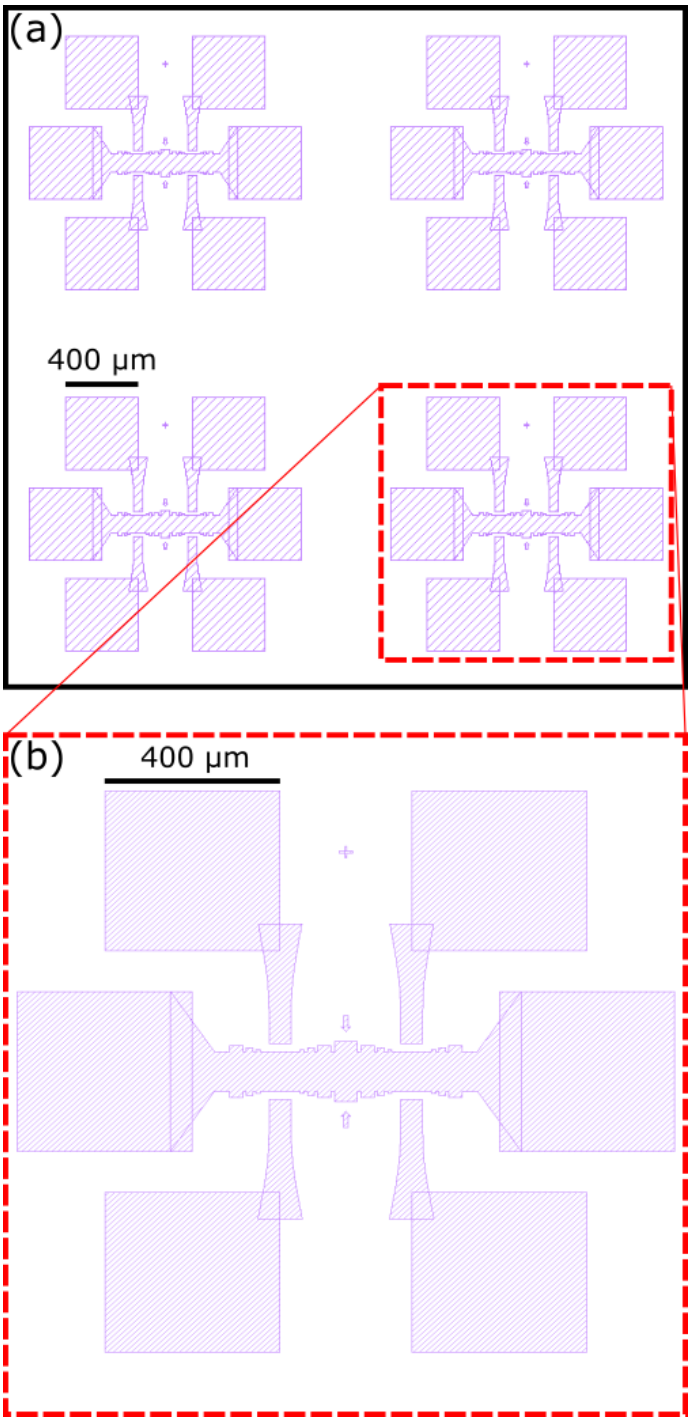

Figure 6.8: Contact design for electrical connection of test devices consisting of micron-scale wires to a benchtop current source. (a) Shows a 2 x 2 array of contact devices designed for writing onto a 5 mm x 5 mm silicon/silicon dioxide wafer. (b) shows alignment features and four contact pads, allowing the connection of nanowires from the contact to the central ground contact.

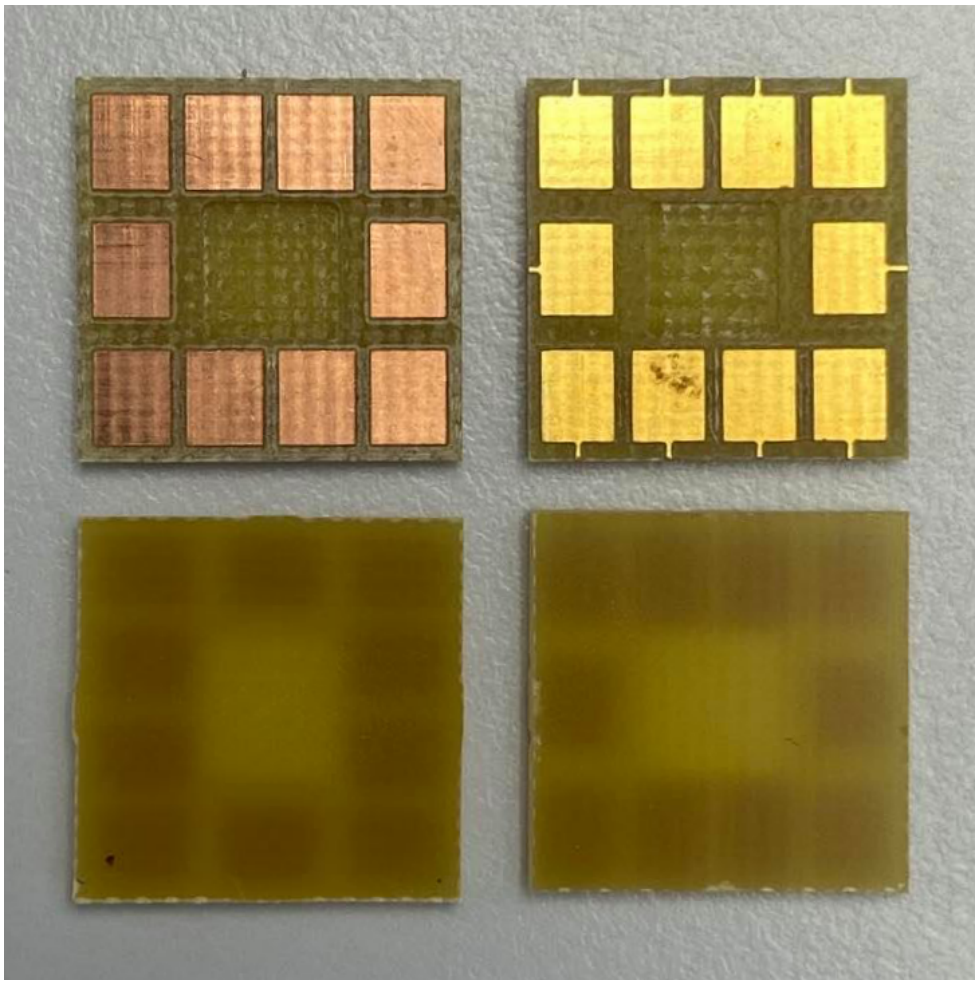

Figure 6.9: PCB sample holders for scanning magnetometry of micron-scale currents. Single sided PCB is used to limit screening of the high frequency magnetic field produced by the antenna. The contacts are gold plated to improve conductivity.

6.6 Remarks

While scanning probe magnetometry was not performed with the time available, substantial progress has been made toward performing the first measurements with this instrument. The first measurements focused on the probe in free space to limit damage to the probe in the event that the phase-locked loop (PLL) or PI controls were set incorrectly. While the free-space approach limited probe damage and potentially prolonged the life of the probe for future use, the floating probe proved vulnerable to drift, affecting optical experiments with long acquisition times. In addition to the probe being vulnerable to drift in free space, this approach also represented a challenge in positioning the NV centre close to the MW source. In this instrument, the MW source is fixed to the sample plane, which ensures the MW power is always large when imaging a sample on the surface. As a result, the MW power is substantially lower when the probe is above the sample.

6.7 Summary

To summarise this chapter has focused on the progress made in this instrument towards performing scanning NV magnetometry. Alignment procedures have been developed to align the 200 nm optically active region of a commercially available scanning NV centre probe with the confocal microscope of this instrument. The measurement protocols for different magnetic imaging modalities have been discussed along with and how they will be realised in this instrument. Finally, suitable test samples have been identified with the expected response of instrument considered.

Chapter 7

Optical Characterisation: Hexagonal Boron Nitride

7.1 Introduction

The development of this instrument was motivated by applications requiring the implementation of high-spatial-resolution magnetometry, specifically the measurement of magnetic fields produced by micron-scale conductors that form atom chips. The magnetometer required the development and synchronous operation of a confocal microscope, to collect NV centre PL, and an atomic force microscope (AFM), to scan an NV centre for magnetic imaging. The constituent parts of the instrument provide a range of imaging modalities that provide complementary tools to investigate samples on the sub-micron scale. In particular, this instrument has been optimised to collect optical emission in the 600-750 nm range and investigate the spectral, temporal, and spatial characteristics of such an emitter.

This chapter demonstrates the how this multi imaging mode instrument has applications beyond scanning probe NV centre magnetometry, particularly the investigation of single-photon emitters, by presenting preliminary results from optical experiments on a 2D material, hexagonal boron nitride (hBN). While this chapter focuses on emitters in hBN,

it also provides a blueprint for optical characterisation of any localised emitter that luminescences in the 600-750 nm detection band of this instrument, which could theoretically be extended to 350-900 nm with minor hardware changes.

7.2 Hexagonal Boron Nitride (hBN)

Hexagonal boron nitride (hBN) is a layered material with a wide bandgap material (6eV) that consists of an equal number of sp^2 boron and nitrogen atoms bonded in a hexagonal structure [153]. The interaction between adjacent layers is of the weak van der Waals type and thus has a structural composition similar to that of graphene. hBN based devices have a wide range of applications which are discussed at length in the paper of Lopes [153]. In particular, hBN shows promise due to its use in van der Waals heterostructures where a thin hBN layer can act as an ultra-smooth substrate [154], an encapsulating layer [155] or a tunnelling barrier [156].

Hexagonal boron nitride (hBN) has been shown to host stable defects that are optically active at room temperature [157, 158, 159]. However, the exact structure of the defect and the role of the fabrication process for introducing the defects in a controllable manner is an active area of research [160]. The further investigation of localised defects in hBN showed that the emission corresponded to some of the brightest single-photon emitters observed at room temperature, with MHz count rates for $\sim 100\,\mu W$ excitation power [157]. The observation of single-photon sources from 2D materials is of great interest as the photon collection efficiency can be greater than for defects hosted in bulk materials, including NV centres in bulk diamond, where total internal reflection reduces the collection efficiency [96]. In addition to hosting bright single-photon emitters at room temperature, hBN displays a range of interesting optical properties. A complete discussion of the functionality and applications of photonics from defects in hBN is available in the paper of Caldwell et al. [161].

The instrument is an ideal tool to probe the nature of defects in hBN, with Chapter

3 demonstrating the ability to measure the spectral, spatial and temporal properties from diffraction-limited sources excited by 515 nm light. Here I present preliminary findings from a 7.18 ±0.05 nm thick layer of hBN grown on silicon carbide (SiC) substrate that was cut at 8°. The sample was produced using high-temperature molecular beam epitaxy (HT-MBE) at a growth temperature of 1390 °C. During the MBE growth, the N_2 flow was 2 sscm while the boron flux generated by a high-temperature Knudsen source at 1875 °C. This sample, reference number - hBN125, was produced by Dr Tin Cheng and Professor Sergei Novikov at the School of Physics and Astronomy at the University of Nottingham.

7.3 Optical Characterisation

7.3.1 Wide-Field Microscopy

The first observations of any sample to be characterised in this instrument are performed with the microscope configured in 100% wide-field operation and 0% confocal operation. In this mode of operation, high contrast (compared 50%/50% confocal/wide-field splitting) images with a large field of view are produced that update with video frame rates. The use of the wide-field mode allows the targeting of devices with small regions of interest prior to further investigation using confocal microscopy. The dimensions of the hBN sample are ≈ 10 mm x ≈ 5 mm, substantially larger than the 50 µm x 50 µm scan range of the confocal microscope, with the sample anticipated to be largely uniform. As there is no specific target or reference marks on the hBN sample, the wide-field microscope is used to produce images of the sample to identify surface contaminants several microns in size. The identified features can then either be avoided during confocal operation, or aligned with the sample scanning FOV, to provide a positional reference. Figure 7.1 shows a typical wide-field image of the hBN sample surface featuring surface contaminants.

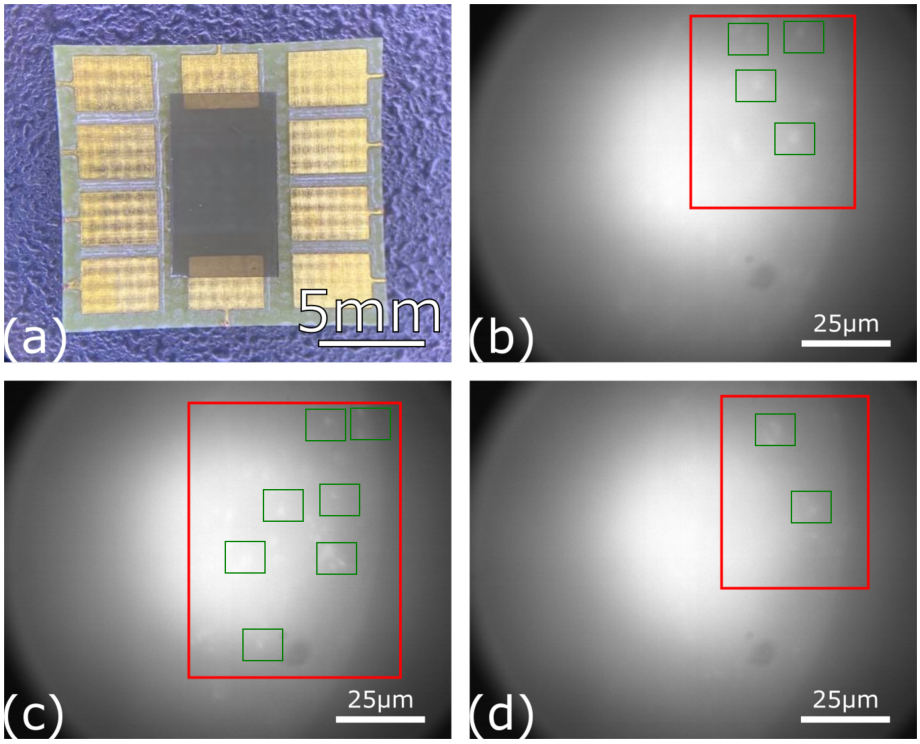

Figure 7.1: (a) Optical microscope image of hBN125, hBN film on SiC substrate sample. (b), (c) and (d) show wide-field images taken using the instrument of different regions of the sample. The red box highlights areas where large surface features likely to correspond to surface contamination can be seen, with the smaller green boxes highlighting specific features.

7.3.2 Confocal Microscopy

The primary motivation for the investigation of hBN samples using this instrument is to characterise the nature of recently observed optically active defects [157]. Therefore spatial maps of the PL were first produced to identify any localised emission. However, the confocal microscope was first focused in reflectance mode, as this ensured a large signal for focusing. In order to focus with the confocal microscope configured for PL collection the xy position of a PL source must be known, this is often not the case when an initial scan is recorded; for example, searching for NV centres in nanodiamonds dispersed on a substrate with low density.

Following focusing in reflectance mode, the confocal microscope is reconfigured into PL mode through the replacement of ND filters after the dichroic mirror, with a notch and long-pass filter (see Chapter 2 for optical diagram and part numbers). As a result, the confocal microscope has a typical collection window of $\approx$ 600-750 nm for PL measurement, depending on the specific filters used. To characterise unknown defects, initially, laser powers $\sim$100 µW are used; significantly greater power has the potential to bleach even photostable emitters. Figure 7.2 shows typical scans of the hBN on SiC substrate.

Figure 7.2(a) and (b) show two xy scans performed on the hBN on SiC substrate sample. The size of the emitter, $\Delta x \approx 2$ µm x $\Delta y \approx 5$ µm in Figure 7.2(a) suggests this PL source is likely to be from a surface contaminant rather than from emission originating from the hBN. Figure 7.2(c) shows a depth scan of emitter 1, with the y value fixed at the position of greatest intensity in 7.2(a). The scan is shown with a logarithmic colour scale to enhance the contrast between the weak background and the bright emitter. The scan confirms the PL source is from a source is located ≈ 2 µm above the surface and therefore a surface contaminant. This emitter was not characterised further. Figure 7.2(b) shows a second scan of the hBN surface in which a smaller emitter was identified, labelled 2 in figure 7.2(b). A depth scan was recorded to determine if the PL originates from the hBN layer, this is shown in Figure 7.2(d). The PL source was found to be within ≈ 1 µm of the surface. The spatial profile of emitter 2, shown in 7.2(b) and 7.2(d), corresponds to the

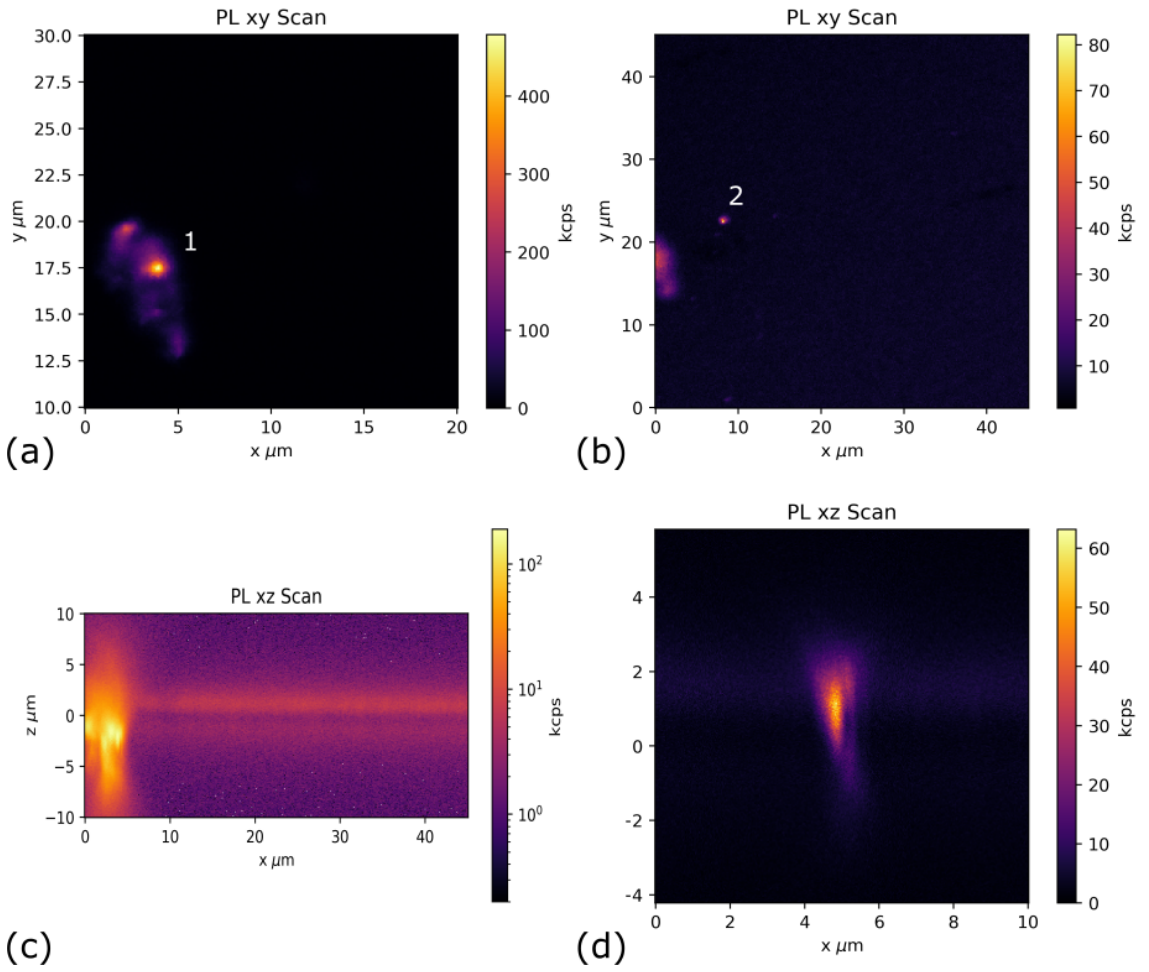

Figure 7.2: (a) xy confocal scans of hBN on SiC substrate. (a) shows an extended PL source, labelled emitter 1, approximately 5 µm in length and 2 µm wide. (b) xy scan of sample approached 2 µm towards the MO compared to (a). Emitter 2 corresponds to PL from a diffraction limited spot size. (c) xz scan of emitter 1 confirming the PL source is 2 µm above the sample surface and therefore not likely to correspond to a defect in hBN. A log colour scale is used to enhance the contrast between the bright emitter and weak background (d) xz scan focused on emitter 2, the emitter is shown to be close to the surface, within the ≈ 1 µm axial resolution of the confocal microscope. The background count from the surface can be seen as thin blue band.

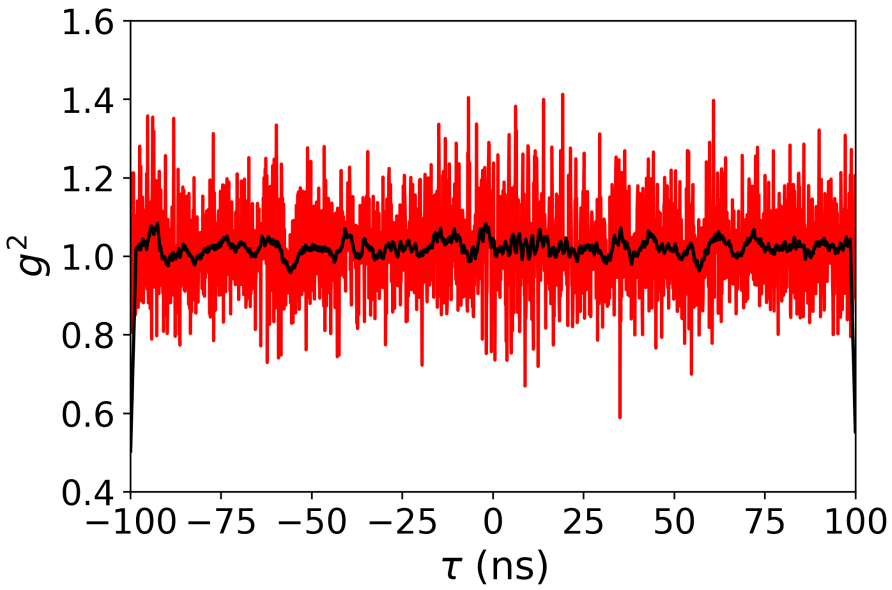

Figure 7.3: g^2 measurement from diffraction limited PL source (labelled emitter 2 in Figure7.2) in hBN on SiC. Total integration time was 2000 s. The black line shows a 30 point moving average.

diffraction limited size consistent with the source being a single photon emitter.

7.3.3 Single Photon Detection

To determine whether emitter 2 corresponded to emission from single photon emitter, the second order correlation function was measured using HBT interferometry. To perform g^2 measurements in this instrument a series of small range xyz confocal scans are first performed, with the scan stages set to the position of the recorded maximum intensity along each axis. The SPAD signal is then redirected from a NI card, used to integrate the counts for confocal scanning, into a time correlated single photon counting module, see Chapter 3 for an in-depth discussion of the hardware configuration. Figure 7.3, shows second order correlation function measurement. The PL signal from emitter 2 was not attributed to a single photon emitter as g^2 was not measured below the single emitter threshold of $g^2 = 0.5$.

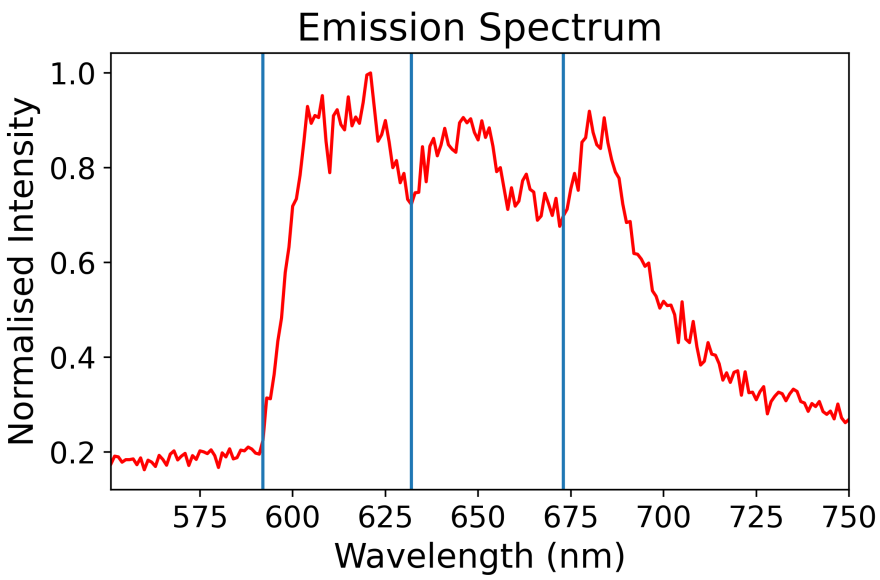

Figure 7.4: Emission spectrum of the object labelled as emitter 2 in Figure 7.2. The grating was scanning in 1 nm steps with a 4 second measurement time per step.

7.3.4 Emission Spectroscopy

To record emission spectra in this instrument the xyz position of the sample under the confocal microscope is first optimised by performing a series of small xyz scans, with the sample position then set to the identified maximum. The fiber from the confocal aperture is removed from the SPAD detection box and then directed into the spectrometer, see Chapter 3 for a more detailed discussion. The emission spectrum from emitter 2 (see Figure 7.2) was record from 550-750 nm with the PL signal recorded in 1 nm wavelength bins, with a 4 second integration time per bin. Figure 7.4 shows the recorded emission spectrum of emitter 2, in which three isolated peaks can be seen. The appearance of three distinct peaks suggests emitters with 3 different energy levels are contributing to the PL measurement. The blue lines shown in Figure 7.4 correspond to estimates of the zero phonon line associated with each isolated peak and are shown at 592 nm, 632 nm and 673 nm. However, the zero phonon of the lowest wavelength emitter could be significantly lower than 592 nm, with frequencies lower than 593 nm greatly attenuated by the long pass filter on the detection path. While the observation of a single peak in the emission spectrum

would not confirm single photon emitters, the observation of three peaks is consistent with the recorded g^2 measurement shown in 7.3, showing this is not a single photon source.

7.4 Discussion

The sample investigated here, hBN125 grown on a SiC with the Si face orientated at 8° has also been investigated by the group of Professor Igor Aharonovich at the School of Mathematical and Physical Sciences at the University of Technology Sydney. The investigation of this sample and others with a range of growth conditions by Professor Aharonovich found that that the inclusion of carbon atoms in the hBN is required to observe single-photon emission [160]. In the study, two samples produced by Dr Tin Cheng and Professor Sergei Novikov at the School of Physics and Astronomy at the University of Nottingham were investigated with reference numbers hBN125 and hBN124, with both samples grown under the same conditions (described at the start of the chapter). However, in hBN125, the sample investigated in this chapter, the Si face of the SiC substrate was orientated at 8° during MBE growth while hBN the Si face was orientated at 0°. Significantly, more single-photon emitters were found in hBN125 than in hBN124 by Professor Aharonovich's group and this was attributed to variance in the amount of carbon incorporated into the hBN from the diffusion of carbon from the SiC substrate during growth [160].

The investigation of hBN125 using this instrument did not observe single-photon emission. However, only a single emitter was characterised from this sample and further investigation of this may lead to the observation of single-photon emitters. The emission spectrum recorded by this instrument from hBN125 shows 3 isolated peaks, which is in agreement with emitters in hBN125 measured by Professor Aharonovich's group [160]. The reproduction of the findings of published work demonstrates the potential of this instrument for future investigations of potential single-photon emitters in 2D materials.

7.5 Summary

To summarise, preliminary measurements have been made on hBN on a SiC substrate, providing a demonstration of this instrument as a tool to characterise samples on a sub-micron length scale. Confocal microscopy was performed and identified PL from a diffraction-limited spot size in hBN, showing the instrument's capability to observe localised PL sources. The measurement of the second-order correlation function and emission spectrum of the same PL source demonstrates the functionality of the instrument to measure spectral and temporal characteristics of localised luminescent sources emitting in the 600-750 nm band. So far, only a single emitter has been characterised, and single-photon emission behaviour was not observed. Further investigation of this sample is required to determine the nature of the optically active defects across the whole area of this sample. Future work on both this sample and similar samples, such as flakes and thin films with localised luminescence, could also include investigation using the AFM integrated into the instrument. The combined AFM/confocal imaging mode, either operated sequentially or simultaneously, is particularly beneficial for correlating topography/PL measurements on samples such as films or flakes which do not have obvious reference marks. This instrument has also previously been used to measure electroluminescence from exfoliated layers of hBN placed between two thin layers of graphene connected to gold contacts [162]. While simultaneous AFM and confocal operation was not developed at this time, the AFM component of this instrument has been shown to detect flakes thinner than the 3 nm noise floor. The sub noise floor imaging was possible as when an Akiyama probe was operated in constant drive mode, the dissipation of energy from the probe was less above a thin hBN flake than above the silicon dioxide substrate [162]. The observation of localised luminescence in this chapter combined with the previous demonstration of electroluminescence measurements and AFM imaging of thin flakes demonstrate the potential of this instrument for future experiments investigating 2D materials.

Chapter 8

Conclusion

8.1 Conclusion

This thesis has focused on the design, assembly and operation of a custom-built instrument for characterising samples on the nanoscale based on a scanning NV centre magnetometer. While this instrument has not yet been used to produce 2D magnetic field maps, significant progress has been made in the development of the hardware and experimental control sequences required; including the assembly of a custom-built confocal microscope and atomic force microscope system that can be operated simultaneously. To complete the hardware requirements for scanning NV magnetometry, this instrument has been equipped with a robust microwave delivery system and a rotational mount to apply magnetic bias fields with a range of strengths and orientations at the microscope focus. In the last couple of months of the project, work began to perform scanning probe magnetometry with specialist AFM probes for scanning NV magnetometry that recently became commercially available. Procedures for nanoscale probe-instrument alignment were developed along with experimental routines to perform scanning probe magnetometry. Performing magnetometry in the very near future with this instrument is straightforward with the functionality of all the components demonstrated through the observation of optically detected magnetic resonance in nanodiamonds.

The ability of the instrument to measure the spectral, spatial and temporal characteristics of luminescent sources and correlate the optical measurements with topographical measurements from the AFM open up a wide range of applications for this instrument. In particular, the measurement of single-photon sources, such as deep band gap defects in hexagonal boron nitride (hBN).

8.2 Summary of Work

A custom-built confocal microscope with the aim of collecting photoluminescence for NV centre magnetometry has been constructed. The confocal microscope is primarily operated in sample scanning mode giving a measurement area of 50 µm x 50 µm. The optical signal from the confocal microscope can either be backscattered 515 nm laser light or photoluminescence in the 600-750 nm range (which can easily be extended to 350-900 nm with minor hardware modifications). When operated in PL mode, the primary mode of operation, the lateral spatial resolution was shown to be ≤ 500 nm and ≈ 1.7 µm along the optical axis. The functionality of the confocal microscope was extended further with the addition of a spectrometer and a Hanbury-Brown-Twiss (HBT) interferometer, enabling the investigation of temporal and spectral characteristics from diffraction-limited luminescent sources. The performance of the spectrometer was first shown using a red LED with a known profile, while the HBT interferometer was used to verify photoluminescence corresponded to the emission from two dipole emitters. Finally, a diffraction-limited wide-field microscope was incorporated into the instrument without degrading confocal performance.

A custom AFM system was developed to work simultaneously with the confocal microscope in ambient conditions, for eventual scanning NV centre magnetometry. The xy scan range is 50 µm by 50 µm with a z range of 50 µm, which is significantly larger than in many commercial AFMs. The large range in the z-axis was chosen to enable scanning NV magnetometry on atom chips, which have features that are several microns tall, with the region several microns above the sample also of interest for scanning NV magnetometry measurements. The performance of the AFM, when operated with an Akiyama probe (the

primary probe for AFM measurement) was demonstrated using a calibration sample and the noise floor calculated as $\approx 3\,\text{nm}$. The ability to perform confocal microscopy simultaneously during an AFM measurement was demonstrated by presenting measurements from a test sample of nanodiamonds deposited onto a $Si/Si0_2$ substrate. The dual-mode of operation shows that optical measurements from the confocal microscope and topographical measurements from the AFM can be correlated with sub-micron accuracy and that the tightly controlled tip-sample distance during a scan acts to refocus the MO with changes in sample topography.

Chapter 5 introduced the final instrumentation required to observe optically detected magnetic resonance in NV centres for magnetometry. The design of a mechanically robust system for high power microwave generation, based on a planar coil was presented along with a custom-built rotational mount for bias field generation. The rotational mount produced is capable of generating 1-10 mT (depending on the magnet used) in a range of radial orientations. The first measurements of optically detected magnetic resonances from photoluminescent sources in nanodiamonds were presented in Chapter 5, contrasts of up to 50% were observed and sufficient microwave power was generated to saturate the resonance. While this signal has not yet been attributed to NV centres, it demonstrates the capability to perform ODMR on an NV centre should one be addressed.

The progress made towards scanning NV centre magnetometry utilising a commercially available AFM probe is presented in Chapter 6. Procedures for aligning the active area of the probe with nanometer precision in this instrument were discussed. Finally, the design of test samples for the scanning probe magnetometer were presented.

This thesis's final chapter presents an investigation into localised photoluminescence in hexagonal boron nitride (hBN). A diffraction-limited region of localised emission from hBN was identified in a thin film of hBN on a silicon carbide substrate via confocal microscopy. The second-order correlation function of the localised source was measured, and it was not found to correspond to emission from a single-photon source. However, this chapter demonstrated the capability to investigate potential single-photon sources in 2D materials.

The emission spectrum was recorded for the region of localised photoluminescence and showed three distinct peaks, suggesting three energy levels contributed to the PL signal.

8.3 Future Work

The most immediate development for this instrument will be to demonstrate this instrument's functionality in scanning NV magnetometry mode. Following the observation of the ODMR response, the magnetometer's sensitivity can be estimated from features of the resonance, namely the contrast, linewidth and count rate. It is anticipated that in CW-ODMR, the sensitivity will be around $\sim 1\,\mu\mathrm{T}/\sqrt{\mathrm{Hz}}$.

The NV centres' orientation in the probe can then be determined by monitoring the ODMR response for a range of different magnetic field orientations and strengths at the confocal microscope. With the NV centre quantisation in the lab reference frame known, the magnetic sensing orientation will be determined, providing an insight into the sample and the selection of an appropriate bias field direction. The first samples imaged will be a magnetic hard disk, with the response compared to the simulation discussed in Chapter 7. The second sample measured will be the magnetic fields in micron-sized wires mounted onto the contact structures discussed in Chapter 6.

The future work associated with this project can be considered in terms of two distinct goals; the further development and optimisation of this instrument and future investigations utilising this versatile instrument.

8.3.1 Instrumental Development

Optical Instrumentation

The confocal microscope could be improved with a more accurate method to position the scan and tube lens, which would enable more accurate alignment and, therefore, improve the collection efficiency. A method to increase the precision in which the laser beam's angle

and position relative to the MO can be controlled would also offer greater control over the alignment process, helping to maximise performance, both in terms of collection efficiency and beam scanning field of view.

Hardware improvements could include the addition of a piezoelectric xy stage to scan the microscope objective in-plane above the sample. Scanning the MO provides a method to scan the beam in the sample plane without significantly modifying the optical path, as is the case with galvanometric scanning mirrors. While this approach would not offer an increased range compared to sample scanning, it provides a method of fine alignment between the confocal microscope and AFM in the case where the probe must remain fixed.

Additional hardware improvements include the integration of electronic switches to route the SPAD signal between the NI card for spatial mapping and the Picoharp 'time-tagger' for g^2 measurements. Currently, the output from the SPADS is physically migrated between the input terminals of the NI card and 'time-tagger', and the use of a high-speed switch would enable remote and time-efficient switching between imaging modes without compromising signal integrity.

The introduction of a cooled CCD in the spectrometer would enable the spatial and spectral profiling of weak emitters as well as shortening the acquisition times for measuring spectra in this instrument.

Finally, the wide-field camera could be extended up to the theoretical limit of the MO (265 µm) with an alternative camera and relay lens pair.

AFM

The AFM in this instrument was shown to have a noise floor of 3 nm. However, the dominant source of the z noise was not identified. The instrumental development of the AFM includes measuring the power spectrum of the noise on the AFM signal to identify key frequencies and thus determine the dominant noise sources. The resolution of the AFM could be improved by isolating and decreasing the sources of noise, which could include

improved vibrational isolation or implementing hardware changes along the detection signal line.

Scanning Probe Magnetometer

Scanning probe magnetometry will first be performed in this instrument using Qnami Quantilever probes operating in FM-AFM mode. The Q factor of a Quantilever was measured to be ≈ 120, an order of magnitude less than a bare tuning fork. To increase the Q for improved AFM operation, a mass equal to that of the quartz rod and cantilever could be added to the unloaded tine to rebalance the tuning fork, thus increasing the Q factor.

The most sensitive magnetometry using NV centres utilises the pulsed application of the laser and microwaves. The production of experimental routines would increase the sensitivity towards the fundamental limit, set by the linewidth of the ODMR resonance ($\sim 10\,\mathrm{nT}/\sqrt{\mathrm{Hz}}$).

8.3.2 Applications

Scanning NV Magnetometry

A key goal for this instrument is to investigate the performance of atom chip devices by measuring the magnetic trapping potential above the chip. Following measurement of the trapping potential via the scanning NV magnetometer, the local current density within the atom chip conductors can be determined via numerical inversion of the Biot-Savart law [163]. Imaging the spatial variation of the current density in the chip would provide rapid feedback on the fabrication process enabling devices with improved performance to be fabricated in future.

The scanning probe NV magnetometer will also be used to investigate the magnetic properties of spintronic devices fabricated within the School of Physics at the University

of Nottingham. In such devices, information is stored in magnetic order, and the study of experimental structures is motivated by their potential in producing scalable devices for computer memory. The properties that make spintronic devices promising for magnetic memory applications, such as small domain sizes and weak stay fields, can make such devices challenging to measure with conventional techniques. As such, the scanning probe NV magnetometer represents a promising tool to observe magnetic order in spintronic devices. There are two main types of spintronic devices currently being developed within the School of Physics and Astronomy at the University of Nottingham that will be investigated using this instrument.

Professor Andrew Rusthforth's research group focuses on developing devices that manipulate the magnetic order in magnetostrictive materials such as Iron Galium (FeGa). The devices consist of a piezoelectric element used to apply strain control to the magnetic order in the FeGa [164].

The second type of spintronic device produced at Nottingham is based on antiferromagnetic materials. In particular, devices fabricated from copper manganese arsenide (CuMnAs), which have shown considerable potential for antiferromagnetic based memory [165].

Multimode Imaging

The instrument's ability to measure the spectral, spatial and temporal characteristics of luminescent sources and correlate the optical measurements with topographical measurements from the AFM open up a wide range of applications for this instrument. In particular, the measurement of optically active defects in hexagonal boron nitride. One source for such materials is the Nottingham high-temperature MBE (HT-MBE) group that continues to research the growth and doping of hBN and heterostructures of hBN and graphene.

A new research program in Nottingham is aiming to grow Indium Selenide by MBE, and this instrument provides the ideal tool to characterise such devices. The ability to cor-

relate topographic information acquired via dynamic AFM measurements with the study of luminescent properties is a powerful combination for samples, such as InSe flakes and devices, which do not have defined location markers.

The instrument has been designed to measure ODMR from NV centres and, as such, is well suited to measure ODMR for other point defects. The observation of ODMR from defects of unknown composition can provide information on the defect structure as well as demonstrate the potential of the defect for use in quantum information and sensing applications [166]. For example, in 2019, ODMR was measured at room temperature from point-like defects in hBN [167, 168].

Bibliography

[1] E. Boto, N. Holmes, J. Leggett, G. Roberts, V. Shah, S. S. Meyer, T. M. Tierney L. Duque Muñoz, K. J. Mullinger, S. Bestmann, G. R. Barnes, R. Bowtell, and M. J. Brookes. Moving magnetoencephalography towards real-world applications with a wearable system. *Nature*, **555**:657–661, (2018).

[2] K. Chang, A. Eichler, J. Rhensius, L. Lorenzelli, and C. L. Degen. Nanoscale imaging of current density with a single-spin magnetometer. *Nano. Lett.*, **17**:2367–2373, (2017).

[3] M. Keil, O. Amit, S. Zhou, D. Groswasser, Y. Japha, and R. Folman. Fifteen years of cold matter on the atom chip: promise, realizations, and prospects. *J. Mod. Opt.*, **63**:1840–1885, (2016).

[4] J. Reichel and V. Vuletic. *Atom Chips*. WILEY-VCH Verlag GmbH & CO. KGaA, Weinheim, Germany, (2011).

[5] W. Ketterle and Pritchard D. E. Trapping and focusing ground state atoms with static fields. *Appl. Phys. B*, **54**:403–406, (1992).

[6] T. Calarco, E. A. Hinds, D. Jaksch, J. Schmiedmayer, J. I. Cirac, and P. Zoller. Quantum gates with neutral atoms: Controlling collisional interactions in time-dependent traps. *Phys. Rev. A*, **61**:022304, (2000).

[7] M. H. Anderson, J. R. Ensher, M. R. Matthews, C. E. Wieman, and E. A. Cornell. Observation of bose-einstein condensation in a dilute atomic vapor. *Science*, **269**:198–201, (1995).

[8] J. Fortágh, H. Ott, S. Kraft, A. Günther, and C. Zimmermann. Surface effects in magnetic microtraps. *Phys. Rev. A*, **66**:041604, (2002).

[9] J. Fortágh and C. Zimmermann. Magnetic microtraps for ultracold atoms. *Rev. Mod. Phys.*, **79**:235–289, (2007).

[10] P. Krüger, S. Wildermuth, S. Hofferberth, L. M. Andersson, S. Groth, I. Bar-Joseph, and J. Schmiedmayer. Cold atoms close to surfaces: measuring magnetic field roughness and disorder potentials. *J. Phys. Conf. Ser.*, **79**:56–65, (2005).

[11] D. Bartoszek-Bober, R. Panas, and T.Kawalec. Magnetic trapping on an atom chip. *Photonics Lett. Pol.*, **5**:109–11, (2013).

[12] S. Groth, P. Krüger, S. Wildermuth, R. Folman, T. Fernholz, J. Schmiedmayer, D. Mahalu, and I. Bar-Joseph. Atom chips: Fabrication and thermal properties. *App. Phys. Lett.*, **85**:2980–2982, (2004).

[13] A. Kasper, S. Schneider, Ch vom Hagen, M. Bartenstein, B. Engeser, T. Schumm, I. Bar-Joseph, R. Folman, L. Feenstra, and J. Schmiedmayer. A bose-einstein condensate in a microtrap. *J. Opt. B: Quantum Semiclass.*, **5**:S143, (2003).

[14] T. Schumm, J. Estéve, C.Fig, J.-B. Trebbia, C. Aussibal, H. Nguyen, D. Mailly, I. Bouchoule, C. I. Westbrook, and A. Aspect. Atom chips in the real world: the effects of wire corrugation. *Eur. Phys. J. D*, **32**:171–180, (2005).

[15] J. Estéve, C. Aussibal, T. Schumm, C. Figl, D. Mailly, I. Bouchoule, C. I. Westbrook, and A. Aspect. Role of wire imperfections in micromagnetic traps for atoms. *Phys. Rev. A*, **70**:043629, (2004).

[16] Disordered Bose-E, M. D. Lukin, and E. Demler. Disordered bose-einstein condensates in quasi-one-dimensional magnetic microtraps. *Phys. Rev. Lett.*, **92**:076802, (2004).

[17] S. Aigner, L. Della Pietra, Y. Japha, O. Entin-Wohlman, T. David, R. Salem, R. Folman, and J. Schmiedmayer. Long-range order in electronic transport through disordered metal films. *Science*, **319**(5867):1226–1229, (2008).

[18] P. Krüger, L. M. Andersson, S. Wildermuth, S. Hofferberth, E. Haller, S. Aigner, S. Groth, I. Bar-Joseph, J., and Schmiedmayer. Potential roughness near lithographically fabricated atom chips. *Phys. Rev. A*, **76**:063621, (2007).

[19] F. Casola, T. van der Sar, and A. Yacoby. Probing condensed matter physics with magnetometry based on nitrogen-vacancy centres in diamond. *Nat. Rev. Mater.*, **3**:17088, (2018).

[20] M. Moore. Diamond: Natural. In *Reference Module in Materials Science and Materials Engineering*. Elsevier, (2016).

[21] A. M. Zaitsev. *Optical Properties of Diamond: A Data Handbook*. Springer-Verlag, Berlin Heidelberg, (2001).

[22] T. Lühmann, R. John, J. Meijer R. Wunderlich, and S. Pezzagna. Coulomb-driven single defect engineering for scalable qubits and spin sensors in diamond. *Nat. Commun.*, **10**:4956, (2019).

[23] D. D. Awschalom, R. Hanson, J. Wrachtrup, and B. B. Zhou. Quantum technologies with optically interfaced solid-state spins. *Nat. Photon.*, **12**:516–527, (2018).

[24] M. Berthel, O. Mollet, G. Dantelle, T. Gacoin, S. Huant, and A. Drezet. Photophysics of single nitrogen-vacancy centers in diamond nanocrystals. *Phys. Rev. B*, **91**:035308, (2015).

[25] M. W. Doherty, N. B. Manson, P. Delaney, F. Jelezko, J. Wrachtrup, and L. C. L. Hollenberg. The nitrogen-vacancy colour centre in diamond. *Phys. Rep.*, **528**:1–45, (2013).

[26] N. B. Manson, J. P. Harrison, and M. J. Sellars. Nitrogen-vacancy center in diamond: Model of the electronic structure and associated dynamics. *Phys. Rev. B*, **74**:104303, (2006).

[27] L. Robledo, H. Bernien, T. van der Sar, and R. Hanson. Spin dynamics in the optical cycle of single nitrogen-vacancy centres in diamond. *New J. Phys.*, **13**:025013, (2011).

[28] L. Rondin, J.-P. Tetienne, T. Hingant, J.-F. Roch, P. Maletinsky, and V. Jacques. Magnetometry with nitrogen-vacancy defects in diamond. *Rep. Prog. Phys.*, **77**:056503, (2014).

[29] N. Aslam, G. Waldherr, P. Neumann, F. Jelezko, and J. Wratchup. Photoinduced ionization dynamics of the nitrogenvacancy defect in diamond investigated by single-shot charge state detection. *Phys. Rev. B*, **15**:013064, (2013).

[30] G. Davies and M. F. Hamer. Optical studies of the 1.945 eV vibronic band in diamond. *Proc. R. Soc. Lond. A*, **348**:285–298, (1976).

[31] V. M. Acosta, A. Jarmola, E. Bauch, and D. Budker. Optical properties of the nitrogen-vacancy singlet levels in diamond. *Phys. Rev. B*, **82**:201202, (2010).

[32] J. F. Barry, J. M. Schloss, E. Bauch, M. J. Turner, C. A. Hart, L. M. Pham, and R. L. Walsworth. Sensitivity optimization for NV-diamond magnetometry. *Rev. Mod. Phys.*, **92**:015004, (2020).

[33] J.-P. Tetienne, L. Rondin, P. Spinicelli, M. Chipaux, T. Debuisschert, J.-F. Roch, and V. Jacques. Magnetic-field-dependent photodynamics of single NV defects in diamond: An application to qualitative all-optical magnetic imaging. *New J. Phys.*, **14**:103033, (2012).

[34] P. Kehayias, M. J. Turner, R. Trubko, J. M. Schloss, C. A. Hart, M. Wesson, D. R. Glenn, and R. L. Walsworth. Imaging crystal stress in diamond using ensembles of nitrogen-vacancy centers. *Phys. Rev. B*, **100**:174103, (2019).

[35] A. Dréau, M. Lesik, L. Rondin, P. Spinicelli, O. Arcizet, J.-F. Roch, and V. Jacques. Avoiding power broadening in optically detected magnetic resonance of single NV defects for enhanced DC magnetic field sensitivity. *Phys. Rev. B*, **84**:195204, (2011).

[36] M. W. Doherty, J. Michl, F. Dolde, I. Jakobi, P. Neumann, N. B. Manson, and J Wrachtrup. Measuring the defect structure orientation of a single NV^- centre in diamond. *New J. Phys.*, **16**:063067, (2014).

[37] R. J. Epstein, F. M. Mendoza, Y. K. Kato, and D. D. Awschalom. Anisotropic interactions of a single spin and dark-spin spectroscopy in diamond. *Nat. Phys.*, **1**:94–98, (2005).

[38] P. Maletinsky, S. Hong, M. S. Grinolds, B. Hausmann, M. D. Lukin, R. L. Walsworth, M. Loncar, and A. Yacoby. A robust scanning diamond sensor for nanoscale imaging with single nitrogen-vacancy centres. *Nat. Nanotechnol.*, **7**:320–324, (2012).

[39] J. F. Barry, M. J. Turner, J. M. Schloss, D. R. Glenn, Y. Song, M. D. Lukin, H. Park, and R. L. Walsworth. Optical magnetic detection of single-neuron action potentials using quantum defects in diamond. *PNAS*, **113**:14133–14138, (2016).

[40] N. Hedrich, D. Rohner, M. Batzer, P. Maletinsky, and B. J. Shields. Parabolic diamond scanning probes for single-spin magnetic field imaging. *Phys. Rev. App.*, **14**:064007, (2020).

[41] E. D. Herbschleb, H. Kato, Y. Maruyama, T. Danjo, T. Makino, S. Yamasaki, I. Ohki, K. Hayashi, H. Morishita, M. Fujiwara, and N. Mizuochi. Ultra-long coherence times amongst room-temperature solid-state spins. *Nat. Commun.*, **10**:3766, (2019).

[42] B. Naydenov, F. Dolde, L. T. Hall, C. Shin, H. Fedder, L. C. L. Hollenberg, F. Jelezko, and J. Wrachtrup. Dynamical decoupling of a single-electron spin at room temperature. *Phys. Rev. B*, **83**:081201, (2011).

[43] G. Balasubramanian, P. Neumann, D.Twitchen, M. Markham, R. Kolesov, N.Mizuochi, J. Isoya, J. Beck J. Achard, J. Tissler, V. Jacques, P. R. Hemmer, F. Jelezko, and J.Wrachtrup. Ultralong spin coherence time in isotopically engineered diamond. *Nat. Mater*, **8**:383–387, (2009).

[44] G. Balasubramanian, I. Y. Chan, R. Kolesov, M. Al-Hmoud, J. Tisler, C. Shin, C. Kim, A. Wojcik, P. R. Hemmer, A. Krueger, T. Hanke, A. Leitenstorfer, R. Bratschitsc, F. Jelezko, and J. Wrachtrup. Nanoscale imaging magnetometry with diamond spins under ambient conditions. *Nature*, **455**:648–651, (2008).

[45] S. Steinert, F. Dolde, P. Neumann, A. Aird, B. Naydenov, G. Balasubramanian, F. Jelezko, and J. Wrachtrup. High sensitivity magnetic imaging using an array of spins in diamond. *Rev. Sci. Instrum.*, **81**:043705, (2010).

[46] I. K. Kominis, T. W. Kornack, J. C. Allred, and M. Romalis. A subfemtotesla multichannel atomic magnetometer. *Nature*, **422**:596–599, (2003).

[47] F. Alghannam and P. Hemmer. Engineering of shallow layers of nitrogen vacancy colour centres in diamond using plasma immersion ion implantation. *Sci. Rep.*, **9**:5870, (2019).

[48] D. Collomb, L. Penglei, and S. J. Bending. Nanoscale graphene hall sensors for high-resolution ambient magnetic imaging. *Sci. Rep.*, **9**:14424, (2019).

[49] M. W. Morgan and S. P. Alvarez. Colloquium: Quantum limits to the energy resolution of magnetic field sensors. *Rev. Mod. Phys.*, **92**:021001, (2020).

[50] K. K. Chang. *Scanning Magnetometry with NV Centers in Diamond*. PhD thesis, ETH Zürich, (2016).

[51] J.L Webb, J. D. Clement, L. Troise, S. Ahmadi, G. J. Johansen, A. Huck, and U. L. Andersen. Nanotesla sensitivity magnetic field sensing using a compact diamond nitrogen-vacancy magnetometer. *Appl. Phys. Lett.*, **114**:231103, (2019).

[52] E. V. Levine, M. J. Turner, P. Kehayias, C. A. Hart, N. Langellier, R. Trubko, D. R. Glenn, R. R. Fu, and R. L. Walsworth. Principles and techniques of the quantum diamond microscope. *Nanophotonics*, **8**:1945 – 1973, (2019).

[53] L. Thiel, D. Rohner, M. Ganzhorn, P. Appel, E. Neu, B. Müller, R. Kleiner, D. Koelle, and P. Maletinsky. Quantitative nanoscale vortex imaging using a cryogenic quantum magnetometer. *Nat. Nanotechnol.*, **11**:677–681, (2016).

[54] K. Ohashi, T. Rosskopf, H. Watanabe, M. Loretz, Y. Tao, R. Hauert, S. Tomizawa, T. Ishikawa, J. Ishi-Hayase, S. Shikata, C. L. Degen, and K. M. Itoh. Negatively charged nitrogen-vacancy centers in a 5 nm thin 12c diamond film. *Nano Lett.*, **13**:4733–4738, (2013).

[55] M. Schaffry, E. M Gauger, J. J. L. Morton, and S. C. Benjamin. Proposed spin amplification for magnetic sensors employing crystal defects. *Phys. Rev. Lett.*, **107**:207210, (2011).

[56] B. M. Chernobrod and G. P. Berman. Spin microscope based on optically detected magnetic resonance. *J. App. Phys.*, **97**:014903, (2005).

[57] C. L. Degen. Scanning magnetic field microscope with a diamond single-spin sensor. *App. Phys. Lett.*, **92**:243111, (2008).

[58] J. M. Taylor, P. Cappellaro, L. Childress, L. Jiang, D. Budker, P. R. Hemmer, A. Yacoby, R. L. Walsworth, and M. D. Lukin. High-sensitivity diamond magnetometer with nanoscale resolution. *Nat. Phys.*, **4**:810–816, (2008).

[59] L. Rondin, J.-P. Tetienne, P. Spinicelli, C. Dal Savio, K. Karrai, G. Dantelle, A. Thiaville, S. Rohart, J.-F. Roch, and V. Jacques. Nanoscale magnetic field mapping with a single spin scanning probe magnetometer. *App. Phys. Lett.*, **100**:153118, (2012).

[60] J.-P. Tetienne, T. Hingant, L. J. Martínez, S. Rohart, A. Thiaville, L. Herrera Diez, K. Garcia, J.-P. Adam, J-V. Kim, J.-F. Roch, I. M. Miron, G. Gaudin, L. Vila, B. Ocker, D. Ravelosona, and V. Jacques. The nature of domain walls in ultrathin ferromagnets revealed by scanning nanomagnetometry. *Nat. Commun.*, **6**:6733, (2014).

[61] A. Cuche, A. Drezet, Y. Sonnefraud, O. Faklaris, F. Treussart, J.-F. Roch, and S. Huant. Near-field optical microscopy with a nanodiamond-based single-photon tip. *Opt. Express*, **17**:19969–19980, (2009).

[62] P. Appel, E. Neu, M. Ganzhorn, A. Barfuss, M. Batzer, M. Gratz, A. Tschöpe, and P. Maletinsky. Fabrication of all diamond scanning probes for nanoscale magnetometry. *Rev. Sci. Instrum.*, **87**:063703, (2016).

[63] Qnami. Quantilever specification. `https://qnami.ch/portfolio/quantilever-mx/`. Accessed 30 November 2020.

[64] Zabre. Quantum sensor tips. `https://qzabre.com/tips/`. Accessed 27 December 2020.

[65] I. Gross, W. Akhtar, V. Garcia, L. J. Martínez, S. Chouaieb, K. Garcia, C. Carrétéro, P. Appel A. Barthélémy, P. Maletinsky, J.-V. Kim, N. Jaouen J. Y. Chauleau, M. Viret, M. Bibes, S. Fusil, and V. Jacques. Real-space imaging of non-collinear antiferromagnetic order with a single-spin. *Nature*, **549**:252–256, (2017).

[66] T. Kosub, M. Kopte, R. Hühne, P. Appel, B. Shields, P. Maletinsky, R. Hübner, M. O. Liedke, J. Fassbender, O. G. Schmidt, and D. Makarov. Purely antiferromagnetic magnetoelectric random access memory. *Nat Commun.*, **8**:13985, (2017).

[67] A. Haykal, J. Fischer, W. Akhtar, J.-Y. Chauleau, A. Finco D. Sando, F. Godel, Y. A. Birkhölzer, C. Carrétéro, N. Jaouen, M. Bibes, M. Viret, S. Fusil, V. Jacques, and V. Garcia. Antiferromagnetic textures in bifeo3 controlled by strain and electric field. *Nat. Commun.*, **11**:1704, (2020).

[68] J.-Y. Chauleau, T. Chirac, S. Fusil, V. Garcia, W. Akhtar, J. Tranchida, P. Thibaudeau, I. Gross, C. Blouzon, A. Finco, M. Bibes, B. Dkhil, D. D. Khalyavin, P. Manuel, V. Jacques, N. Jaouen, and M. Viret. Electric and antiferromagnetic chiral textures at multiferroic domain walls. *Nat. Mater.*, **19**:386–390, (2020).

[69] Zabre. QSM – Quantum Scanning Microscope. `https://qzabre.com/microscope/`. Accessed 30 December 2020.

[70] Qnami. Proteusq specification. `https://www.horiba.com/en_en/products/detail/action/show/Product/proteusq-2011/`. Accessed 18 November 2020.

[71] A. Horsley, P. Appel, J. Wolters, J. Achard, A. Tallaire, P. Maletinsky, and P. Treutlein. Microwave device characterization using a widefield diamond microscope. *Phys. Rev. App.*, **10**:044039, (2018).

[72] I. Fescenko, A. Laraoui, J. Smits, N. Mosavian, P. Kehayias, J. Seto, L. Bougas, A. Jarmola, and V. M. Acosta. Diamond magnetic microscopy of malarial hemozoin nanocrystals. *Phys. Rev. App.*, **11**:034029, (2019).

[73] Y. Ruan, D. A. Simpson, J. Jeske, H. Ebendorff-Heidepriem, D. W. M. Lau, J. Hong, B. C. Johnson, T. Ohshima, S. V. Afshar, L. C. L. Hollenberg, A. D. Greentree, T. M. Monro, and B. C. Gibson. Magnetically sensitive nanodiamond-doped tellurite glass fibers. *Sci. Rep.*, **8**:1–6, (2018).

[74] M. Minksy. Memoir on Inventing the Confocal Scanning Microscope. *Scanning*, **10**:128–138, (1987).

[75] C. J. R. Sheppard and D. M. Shotton. *Confocal Laser Scanning Microscopy.* BIOS Scientific Publishers, Oxford, Great Britain, (1997).

[76] R. H. Webb. Confocal optical microscopy. *Rep. Prog. Phys.*, **59**:427–471, (1996).

[77] J. Pawley. *Handbook of Biological Confocal Microscopy.* Springer US, Springer, Boston, MA, (2006).

[78] T. Wilson and A. R. Carlini. Size of the detector in confocal imaging systems. *Opt. Lett.*, **12**:227–229, (1987).

[79] T. Wilson. Optical sectioning in confocal fluorescent microscopes. *J. Microsc.*, **154**(2):143–156, 1989.

[80] Thorlabs. Thorlabs microscope objective tutorial. `https://www.thorlabs.com/newgrouppage9.cfm?objectgroup_id=1044`. Accessed 10 March 2021.

[81] S. A. Momenzadeh, R. J. Stöhr, F. F. de Oliveira, A. Brunner, A. Denisenko], S. Yang, F. Reinhard, and J. Wrachtrup. Nanoengineered diamond waveguide as a robust bright platform for nanomagnetometry using shallow nitrogen vacancy centers. *Nano Lett.*, **15**:165–169, (2015).

[82] J. M. Binder, A. Stark, N. Tomek, J. Scheuer, F. Frank, K. D. Jahnke, C. Müller, S. Schmitt, M. H. Metsch, T. Unden, T. Gehring, A. Huck, U. L. Andersen, L. J. Rogers, and F. Jelezko. Qudi: A modular python suite for experiment control and data processing. *SoftwareX*, **6**:85–90, (2017).

[83] openDACS. Seekat (arduino duo). `http://opendacs.com/`. Accessed 7 February 2021.

[84] Analog Devices. Ad5764 specification. https://www.analog.com/media/en/technical-documentation/data-sheets/AD5764.pdf. Accessed 08 March 2021.

[85] D. Nečas and P. Klapetek. Gwyddion: an open-source software for spm data analysis. *Cent. Eur. J. Phys.*, **10**:181–188, (2012).

[86] C. J. Cogswell, C. J. R. Sheppard, M. C. Moss, and C. V. Howard. A method for evaluating microscope objectives to optimize performance of confocal systems. *J. Microsc.*, **158**:177–185, (1990).

[87] A. Beveratos, R. Brouri, T. Gacoin, J.-P. Poizat, and P. Grangier. Nonclassical radiation from diamond nanocrystals. *Phys. Rev. A*, **64**:061802, (2001).

[88] Olympus. Lmplflnx100 sepcification. https://www.olympus-ims.com/en/microscope/lmplfln/#!cms[focus]=cmsContent11413&cms[tab]=undefined. Accessed 11 March 2021.

[89] Semrock. Maxmirror ultra-broadband mirrors product data sheet. https://www.semrock.com/Data/Sites/1/semrockpdfs/IDX2657-SMK\%20MaxMirrorDataSheet-FIN-web.pdf. Accessed 9 March 2021.

[90] Semrock. 514 nm laser brightline® single-edge laser dichroic beamsplitter part number: Di02-r514-25x36 specification. https://www.semrock.com/FilterDetails.aspx?id=Di02-R514-25x36. Accessed 9 March 2021.

[91] Semrock. 514 nm stopline® single-notch filter part number: Nf03-514e-25 specification. https://www.semrock.com/filterdetails.aspx?id=nf03-514e-25. Accessed 9 March 2021.

[92] Semrock. 593 nm blocking edge brightline® long-pass filter part number: Ff01-593/lp-25 specification. https://www.semrock.com/filterdetails.aspx?id=ff01-593/lp-25. Accessed 9 March 2021.

[93] Thorlabs. Polkdot beam splitters specification. https://www.thorlabs.com/newgrouppage9.cfm?objectgroup_id=1110. Accessed 9 March 2021.

[94] Thorlabs. Ac127-030-a specification. https://www.thorlabs.com/newgrouppage9.cfm?objectgroup_id=120&pn=AC127-030-A#2200. Accessed 9 March 2021.

[95] Excelitas Technologies. Spcm-aqrh specification. https://www.excelitas.com/product/spcm-aqrh. Accessed 9 March 2021.

[96] D. Le Sage, L. M. Pham, N. Bar-Gill, C. Belthangady, M. D. Lukin, A. Yacoby, and R. L. Walsworth. Efficient photon detection from color centers in a diamond optical waveguide. *Phys. Rev. B*, **85**:121202, (2012).

[97] T. Plakhotnik, W. E. Moerner, V. Palm, and U. P Wild. Single molecule spectroscopy: maximum emission rate and saturation intensity. *Opt. Commun.*, **11**:83 – 88, (1995).

[98] D. Duan, G. X. Du, V. K. Kavatamane, S. Arumugam, Y.-K. Tzeng, H-C Chang, and G. Balasubramanian. Efficient nitrogen-vacancy centers' fluorescence excitation and collection from micrometer-sized diamond by a tapered optical fiber in endoscope-type configuration. *Opt. Express*, **27**:6734–6745, (2019).

[99] Olympus. Mplflnx100 sepcification. https://www.olympus-ims.com/en/microscope/mplfln/#!cms[focus]=cmsContent11391&cms[tab]=undefined. Accessed 11 March 2021.

[100] R. Hanbury Brown and R. Q. Twiss. Interferometry of the intensity fluctuations in light - i. basic theory: the correlation between photons in coherent beams of radiation. *Proc. Roy. Soc. Lon. A.*, **242**:300–324, (1957).

[101] M. D. Eisaman, J. Fan, A. Migdall, and S. V. Polyakov. Invited review article: Single-photon sources and detectors. *Rev. Sci. Instrum.*, **82**:071101, (2011).

[102] M. Fox. *Quantum optics: an introduction*. Oxford Univ. Press, Oxford, (2006).

[103] E. Suarez, D. Auwarter, T. J. Arruda R., Bachelard, P. W. Courteille, C. Zimmermann, and S. Slama. Photon-Antibunching in the fluorescence of statistical ensembles of emitters at an optical nanofiber-Tip. *New J. Phys.*, **21**:035009, (2018).

[104] R. Brouri, A. Beveratos, J.-P. Poizat, and P. Grangier. Photon antibunching in the fluorescence of individual color centers in diamond. *Opt. Lett.*, **25**:1294–1296, (2000).

[105] C. Wang, J. Wang, Z. Xu, J. Li, R. Wang, J. Zhao, and Y. Wei. Afterpulsing effects in SPAD-based photon-counting communication system. *Opt. Commun.*, **443**:202–210, (2019).

[106] C. Kurtsiefer, S. Mayer, P. Zarda, and H. Weinfurter. Stable solid-state source of single photons. *Phys. Rev. Lett.*, **85**:290–293, (2000).

[107] T. M. Babinec, B. J. M. Hausmann, M. Khan, Y. Zhang, J. R. Maze, P. R. Hemmer, and M. Lončar. A diamond nanowire single-photon source. *Nat. Nanotechnol.*, **5**:195–199, (2010).

[108] N. B. Manson, M. Hedges, M. S. J. Barson, R. Ahlefeldt, M. W. Doherty, H. Abe, T. Ohshima, and M. J. Sellars. $NV^- - N^+$ pair centre in 1b diamond. *New J. Phys.*, **20**:113037, (2018).

[109] NICHIA. Red led specification. `http://www.nichia.co.jp/en/product/led_product_data.html?type=\%27NESM026D\%27`. Accessed 8 February 2021.

[110] D. A. Simpson, J.-P. Tetienne, J. M. McCoey, K. Ganesan, L. T. Hall, S. Petrou, R. E. Scholten, and L. C. L. Hollenberg. Magneto-optical imaging of thin magnetic films using spins in diamond. *Sci. Rep.*, **6**:22797, (2016).

[111] NANOSENSORS. Akiyama-probe (a-probe) techincal guide. `https://www.akiyamaprobe.com/APROBE_TechNote_Dimensions_v2.pdf`. Accessed 18 November 2020.

[112] C. A. Schneider, W. S. Rasband, and K. W. Eliceiri. NIH Image to ImageJ: 25 years of image analysis. *Nat. Methods.*, **9**:671–675, (2012).

[113] Invitrogen. Focalcheck™fluorescence microscope test slides. `https://www.thermofisher.com/order/catalog/product/F36909#/F36909`. Accessed 21 February 2021.

[114] G. Binnig, H. Rohrer, Ch. Gerber, and E. Weibel. Surface studies by scanning tunneling microscopy. *Phys. Rev. Lett.*, **49**:57–61, (1982).

[115] G. Binnig, C. F. Quate, and Ch. Gerber. Atomic force microscope. *Phys. Rev. Lett.*, **56**:930–933, (1986).

[116] F. J. Giessibl. Advances in atomic force microscopy. *Rev. Mod. Phys.*, **75**:949–983, (2003).

[117] M. Z. Bazant, E. Kaxiras, and J. F. Justo. Environment-dependent interatomic potential for bulk silicon. *Phys. Rev. B*, **56**:8542–8552, (1997).

[118] F. Ohnesorge and G. Binnig. True atomic resolution by atomic force microscopy through repulsive and attractive forces. *Science*, **260**:1451–1456, (1993).

[119] Y. Martin, C. C. Williams, and H. K. Wickramasinghe. Atomic force microscope–force mapping and profiling on a sub 100-Å scale. *J. App. Phys.*, **61**:4723–4729, (1987).

[120] T. R. Albrecht, P. Grütter, D. Horne, and D. Rugar. Frequency modulation detection using high-q cantilevers for enhanced force microscope sensitivity. *J. App. Phys.*, **69**:668–673, (1991).

[121] F. J. Giessibl. The qplus sensor, a powerful core for the atomic force microscope. *Rev. Sci. Instrum.*, **90**:011101, (2019).

[122] F. J. Giessibl. A direct method to calculate tip-sample forces from frequency shifts in frequency-modulation atomic force microscopy. *App. Phys. Lett.*, **78**:123–125, (2001).

[123] F. J. Giessibl and H. Bielefeldt. Physical interpretation of frequency-modulation atomic force microscopy. *Phys. Rev. B*, **61**:9968–9971, (2000).

[124] F. J. Giessibl, H. Bielefeldt, S. Hembacher, and J. Mannhart. Calculation of the optimal imaging parameters for frequency modulation atomic force microscopy. *App. Surf. Sci.*, **140**:352–357, (1999).

[125] Q. Zhong, D. Inniss, K. Kjoller, and V. B. Elings. Fractured polymer/silica fiber surface studied by tapping mode atomic force microscopy. *Surf. Sci.*, **290**:L688–L692, (1993).

[126] V. Elings and J. Gurley. U. S. Patent No. 5,266,801, (1993).

[127] NANOSENSORS™. A-probe guide. `https://www.akiyamaprobe.com/AKIYAMA-PROBE_Guide_v2.pdf`. Accessed 9 February 2021.

[128] T. Akiyama, U. Staufer, and N. F. de Rooij. Self-sensing and self-actuating probe based on quartz tuning fork combined with microfabricated cantilever for dynamic mode atomic force microscopy. *App. Surf. Sci.*, **210**:18–21, (2003).

[129] A. Castellanos-Gomez, N. Agraït, and G. Rubio-Bollinger. Dynamics of quartz tuning fork force sensors used in scanning probe microscopy. *Nanotechnology*, **20**:215502, (2009).

[130] Piezoconcept. Lfhs2 specification. `http://www.piezoconcept.com/products-2-axis-stages/lfhs-2-2/`. Accessed 07 March 2021.

[131] Piezoconcept. Z-stage.50 specification. `http://www.piezoconcept.com/all-products/z-1/`. Accessed 07 March 2021.

[132] Park Systems. Park systems nx10 techincal information. `https://parksystems.com/products/small-sample-afm/park-nx10/technical-info`. Accessed: 14 December 2020.

[133] L. Childress, M. V. Gurudev Dutt, J. M. Taylor, A. S. Zibrov, F. Jelezko, J. Wrachtrup, P. R. Hemmer, and M. D. Lukin. Coherent dynamics of coupled electron and nuclear spin qubits in diamond. *Science*, **314**:281–285, (2006).

[134] M. Chipaux, A. Tallaire, J. Achard, S. Pezzagna, J. Meijer, J. F. Roch V. Jacques, and T. Debuisschert. Magnetic imaging with an ensemble of nitrogen-vacancy centers in diamond. *Eur. Phys. J. D*, **69**:166, (2016).

[135] K. Bayat, J. Choy, M. F. Baroughi, S. Meesala, and M. Loncar. Efficient, uniform and large area microwave magnetic coupling to NV centers in diamond using double split-ring resonators. *Nano Lett.*, **14**:1208–1213, (2014).

[136] N. Zhang, H. Yuan, C. Zhang, L. Xu, J. Zhang, G. Bian, P. Fan, H. Yuan, and J. Fang. Microwave field uniformity impact on DC magnetic sensing with NV ensembles in diamond. *IEEE Sens. J.*, **19**:451–456, 2019.

[137] N. Zhang, C. Zhang, L. Xu, M. Ding, W. Quan, Z. Tang, and H. Yuan. Microwave magnetic field coupling with nitrogen-vacancy center ensembles in diamond with high homogeneity. *Appl. Magn. Reson*, **47**:589–599, (2016).

[138] G. Mariani, S. Nomoto, S. Kashiwaya, and S. Nomura. System for the remote control and imaging of MW fields for spin manipulation in NV centers in diamond. *Sci. Rep*, **10**:4813, (2020).

[139] K. Sasaki, Y. Monnai, S. Saijo, R. Fujita, H. Watanabe, J. Ishi-Hayase, K. M. Itoh, and E. Abe. Broadband, large-area microwave antenna for optically-detected magnetic resonance of nitrogen-vacancy centers in diamond. *Rev. Sci. Instrum.*, **87**:053904, (2016).

[140] Corning. Macor properties. `https://www.corning.com/media/worldwide/csm/documents/71759a443535431395eb34ebead091cb.pdf`. Accessed 28 January 2021.

[141] S. Knauer and J. P. Hadden adn J. G. Rarity. In-situ measurements of fabrication induced strain in diamond photonic-structures using intrinsic colour centres. *npj Quantum Inf*, **6**:50, (2020).

[142] R.G. Dall and A.G. Truscott. Bose–einstein condensation of metastable helium in a bi-planar quadrupole ioffe configuration trap. *Opt. Commun.*, **270**:255–261, (2007).

[143] BUNTING E-MAGNETS. Neodymium rod magnets. `https://e-magnetsuk.com/product/neodymium-rod-magnets/`. Accessed 1 February 2021.

[144] J. M. Camacho and V. Sosa. Alternative method to calculate the magnetic field of permanent magnets with azimuthal symmetry. *Revista mexicana de física E*, **59**:8–17, (2013).

[145] A. Gruber, A. Dräbenstedt, C. Tietz, L. Fleury, J. Wrachtrup, and C. von Borczyskowski. Scanning confocal optical microscopy and magnetic resonance on single defect centers. *Science*, **276**:2012–2014, (1997).

[146] H.-J. Wang, C. S. Shin, S. J. Seltzer, C. E. Avalos, A. Pines, and V. S. Bajaj. Optically detected cross-relaxation spectroscopy of electron spins in diamond. *Nat. Commun.*, **105**:4135, (2014).

[147] K. Jensen, V. M. Acosta, A. Jarmola, and D. Budker. Light narrowing of magnetic resonances in ensembles of nitrogen-vacancy centers in diamond. *Phys. Rev. B*, **87**:014115, (2013).

[148] P. Rice, S. E. Russek, and B. Haines. Magnetic imaging reference sample. *IEEE Trans. Magn*, **32**:4133–4137, (1996).

[149] L. Quéval. Bsmag toolbox user manual. `http://www.lqueval.com`. Accessed 11 March 2021.

[150] R. Folman, P. Kruger, J. Schmiedmayer, J. Denschlag, and C. Henkel. Microscopic atom optics: From wires to an atom chip. *Adv. At., Mol. Opt. Phys.*, **48**:263, (2002).

[151] KLayout. Open source 2d cad software. `https://www.klayout.de/intro.html`. Accessed 19 March 2021.

[152] K. C. Balram, D. A. Westly, M. Davanco, K. E. Grutter, Q. Li, T. Michels, C. H. Ray, L. Yu, R. J. Kasica, C. B. Wallin, I. J. Gilbert, Brian A. Bryce, G. Simelgor, J. Topolancik, N. Lobontiu, Y. Liu, P. Neuzil, V. Svatos, K. A. Dill, N. A. Bertrand, M. Metzler, G. Lopez, D. A. Czaplewski, L. Ocola, K. A. Srinivasan, S. M. Stavis, V. A. Aksyuk, J. A. Liddle, S. Krylov, and B. R. Ilic. The nanolithography toolbox. *J. Res. Natl. Inst. Stand.*, **121**:464–475, (2016).

[153] J. Marcelo J. Lopes. Synthesis of hexagonal boron nitride: From bulk crystals to atomically thin films. *Prog. Cryst. Growth Charact. Mater.*, **67**:100522, (2021).

[154] C. R. Dean, A. F. Young, I. Meric, C. Lee, L. Wang, S. Sorgenfrei, K. Watanabe, T. Taniguchi, P. Kim, K. L. Shepard, and J. Hone. Boron nitride substrates for high-quality graphene electronics. *Nat Nanotechnol.*, **5**:722–726, (2010).

[155] A. S. Mayorov, R. V. Gorbachev, S. V. Morozov, L. Britnell, R. Jalil, L. A. Ponomarenko, P. Blake, S. K. Novoselov, K. Watanabe, T. Taniguchi, and A. K. Geim. Micrometer-scale ballistic transport in encapsulated graphene at room temperature. *Nano. Lett.*, **11**:2396–2399, (2011).

[156] L. Britnell, R. V. Gorbachev, R. Jalil, B. D. Belle, F. Schedin, A. Mishchenko, T. Georgiou, M. I. Katsnelson, L. Eaves, S. V Morozov, N. M. R. Peres, J. Leist, A. K. Geim, K. S. Novoselov, and L. A. Ponomarenko. Field-effect tunneling transistor based on vertical graphene heterostructures. *Science*, **335**:947–950, (2012).

[157] T. T. Tran, M. Toth K. Bray, M. J. Ford, and I. Aharonovich. Quantum emission from hexagonal boron nitride monolayers. *Nat. Nanotechnol.*, **11**:37–41, (2016).

[158] A. L. Exarhos, D. A. Hopper, R. R., A. Alkauskas, and L. C. Bassett. Optical signatures of quantum emitters in suspended hexagonal boron nitride. *ACS Nano*, **11**:3328–3336, (2017).

[159] N. R. Jungwirth and G. D. Fuchs. Optical absorption and emission mechanisms of single defects in hexagonal boron nitride. *Phys. Rev. Lett.*, **119**:057401, (2017).

[160] N. Mendelson, D. Chugh, J. R. Reimers, T. S. Cheng, A. Gottscholl, H. Long6, C. J. Mellor, A. Zettl, V. Dyakonov, P. H. Beton, S. V. Novikov, C. Jagadish, H. H. Tan, M. J. Ford, M. Toth, C. Bradac, and I. Aharonovich. Identifying carbon as the source of visible single-photon emission from hexagonal boron nitride. *Nat. Mater.*, **11**:321–328, (2021).

[161] J. D. Caldwell, I. Aharonovich, G. Cassabois, J. H. Edgar, B. Gil, and D. N. Basov. Photonics with hexagonal boron nitride. *Nat. Rev. Mater.*, **4**:552–576, (2019).

[162] R. E. Vanhouse. *The Construction and Testing of a Multi-mode Scanning Confocal and Atomic Force Microscope.* PhD thesis, School of Physics and Astronomy, University of Nottingham, (2020).

[163] A. Y. Meltzer, E. Levin, and E. Zeldov. Direct reconstruction of two-dimensional currents in thin films from magnetic-field measurements. *Phys. Rev. App.*, **8**:064030, (2017).

[164] D. E. Parkes, R. Beardsley, S. Bowe, I. Isakov, P. A. Warburton, K. W. Edmonds, R. P. Campion, B. L. Gallagher, A. W. Rushforth, and S. A. Cavill. Voltage controlled modification of flux closure domains in planar magnetic structures for microwave applications. *App. Phys. Lett.*, **105**:062405, (2014).

[165] P. Wadley, B. Howells, J. Železný, C. Andrews, V. Hills, R. P. Campion, V. Novák, K. Olejník, F. Maccherozzi, S. S. Dhesi, Y. S. Martin, T. Wagner, J. Wunderlich, F. Freimuth, Y. Mokrousov, J. Kuneš, J. S. Chauhan, M. J. Grzybowski, A. W. Rushforth, K. W. Edmonds, B. L. Gallagher, and T. Jungwirth. Electrical switching of an antiferromagnet. *Science*, **351**:587–590, (2016).

[166] A. Sajid, K. S. Thygesen, J. R. Reimers, and M. J. Ford. Edge effects on optically detected magnetic resonance of vacancy defects in hexagonal boron nitride. *Commun. Phys.*, **3**:153, (2020).

[167] A. Gottscholl, M. Kianinia, V. Soltamov, S. Orlinskii, G. Mamin, C. Bradac, C. Kasper, K. Krambrock, A. Sperlich, M. Toth, I. Aharonovich, and V. Dyakonov. Initialization and read-out of intrinsic spin defects in a van der waals crystal at room temperature. *Nat. Mater.*, **335**:540–545, (2020).

[168] N. Chejanovsky, A. Mukherjee, Y. Kim, A. Denisenko, A. Finkler, T. Taniguchi, K. Watanabe, D. Bhaktavatsala Rao Dasari, J. H. Smet, and J. Wrachtrup. Single spin resonance in a van der waals embedded paramagnetic defect. *Nat. Mater.*, **20**:1079–1084, (2021).